CARTILAGE TISSUE ENGINEERING FOR RHINOPLASTY

Atheer B Ujam

UCL Great Ormond Street Institute Of Child Health
University College London

Thesis submitted to UCL for the degree of Doctor of Philosophy

June 2020

DECLARATION

I, Atheer Ujam confirm that the work presented in this thesis is my own. Where information has been derived from other sources, I confirm that this has been indicated in the thesis and acknowledged.

ACKNOWLEDGMENTS

I would like to express my sincere gratitude to my supervisors Professor Patrizia Ferretti and Mr Neil Bulstrode for their continuous support throughout this research. I would like to thank Professor Ferretti for her encouragement, guidance, enthusiasm for teaching, and sparking curiosity in this thesis. Thank you for giving me this opportunity. I would also like to thank Mr Bulstrode for his guidance throughout this research. You were always generous with your time.

To Dr Dale Moulding, I am grateful for your help with many of the images presented in this work. I would like to thank Dr Eleanora Zucchelli for her support, her willingness to help and in teaching me the fundamentals of many methods used in this thesis. Your meticulous approach to science was inspirational. To Dr Oliver Gardner, who provided so much motivation, support and help with many of the experiments. I am extremely grateful for your time, advice, and sharing your passion for cartilage tissue engineering. You were truly inspirational. A special thanks to Dr Amel Ibrahim and Dr Natacha Agabalyan for their support during the early part of the thesis. Thank you also to Estephania Candelo Gomez for your help with 3D-bioprinting. To my other lab colleagues Citlali, Olivia, Despoina, and Jenny you were always there to help and with Eleanora, Natacha, and Olly made my time there enjoyable and memorable.

I am grateful to Sheng Long and Professor Wenhui Song for their help in 3D printing, to Olumide Ogunbiyi, and Aimee Avery for their help with embedding and to Dr Allessandro Borghi for his help with mechanical testing. I am very grateful to Professor Martin Birchall and Professor James McCaul for their guidance and to Mr Robert Bentley for approving my time out of surgical training to pursue this PhD. To the British Association of Oral and Maxillofacial surgeons, Saving Faces, the Royal College of Surgeons of England, GOSH BRC and the Enid Linder foundation who helped fund this thesis, I am incredibly thankful. I must also thank the patients and their parents who consented to provide tissue for this research.

I would like to thank Mr Nasser Nasser, who introduced me to the world of rhinoplasty. You are a wonderful mentor, an inspirational surgeon but above all a kind and dear friend. To my friend Mr Navin Vig, thank you for your support, advice, and pearls of wisdom on surviving a PhD.

Finally, I would like to acknowledge with gratitude, the support, motivation and love of my family- my brothers Layth and Samir; my sister Lemees; my wife Zainab and daughters Larsa, Haaleh and Faye. I am grateful to my mother, for her love and sacrifices over the years to make this PhD possible and to my father for his love, inspiration, and guidance on life, surgery and success; you set the standard.

ABSTRACT

Nasal surgery (rhinoplasty) has evolved considerably since its origins in Egypt around 1600BCE, yet modern reconstruction still relies on grafts harvested from autologous rib cartilage. Rib cartilage is an excellent graft material, but chest donor site morbidity can be a significant problem. The aim of this thesis was to create a patient specific cartilage surgical product using autologous stem cells that would provide surgeons with an effective alternative to rib cartilage.

Adipose-derived stem cells (ADSCs) and cartilage-derived stem/precursor cells (CSPCs) were used in this thesis as they can be harvested through minimally invasive procedures and their chondrogenic potential already widely established.

Using a novel tissue clearing protocol for whole mount imaging, primary experiments confirmed the ability of both cell types to self-organize and generate cartilage-like extracellular matrix (ECM) in 3D spheroids.

Three different methods of engineering cartilage in 3D were investigated. Firstly, a clinically approved collagen matrix was used as a scaffold and seeded with cells. Immunocytochemistry and histological staining demonstrated cartilage like ECM on the scaffold surface in preference to deeper regions. The collagen matrix proved too be tight and constrictive on cell expansion.

Secondly, a 3D bioprinter was used to print cells mixed with cellulose/alginate “bioink” hydrogels. This bioink failed to demonstrate cartilage like ECM in static culture and in a chick embryo chorioallantoic membrane (CAM) model.

Lastly, a cell laden fibrin hydrogel was “sandwiched” between 2 layers of polycaprolactone (PCL) sheets to provide mechanical support and grafted onto CAM. Histological analysis of cell laden fibrin confirmed regions of chondrogenesis by positive staining of collagen and glycosaminoglycans.

In conclusion, the results provide further understanding of how these cells respond to different 3D environments and the effect on chondrogenesis. Combining 3D bioprinting with a sandwich design may be an effective future approach to product development.

IMPACT STATEMENT

Rhinoplasty surgery (surgery to the nose) is one of the most commonly performed surgical procedures of the head and neck region and may be indicated in patients with congenital deformities, traumatic injuries, infective diseases, inflammatory disorders, or cancer of the nose. Nasal deformity can severely affect the quality of life of these patients because of both psychological and functional problems.

Tissue engineering is a rapidly expanding field that offers much promise for therapeutic intervention. The use of an autologous, easily accessible cell source for the repair of nasal defects would reduce the morbidity associated with current rhinoplasty techniques that rely on harvesting rib or ear cartilage to reconstruct the nose.

A better understanding of the environmental conditions that lead to the differentiation into specific tissues from somatic stem cells and to phenotypic stability of the tissue generated will provide an important platform for developing effective and safe approaches to tissue engineering using autologous cell sources. In this thesis, I have demonstrated the ability of adipose derived stem cells (isolated from human fat) and cartilage stem precursor cells (isolated from human ear) to generate mature cartilage in 3-dimensional (3D)-culture systems. Analysis of my results in this thesis and my development of new protocols have wide benefits to both inside and outside academia.

Within the immediate professional circle, there are teams developing tissue engineered airways and cartilage for ear reconstruction, both teams may benefit from my results. The data I have produced relating to biodegradable materials would be particularly useful to them. Other research groups in the UK developing novel strategies to replace damaged cartilage will also benefit from this research. For example, researchers aiming to repair or regenerate cartilage within the temporomandibular joint for arthritic changes will benefit from our results and techniques to grow mature cartilage.

There is massive interest within Orthopaedic surgery in the development of novel therapies using stem cells to regenerate joint cartilage. Furthermore, in the field of Ophthalmology, there is great interest in cartilage tissue engineering for reconstruction of eyelids (tarsal plate) following traumatic injury or cancer resection. Therefore, this research will be of interest to clinician scientists wishing to develop autologous cell-based therapies based on the use of somatic stem cells for the repair of cartilages in a variety of pathologies. The novel information generated will also benefit researchers working on stem cell biology and modulation of cell plasticity.

Given that I have used a variety of novel biodegradable scaffolds, this research will also be extremely useful to material scientists and engineers designing and developing novel scaffolds/scaffold topography and bioreactors that will be required to support generation of tissues with the desired stable phenotype on a larger scale. Hence the results of this research will benefit colleagues across several disciplines.

The results will be published in relevant tissue regeneration and surgical journals so that my methodology and results can be made available to other researchers within the same field and beyond. I have presented this research at local, national, and international scientific, and clinical meetings.

TABLE OF CONTENTS

Contents

CARTILAGE TISSUE ENGINEERING FOR RHINOPLASTY 1
DECLARATION 2
ACKNOWLEDGMENTS 3
ABSTRACT 4
IMPACT STATEMENT 5
TABLE OF CONTENTS 7
LIST OF FIGURES 10
LIST OF TABLES 16
LIST OF ABBREVIATIONS 17
Chapter 1 19
1.1 Introduction 20
1.2 The human nose 22
1.2.1 Nasal embryology 22
1.2.2 Nasal anatomy 24
1.2.3 Cartilage structure and molecular biology 30
1.3 Nasal deformity and septal injury 36
1.3.1 Congenital and acquired nasal deformity 36
1.4 Nasal reconstruction 41
1.4.1 A brief history of rhinoplasty 41
1.4.2 Historical use of grafting material in rhinoplasty surgery 43
1.4.3 Rhinoplasty 45
1.5 Tissue engineering cartilage – an alternative to rib harvesting 49
1.5.1 Mesenchymal stem cells 49
1.5.2 Scaffold and scaffold free 3D models for chondrogenesis 54
1.5.3 Imaging techniques for 3D cell culture analysis 64
1.6 Aims of the project 68
Summary 70
Chapter 2 71
2.0 Material and methods 72
2.1 Tissue acquisition 72
2.1.1 Adipose tissue and ear cartilage initial processing 72
2.2. Cell culture 73
2.2.1 Primary cell cultures 73
2.2.2 Cell expansion 76
2.2.3 Cell differentiation 77
2.2.3.1 Adipogenic differentiation 77

2.2.3.2 Chondrogenic differentiation 77
2.2.3.3 Osteogenic differentiation 77
2.2.4 Three-dimensional spheroid cell cultures 78
2.3 Preparation for cell imaging and analysis 78
2.3.1 Histology – Paraffin embedding and sectioning 78
2.3.2 Immunocytochemistry and Immunofluorescence 80
2.3.3 Tissue Clearing protocols 82
2.3.4 Microscopy 84
2.4 Integra Dermal Regeneration template 85
2.4.1 Integra cell seeding 86
2.5 Chick Chorioallaotic Membrane Assay 88
2.5.1 CAM Preparation 88
2.6 Three dimensional Bioprinting 90
2.6.1 Printing preparation 90
2.7 Three-dimensional printing of Polycaprolactone 94
2.7.1 Printer setup 94
2.8 Fibrin experiments 96
2.8.1 Fibrinogen/thrombin experiment protocols 96
2.9 PLA pocket 3D printing 100
2.9.1 Design software 100
2.10 Mechanical testing of lamb septum 100
2.10.1 Mechanical testing – Three-point bending 102
2.11 Statistics 103
Chapter 3 104
3.0 Background 105
3.1 Results 107
3.1.1 Spheroid cultures from ADSC and cartilage stem precursor cells (CSPCs). 107
3.2 Confocal microscopy analysis of whole mount spheroids 107
3.2.1 Determination of the most effective spheroid clearing method. 107
3.2.1.1 Spheroid imaging technique for BABB optical clearing 111
3.2.1.2 Development of microscope safe techniques for imaging 111
3.2.1.4 Inverted drop technique 113
3.2.2 Whole mount immunostaining and optical clearing of spheroids. 114
3.3 Discussion 131
3.3.1 Clearing solutions 131
3.3.2 Optimization of whole mount immunostaining protocol and optical clearing for inner-tissue imaging in small and large spheroids 132
3.4 Conclusion 133
Chapter 4 135

4.0 Background 136
4.1 Results 138
4.1.1 Analysis of ADSCs seeded on Integra bilayer membrane 138
4.1.2 Analysis of ADSCs seeded on single layer Integra 147
4.2.3 Characterisation of Integra grafts on CAM in-vivo model 162
..... 165
4.2.4 Pocket design and printing 166
4.3 Discussion 173
4.4 Conclusions 175
Chapter 5 177
5.0 Background 178
5.1 Results 181
5.1.1 Isolation of human auricular CSPCs and assessment of their differentiation potential 181
5.1.2 Viability of CSPCs in alginate/cellulose bioink 185
5.1.3 Expression of cartilage markers in 3D bioprinted CSPCs laden alginate/cellulose bioink 191
5.1.4 Expression of cartilage markers in 3D bioprinted CSPCs laden alginate/cellulose bioink in a CAM in-vivo model 201
5.2.5 Optimisation of PCL printing for sandwich design septal graft 208
5.2.6 Analysis of CSPCs in a fibrin-based hydrogel. 212
5.3 Discussion 221
5.4 Conclusion 224
Chapter 6 225
6.0 Summary of findings 226
6.1 Conclusion 228
6.1 Future work 229
APPENDIX 230
Figures 231
Media files 234
BIBLIOGRAPHY 235

LIST OF FIGURES

Figure 1.0. Facial embryology 22

Figure 1.1. Development of the nasal septum 23

Figure 1.2. Anatomy of the adult nose 24

Figure 1.3. Nasal septal dimensions 26

Figure 1.4. An overview of all the nasal cartilages 27

Figure 1.5. Hyaline cartilage histology 30

Figure 1.6. Occupational nasal injury with metal grinder in an adult patient 37

Figure 1.7. Secondary cleft nasal deformities 40

Figure 1.8. Rhinoplasty- The Italian method 42

Figure 1.9. Nasal subunits 45

Figure 1.10. Rib harvesting 47

Figure 1.11. Costochondral grafts for rhinoplasty 48

Figure 1.12. Adult right ear conchal bowl cartilage harvesting, posterior approach ... 52

Figure 1.13. Bilayer Integra dermal regeneration template 60

Figure 1.14. Three strategies to generating cartilage tissue 70

Figure 2.0. Lipoaspirate from paediatric patients 73

Figure 2.1. Stromal vascular fraction 74

Figure 2.2. Human ear cartilage 75

Figure 2.3. Antibody applied to cover slips 80

Figure 2.4. Integra Dermal Regeneration template (IDRT) 85

Figure 2.5. Integra seeded with $6x10^6$ Ch90 mCherry cells 87

Figure 2.6. CAM experiment 89

Figure 2.7. Cell/Bioink mixing protocol 92

Figure 2.8. 3D printing of PCL 95

Figure 2.9. Fibrin constructs 96

Figure 2.10. PCL/Fibrin Sandwich construct fabrication 98

Figure 2.11. PCL fibrin sandwich and controls 99

Figure 2.12. Lamb nasal septum harvesting 101

Figure 2.13. Three-point bending test 102

Figure 3.0. Spheroid macroscopic appearance after clearing with different ..... protocols 109

Figure 3.1. Two-photon microscopy optical sectioning of Hoechst dye-stained spheroids after clearing with different protocols 110

Figure 3.2. Figure 3.2. Spheroid confocal imaging with water dipping objective 112

Figure 3.3. Fig 3.3. Inverted drop BABB cleared spheroid technique 113

Figure 3.4. Undifferentiated ADSC-derived spheroids (6 weeks, 1x10^5cells) stained for 24 (A) and 48 (B) hours with Hoechst nuclear dye and cleared with BABB 115

Figure 3.5. Immunostaining with the 48 hour protocol of BABB-cleared ADSC spheroids (1.0x10^5 cells, n=1) chondrogenically differentiated for 6 weeks 117

Figure 3.6. Immunostaining with the 48 hour protocol of BABB-cleared ADSC spheroids (1.0x10^5 cells, n=1) chondrogenically differentiated for 6 week..... 118

Figure 3.7. Confocal imaging with immersion objective at surface (-25µm) of spheroid in figure 3.6..... 119

Figure 3.8. Immunostaining with the 96 hour staining protocol of BABB-cleared undifferentiated ADSC spheroids (3.0x10^5 cells, n=1..... 121

Figure 3.9. Immunostaining with the 96 hour staining protocol of BABB-cleared ADSC spheroids (3.0x10^5 cells, n=1) chondrogenically differentiated for 6 weeks..... 122

Figure 3.10. Genetically labelled ADSCs and CSPCs..... 123

Figure 3.11. Surface debris on BABB cleared chondrogenically differentiated GFP+ ADSC spheroids (1x10^5, 6 weeks incubation, n=3) stained with Hoechst dye..... 125

Figure 13.12. Whole-mount Hoechst staining for 96 hours of BABB cleared ADSC $eGFP^+$ labelled spheroids 1x10^5 cells, 6-week incubation in chondrogenic medium. 126

Figure 3.13. Core regions of the spheroid Fig 3.10 127

Figure 3.14. Immunostaining with the 96 hour protocol of BABB-cleared $eGFP^+$ labelled ADSC spheroid (1.0x10^5 cells, n=3), chondrogenically differentiated for 6 weeks 129

Figure 3.15. Immunostaining with the 96 hour protocol of BABB-cleared mCherry labelled CPSC spheroid (1.0x10^5 cells, n=3), chondrogenically differentiated for 6 weeks 130

Figure 4.0. Initial Integra experiment using bilayer Integra cut into 8mm discs seeded with $eGFP^+$ and $mCherry^+$ labelled ADSC..... 139

Figure 4.1. Fluorescent inverted microscope images of $eGFP^+$ and $mCherry^+$ labelled ADSCs (1x10^4 cells) seeded onto Integra membrane in control (A) and chondrogenically differentiated (B) medium. Images at 1 week and 10 weeks culture..... 140

Figure 4.2. Two-Photon confocal fluorescent imaging at the centre of an Integra disc without cells 141

Figure 4.3. Confocal microscopy of Integra bilayer matrix disc seeded with mCherry labelled ADSCs ($1x10^4$) stained with Hoechst nuclear stain in chondrogenic medium at 18 weeks culture 143

Figure 4.4. Confocal imaging of chondrogenically differentiated Integra bilayer discs. (A) 3D image (z-stack) of $eGFP^+$ Integra 144

Figure 4.5. Two-photon confocal imaging at the middle depth of Integra discs seeded with $eGFP^+$ labelled ADSC. Chondrogenic differentiation and undifferentiated control 145

Figure 4.6. Two-photon confocal imaging at the middle depth of Integra discs seeded with $mCherry^+$ labelled ADSC 146

Figure 4.7. Macroscopic appearance of Integra (1x1cm squares) with and without ASDCs or CSPCs and either maintained in control or chondrogenic medium 148

Figure 4.8. Live dead assay of ear cartilage derived precursor cells in Integra matrix at day 7 incubation in control medium 149

Figure 4.9. Confocal images of Integra seeded with eGFP-labelled ADSCs (H37).. 151

Figure 4.10. Confocal images of Integra seeded with mCherry-labelled CSPCs (Ch90) stained for collagen II 152

Figure 4.11. Confocal images of chondrogenically differentiated mCherry-labelled CSPCs in Integra 153

Figure 4.12. CSPC (Ch90 p13) mCherry labelled cells seeded at 6million onto Integra and spun for 30 seconds at 5000rpm 155

Figure. 4.13. H & E and Alcian blue staining of paraffin embedded sections of Integra without cells and with undifferentiated CSPCs 157

Figure 4.14. Paraffin embedded sections of Integra seeded with $5x10^5$ CSPCs (Ch90) in chondrogenic medium 158

Figure 4.15. Integra with CH90 CSPC. Paraffin embedded section stained with H&E and Alcian blue 160

Figure 4.16. Spheroid-like masses at the surface of an Integra matrix with CH90 CSPC in differentiation medium incubated for 22 weeks. Paraffin embedded sections stained with H&E and Alcian blue 161

Figure 4.17. In ovo images of Integra CAM grafts at day 7 implantation at low and higher magnification 163

Figure 4.18. Brightfield polarised microscopy of CAM grafted Integra sheet without seeded cells stained with toluidine blue and picrosirius red 164
Figure 4.19. Brightfield polarised microscopy of CAM grafted Integra sheet without seeded cells stained with toluidine blue (A) and picrosirius red (B), (magnified image Fig 4.21) 165
Figure 4.20. Pocket design concept 167
Figure 4.21. Pocket designs with holes 167
Figure 4.22. Photograph of PLA septal pockets printed with PLA filament to full scale 168
Figure 4.23. PLA squares printed at 10x10x1mm dimension with 2-layer print at 80% infill density 169
Fig 4.24. Assessment of eGFP-labelled ADSC (H37 P8) migration through Integra and PLA square 24 hours after seeding 170
Figure 4.25. Integra insertion into PLA pocket 172
Fig 4.26. PLA modification 176
Figure 5.1. Ear cartilage explant (CH105) stem cell isolation, expansion and trilineage differentiation. (Ai) Ear cartilage explant 182
Figure 5.2. Histology of normal ear cartilage (CH105) stained with H&E and AB 184
Figure 5.3. 2-photon confocal imaging of mCherry^{+} labelled CSPCs within alginate/cellulose bioink 186
Figure 5.4. Fluorescent microscopy images of CSPC viability and mortality in 3D bioprinted cell laden RGD bioink 187
Figure 5.5. Fluorescent microscopy images of CSPC viability and mortality in 3D bioprinted cell laden alginate/cellulose bioink 188
Figure 5.6. A comparison of CSPC viability and mortality in non-printed and printed cartilage constructs 189
Figure 5.7. Live/dead assay of printed CSPC laden bioink crosslinked with calcium chloride for three different lenghts of time 190
Figure 5.8. Toluidine blue red staining of sections from CSPCs bioprinted in alginate/cellulose bioink and cultured in either control or chondrogenic medium for 21 days 192
Figure 5.9. Picrosirius red staining of sections from CSPC bioprinted in alginate/cellulose bioink and cultured in either control or chondrogenic medium for 21 days 193

Figure 5.10. Toluidine blue staining of sections from CSPCs bioprinted in alginate/cellulose bioink and cultured in either control or chondrogenic medium for 6 months 195
Figure 5.11. Picrosirius red staining of 6 months undifferentiated (control) and differentiated CSPCs bioprinted in alginate/cellulose bioink 196
Figure 5.12. Expression of Collagen II and Vimentin at 21-day incubation in a section from a control bioprinted construct 198
Figure 5.13. Expression of Collagen II and Vimentin at 21-day incubation in a section of chondrogenically differentiated CSPCs bioprinted in alginate/cellulose. 199
Figure 5.14. Expression of Collagen II and Vimentin at 21-day incubation in a section of a chondrogenically differentiated CSPCs bioprinted in alginate/cellulose 200
Figure 5.15. Macroscopic view of 21-day pre-cultured control and pre-differentiated bioprints of CH90 CSPC in alginate/cellulose bioink 202
Figure 5.16. Toluidine blue and Picrosirius red staining of an undifferentiated (control) bioprinted construct grafted onto the chick chorioallantoic membrane (CAM) 204
Figure 5.17. Toluidine blue and Picrosirius red staining of a chondrogenically differentiated bioprinted construct grafted onto CAM 205
Figure 5.18. Toluidine blue staining of chondrogenically differentiated bioprints in CAM 206
Figure 5.19. Toluidine blue staining of chondrogenically differentiated bioprints (2^{nd} biological replicate) in CAM 207
Figure 5.20. PCL printing Grid and Rectilinear infill patterns 209
Figure 5.21. 10x10x1mm PCL prints using Grid infill pattern with 70%infill density . 210
Figure 5.22. Toluidine blue and Picrosirius red staining of day 0 CSPC laden fibrin constructs 214
Figure 5.23. Toluidine blue stain of control CSPC laden fibrin constructs at day 21 215
Figure 5.24. Picrosirius red stain of control CSPC laden fibrin constructs at day 21. (A) low magnification brightfield image of construct 216
Figure 5.25. Toluidine blue stain of chondrogenic differentiated CSPCs laden fibrin constructs at day 21 217
Figure 5.26. Brightfield images of Picrosirius red stain of chondrogenic differentiated CSPCs laden fibrin constructs at day 21 218
Figure 5.27. Polarised light images of Picrosirius red stain of chondrogenic differentiated CSPCs laden fibrin constructs at day 21 219

Figure 5.28. CAM grafts of PCL discs. PCL mesh printed with 500µm nozzle at 650kPa extrusion pressure and cut out with 8mm punch 220
Figure A1. Lamb nasal septum mechanical testing data 231
Figure A2. Graphs of results of lamb nasal septum mechanical testing 232
Figure A3. Confocal imaging of non-cleared, 6 week chondrogenically differentiated eGFP labelled ADSC spheroid ($1.0x10^5$ cells). Images taken with dipping objective at surface and -250µm..... 234

LIST OF TABLES

Table 1.0. Summary of key features of the three types of human cartilage 32

Table 1.1. Collagen 33

Table 1.2. Summary of publications using Integra as a cell scaffold 62

Table 2.0. Summary of patient samples used in this thesis 72

Table 2.1. List of primary and secondary antibodies used for immunocytochemistry . 82

Table 2.2. Summary of antibody immunostaining and clearing for whole mount spheroids 83

Table 3.0. Cell lines used to generate spheroids in this chapter 107

Table 4.0. Cell lines used in Integra experiments 138

LIST OF ABBREVIATIONS

2D	Two -Dimensional
3D	Three-Dimensional
AB	Alcian Blue
Ab	Antibody
ADSC	Adipose-Derived Stem Cells
ASA	Anterior septal angle
BABB	Benzyl Alcohol:Benzyl Benzoate
BM	Bone Marrow
CAM	chorioallantoic membrane
COL II	Collagen 2
CSPCs	Cartilage Stem/Precursor Cells
CT	Computerised tomography
dH_20	Distilled Water
DMEM	Dulbecco`s Modified Eagle Medium
DMSO	Dimethyl sulfoxide
ECM	Extracellular Matrix
EDTA	Ethylenediaminetetraacetic acid
EGFP	Enhanced Green Fluorescent Protein
ES-FBS	Fetal Bovine Serum
FDA	Food and Drug Administration
FDM	Fused Deposition Modelling
GAG	Glycosaminoglycan
H&E	Haematoxylin And Eosin
HCL	Hydrochloric acid
HOX	Homeobox Transcription Factor
HPL	Human platelet lysate
IDRT	Integra Dermal Regeneration Template
IF	Immunofluorescence
IHC	Immunohistochemistry
ISCT	International Society for Cell & Gene Therapy
ITS	Insulin-Transferrin-Selenium

LBL	Layer by Layer
MHDS	Multihead Deposition System
MRI	Magnetic resonance imaging
MRSA	Methicillin-resistant Staphylococcus aureus
MSCs	Mesenchymal Stem Cells
MW	Molecular Weight
PBS	Phosphate-Buffered Saline
PBS-T	Phosphate-Buffered Saline with Tween
PCL	Polycaprolactone
PCR	Polymerase Chain Reaction
PFA	Paraformaldehyde
PGA	Polyglycolide or poly(glycolic acid)
PGs	Proteoglycans
PLLA	Poly-L-lactide
PDLLA	Poly-DL-lactide
PSA	Posterior septal angle
RI	Refractory Index
S.Aureus	Staphylococcus aureus
SEM	Scanning electron microscopy
SMAS	Superficial musculo-aponeurotic system
STL	StereoLithography also Standard Tessellation Language
SVF	Stromal Vascular Fraction
TGFβ	Transforming Growth Factor beta
TMJ	Temporomandibular joint
UV	Ultra-violet
VIM	Vimentin

Chapter 1

INTRODUCTION

1.1 Introduction

In 2013 Bangalore, India, having just harvested rib cartilage to reconstruct a 15-year-old girls cleft nose, I became conscious of the possibility that there must be a better way to obtain cartilage that avoids leaving patients with a permanent chest scar- a constant reminder of their surgery. This was the spark that initiated my quest to undertake research into cartilage tissue engineering.

Costochondral rib grafts provide excellent cartilage volume and quality to reconstruct many regions of the face, particularly the nose. The problem is the associated chest wall deformity, scar, risk of pneumothorax and pain. Rib cartilage remains the gold standard for nasal grafts as it can be carved to reconstruct and repair nasal septum, upper and lower lateral cartilages, and the dorsum. Historically, surgeons have tried different graft materials both synthetic and natural, but none have proven to be predictable and long lasting.

In this thesis, I have explored the potential of regenerative medicine and stem cell biology to provide an alternative source of cartilage that can be used clinically in rhinoplasty surgery to replace or augment the cartilages of the nose. Given the simple flat shape and dimensions of nasal septum, I chose to investigate septal cartilage as the primary cartilage to generate.

The path to generating a nasal septal graft is not simple and comes with numerous challenges and practical considerations. Primarily, this is not only to generate mature cartilage but to be able to translate this to the operating room in a product that surgeons can handle and manipulate confidently. Furthermore, the “regenerated” cartilage must withstand the forces of overlying skin drape and maintain a similar shape, volume, and dimension over time to avoid resorption and late onset relapse. Unlike traditional tissue engineering methods that rely on stem cells seeded directly onto a hard polymer scaffold, this thesis focused on a product design that contains a central cartilaginous region “sandwiched” between two sheets of resorbable polymer material. This central region represents stem cells mixed within a hydrogel to provide a three-dimensional (3D) environment for the cells to expand and deposit chondrogenic matrix. The advantage of this concept is that the cartilage core will mature independently of the resorption of the outer scaffold material that serves only to provide mechanical strength. The result should be a uniform homogenous layer of cartilage in-situ within the nose. In many ways, this can be considered a “scaffold free” approach to cartilage tissue engineering.

Using adipose derived stem cells (ADSC) and cartilage-derived stem/precursor cells (CSPCs) mixed with different hydrogels, I have investigated 3 different approaches to fabrication of the nasal septal product that exploits the advantages of the “sandwich” concept. The pathway to regenerate nasal septal cartilage begins by demonstrating that ADSCs and CSPCs have an intrinsic preference to expand in 3D to maintain their chondrogenic differentiated state and this forms the basis of the results in chapter 3. The results of using different hydrogels and polymer scaffolds that may be suitable for the septal product is then discussed in subsequent chapters. Furthermore, utilising 3D bioprinting technology and printing cells with “bioink” forms a significant part of the thesis.

1.2 The human nose

1.2.1 Nasal embryology

During the 5th week of embryological development, maxillary, mandibular and frontonasal prominences become evident. Thickenings of surface ectoderm on both sides of the frontonasal prominence form the nasal (olfactory) placodes. Invaginations within the placodes form primitive nasal pits. The surrounding mesenchymal proliferation adjacent to the nasal pits creates the medial and lateral nasal prominences (Fig. 1.0). By the 7th week of development, medial growth of the maxillary prominences results in compression of the medial nasal prominences and ultimately their fusion. This medial growth results in the formation of the upper lip (formed by fusion of the medial nasal prominences together and to the maxillary prominences). Finally, the nose by the 10th week takes shape and is formed by five facial prominences (T.W.Sadler, 1995).

The nasal sacs are formed by progressive deepening of the nasal pits at the start of 6th week development which later form the primary nasal cavities.

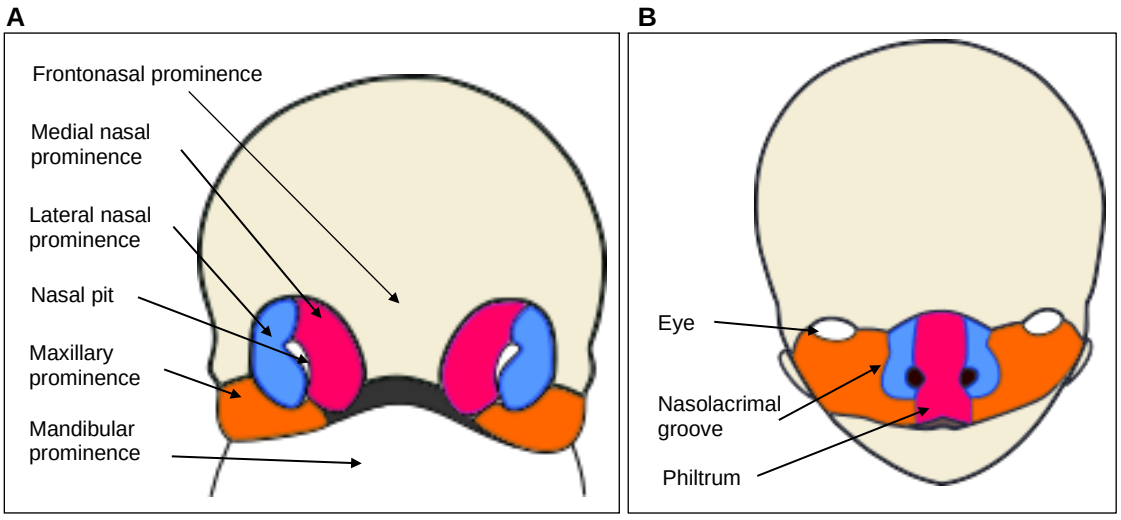

Figure 1.0. Facial embryology. (A) Front view of a five-week developing embryo. The medial and lateral nasal prominences surround the nasal pit which later form the central and lateral regions of the nose. **(B)** Formation of the nose is dependent on full fusion of the medial nasal prominences to the maxillary prominences. By 10 weeks, the early nose has taken shape being formed from the two maxillary prominences, two lateral nasal prominences and the fused medial nasal prominences. The lateral nasal prominences develop to form the nasal alae, the medial nasal prominences also contribute to the upper lip philtrum (*Reproduced from T.W.Sadler. (1995) Langmans Medical Embryology, Williams & Wilkins*).

By the 6th week, a thin membrane that separates the nasal cavity from the oral cavity (oronasal membrane) ruptures to form the primitive posterior choanae. By the 8th week, the two primary choanae have enlarged and the nasal septum will develop from tissue between them, with growth in a ventro-dorsal direction (Fig. 1.1). Development of the nasal septum appears to be derived from tissue between the primary choanae (Steding and Jian, 2010).By this time the palatal shelves begin to fuse with each other and the developing nasal septum. The intermaxillary segment formed by fusion of the nasomedial processes will later form the primary palate, tip and crest of the nose and will contribute to the nasal septum (Neskey et.al 2009).

In summary, the nasal septum develops within the frontonasal prominence from mesenchyme condensation that forms the precartilaginous nasal septum. By the middle of the 6th week, cartilage from the body of the developing sphenoid bone extends forward into the nasal septum, forming the primary cartilage of the septum.

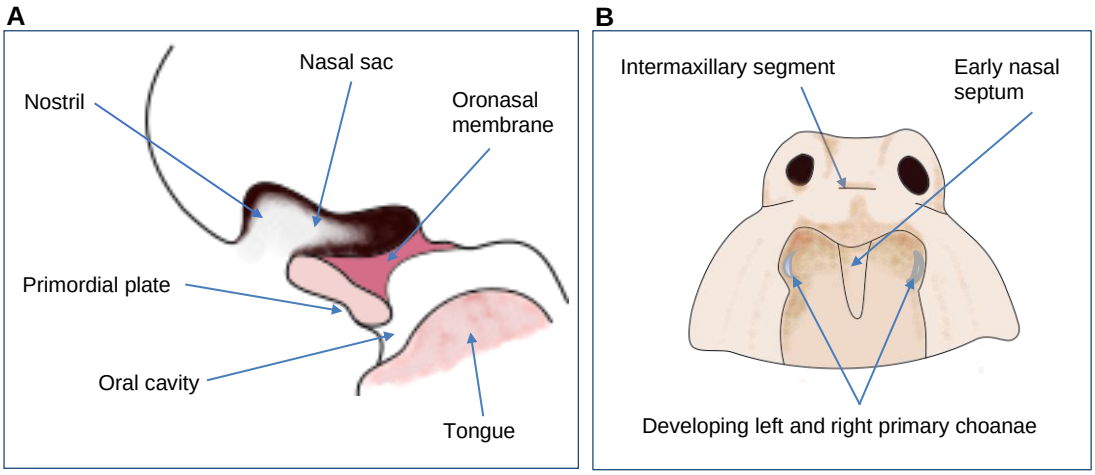

Figure 1.1. Development of the nasal septum. (A) The rupture of the oronasal membrane creates a communication between the nose and the oral cavity and demarcates the area of the primary choana. **(B)** Caudal view of the oronasal cavity at seven weeks. The nasal septum will later develop in an area between the two primary choana in a ventro-dorsal direction and by the middle of the 8th week will have fused with the palatal shelves.

1.2.2 Nasal anatomy

The nose is formed by a framework of bone and cartilage covered by skin and lined by nasal mucosa. Beneath the layer of skin there is subcutaneous fat, numerous nasal muscles, paired upper and lower lateral cartilages, a cartilaginous septum that divides the nasal cavity in two and a pair of nasal bones (Fig. 1.2). The nasal superficial musculoaponeurotic system (SMAS) is an anatomical structure that extends from the glabellar region to the nostril margin that unifies the muscles and ligaments (including the dermocartilaginous ligament) that overly the bony and cartilaginous nasal framework (Pitanguy et al., 1995; Saban et al., 2008). This cartilaginous and bony framework is fundamental to the function and aesthetics of the nose. Despite being relatively small, and thin, they support the soft tissue of the nose and the weight of the overlying skin drape. Internally, the nose is lined by a layer of mucous membrane but is stratified squamous epithelium anteriorly at the nasal vestibule (Menick, 2010).

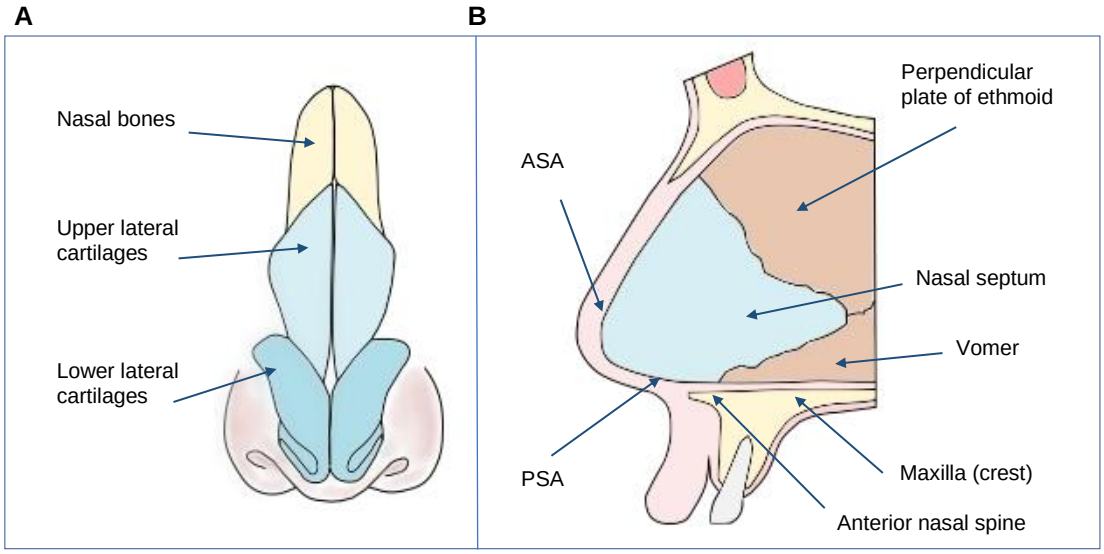

Figure 1.2. **Anatomy of the adult nose. (A)**There are a pair of upper lateral and lower lateral cartilages and a single midline septum (reproduced from www.mayoclinic.org). **(B)** Behind the nasal septum are two bone attachments, the ethmoid superiorly and the vomer inferiorly. The lower edge of the septum rests on the maxillary crest. The anterior septal angle (ASA) represents the junction of the dorsal and caudal borders of the septum and the posterior septal angle (PSA) represents the junction between the caudal and inferior border.

1.2.2.1 Nasal septum

The nasal septum is divided into the cartilaginous region and the bony portion involving the perpendicular plate of ethmoid superiorly and the vomer inferiorly. The cartilaginous septum is traditionally described as quadrangular in shape with two surgically important septal angles, the anterior and posterior septal angles.

The dimensions of the cartilaginous septum have been investigated extensively, with the data demonstrating males having greater variability in cartilage area compared to female noses (more cartilage in males) and that significant variation exists between adults (Miles et al., 2007). Hwang et al.2010, examined 14 Korean adult cadavers and showed a mean length of the cartilaginous septum as 3.31± 0.53 cm and a mean height of 2.99± 0.47cm. This study found that septal thickness varied with the thickest region being the septal base anterior to the vomer and measured 2.19-3.03mm. The region just above the base (taken as maxillary crest) at 20% of the septal height, was found to be the thinnest at a measurement of 0.74-0.97mm thick (Hwang et al., 2010).

Other studies have investigated the different lengths of each margin of the cartilaginous septum, offering further useful measurements required to design tissue engineered cartilage. In one study, nasal septal margins (dorsal, cephalic, ventral and caudal) were measured from ten adult Filipino Malay cadavers with the mean area of the septal cartilage measured as 652.5mm^2 (Pernia et al., 2011). The mean length of each margin of the nasal septum was also measured (Fig 1.3).

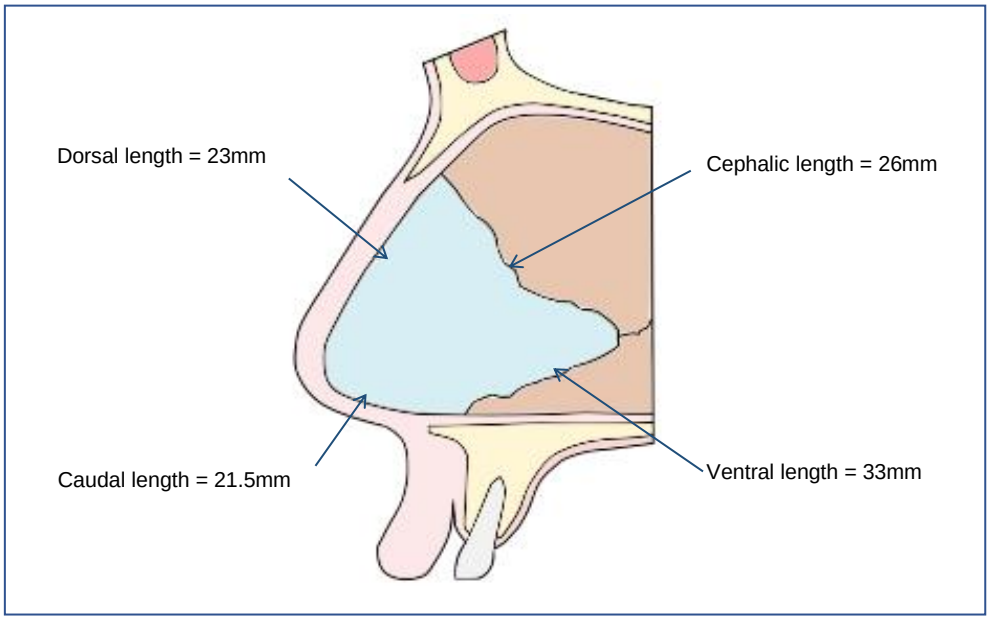

Figure 1.3. Nasal septal dimensions. Measurements represent mean lengths of the margins of the septum. The mean area of septal cartilage measured in this study was 652.5mm^2.

1.2.2.2 Upper and lower lateral cartilages

The upper and lower lateral cartilages of the nose are essential for nasal function and both contribute greatly to nasal appearance. The upper lateral cartilages extend laterally from the dorsal septum, are attached to the nasal bones superiorly and to the nasal process of the maxilla posteroinferiorly. These paired cartilages extend laterally from the dorsum and form the lateral walls of the middle third of the nose (Fig 1.4).Caudally they are attached to the lower lateral cartilages (Rohrich et al., 2016). They are an important component of the internal nasal valve that contributes to air flow resistance through the nasal passages (Wexler and Davidson, 2004). The rhinoplasty surgeon must have a firm understanding of the function and anatomy of the upper lateral cartilages to achieve both a functional and aesthetic nasal result (Pensler, 2009). There is limited evidence regarding the dimensions of the upper lateral cartilages but cadaveric studies indicate that the caudal-cephalic length is at least 15.8mm on average, with further overlap at the cephalic border with the nasal bones by 6-8mm or as much as 11mm (Rohrich et al., 2016) (Palhazi et al., 2015).

The lower lateral cartilages are essential components of the external nasal valve which is in the region around the nostril opening. Abnormalities of the cartilages here may cause significant nasal obstruction and reduced nasal breathing (Hamilton, 2017).

The lower lateral cartilages (alar cartilage) can be found with variable morphology. The lateral aspect (lateral crus) which contributes to the dome of the tip of the nose can be convex or concave. There is also variation in the size of the height and width of the lateral crus, with average measurements of 1.1cm and 2.2cm respectively (Natvig et al., 1971; Zelnik and Gingrass, 1979).

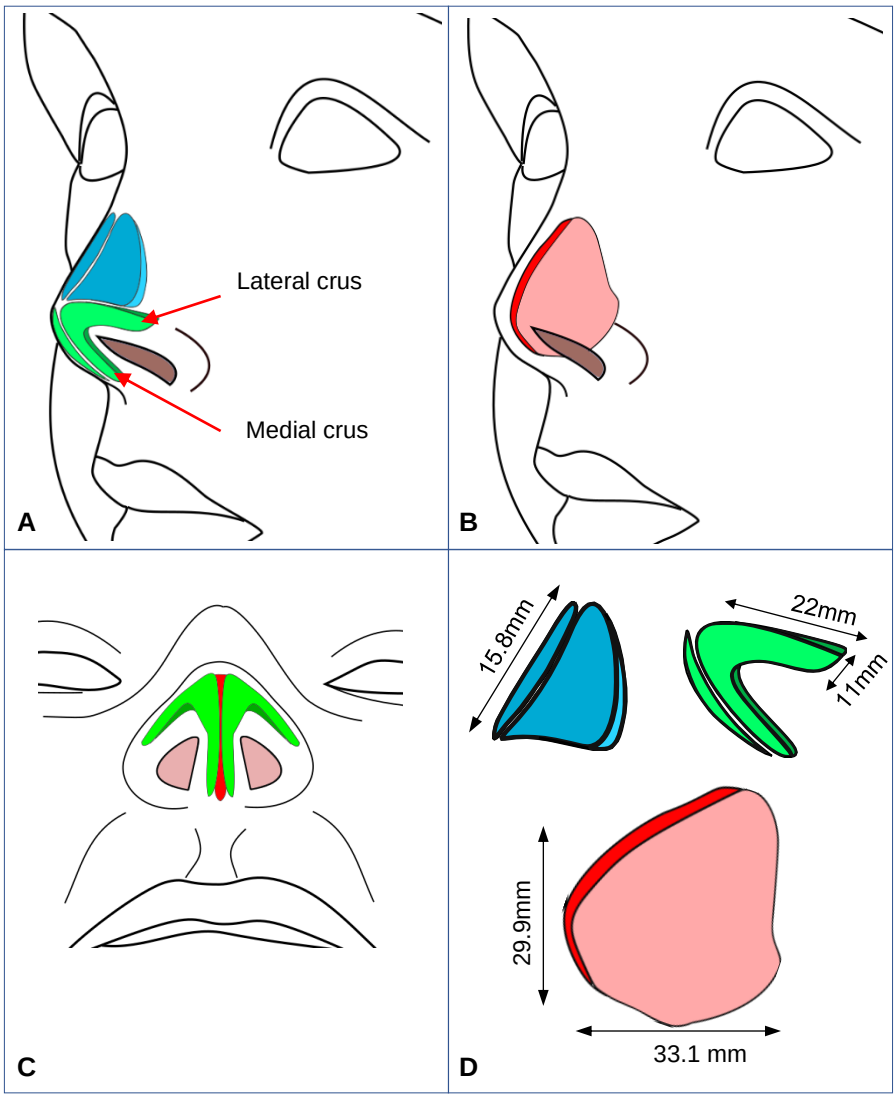

Figure 1.4. An overview of all the nasal cartilages. (A) The upper lateral cartilages (blue) and the lower lateral cartilages (green) are paired and contribute to the nasal tip and dorsum**. (B)** Deep to the lateral cartilages is the nasal septal cartilage (red) which divides the airway into left and right passages and at its cephalic edge also contributes to the dorsum of the nose. Traditionally, the septum is described as quadrangular in shape. **(C)** Caudal view of the nasal tip highlighting the lower lateral (alar) cartilages and the position of the septum. **(D)** Approximate dimension of the cartilages**.** Orientation of the individual cartilages are as depicted in (A) and (B). *Drawings by A Ujam.*

1.2.2.3 Paediatric nasal anatomy and development

There are important differences between the nose of a new-born, children, and adults. Nasal reconstructive surgery requires an understanding of this differing anatomy to avoid potential complications, and is essential in tissue engineering patient specific cartilage (Verwoerd and Verwoerd-Verhoef, 2007). The paediatric nasal septum is a combination of thin regions and thicker growth zones. Typically, neonatal nasal septal thickness varies from 0.4mm anteriorly to 3.5mm in the posterior region. Furthermore, there is a difference in the histology between the thin anterior region and the other posterior regions of the septum (Loosen, 2000). In contrast, the mature adult nose is anatomically easier to define and dissect surgically as all the cartilages are separated into upper lateral, lower lateral and the septum.

By the age of two years old the cartilaginous septum reaches adult dimensions (Loosen et al., 1996). Importantly, the nasal septum in children, adolescents and adults demonstrates differential zones of growth. Vetter et al investigated growth activity in human septal cartilage from prepubertal, pubertal and adult patients undergoing septoplasty using ^{35}S-labeled $NaSO_4$ and determined that there is high growth activity in the anterior free end of the septum in all age groups. In the prepubertal age group the supra-premaxillary area also showed similar high growth activity (Vetter et al., 1983). Further study of human nasal septum by Vetter et al demonstrated that the anterior free end of the septal cartilage shows high metabolic activity by proteoglycan synthesis and chondrocyte proliferation from childhood to adult age (Vetter et al., 1984). Other biochemical changes to the septum with aging is the significant reduction in proteoglycan content (Lee et al., 2013) . Other studies have also highlighted the importance of the anterior nasal septum. Studies on 42 identical twins with different septal deformities indicate that anterior septal deformities result in underdeveloped cartilaginous noses and a shorter antero-posterior dimension of the maxilla (Grymer et al., 1991).

With regards to significant nasal growth (growth spurt), this appears to be from around 8 years to 12 years of age for girls and around 13 years for boys. This growth spurt lasts for a few years and by the age of 13.4 years for girls and 14.7 years for boys, nasofacial growth velocity has decreased significantly. This is followed by slower nasal growth (nasal length and nasal protrusion) until the early twenties (Verwoerd and Verwoerd-Verhoef, 2010; Zankl et al., 2002).

1.2.2.4 Nasal septal mechanical properties

Nasal reconstruction commonly requires cartilage to be harvested from either the septum, ear, or rib. With regards to costochondral grafts, the surgeon can manipulate the harvested cartilage to the desired shape and thickness and, where rigidity and strength are essential such as septal or columellar grafts, rib cartilage is an excellent option. If engineered cartilage is to become a clinically realistic alternative option to costochondral grafting for nasal reconstruction, its mechanical properties must be similar to native cartilage. Furthermore, an engineered septum must have sufficient mechanical properties not only to withstand the forces of local soft tissue and avoid deformity but must also have the sturdiness of being held by surgical instruments and positioned into the required surgical location. Native septum mechanical properties have been reasonably well investigated, more so with the widening interest in regenerative medicine and tissue engineering.

The mechanical behaviour of cartilage can be characterised in several ways, and importantly, must reflect the typical deformations experienced clinically. One technique uses a three-point bending apparatus mounted in a mechanical spectrometer. Roy et al. investigated the mechanical properties of 4-8 week old fresh auricular cartilage and costal cartilage from pigs. The modulus of auricular cartilage in bending was found to be 4.6 MPa and that of costal cartilage 7.1MPa (Roy et al., 2004a). Other studies have investigated human septal tissue using 3-point bending test and found that the flexural modulus was 1.97± 1.25 MPa(Caffrey et al., 2013).

Richmon et al. 2006, studied the compressive and tensile biomechanical properties of human nasal septal cartilage. In their research, they investigated the compressive properties of 21 septal cartilage specimens in along different axes of compression using a mechanical spectrometer. Their results showed that septum has a compressive stiffness that is significantly higher in the vertical (compressive modulus 0.7±0.12 MPa) and caudal-cephalic orientation (0.66±0.01MPa) than in the medial orientation (0.44±0.04MPa) (Richmon et al., 2006). This anisotropic property of nasal septal cartilage is useful to define when determining the required properties of a tissue engineered cartilage graft. Richmon et al. also investigated the tensile properties of 300µm thick human nasal septum under dynamic and equilibrium tensile testing conditions from 28 patients. They found no difference in tensile properties between male and female samples and no significant effect of orientation (unlike compression) on tensile properties. Equilibrium modulus was found to be 3.01±0.39 MPa and dynamic modulus 4.99±0.49 MPa. (Richmon et al., 2005), which is nearly identical to that of auricular cartilage. A tissue engineered graft should have similar, if not better biomechanical properties.

1.2.3 Cartilage structure and molecular biology

Chondrocytes are highly differentiated cells that are solely responsible for producing cartilage in the human body. They are derived from chondroblast mesenchymal progenitor cells. These cells synthesize the extracellular matrix (ECM) of cartilage, the organisation of which provides the structural and molecular environment surrounding the chondrocytes (Fig 1.5).

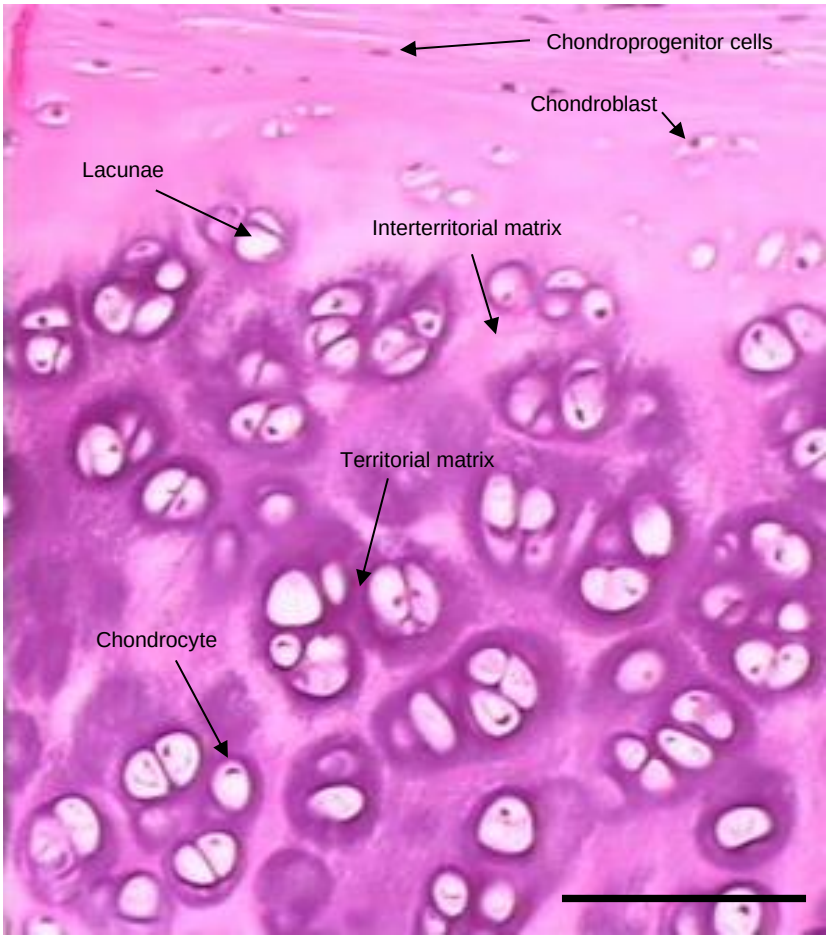

Figure 1.5. Hyaline cartilage histology. Chondroblasts and immature chondrocytes are found at the periphery in the perichondrial layer and are flat and single cells. Mature chondrocytes are found in central areas of cartilage and are embedded in ECM. They reside in lacunae and are large (undergoing hypertrophy) with a basophilic cytoplasm. They are also found as several cells together known as isogenic groups, a result of their cell division. Territorial matrix surrounds the lacunae and is basophilic, whereas the matrix between chondrocytes is lighter staining and is called interterritorial. Scale bar: 100µm.
Reproduced from: https://www.slideshare.net/sonnareach168/lecture5-cartilage-bone.

Few cells are required to produce mature functional cartilage and there is an inverse relationship between cell density and cartilage thickness. Chondrocytes account for only 1% of the volume of mature cartilage. In mature adult cartilage, water accounts for 70-80% of the weight of cartilage tissue (Homicz et al., 2003; Mahmoudifar and Doran, 2012)

Due to its low oxygen demands and poor vascularity, chondrocytes rely on anaerobic metabolism for their energy needs and therefore produce lactate from glucose metabolism. Once mature cartilage has formed and maximal growth has been achieved, chondrocytes cell division stops.

Cartilage is a specialised connective tissue having important properties of being stiff yet permanently flexible and resilient. It is found throughout the body with three different morphologies and composition.

1. Hyaline cartilage is found throughout the body and is located mainly on the articulating surfaces of bones and their joints (articular cartilage). Other forms of hyaline cartilage are found at the sternal ends of ribs (costal cartilage) and within the nose such as septal cartilage. Hyaline cartilage is also found in the developing foetal skeleton which is then replaced by bone during endochondral ossification. Typically, hyaline cartilage has a uniform appearance and is semi-solid.
2. Fibrocartilage is found in regions of the body where significant mechanical stress is encountered and therefore has high tensile strength. An example is the annulus fibrosus which is the tough exterior of the intervertebral discs of the spine and the menisci of the knee joint. Fibrocartilage is also found at the pubic symphysis, the distal radioulnar joint of the wrist as well as at the sites of tendon and ligament attachment to bone. Collagen type I is the main ECM protein in fibrocartilage.
3. Elastic cartilage has excellent elasticity properties that allow stretching of tissues. An example is the epiglottis and the cartilage of the external ear.

The key differences between the three types of cartilage are summarised in table 1.

Type	ECM	Cells	Arrangement	Perichondrium	Location
Elastic	Type II collagen Elastic fibres Aggrecan Proteoglycans & GAGs	Chondroblasts Chondrocytes Fibroblasts in perichondrium	In lacunae as small isogenous groups	Present Contains: Small vessels, nerves & MSCs	Ear Auditory tube Epiglottis
Hyaline	Type II collagen Aggrecan & GAGs	Chondroblasts Chondrocytes Fibroblasts in perichondrium	Isolated in lacunae or in small isogenous groups	Present Contains: Small vessels, nerves & MSCs	Nasal septum Tracheal rings Sternal end of ribs Skeletal precursor Articular ends of long bones
Fibrous	Type I & II collagen Aggrecan	Chondrocytes Fibroblasts	Isolated in lacunae and in small groups aligned in rows	Absent	Intervertebral discs Pubic symphysis Temporomandibular joint (TMJ)

Table 1.0. Summary of key features of the three types of human cartilage.

1.2.3.1 Collagen

The composition of cartilage is determined by the secretion of components of the ECM by chondrocytes. By dry weight, collagen is the most abundant component of adult cartilage (50%-90%). There are 28 types of collagen that have been identified but type II collagen (90-95% of cartilage collagen) is specific to cartilage and is a marker of chondrocyte differentiation. Collagen is a protein composed of three polypeptide alpha chains to form a tropocollagen molecule. Each alpha chain twists into a left-handed helix, and the three twisted chains are then twisted together in a right-handed triple helix to form a rope like (fibrillar) structure stabilised by hydrogen bonds (Ricard-Blum, 2011). This coiled-coil molecular structure has a length of approximately 300nm and is 1.5nm in diameter.

Through covalent cross-linking these molecules collectively form collagen fibrils with a diameter of 50-80nm. These fibrils create a structural scaffold and a collagen network which provides strength in the cartilage. This biologically functional form of collagen results from translational modifications that require both specific and nonspecific enzymes and occurs at intra- and extracellular locations. Fibril morphology differs between the different collagen types, in cartilage for example the fibrils of type II collagen are thinner than those of type I which is found in other connective tissues. Type II collagen also forms cross links with type IX collagen that is also specific to cartilage. Collagens found in cartilage and their respective genes are summarised in Table 1.1.

Collagen type	Gene	Gene size (kb)	No of exons	Chromosomal location
II	COL2A1	32	54	12q13.11
IX	COL9A1	87	38	6q13
	COL9A2	17	32	1p34.2
	COL9A3	24	32	20q13.33
X	COL10A1	7	3	6q22.1
XI	COL11A1	232	67	1p21.1
	COL11A2	30	64	6p21.2
	COL2A1[a]	32	54	12q13.11

[a]The alpha 3(XI) chain is encoded by the COL2A1 gene.

Table 1.1. Collagen. Type II, IX, X and XI collagens and their chromosomal location, number of exons and respective gene size.

1.2.3.2 Glycosaminoglycans and Proteoglycans

Glycosaminoglycans (GAGs) are linear chain structure polysaccharides that contribute significantly to the biomechanical properties of cartilage. Proteoglycans are secreted by chondrocytes and are macromolecules with a branched structure due to the covalently attached sulphated GAGs to a protein core. Proteoglycans in the ECM undergo enzymatic breakdown and synthesis continuously at a steady rate and is regulated by chondrocytes. Their main role is in providing stiffness and elasticity of cartilage tissue and due to their polyanionic nature, they help retain water within the ECM of cartilage. Important cartilage proteoglycans are aggrecan, decorin, versican, biglycan and fibromodulin.

Aggrecan is a cartilage specific proteoglycan that contributes greatly to the load bearing properties of cartilage. Its main action depends on its binding to hyaluronan with high affinity to produce large multimolecular aggregates. Hyaluronan is an important anionic, nonsulfated glycosaminoglycan produced by chondrocytes that appears to provide a gel to which chondrocytes attach that helps stabilise the ECM (Muir, 1995).
As well as collagen, GAGs and proteoglycans, there are other minor components of cartilage ECM. Chondrocyte adhesion to the ECM is enhanced by cell adhesion proteins and glycoproteins such as chondronectin and anchorin.

1.2.3.3 Signalling pathways in chondrogenesis

Chondrogenesis is an important process for cartilage tissue formation and for bone development through endochondral ossification. The nasal septum and lateral cartilages develop from mesenchyme derived neural crest cells that originate in the neuroectoderm of the forebrain (Neskey et al., 2009). Critically, the proliferation and condensation of chondroprogenitor mesenchymal cells is the initiating mechanism of chondrogenesis. These undifferentiated cells begin to produce extracellular matrix containing hyaluronan, tenascin, fibronectin, type I collagen and the cell adhesion molecules neural cadherin (N-cadherin) and neural cell adhesion molecule (N-CAM)(DeLise et al., 2000). N-CAM and N-cadherin are important in the establishment of cell-cell interactions that will aid the process of chondrogenic differentiation. Type I collagen and hyaluronan have a role in regulating chondrogenesis by initially limiting cell-cell interactions, but with subsequent increase in hyaluronidase activity their action is reduced. Therefore, increased mesenchymal cell density leads to cell-cell contact and chondrogenesis. Once the cells become differentiated and become chondroblasts then chondrocytes, they begin to secrete collagen type II, IX, XI and aggrecan.

At this point cell morphology changes from fibroblast-like to round and collagen type X is expressed. With maturation, collagen type II and aggrecan become major components of the ECM. As well as cell-cell interactions and macromolecule role in chondrogenesis, there are several signalling molecules that are essential for maintaining chondrocyte function and phenotype including bone morphogenic proteins (BMPs), fibroblast and insulin-like growth factors (FGF, IGF) and transforming growth factors (TGFs) (Matta and Mobasheri, 2014). These proteins, as well as other morphogens such as sonic hedgehog (Shh) and Wingless (Wnt), act through receptors to activate downstream targets to bring about changes in gene expression.

The Sox genes belong to the high mobility group (HMG) box superfamily and encode for transcription factors essential for chondrogenesis and other developmental processes. There are three cartilage specific transcription factors (Sox9, L-Sox5 and Sox6) that play a vital role in ECM protein expression. Sox9 appears to be the most critical transcription factor required for mesenchymal cell condensation and for maintenance of their chondroprogenitor phenotype. The direct targets of Sox9 appear to be collagen types II, IX and XI, and aggrecan genes (Lefebvre and Dvir-Ginzberg, 2017). It is expressed in chondroprogenitors, all differentiated chondrocytes, (but not in hypertrophic chondrocytes) and is required in several successive steps of chondrocyte differentiation pathway (Akiyama et al., 2002).This includes its role in mesenchymal condensation, chondrocyte differentiation and proliferation.

1.3 Nasal deformity and septal injury

1.3.1 Congenital and acquired nasal deformity

Nasal deformity in the general population may result from either congenital or acquired pathologies. In some cases, complex reconstruction will require microvascular free tissue transfer, skin grafting or local flaps in combination with cartilage grafting harvested from either the ear or rib. Nasal septum can itself be used as a graft to reconstruct other regions of the nose for aesthetic and functional benefits, but only if harvested if sufficient septum is available. Other cases may require cartilage grafting alone to replace missing or damaged native cartilage. Acquired problems include traumatic injury from road traffic accidents, interpersonal violence, work related accidents (grinders, saws, power tools), occupational hazardous chemical exposure, human bites and animal bites. Congenital abnormalities of the nose will be encountered in many craniofacial syndromes, cleft lip and palate patients as well as vascular malformations and tumours of the nose (Losee et al., 2004).

1.3.1.1 Trauma

The nose is fractured more often than any other region of the face in adult patients who have sustained facial injury as a result of recreational activity (most commonly bicycle injury) and in the USA, it is estimated that there are approximately 50000 nasal fractures every year (Allareddy et al., 2011; Plawecki et al., 2017). Although the majority of injuries can be correct by simple manipulation, there is often the need for comprehensive septorhinoplasty where cartilage grafting is required not just to correct a deformity but to restore normal function (Fig 1.6). In such cases, cartilage may be required for spreader grafts, dorsal grafts for saddle deformity, septal extension grafts, columellar strut grafts to re-establish tip projection and lateral crural strut grafts to support the ala (Fedok and Rihani, 2015). Trauma in the paediatric population may cause saddle nose deformity, columella retraction, septal perforation (caused by digital nasal trauma) and short nose due to disruption of growth with aging (Chang et al., 2017; Kopacheva-Barsova and Arsova, 2016).

Figure 1.6. Occupational nasal injury with metal grinder in an adult patient. (A) Deep laceration caused by a metal grinder. Laceration extends deep into the nasal passages and runs from the injured left upper lateral cartilage (yellow arrow) down to the nasal dome and alar rim (red arrow). **(B) Intra-operative image**. Left lower lateral cartilage has been transected (blue arrow) and the junction between medial and lateral crus. **(C)** Primary repair of cartilages and soft tissue gives an acceptable result. However, the patient required secondary corrective surgery with an auricular cartilage graft after 18 months to improve alar rim contour.

1.3.1.2 Inflammatory causes of septal injury

Occupational rhinitis caused by irritants may progress to severe inflammation and septal perforation. Workers in the chemicals industry that are exposed to nickel, copper, chrome, silicone, cadmium, cement, platinum salts and arsenic may be at risk of nasal bleeding, rhinorrhoea and cartilage septal destruction(Castano et al., 2007; Joshi, 2004; Lin et al., 1994; Williams, 2000). Less common, systemic inflammatory conditions may also cause destruction of the nose such as Wegener granulomatosis (Granulomatosis with polyangiitis).

Other autoimmune conditions such as systemic lupus erythematosus, rheumatoid arthritis and Crohns colitis may also affect the nasal septum and cause significant permanent destruction of the underlying cartilage(Guntupalli et al., 2017). Cocaine-induced midline destructive lesion of the septum is also a well-recognized cause of serious septal destruction and perforation. Acquired septal perforation may also be a complication of nasal surgery or long term intranasal steroid use (Pereira et al., 2018).

1.3.1.3 Infectious disorders of the nose

Infections of the nose and the nasal septum is generally uncommon. Frequently, the presentation is a nasal septal abscess which has numerous aetiologies. Nasal septal abscess formation often occurs as a complication of nasal trauma leading to a septal haematoma (Menger et al., 2008). Anatomically, pus is formed between the cartilaginous septum and the overlying mucoperiosteum that if left untreated can cause aggressive destruction of the septum leading to perforations and deformity. Furthermore, the spread of infection from the nose may lead to serious systemic complications such as facial cellulitis and cavernous sinus thrombosis. Urgent management of septal infections with drainage of pus and appropriate antibiotics is paramount avoid both local and systemic complications. Cheng et al 2019, reviewed cases diagnosed with nasal septal abscess over a 10 year period retrospectively and identified staphylococcus aureus (S.Aureus), methicillin-resistant S.Aureus and klebsiella as the pathogenic microorganisms in 6 cases and manged with drainage and antibiotics successfully. Two cases later developed saddle nose deformity as a result of septal destruction (Cheng et al., 2019). Other pathogens identified include Haemophilus influenzae and Streptococcus pneumoniae including in rare cases, bacteria of dental origin (Streptococcus Milleri) following root canal treatment of upper incisor teeth (Aremu et al., 2011; Ginsburg, Charles M.; Leach, 1995).

High risk patients for septal infections include diabetics, HIV infection and immunocompromised patients secondary to medications. In such patients, the pathogen is often opportunistic and can be either bacterial or fungal including mycobacterium (Asakura et al., 2016; Xu et al., 2016). Other sources of nasal infection can be related to seeding of pathogens after endoscopic nasal and sinus surgery (Patel and Orlandi, 2015).

1.3.1.4 Congenital disorders of the nose

There are numerous congenital deformities that involve the nose and in very rare cases there is complete absence-arhinia (Brusati et al., 2009).The incidence of congenital nasal deformity ranges from 1-4% (1 in every 20000 to 40000 live births) and appears to be related mostly to intrauterine development (Hartikainen-Sorri et al., 1984; Losee et al., 2004). Every cleft lip patient has by definition a nasal deformity. The clinical presentation of congenital deformities varies widely even within patients with the same syndrome. This will result from either small hypoplastic cartilages or nasal bones, or their deformity resulting in abnormal nasal appearance. Other deformities will result from congenital clefts, tumours, cysts or vascular malformations and may present as simple mild alar notching or retraction (Ujam and Bulstrode, 2019).
Several syndromes are associated with nasal deformity, these include:

- **Waardenburg Syndrome** - Flat nasal root
- **Stickler Syndrome** - Short upturned nose
- **Apert Syndrome** - saddle nose
- **Crouzon Syndrome** – beak nose deformity
- **Downs syndrome** – flat nasal bridge
- **Binder syndrome** – short columella
- **Goldenhar syndrome**– nasal hypoplasia

Losee et al. 2004 investigated 261 patients with congenital nasal anomalies (excluding cleft lip nasal deformities) in a retrospective review and devised the following classification system:

- **Type I** – Hypoplasia and atrophy
- **Type II** – Hyperplasia and duplications
- **Type III** – Clefts (including Tessier classification)
- **Type IV** – Neoplasms and vascular anomalies

Their data demonstrated an incidence of 62%, 1%, 16% and 20% for deformity types I, II, III and IV respectively. Type I anomalies were the most frequent and as they include syndromic infants with craniofacial problems. Type I anomalies included unilateral nostril agenesis, arrhinia, congenital absence of columella, absence of nasal cartilage, nasomaxillary hypoplasia (Binder syndrome) with short columella and other syndromes such as Goldenhar with nasal hypoplasia.

In cases of cleft lip, primary surgery results in several deformities including a short columella, septal deviation, and poor tip projection (Fig. 1.7). Such cases will require secondary rhinoplasty procedures that will also require cartilage grafting commonly taken from the rib (Angelos and Wang, 2012; Ujam et al., 2019).

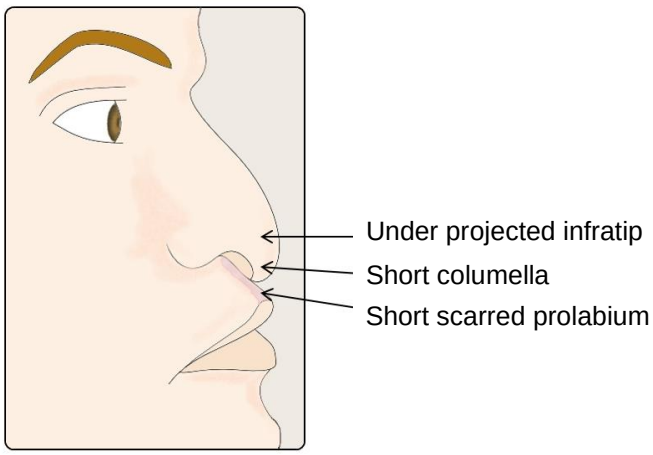

Figure 1.7. **Secondary cleft nasal deformities.** These nasal deformities often require costochondral grafting to improve tip projection with a columellar strut graft, to improve columellar length and to augment the prolabium which is often deficient.

The above-mentioned deformities are just a few examples of potential indications for rhinoplasty in children and adults, some of which will require invasive costochondral graft harvesting. Overall, there is a great need for cartilage in nasal surgery.

1.4 Nasal reconstruction

1.4.1 A brief history of rhinoplasty

The history of rhinoplasty is fascinating. American Egyptologist Mr Edwin Smith purchased an ancient scroll in 1862 which later become known as The Edwin Smith Surgical Papyrus. Found in Luxor, Egypt and believed to originate from 3000BC, the scroll was to be translated by James Breasted in his 1930 publication (Breasted, 1930). The 48 surgical cases that are documented include treatment of simple and comminuted nasal fractures. It is speculated that the work is authored by the great Egyptian physician Imhotep (Cunha, 1949; Sprunt, 1955).

In India around 600BC, nasal reconstructive surgery was pioneered by Professor Sushruta who focused on cheek and then forehead flaps (became known as the Indian nose method) to reconstruct mutilated noses. His work written in Sanskrit, is recorded in the book “The Sushruta Ayureveda” and covers numerous surgical procedures including notably, rhinoplasty (Eisenberg, 1982).

The middle ages saw the fall of the Western Roman Empire and dominance of Christianity. The church for over a thousand years considered surgery and in particular dissection of the dead abhorrent and dishonourable. The forbidding of surgical procedures held back the evolution of nasal surgery until the Renaissance period where Gaspare Tagliacozzi from Bologna published his famous book *De Curtorum chirurgia per insitionem* in 1597. His surgical techniques involving the use of upper arm skin flaps to reconstruct the nose (Fig 1.8) became known as the “Italian” or the “Tagliocotian” rhinoplasty (Adamson, 1988; Bennett, 1984).

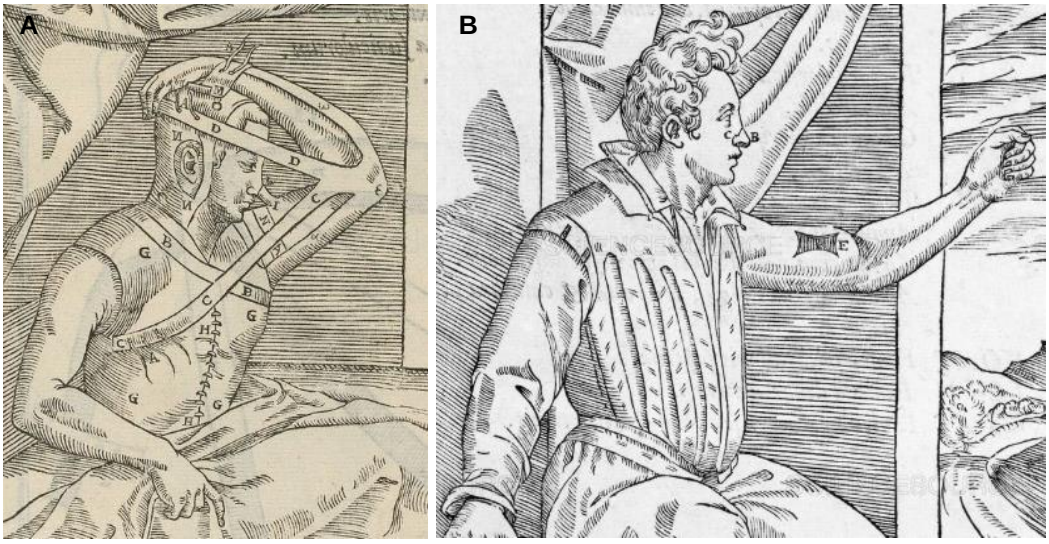

Figure 1.8. **Rhinoplasty- The Italian method**. **(A)** Nasal reconstruction using a forearm flap as described by Gaspare Tagliacozzi in *De Curtorum Chirurgia Insitionem* (1597). **(B)** The flap would be divided once the skin had developed its own blood supply on the nose.

It was not until the 18th century that the Indian rhinoplasty was bought to Europe through publication in a British general lay journal- the Gentleman's Magazine 1794 with the title " A curious surgical operation" (Brain, 1993).

The beginning of the modern era of rhinoplasty surgery is considered to have started in the early 19th century until the middle of the 20th. The term "rhinoplasty" was first described by German surgeon Carl Ferdinand Von Graefe in 1818. Other notable surgeons are German surgeon Johann Dieffenbach who was the first to use ether anaesthesia and published his work in 1845- *Operative Chirurgie.* His work on rhinoplasty and the improvements of the forehead flap was extensive (Adamson and Gantous, 2019).

In 1887 American surgeon John Orlando Roe coined the term "corrective" rhinoplasty and introduced the endonasal approach that completely avoided external scars. Roe is widely considered as the father of aesthetic rhinoplasty (Rogers, 1986; Walter, 1988). Around the same time, another master pioneer rhinoplasty surgeon Jacques Joseph contributed greatly with his 1898 paper *Surgical Correction of the Nose*. His contribution to aesthetic facial surgery is second to none and in particular his work on the association between facial deformity and its psychological impact (Milstein, 1984). Finally, the 20th century saw a significant increase in surgical modifications and new techniques by prominent surgeons like Ralph Millard, Harold Gillies, Gustave Aufricht, Myron Metzenbaum, Samuel Fomon, Maurice Cottle, Irving Goldman, Frederick Menick, and Tony Bull to name but a few.

1.4.2 Historical use of grafting material in rhinoplasty surgery

Over the centuries, numerous different materials have been used to augment the nose to correct deficiencies in bone, cartilage, or both. In the last 200 years surgeons have tried using foreign materials with limited success including gold, platinum, steel, marble, cork, glass, chromium, aluminium, paraffin, rubber and acrylic resin (Regnault, 1980).

Autologous tissue such as bone and cartilage has been popular for over 100 years and widely used in rhinoplasty. The use of costal cartilage for nasal reconstruction is accredited to Von Mangoldt who in 1899 successfully harvested a 5cm x 1cm section of costal cartilage with perichondrium from the 7th rib and grafted this onto the nasal dorsum to correct a saddle nose deformity (Von Mangoldt, 1899). Incredibly, several cases of isografts were documented with predictable success almost 100 years ago (Metzenbaum, 1928). In 1928, American surgeon Myron Metzenbaum described the transplant of a resected bony cartilaginous dorsal hump from one patient immediately into a second patient with a saddle nose deformity (Metzenbaum, 1928). Other autologous sources of grafting material used over the years by numerous surgeons of the early 20th century include tibial bone, iliac crest bone, rib cartilage and fat (Maliniak, 1924). In attempting to avoid the risks of rib cartilage harvesting, several of the pioneering surgeons including Jacques Joseph were using alternatives such as Ivory especially for dorsal augmentation. Some of these Ivory implants have withstood the test of time and have survived over 40 years (Vilar-Sancho, 1987).

1.4.2.1 Modern septorhinoplasty graft materials

Patients with nasal deformity requiring septorhinoplasty with extensive reconstruction are currently given limited options of either a synthetic implant or autologous rib cartilage grafts (Rosenberger and Toriumi, 2016).

Rib cartilage harvesting surgery provides excellent quality and volume of cartilage (hyaline cartilage) allowing total nasal reconstruction by augmentation of missing or damaged septal, alar, lateral cartilages and dorsum (Katira and Guyuron, 2015; Toriumi and Bared, 2012). There are 12 costal cartilage sections found at the anterior ends of the 12 ribs. The 11th and 12 ribs are floating as they do not attach the sternum. The fifth, sixth or 7th rib are commonly selected for harvesting.

Unfortunately, rib harvesting can be associated with significant donor site morbidity such as scar, chest wall deformity, pneumothorax and chronic pain (Marin et al., 2008; Özücer et al., 2018; Sheen, 1998).

There is also evidence that removing ribs whether entirely or partially is associated with a drop in respiratory function, and in children under the age of 10 is associated with increased incidence of chest wall deformity (Hatano et al., 2014; Ohara et al., 1997). Donor site morbidity at the chest wall can be objectively reduced by certain techniques to limit deformity.

Fattah et al. demonstrated a technique that involves wrapping morselised cartilage (cartilage shavings) in a sausage shaped vicryl mesh creating a cylindrical shape bag. This is then inset into the donor rib site and sutured to recreate the continuity of the rib. The analysis of their outcomes showed favourable and reduced chest wall deformity (Fattah et al., 2010). However, overall risks are still significant and rib cartilage harvesting in paediatric cases should therefore be a highly selective process and only performed with complete patient and parent counselling (Ohara et al., 1997). Cartilage grafts are also known to warp which can result in disappointing long term results if not handled carefully or sculpted inadequately even in the hands of master rhinoplasty surgeons (Toriumi, 2000). However, rib cartilage grafts remain to be the undisputed gold standard graft material.

Bone as a grafting material is generally avoided as it has unpredictable levels of resorption and is not as easily manipulated as cartilage. It can be harvested from calvarial bone and is sometimes used to augment the dorsum.

Although synthetic grafts avoid the risk of rib harvesting and allow for quicker procedures, materials such as silicone or porous polyethylene are associated with rejection, high infection rates, capsular contracture and extrusion (Kim et al., 2017; Parker Porter, 2000; Winkler et al., 2012). Many synthetic products are still available but many surgeons will avoid using them if possible or only in selected cases (Adamson, 2000).

1.4.3 Rhinoplasty

1.4.3.1 Aesthetic subunits and nasal analysis

Understanding the aesthetic subunits of the nose is vital for achieving excellent aesthetic rhinoplasty outcomes but also assists the surgeon in the surgical approach (Burget and Menick, 1985; Gonzalez-Ulloa et al., 1954). Keeping scars within boundaries of the subunits and restoring a whole subunit result in better aesthetic outcomes (Fig 1.9).

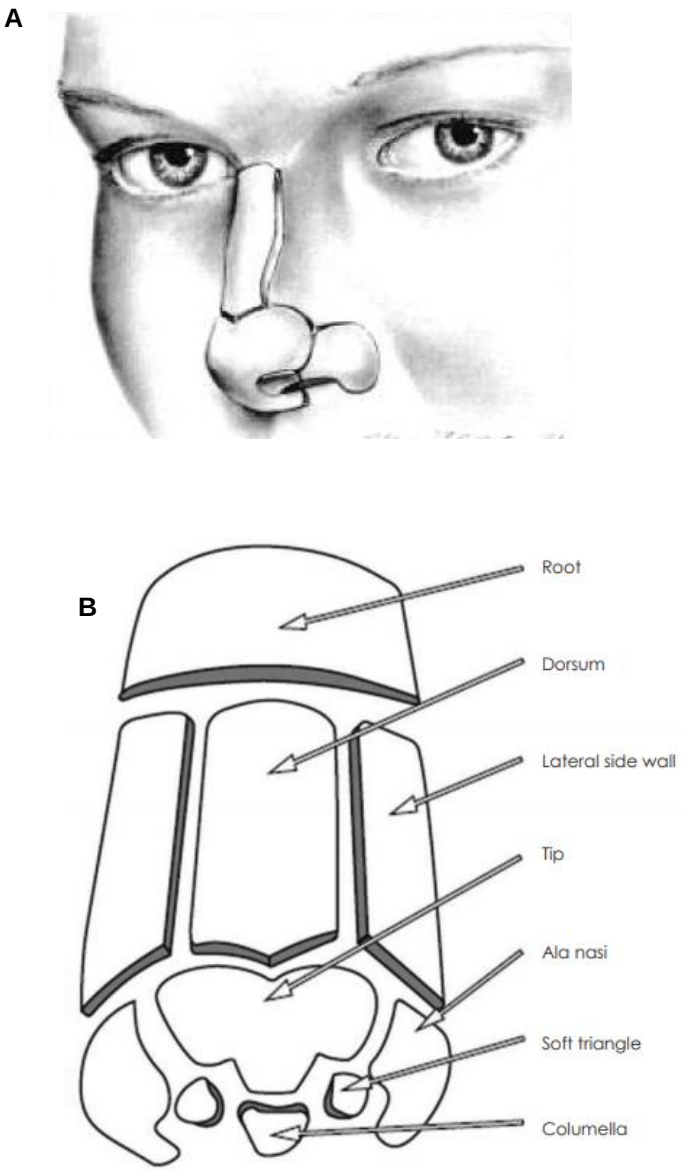

Figure 1.9. Nasal subunits. **(A)** Image from Burget & Menick original publication describing nasal subunits. **(B)** Contemporary detailed illustration of individual subunits of the nose *(Image modified from Kim, M.Yun, Ji. Surgical reconstruction of nasal alar deformities. J Rhinol. 2017 Nov;24(2):65-73).*

Rhinoplasty can be performed as a closed or open tip procedure. The open tip approach requires a small incision at the columella which if sutured correctly and with precision at the end of the procedure, is scar free.

Diagnosis of the underlying nasal problem is fundamental to performing the correct nasal procedure using the appropriate techniques and grafts. Close examination of the patients nose from all angles allows all the key surface landmarks to be assessed and any underlying deformity and asymmetry to be diagnosed. There are many important anatomical features to examine to plan appropriate surgery. Examples include:

- The position of the radix
- Nasal root width
- Dorsal aesthetic line
- Tip rotation and projection
- Supra-tip and infra-tip points
- Alar lobule width
- Hanging or retracted ala
- Columella width

Palpation of the nose will help assess the cartilaginous support to the tip and the strength of the lower lateral cartilages. Assessment of breathing by simple chair side Cottles manoeuvre (cheek is gently pulled laterally on side of nose being tested to open the nasal valves) will diagnose nasal obstruction and should also be performed.

1.4.3.2 Cartilage grafts in rhinoplasty

Most surgeons would recommend autologous cartilage from either the septum (if adequate volume present), auricular cartilage or costochondral cartilage. Frequently, septal, and auricular cartilage harvesting does not provide sufficient quantity of graft and therefore rib (costochondral) cartilage is the material of choice. Every surgeon will have a preference to which rib to harvest but generally 5^{th} ,6^{th} and 7^{th} rib are the most used. The 6^{th} rib has the advantage of being at the level of the inframammary crease and therefore the skin incision and ultimately the scar can be hidden in the inframammary fold. However, for a straighter and longer section of cartilage the 7^{th} rib is better (Toriumi, 2017). The 10^{th} rib cartilage is easy to harvest and gives predicable results (Kim et al., 2015). The authors my personal experience is that the 10^{th} rib is perfectly suited for columellar strut grafts and dorsal onlay grafts and is easy to manipulate (Fig 1.10).

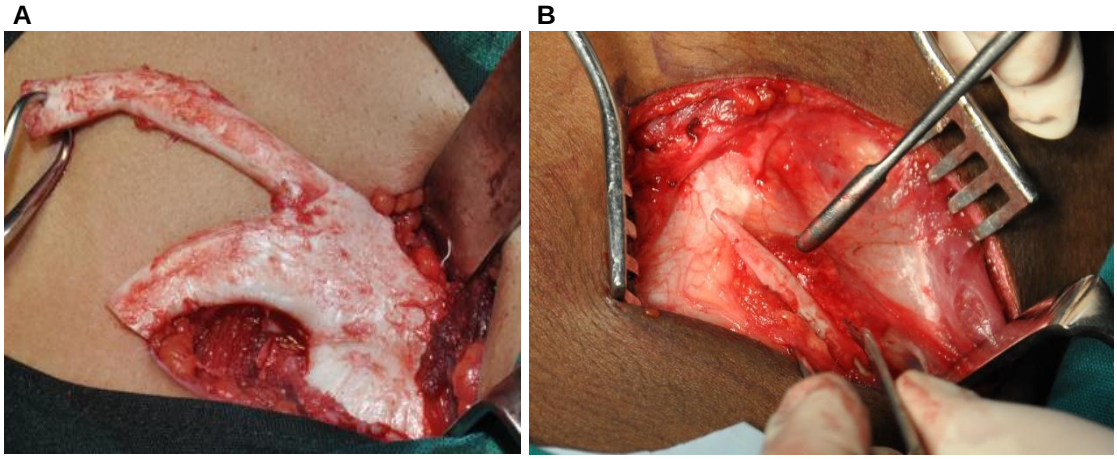

Figure 1.10. Rib harvesting. (A) Costochondral rib harvesting commonly from the 5th, 6th or 7th rib. This procedure is performed under a general anaesthetic and patients must stay overnight for observation and analgesia. The most serious risk in this procedure is pneumothorax if the dissection of the rib is too deep **(B)** The 10th rib being harvested. The natural shape of the cartilage with a pointy tip, makes it an excellent choice for columellar strut and dorsal onlay graft.

Within the literature there are extensive lists of different grafts used by different surgeons either to improve aesthetics or breathing function(Daniel, 2009; Tasman, 2007; Toriumi, 1995). These vary in size and thickness but when a significant volume of cartilage is required, rib cartilage is commonly used. When planning corrective nasal surgery, understanding the underlying problem allows the surgeon to decide on where to harvest cartilage from. The advantage of rib cartilage is that they can be trimmed to the thickness and size that allows the surgeon to reconstruct the entire framework of the nose if required. Examples of grafts rib cartilage are demonstrated in (Fig. 1.11).

Septal cartilage augmentation is indicated where the native septum is deficient in size or structurally inadequate. Grafting can reinforce the strength and elongate the septum (septal extension graft) to provide support for the tip lobule and maintain a straight septum. In the alar region, cartilage needs to be thin and easy to manipulate if required to extend or support the lower lateral cartilages, in other regions, a thick strong section of cartilage is required to be robust and rigid enough to withstand the forces of adjacent soft tissues and skin drape (dorsal graft).

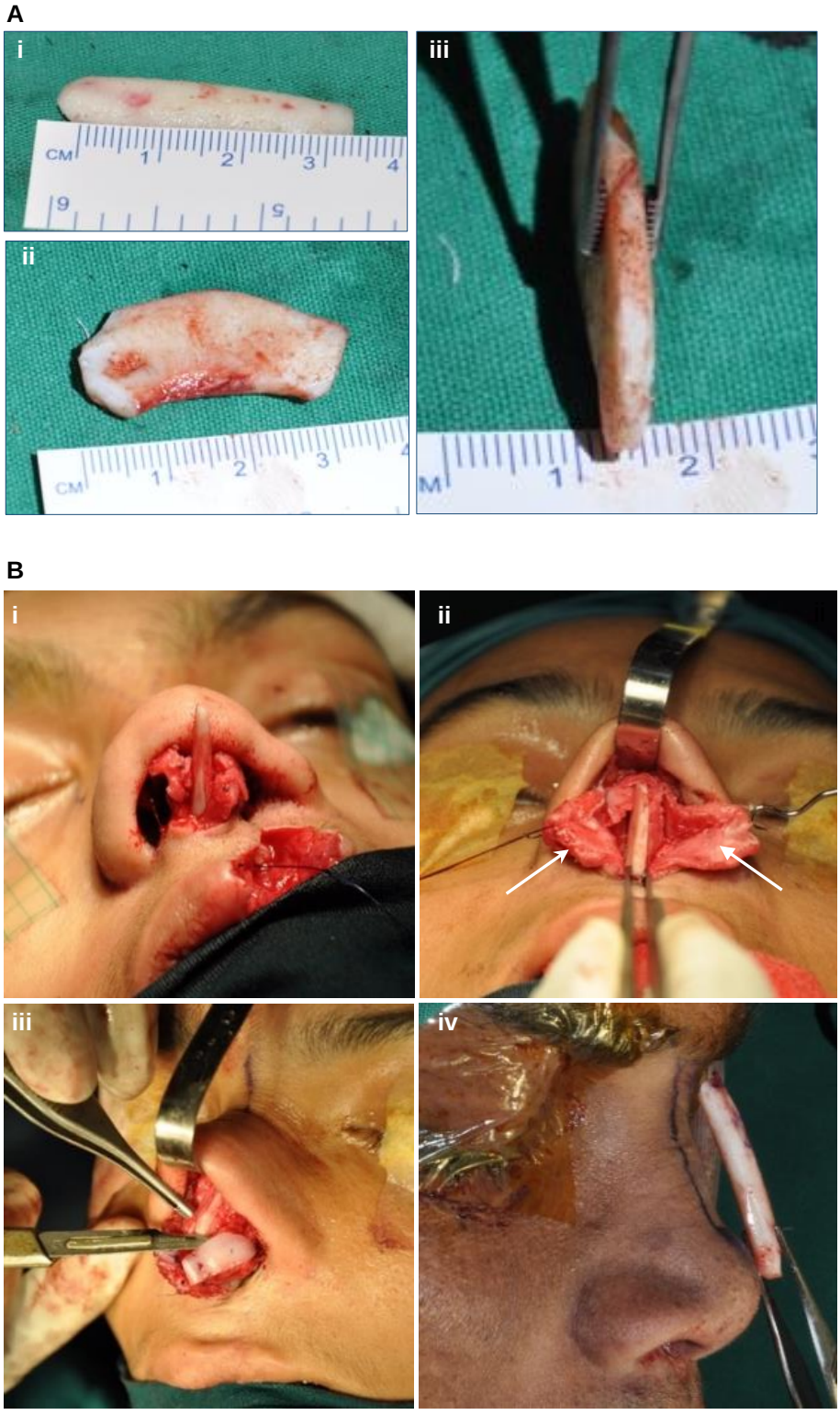

Figure 1.11. Costochondral grafts for rhinoplasty. (A) Intra-operative images of prepared rib graft. **(i)** Costal cartilage trimmed to graft nasal dorsum. **(ii)** Lateral view of costal cartilage shaped for septal grafting. **(iii)** Septal graft thickness approximately 3mm wide. **(B) Grafts in situ**. **(i)**Columellar strut graft sutured inferiorly to the anterior nasal spine. **(ii)** Septal graft inserted into pocket between the mucosal layers (white arrows). **(iii)** Lower lateral cartilage graft to extend the alar. **(iv)** Dorsal graft prior to insertion demonstrating dimensions required to augment the deformity (short nose in this case).

1.5 Tissue engineering cartilage – an alternative to rib harvesting

Stem cells and regenerative medicine offers a potential alternative to current rib cartilage harvesting techniques that will eliminate the associated morbidity. By isolating stem cells from autologous tissue, custom made cartilage grafts may be regenerated in the laboratory and then inserted back into the nose of the same patient. It is not uncommon that patients who undergo septorhinoplasty will require more than one procedure to achieve the desired outcome and the majority of these cases will require a general anaesthetic. This will give surgeons a window of opportunity to harvest and bank tissue that can then be used to isolate, expand and chondrogenically differentiate stem cells to culture for cartilage tissue regeneration.

1.5.1 Mesenchymal stem cells

The benefits of stem cells have been exploited for many years since the 1950`s when in 1956 Dr E Donnall Thomas performed a bone marrow transplant to achieve complete remission in a leukaemia patient (Thomas, 1999). The evolution of the term mesenchymal stem cells (MSC) spans over 50 years and originates from initial research into what was then termed fibroblastic precursors derived from bone morrow. It was not until the early 1990`s that the term MSC was widely accepted (Caplan, 1991). MSC`s can be derived from a variety of tissues including fat (adipose), bone marrow, bone, umbilical blood and Wharton's jelly. They are defined by their intrinsic ability (potency) to give rise to osteoblasts, chondrocytes, adipocytes, myocytes and other mesenchymal cell types and have the ability to self-renew to generate daughter stem cells with a similar developmental potential to the mother cell. MSC`s also display functions of being able to migrate to site of injury and damage within tissue and importantly for their application in tissue engineering, are non-immunogenic (Hass et al., 2011). Furthermore, they are defined by three criteria defined by The International Society for Cell & Gene Therapy (ISCT). Firstly, they must express CD105, CD73 and CD90 and lack expression of CD45, CD34, CD14 (haematopoietic markers) or CD11b, CD79a or CD19 and HLA-DR surface molecules. The other criteria are that they are plastic adherent in standard culture conditions and must differentiate in-vitro to osteoblasts, adipocytes and chondroblasts lineages. Recently, ISCT has clarified MSC nomenclature by recommending that, additionally, the tissue-source origin of the cells is stated (Viswanathan et al., 2019).

1.5.1.1 Adipose tissue derived stem cells

Adipose tissue has been widely investigated over the last 20 years as a source of stem cells to engineer cartilage using chondrogenic differentiation protocols. As an alternative to bone marrow derived stem cells, ADSCs were identified as mesenchymal in origin with multilineage potential in vitro to differentiate into osteogenic, chondrogenic, adipogenic and myogenic lineages. The main advantage of adipose tissue as a source of stem cells is its relative ease of harvesting, commonly via syringe aspiration (liposuction) and not necessitating general anaesthetic in the majority of cases, far simpler than obtaining MSCs from bone marrow. Furthermore, there is often abundant superfluous volume of adipose tissue in most patients. Zuk et al in their widely cited 1991 publication, isolated human ADSC by 0.075% collagenase digestion of lipoaspirate harvested under local anaesthetic. Chondrogenic differentiation of ADSC was confirmed by Alcian blue staining of sulphated proteoglycan matrix and by immunohistochemical Collagen II assays. Further characterisation of ADSC confirmed their mesenchymal status defined by their CD marker profiles (Zuk et al., 2002, 2001).

The ability to isolate consistent homogenous populations (phenotype) of stem cells from adipose tissue (lipoaspirate) is also an important factor in their use for tissue engineering. Aust et al. 2004, showed that ADSCs isolated from multiple donors displayed consistent homogenous cell surface markers and all capable of multilineage pathways (Aust et al., 2004). This predictability and confidence in obtaining stem cells from adipose tissue adds further support to the use of ADSC in considering tissue engineering cartilage. Interestingly, numerous studies have looked at the site of fat harvest as well as the technique to obtain the fat sample and its effect on ADSC isolation and differentiation.

The technique of harvesting fat for surgical procedures can vary between surgeons and indeed there are several nuances to doing so, each favoured or avoided by different surgeons. For example, the donor site can be the inner thigh or the abdomen. The technique may use a sharp ended or a blunt ended canula with or without machine pump assisted suction or the Colman`s technique (3mm blunt cannula with a 10ml syringe). Some surgeons use tumescent solution prior to harvesting the fat. This solution often contains a local anaesthetic, a steroid (e.g. triamcinolone), adrenaline and hyaluronidase enzyme. Again, there is much variation in this.

Jurgens et al. 2008, investigated the yield and functional characteristics of ADSCs derived from adipose tissue from three different sites, thigh, abdomen, and hip. They concluded that the abdomen is preferable to the hip or thigh for harvesting ADSCs as a higher yield of cells is obtained. However, the growth kinetics and differentiation potential were the same at all sites (Jurgens et al., 2008).

More recently, Iyyanki et al. 2015, further investigated this by analysing samples from 19 patients and also concluded that adipose tissue harvested from the abdomen through direct excision or Coleman`s technique yielded the most ADSC (Iyyanki et al., 2015). This simple yet predictable harvesting technique further supports the view that ADSC can be easily and quickly sourced with minimal patient morbidity. The processing of the lipoaspirate to isolate stem cells can be done in one of two established methods, either through digestion using trypsin, or alternatively by direct plating of adipose tissue onto standard culture plates with culture media (explant method). Both techniques enable ADSCs isolation that result in similar ability for multilineage differentiation (Leonardo Guasti et al., 2012a; Zhu et al., 2008)

Selective chondrogenic differentiation of ADSC is required in the context of cartilage tissue engineering and is highly dependent on the addition of induction medium to confluent cells. There are variations of chondrogenic induction media but many share the same composition of essential supplements added to Dulbecco`s Modified Eagles Medium (DMEM): Insulin-transferrin selenium (ITS), dexamethasone, L-Ascorbic acid, Transforming Growth factor beta-1 (TGF-β1). Other published protocols use TGF-β3, and Bone Morphogenic Proteins (BMP`s) (Estes et al., 2010; Leonardo Guasti et al., 2012a; Ronzière et al., 2010).

Chondrogenic differentiation of ADSC is observed on monolayer cultures but is enhanced in three dimensions (3D). Many studies of the differentiation potential of ADSC towards the chondrogenic lineage involve the use of spheroids, pellets, and organoids. These 3D culture systems replicate the natural environment of these cells permitting cell-cell contact and interaction (Estes et al., 2010; Estes and Guilak, 2011). Culturing ADSCs in a 3D microenvironment results a modification in the composition of their secretome, with upregulation of genes related to ECM proteins, cell-adhesions proteins and growth factor proteins (Amos et al., 2010; Kapur and Katz, 2013). With this in mind, it seems that ADSC are an ideal source of stem cells to generate a 3D skeletal tissue such as cartilage. In summary, ADSCs are easy to isolate, expand and differentiate towards the chondrogenic lineage. Our group have extensively investigated ADSCs over the last few years and have established protocols for their isolation, expansion and chondrogenic differentiation including in 3D scaffolds (Guasti et al., 2014). For this reason, I chose to use ADSC for this thesis.

1.5.1.2 Cartilage stem precursor cells

Cartilage is often resected during rhinoplasty and ear surgery and is disposed of. Instead, this spare cartilage can be utilised to isolate stem cells then cultured for cartilage tissue engineering and grafted back into the same patient at a later date as an autologous graft. Cartilage can be sourced from rib, ear, and nasal septum. The site with the least morbidity and the easiest to harvest a small sample of cartilage is the ear. Under local anaesthetic, a small sample of cartilage and perichondrium can be harvested from the conchal bowl posteriorly which will therefore not leave a residual visible scar or ear deformity (Fig 1.12).

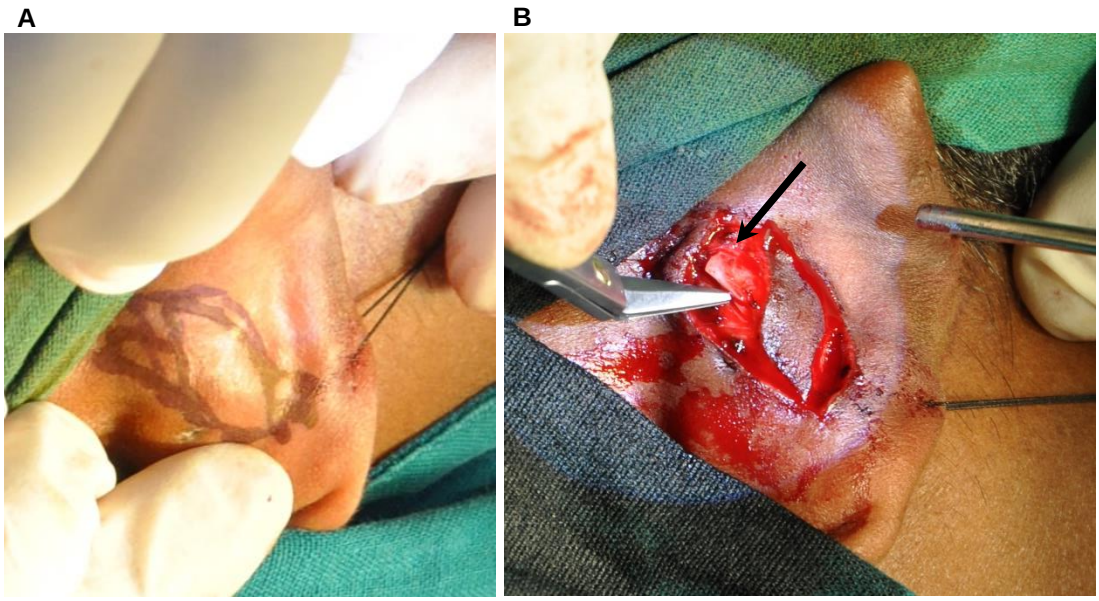

Figure 1.12. Adult right ear conchal bowl cartilage harvesting, posterior approach. (A) In this particular case, a composite graft is being harvested which includes cartilage and the overlying skin. For cartilage only, a straight incision rather than an eclipse is required which would leave a very small unnoticeable scar at the back of the ear. **(B)** Cartilage harvested (arrow).

Cartilage from the ear can then be used to isolate and expand cells in vitro. Rodriguez et al. 1999 characterised the cartilage engineered from isolated human auricular chondrocytes and demonstrated their resemblance to elastic cartilage (Rodriguez et al., 1999). Retention of the cartilage phenotype of chondrocytes (as they tend to dedifferentiate in vitro monolayer culture) appears to be sensitive to culture conditions and can be maintained in vitro by the addition of TGF-β, cortisol and ITS resulting in increased GAG and collagen II synthesis (Tay et al., 2004; Van Osch et al., 2001).

Where previous studies had stripped perichondrium off the ear cartilage, Togo et al instead, focused on studying the perichondrium of the ear as a source of cells. Using adult white rabbit ears, they demonstrated the presence of cartilage progenitor cells in the perichondrium that were able to proliferate and different into multilineages and expand to 35 passages, far more than chondrocytes. Furthermore, these cells seeded on collagen sponge scaffolds and implanted into nude mice deposit GAG and type II collagen consistent with in-vivo cartilage generation (Togo et al., 2006). A similar population was also identified in mice perichondrium in other studies (Kobayashi et al., 2011) This finding was reinforced by Xue et al who confirmed the presence of two cell populations from pig ears, both expressing MSC surface markers. The two populations, cartilage/progenitor cells derived from perichondrium and those derived from the auricular cartilage differed in their proliferation and morphology. Perichondrium derived stem cells appeared fibroblast like and demonstrated higher rates of proliferation. Interestingly, the cartilage derived stem cells were superior in chondrogenic differentiation (Xue et al., 2016). In a subsequent study by the same group, the superior chondrogenesis of auricular cartilage derived stem/progenitor cells (CSPCs) in a mouse in-vivo model was demonstrated when compared to the perichondrium derived cells in identical conditions (Zhang et al., 2019).

In our group, access to ear cartilage from both microtia patients and from children undergoing ear surgery for “bat” ear (taken as a normal control) is easy and samples were frequently available. The advantages of using CSPCs as detailed and the ease of stem cell isolation by explant protocols already established in our group, directed me to their use in this thesis.

1.5.2 Scaffold and scaffold free 3D models for chondrogenesis

Approaches to tissue engineering cartilage rely on either scaffold or scaffold free strategies. Historically, scaffolds have been widely used to allow culture of cells in a 3D model to generate cartilage-like tissue.

1.5.2.1 Scaffold approach

These scaffolds provide a temporary (or permanent) structure to support cells and are generally 3D constructs with pores or hydrogels. Scaffold materials must be biocompatible and not elicit an immunological foreign body reaction. Widely studied polymer materials that are clinically approved and are therefore excellent candidates for scaffold fabrication include polyglycolide (PGA), polylactides (PLLA, PDLA), polycaprolactone (PCL) and collagen. These materials are both biodegradable and bioresorbable (eliminated from body completely). Fabrication of a scaffold entails consideration of numerous factors including the 3D architecture as this can itself effect cell differentiation and tissue generation, for example pore size and degree of hydrophilic composition (Miot et al., 2005). Cells are then seeded onto the scaffold and cultured in either static or dynamic environment that may include a pre-implantation phase of tissue maturation (and differentiation) in a bioreactor followed by surgical grafting (Hutmacher, 2000). However, generally there are numerous problems with using scaffolds including variable cell seeding, cell density, random uncontrolled pattern of scaffold resorption, and achieving effective nutrient diffusion. A scaffold free approach eliminates some of these variables (Ovsianikov et al., 2018).

1.5.2.2 Scaffold free approach

In contrast, the scaffold free approach involves the self-assembly of cells due to cell to cell contact that results in upregulation of N-cadherin expression and spheroid formation (Weber et al., 2011). These 3D spheroids replicate a more normal physiological environment for cells that improves viability, morphology and differentiation that are more relevant than 2D monocultures (Yoon et al., 2012). Lehmann et al. 2013 demonstrated the formation of microtissues from fusion of several spheroids derived from human articular chondrocytes. The morphology of these microtissues resembled native hyaline cartilage with collagen II expression as well as deposition of proteoglycans (Lehmann et al., 2013). Furthermore, the advantage of a scaffold free spheroid based strategy to tissue engineering, is the possibility of generating macro tissues with complex organ-like designs formed of co-cultures of varying cells types (Laschke and Menger, 2017). A useful application for this approach would be in fabricating cartilage tissue lined by epithelium or mucosa.

1.5.2.3 3D printing and 3D bioprinting

Three-dimensional printing and bioprinting has been developed in recent years that combines the benefits of both a scaffold free and scaffold approach (Murphy and Atala, 2014). Advancements in 3D printing technology has enabled tissue engineered constructs to be fabricated from cells printed within a bioink combined with polymer based scaffolds using 3D bioprinters. The advantage of hybrid constructs, those fabricated from cells within a bioink printed onto 3D printed polymers, is the additional mechanical support. Schuurman et al. 2011 investigated such a concept and created 3D hybrid constructs of PCL and cell laden alginate hydrogel by a layer-by-layer deposition of the two. Cells were printed using a pneumatic syringe dispenser with polymer printed on a separate head. Interestingly, cell viability appeared to be high despite being printed onto newly deposited PCL polymer (Schuurman et al., 2011). Other studies that explored this strategy relied on numerous printing technologies. This included printing by a dual head printer based on inkjet printing of cells alternating with electrospinning of PCL fibres to generate layered hybrid constructs (Xu et al., 2013).

In the last 10 years, printing technology has evolved, and the main printers are inkjet, laser assisted, fused deposition modelling and extrusion types, but the processes remain generally unchanged; pre-bioprinting, bioprinting and post bioprinting. Pre-bioprinting involves the creation of a stereolithography (STL) file using 3D computer aided design (CAD) software that may be based on patient specific measurements created from CT/MRI imaging. Bioprinting involves selection of a suitable printer, appropriate bioink and compatible polymer biomaterials (Shafiee and Atala, 2016). Printing both cells and a scaffold polymer will require a printer with at least dual print heads. Bioprinters are now commercially available for research with multi-head printing capabilities that can combine printing cells with thermoplastic polymers such as PLA with the ability to print a wide selection of scaffold architecture. Baena et al 2019, demonstrated the use of such technology by bioprinting chondrocyte laden bioinks with high temperature thermoplastic PLA scaffolds for cartilage tissue engineering using print protocols that avoid cell thermal damage (Baena et al., 2019).

1.5.2.4 Bioinks

Current bioprinting techniques for generating 3D cartilage rely on mesenchymal stem cells mixed with hydrogels also known as “bioinks”. These hydrogels can be natural, man-made or a combination of the two. There has been significant progress in fabricating bioinks that appear to provide a suitable chondrogenic inductive environment. Numerous bioinks have been investigated and developed for bioprinting (Gungor-Ozkerim et al., 2018; Martínez Ávila et al., 2016). These include:

- Alginate, gelatin, collagen, fibrin/fibrinogen, gellan gum, hyaluronic acid (HA), Silk, agarose, cellulose, and chitosan.

The ideal bioink has proved to be challenging to fabricate as several important material properties are collectively required. These include biocompatibility, printability, gelation kinetics, viscosity, hydration degree and viscoelasticity (Chimene et al., 2016). Furthermore, the bioink must allow high cell viability and be inducive to their chondrogenic differentiation potential.

Alginate has been extensively investigated for numerous biomedical applications including as a bioink and is widely available for tissue engineering research applications as a ready-made product. Repeated studies have demonstrated chondrocyte proliferation, synthesis and deposition of collagen type II ECM in alginate culture systems with maintenance of their cartilage phenotype (Beekman et al., 1997; Häuselmann et al., 1992). Alginate is an anionic linear unbranched polysaccharide of 1,4-β-D-mannuronic acid (M blocks) and 1,4-α-L-guluronic acid monomers (G blocks) to form a long chain polymer. It can be derived from the cell walls of brown marine algae (Laminaria and Ascophyllum species) or from soil bacteria Pseudomonas and Azotobacter (Lee and Mooney, 2012). It is biocompatible and can be cross-linked to from gels in the presence of various divalent cations such as Ca^{2+} making it a suitable bioink for 3D bioprinting. Alginate can also be covalently cross-linked to modify its physical properties. Moreover, by modifying the stiffness of alginate, the microenvironment can be altered which can have a significant effect on the fate for MSCs (Freeman and Kelly, 2017). Another advantage of alginate is the wide pore size distribution (5-200nm) which allows diffusion of molecules through the gel. However, significant problems with alginate includes its inherent non-degradability in mammals as they lack the alginase enzyme required to cleave the polymer chains (Gasperini et al., 2014). Nevertheless, ionically cross-linked alginate gels may dissolve by the release of the divalent ions cross linking the gel into the surrounding media.

Alternatively, selective partial oxidation of the G-blocks enables degradable gel formation (Lee and Mooney, 2012). Biodegradability is an essential characteristic for a septal graft as the presence of a foreign body long term may induce an unwanted immune response and rejection. Fundamentally, this is also crucial to allow cellular deposition of cartilage ECM. Another potential limitation of natural alginate is that it does not provide cells adhesion motifs to allow specific cell attachment and its negative charge balance also prevents protein binding. This can be modified by the incorporation of the tripeptide Arginine, Glycine and Aspartate (RGD) peptides by covalent linkage which can promote cellular adhesion and expansion (Bellis, 2011; Genes et al., 2004; Li et al., 2012).

Bioprinting with alginate and alginate/nanocellulose bioinks have been studied over the last few years and have shown some promising results relating to cartilage tissue engineering. Nancellulose and nanofibrillated cellulose (NFC) hydrogels appears to have a positive effect on cell fate processes with seeded chondrocytes maintaining their chondrogenic phenotype (Markstedt et al., 2015a; Müller et al., 2017)

The ability of cellulose nanofibrils to bind water strongly (results is highly hydrated cellulose), its high mechanical strength, biocompatibility and their morphological similarities to collagen are positive properties that means it is potentially an excellent hydrogel for cartilage tissue engineering (Martínez Ávila et al., 2014). It has been used in combination with alginate as a bioink for 3D bioprinting, seeded with human nasal chondrocytes and human bone marrow derived MSCs demonstrating early cartilage formation in vitro and in extended in-vivo studies over 60 days (Apelgren et al., 2017; Markstedt et al., 2015; Martínez Ávila et al., 2016; Möller et al., 2017; Müller et al., 2017)

Another hydrogel that has shown promising results for cartilage tissue engineering is fibrin. The use of fibrin has been demonstrated to support cell adhesion, migration and differentiation (De la Puente and Ludeña, 2014). Fibrin as a scaffold is an attractive material given that it is already widely used in the head and neck region to aid haemostasis following surgical procedures and has been shown to be safe in clinical use (Ujam et al., 2012). Furthermore, it can be produced as an autologous hydrogel using the patient's own serum therefore reducing risk of cross-contamination or foreign body reaction. Potential problems with fibrin as a bioink is its shrinkage , low stiffness and rapid degradation (Ahmed et al., 2008; Noori et al., 2017).

1.5.2.5 Polymer materials for mechanical support

Any scaffold used in combination with cells should be biocompatible, resorbable and have appropriate mechanical strength to allow the surgeon to handle the construct intra-operatively without damage. Selection of an already FDA approved material will make clinical translation quicker and easier.

Examples of such materials include:

- Polylactic acid -PLA
- Polycaprolactone – PCL
- Poly(glycolic acid) – PGA
- Poly(lactic-co-glycolic acid) (PLGA)

Furthermore, by modifying the molecular weight or scaffold orientation of such materials, both their mechanical properties and resorption time can be manipulated to the desired characteristics (Zhang et al., 2012). Interestingly, tissue scaffolds can be embedded with proteins, drugs and cytokines that enhance stem cell activity by numerous effects. For example, the embedding of an antiangiogenic drug (bevacizumab), to a fibrin/hyaluronan scaffold seeded with chondrocytes resulted in improved construct survival rate in nude mice (Centola et al., 2013).

Biodegradable polymers for tissue engineering have been widely studied and their fabrication as scaffolds have been extensively modified and tested. Such scaffolds offer mechanical support and an environment for cell proliferation and generation of the desired tissue in parallel to polymer degradation. The rate of new tissue formation should match that of the polymer degradation. Degradation properties of a 3D scaffold supporting living cells should be tailored to permit cell adhesion and new tissue formation over a desired time with homogenous and uniform polymer resorption and at a controlled rate. Achieving such uniform scaffold degradation is unpredictable given the variables that contribute to this, namely polymer properties, initial cell seeding distribution, cell-scaffold interactions, pH value of the surround microenvironment and the level of physical loading adjacent to the construct once grafted (Lammi et al., 2018; Zhang et al., 2014). There are simply too many uncertainties.

Polycaprolactone (PCL) appears to be an attractive scaffold material as it offers some advantages compared to PLA. In contrast to PLA, Polycaprolactone (PCL) has a lower melting point of 59-64 °C, longer degradation rate but is hydrophobic with low bioactivity resulting in poor cell attachment (Siddiqui et al., 2018).

Bioactivity can be improved by PCL surface functionalization (Permyakova et al., 2019). PCL has been studied both in vitro and in vivo models for cartilage tissue engineering using numerous bioinks and cell types. Kundu et al. 2015 printed constructs utilising layer-by-layer (LBL) deposition of PCL and chondrocytes encapsulated by an alginate hydrogel using a multihead deposition system (MHDS). Constructs were implanted in a subcutaneous pocket in nude mice and analysed for chondrogenesis by histochemical and immunohistochemical staining and identified expression of collagen II and GAG. PCL was found to be easy to print with high fidelity, nontoxic and was conducive to cartilage like tissue generation. However, what was noted is the slow degradation of PCL and its hindering of tissue ingrowth (Kundu et al., 2015).

Due to its higher viscosity 3D printing PCL effectively relies on optimisation of several important variables. This includes print speed, nozzle diameter, nozzle length and shape and print temperature. Optimization of these variables is required to produce high print resolution and fidelity while avoiding prolonged print times.

Conical shaped nozzles of large diameter and printing with lower print temperatures appears to be beneficial when printing cells onto PCL (Ortega et al., 2019).

1.5.2.6 Scaffold sheet - Integra® dermal regeneration template

Collagen has shown potential to be an excellent scaffold given that this is found in native extracellular matrix of cartilage tissue. Collagen products are currently widely used in surgery ranging from haemostatic agents, surgical meshes and in the form of sheets as an alternative to skin grafts. Integra® dermal regeneration template (IDRT) has been used extensively in burns patients and reconstructive surgery for skin cancer patients to cover skin defects and is recommended in the reconstruction of large complex wounds and where there is bone exposure as well as other indications (Magnoni et al., 2019). It has also been applied to intra-oral and nasal defects effectively (Moratin et al., 2019; Rúa Gonzálvez et al., 2018; Seth et al., 2019). Its advantage over other reconstructive options such as a skin graft, is that it is quick, easy to apply and can be used in full thickness skin defects. It is supplied as a two-layer sheet consisting of an outer silicone and an inner layer consisting of a thick matrix layer of pure bovine collagen (92%) and shark glycosaminoglycan (8%) with a mean pore size of 30-120um (Fig. 1.13).

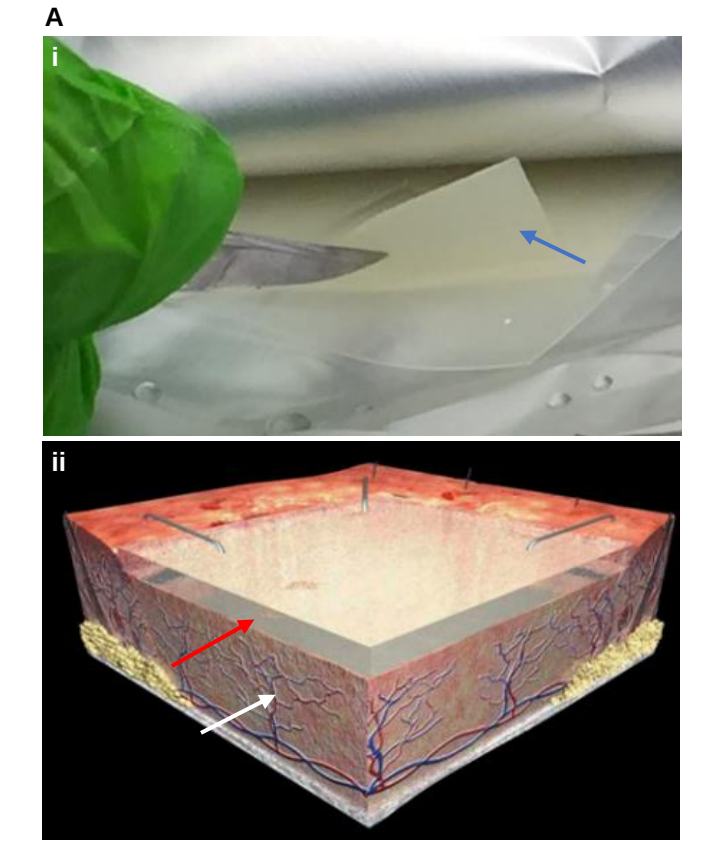

Figure 1.13. Bilayer Integra dermal regeneration template. (Ai) Macroscopic appearance of the sheet (blue arrow). The sheet is soft but can be sutured or stapled to adjacent skin. **(Aii)** Diagram of mechanism of healing within Integra. At 3 weeks the top silicone layer will be removed as by this point cells that have migrated into the Integra from surrounding skin and wound bed begin to form neovascularization (white arrow) and epithelial layer formation (red arrow). **(B)** Integra in clinical use. Here the sheet has been stapled onto a large scalp defect of a patient with basal cell carcinoma (BCC) following wide local excision**.**

The outer layer provides mechanical protection and controls fluid loss, while the inner layer functions as an extracellular matrix and promotes cellular growth and collagen synthesis. The Integra membrane is replaced by host tissue after 3-4 weeks. There is also a single layer version without the silicone. IDRT consists of bovine tendon collagen and shark glycosaminoglycans (chondroitin-6-sulfate) has been used extensively for over 30 years in burns surgery and as a dermal substitute (Chang et al., 2019). Its fabrication relies on a freeze-drying process and its original design took into consideration the physical properties that would permit cell invasion into the membrane and allow cell migration within it. Pore size was determined to be at least 40μm based on characteristic cell diameters (Dagalakis et al., 1980).

Numerous studies have examined the cellular and then the histological changes that take place in patients who have had Integra reconstruction. These appear to confirm that in-vivo, Integra matrix is infiltrated with red blood cells, fibroblasts, and endothelial cells. By the third week, neovascularisation is well established. The presence of collagen and elastic fibres have also been observed (Lee et al., 2015; Moiemen et al., 2011, 2001). Several studies have investigated the potential use of IDRT as a scaffold for tissue engineering or enhanced wound healing by the addition of MSCs seeded onto it (Table 1.2).

Author	Cells	Study	Model	Findings
Wood et al 2006	Swine Dermal/epidermal junction MSC	Wound healing	Yorkshire swine	Epidermis formation within Integra
Edwards et al 2014	Human ADSC Whartons jelly MSC	Wound healing & vascularisation	Babb/c mice	Improved angiogenesis into wound
Formigli et al 2014	Lewis rats Bone marrow MSCs	Skin wound healing	Lewis rats	Accelerated Healing
Wahl et al 2015	Human ADSC	In vitro MSC delivery & healing	In vitro & CAM	Integra superior to chitosan and decellularized dermis
Cherubino et al 2016	Human (Breast) ADSC	Wound healing & vascularisation	Athymic CD1 nude mice	Improved angiogenesis into wound
Bornes et al 2016	Sheep Bone marrow MSCs	Chondrogenesis	In vitro	High cell densities required for chondrogenesis
Zomer et al 2020	Human dermal derived MSCs & ADSCs	Wound healing	C57BL/6 mice	Improved angiogenesis & better-quality scars

Table 1.2. Summary of publications using Integra as a cell scaffold.

Cherubino et al., 2016, investigated the potential of human ADSC seeded onto Integra matrix to promote neovascularisation. Their experiment appears to suggest that Integra sheets seeded with human ADSC and grafted into nude mice (for 4 weeks) form new vascular networks that are not present in Integra sheets without ADSC (Cherubino et al., 2016).

Given that Integra is already in clinical use and that it permits cellular infiltration and collagen deposition, the potential for this matrix to provide a chondrogenic inducive environment was investigated. This set of experiments were designed to determine the ability of both ADSC and cartilage derived stem precursor cells to generate cartilage like ECM within Integra. Formigli et al., 2015, seeded transgenic rat bone marrow MSCs on a sheet of Integra matrix 2x4cm ($1x10^6$ cells) implanted into the dorsum of rats. They showed that seeded Integra demonstrated increased reepithelization and angiogenesis and greater return of skin appendages on a rat wound compared Integra alone (Formigli et al., 2015). Interestingly, Bornes et al. 2016, demonstrated that sheep bone marrow derived stromal cells seeded into Integra sponge cultured in static medium displayed increased levels of chondrogenesis with increasing cell seeding density. Their study showed that cell seeding at a density of $50x10^6$ produced the greatest level of hyaline-like cartilage within an Integra sponge (Bornes et al., 2016).

An evaluation of how human ADSC behave within Integra sheet compared to a chitosan-based film scaffold, fibrin and decellularized dermis was investigated by Wahl et al. 2015. In this interesting and useful study, they showed that Integra sheet seeded with ADSC showed a different cell distribution to the other scaffolds with a gradient pattern from the seeding side to the bottom. Fibrin on the other hand showed a cell distribution throughout the scaffold with a higher cell numbers at the core. Furthermore, cell survival within Integra was the high with minimal cell death after seeding compared to the other scaffolds. Interleukin-6 release was upregulated in the Integra model and may explain the accelerated wound healing and rates of angiogenesis observed in other studies. Scanning electron microscopy of Integra in the same study showed high porosity throughout with a mesh like structure. Cell loading capacity of Integra was determined to be 86.5% ±3.8, an hour after seeding (Wahl et al., 2015).

1.5.3 Imaging techniques for 3D cell culture analysis

Three-dimensional cell culture systems are being increasingly recognised for their advantages and potential in the modelling of cardiac, gastrointestinal, retinal, and neurological human disorders as well as tissue engineering and drug discovery (Clevers, 2016; Drost and Clevers, 2017; Eglen and Reisine, 2019). Although spheroids provide a useful model into cell behaviour in 3D as described, they are small and delicate which makes them difficult to handle and ultimately analyse. There is therefore a need to develop protocols for imaging and staining of 3D spheroid systems in wholemount which would permit non-destructive study of cells in their 3D microenvironment. Standard histological preparation of these small spheroids may result in fragmentation and degradation with unsatisfying results. Manual processing of spheroids for paraffin embedding is labour intensive that may preserve more spheroid morphology than automated techniques, but may still result in unwanted physical changes (Olsen et al., 2014). Alternative techniques that completely avoid sectioning of spheroids would have numerous advantages including reduced risk of degradation, tears and sample irregularities caused by either the microtome blade or water bath. Despite being only a few hundred micrometres, spheroids are difficult to image with standard optical microscopy due to their inherent milky/frosted glass appearance typical of cartilage tissues that is caused by light scattering. This appearance results in lack of clarity and sharpness in deeper regions of tissue and therefore significantly limits the depth of imaging (Richardson and Lichtman, 2015). Optical imaging of cartilage 3D spheroids is therefore not useful, and an alternative is required.

1.5.3.1 Optical sectioning

The development of two-photon excitation microscopy allows “optical sectioning” and detailed 3D imaging of spheroids without the need to section them and appears to be an attractive alternative to conventional histological methods. Two-photon microscopy relies on localised nonlinear excitation to excite fluorescence only within a thin plane and allows excellent depth penetration (Costa et al., 2019; Denk et al., 1990). Confocal microscopes have a limited penetration of approximately 100-200µm but in multiphoton (2-photon) microscopy this can be approximately 1000µm. Theer et al., 2016, in their studies imaged stained vasculature and GFP labelled neurons down to a depth close to 1000µm below the brain surface. Images can be obtained in thin sections and then formatted to 3D reconstruction. Increasing depths of imaging is limited by the onset of out of focus fluorescence generated near the top of the tissue being sampled (Theer et al., 2003; Theer and Denk, 2006).

However, despite 2-photon microscopy improving imaging depths in 3D tissue, some tissue types such as cartilage remain challenging and full depth optical sectioning is still limited to surface layers with loss of detail around 60µm deep (Zucchelli, 2018).

1.5.3.2 Optical clearing

Clearing protocols reduce light scatter (and gives tissue samples higher transparency) and results in deeper imaging of 3D tissue by improved laser penetration and contrast. Tissues inherently have non-homogenous refractory index due to variable composition of lipids, proteins and water. Clearing techniques aim to reduce light scatter by homogenizing the refractive index (RI) across any given tissue sample. Optical clearing is broadly grouped into solvent based and aqueous based techniques and is succinctly described by Richardson et al (2016) and updated and summarized by Costa et al (Costa et al., 2019). Briefly, both strategies are described below.

Solvent based

This commonly requires 2 steps:

1) Dehydration with lipid solvation – commonly using methanol
2) Additional lipid removal and clearing by refractive index matching

Dehydration and removal of lipids results in a homogenous high protein, dense tissue sample. Clearing is then finally achieved by using several available solutions including methylsalicate, benzyl alcohol, benzyl benzoate, dichloromethane and dibenzyl. The final tissue becomes transparent as the clearing solvents refractive index is well matched to the refractive index of the dehydrated sample. Clearing solvents such as benzyl alcohol/benzyl benzoate (BABB) has been shown to be a highly effective clearing agent, but its use is limited by its corrosive nature to common microscope materials and objectives potentially causing irreversible hardware damage. Furthermore it causes dehydration induced shrinkage of the cleared tissue, renders samples brittle and is toxic (Dodt et al., 2007). However, BABB has been used to clear cartilage and has the advantage of working effectively on samples stained for cartilage with Alcian blue (Klymkowsky and Hanken, 1991).

Aqueous based

These techniques were developed to avoid the undesirable effects of the solvent based clearing solutions. They rely on 3 methods of homogenizing the scattering throughout the tissue to achieve a clear sample:

1) Application of a solution that has a matched refractive index to the sample tissue and achieving clearing by passive immersion. Example is Glucose, Fructose, glycerol and formamide (*Clear*^{T}). Homogenization is achieved as water content in the sample is replaced by the clearing solution.
2) Lipid removal then dehydration to lower the refractory index of the tissue sample. Example is Sca*l*e
3) Active or passive lipid removal then immersion in a refractory index matched solution.

Clear^{T} (and *Clear* ^{T2}) was described by Kuwajima et al in 2013 and was developed to tackle the issue of tissue swelling or shrinkage caused by other clearing solutions such as Sca*l*e and BABB. *Clear*^{T} clearing protocol involves sequential incubation of the sample in increasing concentration of formamide solution (20% to 95%) made up with phosphate buffered solution (PBS) over a time of 30 mins to 16 hours depending on the tissue sample and size. *Clear*^{T2} is a 50% formamide/20% polyethylene glycol solution and is applied in a similar way. The protocols described by Kuwajima et al achieved clearing of fixed whole mouse embryos and postnatal brains overnight with no significant change to the sample size. Their study also demonstrated that Clear^{T2} was superior for immunohistochemistry and genetically encoded fluorescence proteins, whereas Clear^{T} was incompatible (Kuwajima et al., 2013). However, this study was based on mouse brains and not dense connective tissue such as cartilage and therefore its clearing potential of such tissue is largely unknown.

Sca*l*e solution developed by Hama et al, is based on a composition of 4M urea, 10% (wt/vol) glycerol and 0.1% (wt/vol) Triton x-100. In their original publication, Hama et al effectively cleared mouse brain samples of 1.5mm thickness, intact whole mouse brains and whole mouse embryos using this solution. The main undesirable effects of Sca*l*e include prolonged time to achieve clearing, sample fragility and sample tissue expansion (Hama et al., 2011).

1.5.3.3 Whole-mount immunolabelling of 3D cultures

Another important factor in optical sectioning is antibody penetration when immunofluorescent staining is used. Limited imaging at deeper levels of the spheroid 3D cultures may not be restricted by confocal laser penetration but by poor antibody penetration instead. Tissue staining methods have been intensively investigated, and many researchers have been faced with the same problem of diffusion-limited staining and antibody penetration. Fluorescent dyes and antibodies to label various molecular markers permeate slowly through tight tissue matrix (Tainaka et al., 2016).

Incubation times of primary and secondary IgG antibodies (approximately 150kDa) can be lengthy due to their slow diffusion, and depending on tissue type and thickness, may range from 1 hr to 6 weeks (Calve et al., 2015; Chung et al., 2013; Nürnberg et al., 2020; Yang et al., 2014).

Calve et al. 2015 visualised deep regions of dense cartilage ECM using a non-destructive optical clearing technique using low MW fluorescently labelled probes to maximise signal penetration and confocal microscopy, to characterise cell-cell interactions. They were able to demonstrate individual chondrocytes distribution to a depth of 300µm using this strategy (Calve et al., 2015).

Achieving detailed images of core regions of 3D cultures is sensitive to antibody penetration, and additionally effective permeabilization protocols for promoting the substitution of water inside tissues with high refractive index medium. Therefore, the use of cell lines that express genetically encoded fluorescent proteins (example GFP) in 3D culture may be advantageous by bypassing these potentially limiting factors (Becker et al., 2012).

1.6 Aims of the project

The aim of this project was to construct a nasal septal cartilage graft product to use in rhinoplasty surgery as an alternative to current cartilage grafting procedures. A scaffold free system using cartilage spheroids as building blocks for large cartilage tissue constructs has many advantages and would remove the need to use biomaterial scaffolds. Challenges with 3D spheroid cultures, however, is that they are labour intensive to generate and require long culture times. Therefore, other strategies to achieve the aim of this project where adopted that exploit the behaviour of cells in 3D in combination with resorbable biomaterial scaffolds.

The objectives of the thesis were:

1. **To analyse cartilage 3D spheroids in vitro using non-destructive methods**. Cell behaviour in 3D underpins the understanding of cell-cell and cell-ECM interactions. Optical clearing and optical sectioning are non-destructive imaging techniques that permit detailed analysis of 3D spheroids, but the dense nature of these tissues limits imaging in their deeper regions. This thesis interrogates aspects of these modern imaging methods including optimisation of permeabilization, antibody staining, optical clearing, and confocal microscopy protocols.

2. **Asses the degree of chondrogenesis in Integra matrix when seeded with ADSCs and CSPCs and analyse its suitability to be used within a 3D printed PLA septal pocket.**
   Cartilage tissue engineered in vitro will require time to mature to allow ECM deposition by cells. To expedite in vitro to patient translation, a novel “pocket” design constructed from a resorbable polymer will provide mechanical support to the maturing cartilage tissue after it is inserted into the patient septal region. I designed and 3D printed a PLA pocket and investigated the potential of ADSCs and CSPCs to deposit cartilage like ECM when seeded onto Integra matrix. The feasibility of inserting Integra seeded with cells into this pocket was assessed.

3. **To assess the level of maturation of chondrogenically induced CSPCs in 3D bioprinted constructs and fibrin hydrogel**
   3D bioprinting technology provides a novel strategy to generate custom made and patient specific nasal grafts. Studies analysing the ability to bioprint ADSC and nasal septal chondrocytes for cartilage tissue engineering have been shown promising results but bioprinting of auricular cartilage derived stem/precursor cells has not been investigated.

CSPCs were bioprinted and cultured over an extended 6-month time period to assess cell viability and their chondrogenic potential. I also compared the behaviour of these cells in commercially available fibrin hydrogel.

4. **To assess the level of chondrogenesis in a "Sandwich" construct of cell seeded Fibrin hydrogel within PCL mesh sheets.**

   This strategy takes advantage of fibrin hydrogel which is already FDA approved and in clinical use. Cells seeded in fibrin and sandwiched between two PCL sheets for mechanical support appears to be simple, quick and easy to upscale to large constructs. Bioprinting PCL is advantages for this purpose as it has a low melting point and therefore, less risk of thermal injury to cells if printed simultaneously. Printing reproducible PCL mesh requires control of numerous printing parameters. I developed a new protocol for printing reproducible PCL mesh and assessed a "sandwich" design for its feasibility as a nasal septal product. This would form the basis of future studies to use fibrin as a bioink (not commercially available at the time of this thesis) to print directly onto PCL.

Summary

In this thesis three pathways to a potential solution to generate cartilage were investigated (Fig 1.14). Experiments developed sequentially from A-C.

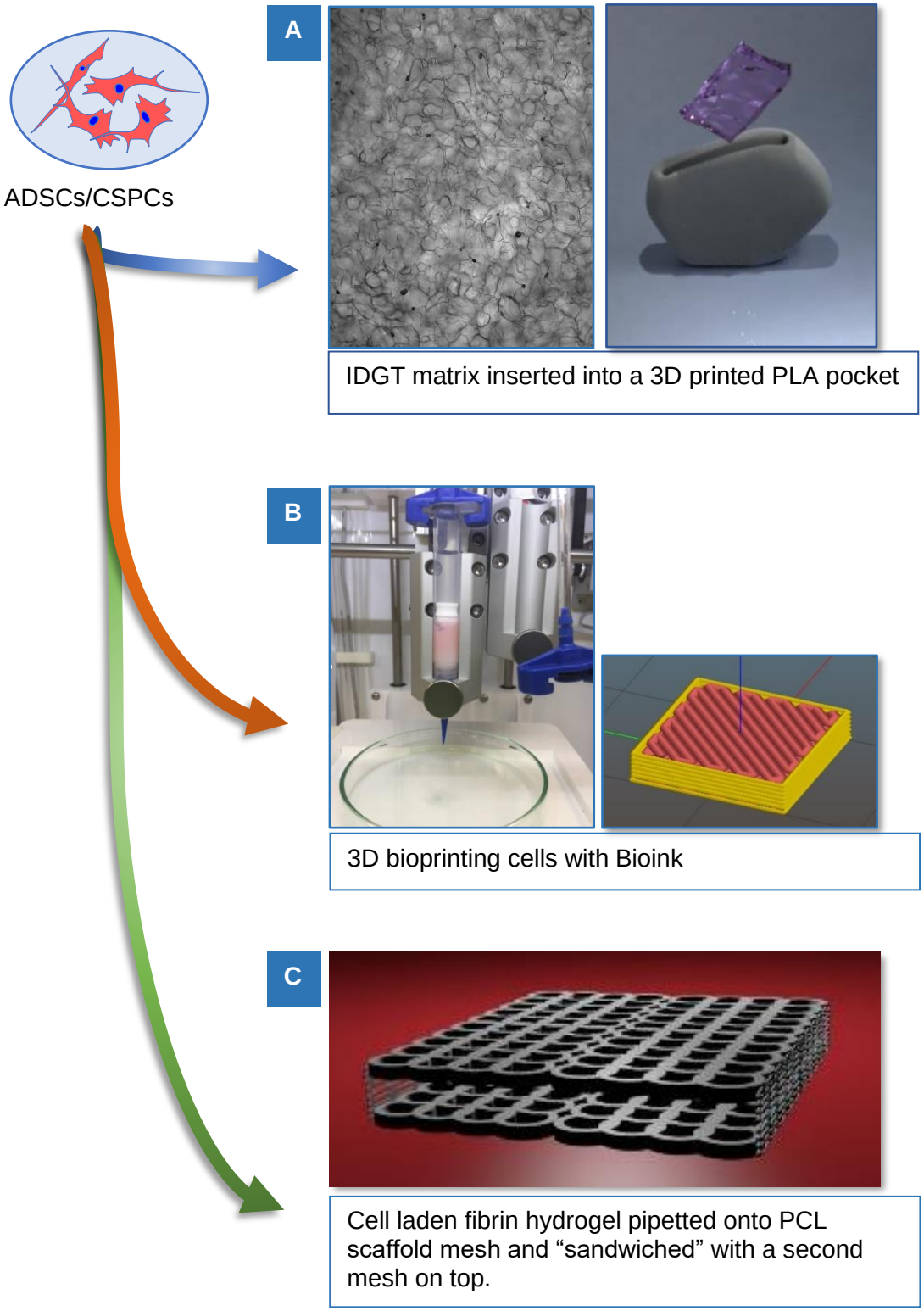

Figure 1.14. Three strategies to generating cartilage tissue. **(A)** Cells seeded into Integra then placed into a PLA pocket. **(B)** 3D printed cells using bioink. **(C)** Cell seeded hydrogel sandwiched between two layers of PCL mesh.

Chapter 2

MATERIALS AND METHODS

2.0 Material and methods

This chapter describes the details of methodology used in this thesis. The description of additional methods used as part of development of new protocols, technical and procedural modifications and optimisations of current techniques are discussed in individual chapters.

2.1 Tissue acquisition

Experimental work in this thesis involved the use of 3 groups of cells: Adipose derived stem cells (ADSC), adipose explant derived stem cells (AEDSC), microtia ear derived cartilage stem precursor cells (CSPCs) and normal ear CSPCs. All samples were provided by the same consultant surgeon at UCL Great Ormond Street Hospital for children, under ethical approval from the Camden and Islington Community Local Research Ethics Committee (London, U.K.). The clinical background of these patients varied but included cranio-facial microsomia, microtia, prominent ears and one patient with a facial haemangioma requiring fat transfer reconstruction. A summary of all the cell lines used in this thesis is presented in table 2.0.

2.1.1 Adipose tissue and ear cartilage initial processing

Samples were provided fresh at the time of surgery and the patient details recorded without patient identification, therefore remaining anonymous. Samples were provided in sterile syringes for adipose tissue or sterile gauze for cartilage samples, isolated in sealed plastic bags and stored at 4°C until processed no later than 24hrs after harvesting. For every lipoaspirate and cartilage sample provided, samples were divided into 3 groups for future RNA extraction, histology and for cell culture (Fig. 2.0). ADSC lines were derived using two previously well-established protocols; either enzymatic or by the explant method (L. Guasti et al., 2012).

Sample	Diagnosis	Gender/Age	Cell line identification
Ear cartilage	Hemifacial microsomia	Male 12yrs	Ch32
Ear cartilage	Normal	Male 9yrs	CH90
Ear cartilage	Normal	Male 13yrs	CH105
Fat	Hemifacial microsomia	Male 17yrs	H40 ADSC
Fat	Lipoma	Female 14yrs	H33 ADSC
Fat	Hemifacial microsomia	Female 10yrs	H37 ADSC

Table 2.0. Summary of patient samples used in this thesis.

A

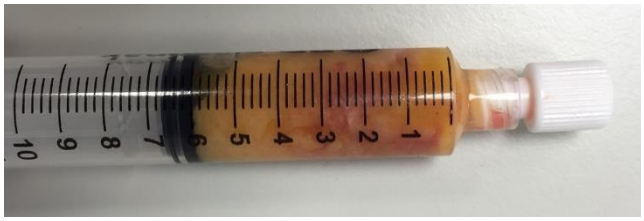

B

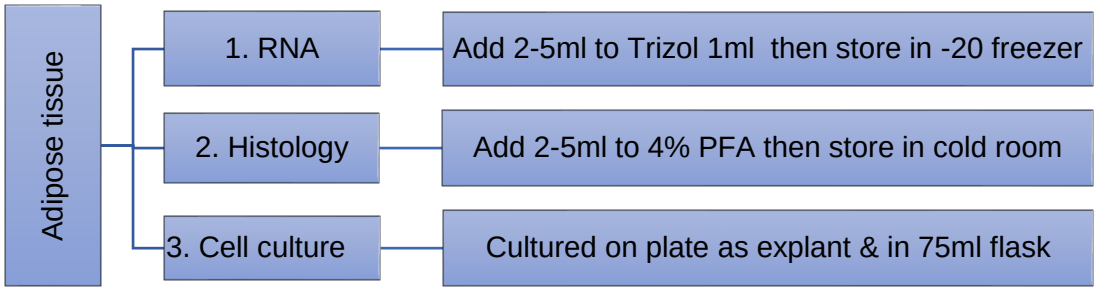

Figure 2.0 Lipoaspirate from paediatric patients. (A) Adipose tissue harvested from abdominal fat or from inner thigh. Typical sample volumes ranged between 10-15ml for each case. **(B) Adipose tissue processing**. For each lipoaspirate sample, adipose tissue was stored for RNA extraction by adding 1ml Trizol (Ambion – Life Technologies) and stored in -20°C freezer, another sample added to 4% paraformaldehyde (PFA) and stored at 4°C, and the majority of the adipose tissue used for generating a new stem cell line.

2.2. Cell culture

Culture media was comprised of Dulbecco's modified Eagle's medium (DMEM) high glucose Glutamax (Gibco Life Technologies #31966021) supplemented with 10% embryonic stem cell-qualified foetal bovine serum (ES-FBS; Merck #ES-009-B) and 1% penicillin/streptomycin (Gibco Life Technologies #15140122). In all new cell lines, cell isolation was also undertaken using media supplemented with human plasma lysate (HPL StemCell Technologies #06962) instead of ES-FBS. All cells were incubated at 37°C in a humidified incubator with 5% CO_2. Cell culture reagents were procured from Thermo Fisher Scientific (MA USA). Details of cell lines used for each experiment are highlighted at the beginning of each chapter.

2.2.1 Primary cell cultures

2.2.1.1 Isolation of paediatric Adipose derived stem cells

Lipoaspirate tissue was placed into a 50ml falcon tube and washed with 25ml PBS (PBS; Life Technologies, Rockville, MD). The solution was allowed to settle and then as much of the liquid layer as possible was removed with a pipette.

An equal volume of trypsin x1 concentration was added (0.05% trypsin/1 mM EDTA, Gibco Life Technologies #15400054) and the tube placed onto 37°C incubator roller for an hour. Following this, an equal volume of culture medium was added, and the tube spun at 1000rpm for 5 mins. This left a fat layer on top and a stromal vascular fraction (SVF) at the bottom (Fig. 2.1).

The top adipose layer was poured off as well as the red cell layer and the SVF was resuspended with 10ml of medium and seeded into a T75 flask. The flask was placed in CO_2 incubator at 37°C and the media completely changed after 24hrs.

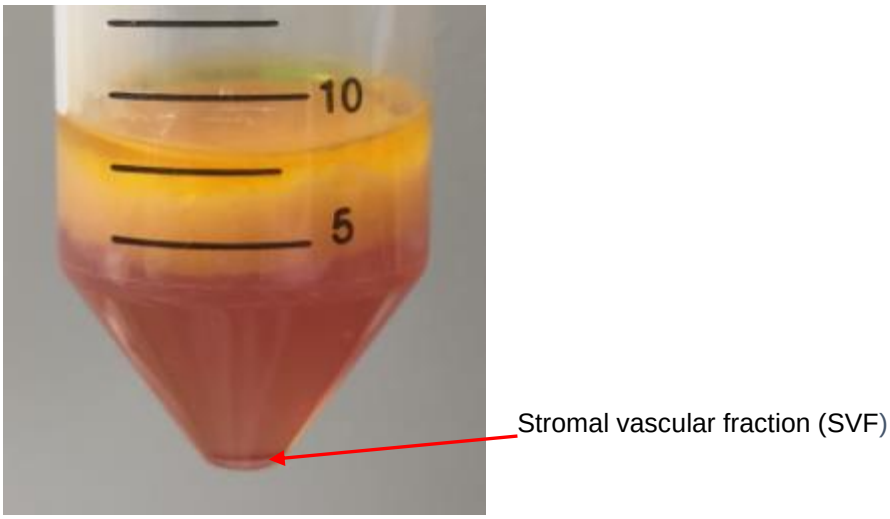

Figure 2.1 Stromal vascular fraction. Following a 5-minute centrifuge at 1000rpm, the top layer formed of adipose tissue and red blood cells was poured away to leave the SVF pellet at the bottom.

2.2.1.2 Adipose explant derived stem cells

A volume 2-5ml of lipoaspirate was syringed into a small plastic sterile petri-dish. Using sterile forceps, a small mass of adipose tissue was gently placed into each well of a 48 well plate and 200µl of culture medium was carefully added. After 2 hours of incubation in a CO_2 incubator at 37°C, an additional 1ml of media was slowly added to cover each well, being cautious not to disturb the attachment of the adipose tissue to the plastic. The plate was incubated and examined under a microscope after 24 hrs, at which point the medium was replaced with a similar 1ml of DMEM.

2.2.1.3 Isolation of cartilage stem/precursor cells from human ear cartilage

Cartilage stem precursor cell lines were derived using surplus cartilage from paediatric patients undergoing surgery for craniofacial deformities (mainly microtia). Cartilage samples were either from rib following costochondral rib harvesting procedure or auricular cartilage. Patient cartilage samples were washed in sterile PBS followed by careful trimming of excess fat and connective tissue then diced into 5mm wide sections and placed in 24 well plates. Culture medium was gently added (200µl) as to not lift the explants off the well bed. After 2 hours of incubation in CO_2 incubator at 37°C, the wells were flooded with an additional 1ml of DMEM culture medium (Fig 2.2). Once cells were identified on the plate and had become approximately 80% confluent, the explants were removed and disposed of.

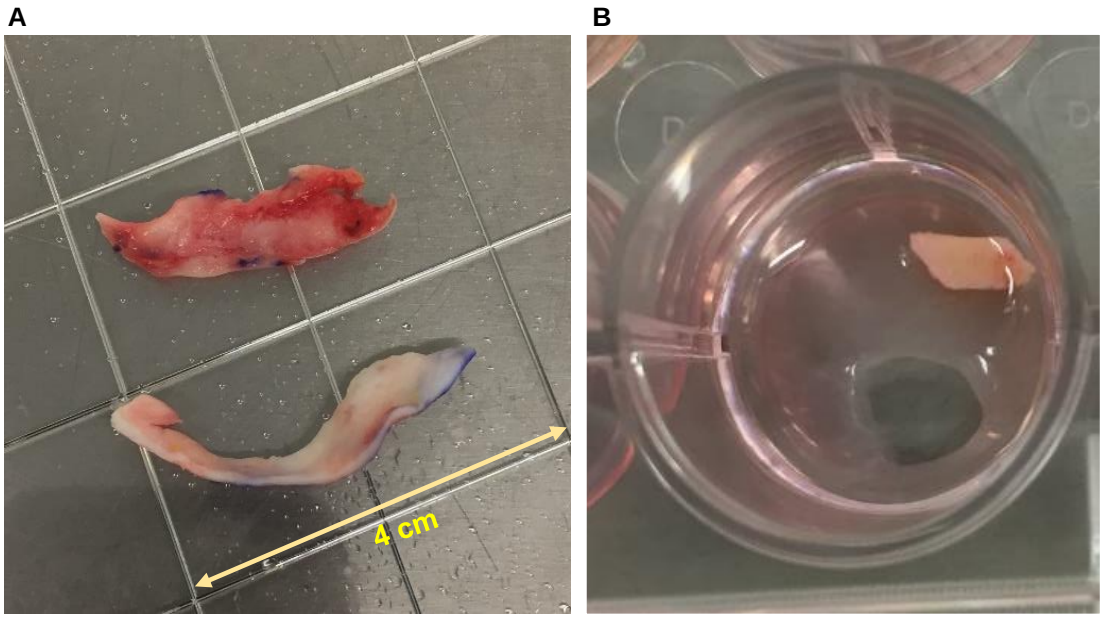

Figure 2.2. Human ear cartilage. A) Normal healthy cartilage resected from a paediatric patient undergoing surgery for prominent ear correction. **B)** Cartilage explant cut with scalpel into small 5mm sections and incubated in 24 well plate.

2.2.2 Cell expansion

All cell lines were expanded as monolayer cultures on plastic and examined daily with fresh media added every 2-3 days. Passaging (subculture) was prompted when cells reached 80-90% confluency (to minimise cell stress and prevent loss of multipotency) and involved removal of the medium in each well along with any tissue.

2.2.2.1 ADSC

When ADSCs in tissue culture flasks and individual wells (for explants) reached the target confluency, they were washed twice in PBS, detached using 0.05% trypsin/1mM EDTA for 5 minutes at 37°C ,then spun at 1000rpm for 5 mins with the resulting cell pellet resuspended in fresh medium and plated on a new larger tissue culture flask at a density of 2-3x10^3/cm^2. Cells were counted using TC20^{TM} Automated Cell Counter (Bio-Rad, USA), or a haemocytometer following the addition of trypan blue for a final dilution of 1:10.

2.2.2.2 Cartilage explants

For the explant protocols cells migrating away from the cartilage were identified at approximately day 7 at which point the cartilage section was removed. Cells were then passaged by washing the individual plate wells with PBS twice and detaching the cells using 0.05% trypsin/1mM EDTA for 5 minutes at 37°C. This reaction was terminated by the addition of a similar volume of medium. The combined detached cells were centrifuged and seeded in an identical way to ADSC.

2.2.2.3 Mycoplasma testing

For each cell line isolated and expanded, mycoplasma testing was performed to exclude mycoplasma contamination using MycoAlertTM PLUS mycoplasma detection kit (Lonza, Basel, Swiss). Once a new cell line had been confirmed negative for mycoplasma, they were cultured in incubators in a designated tissue culture room. Cell cultures were then tested monthly for mycoplasma as part of a surveillance schedule.

2.2.2.4 Cryopreservation

For each new cell line successfully expanded, cryopreservation was undertaken by adding 10% dimethyl sulfoxide (DMSO) to ES-FBS or Human platelet lysate (HPL) serum depending on the culture medium used and the cells banked (at -130°C) in a minimum of 10 separate cryogenic vials with 1x10^6 cells per vial.

2.2.3 Cell differentiation

To characterise cells isolated from lipoaspirate or cartilage and to determine their MSC status, new cell lines were differentiated along tri-lineage protocols (adipogenic, chondrogenic and osteogenic) already established in our group (Leonardo Guasti et al., 2012b). ADSC were seeded in 48 multi-well plates at $2x10^4$ cells/well and allowed to expand until 100% confluency (approx. 7 days). For each differentiation protocol, fresh culture medium was added 3 times a week and the experiment terminated at the 3-week time point. Each tri-lineage differentiation was done in quadruplicate.

2.2.3.1 Adipogenic differentiation

At confluency, 500µl of culture medium supplemented with 10 ng/ml insulin, 500 µM 3-isobutyl-1-methylxanthine, 1 µM dexamethasone, and 1 µM rosiglitazone was added to each differentiation well. At 3 weeks, cells were washed with PBS, fixed with 4% PFA, washed with 60% isopropranolol for 5 mins, and then stained with Oil Red O solution.

2.2.3.2 Chondrogenic differentiation

At confluency, 500µl of culture medium supplemented with 0.1 µM dexamethasone, 10 ng/ml transforming growth factor (Tgf) β-1 (Gibco, Life Technologies PHG9214), insulin-transferrin-selenium (ITS) (Gibco, Life Technologies #41400-045), and 50 µg/ml ascorbate (Sigma L-ascorbic acid A4034) was added to each well. At 3 weeks, cells were washed in PBS, fixed with 4% PFA, rinsed with 0.1N HCL for 5 mins then stained with 1% Alcian blue solution overnight.

2.2.3.3 Osteogenic differentiation

At confluency, 500µl of culture medium supplemented with 0.1 µM dexamethasone, 100 µg/ml ascorbate, and 10 mM β-glycerophosphate was added to each well. At 3 weeks, cells were washed with PBS, fixed with ice cold 70% ethanol for an hour then stained with 1% Alizarin red solution.

2.2.4 Three-dimensional spheroid cell cultures

To investigate ADSC and CSPCs behaviour in 3D, spheroids of different sizes were generated using either $1x10^5$ or $3x10^5$ cells and differentiated over 6 and 10 weeks using protocols already established in our group (New et al., 2017). Briefly, ADSCs/CPSCs were collected by treatment with 0.05% trypsin-EDTA and centrifuged at 1000rpm for 5 min. Cells were then counted and resuspended in 250µl culture medium and aliquoted into 1.5 ml Eppendorf tubes so that each tube contained the required number of cells. The Eppendorf tubes were centrifuged at 300g for 5 mins then incubated at 37°C, 5% CO_2 overnight with the tops loosely applied to allow gas exchange.

2.2.4.1 Spheroid Chondrogenic differentiation

Cell aggregation with spheroid formation typically occurred around 24-48hrs of incubation. At this point proliferation medium was changed to chondrogenic differentiation medium, whilst control spheroids remained in the same proliferation medium changed every 2-3 days over a 6 week period. Spheroids were gently agitated at each medium change to prevent them adhering to the tube surface and to allow full exposure to medium. The experimental design included generation of triplicates of each spheroid created, both for controls and chondrogenically differentiated samples. At the end of incubation periods, spheroids where fixed with 4% paraformaldehyde (PFA), washed in 1xPBS and stored at 4°C until required for staining and imaging.

2.3 Preparation for cell imaging and analysis

2.3.1 Histology – Paraffin embedding and sectioning

Samples for histology were washed twice in PBS and placed in 10% buffered formalin for a minimum of one hour. Samples were given to the research pathology laboratory services at Great Ormond Street Hospital for automated processing. All samples were embedded in paraffin wax. Paraffin embedded samples were then sectioned on a manual rotary microtome at 5µm thick sections and placed in a water bath to permit mounting onto superfrost glass slides (Fisher Scientific 22-037-246), followed by 3 hours of drying at 60°C.

In preparation for staining, paraffin sections were passed through 2 cycles of xylene (5 mins each) and then decreasing strengths of ethanol at 100%, 95%, 70% and 50% for 3 mins (5 mins for 100%). To complete the rehydration process, the slides were immersed in water.

2.3.1.1 Toluidine blue staining

For toluidine blue staining, rehydrated sections were immersed into 0.1% toluidine blue solution for 2 mins then into water for a further 2 mins. Slides were gently dried and then placed in an oven for 2 hours at 37°C. Slides were then mounted using Permount Mounting Medium (Fischerscientific SP15-100) and allowed to dry for 48 hrs.

2.3.1.2 Picrosirius red staining

This was undertaken in a similar method to toluidine blue, but slides were stained for 2 hours then dehydrated through increasing strengths of ethanol (50%, 75%, 95%) for 3 minutes at each strength. The slides were finally placed in 100% ethanol for 2x5 min cycles. Slides were mounted as described above.

2.3.1.3 Haematoxylin and Eosin staining (H&E)

All H&E staining as kindly provided by the research pathology laboratory services at Great Ormond Street Hospital.

2.3.1.4 Alcian Blue staining

Alcian blue (AB) is used for cartilage staining to identify acidic polysaccharides such as GAGs and its pH must be controlled between 1.0 (for sulphated polysaccharides) to 2.5 (additional staining of carboxylated acid mucopolysaccharides). Alcian blue was made from 1% AB powder 8GX (BDH, Crawley, UK) in 0.1 N HCL.

Cells were washed three times in 1xPBS and once in 0.1N HCL for 5 mins followed by application of AB stain overnight at room temperature on a slow shaker. Cells were then washed twice (5 mins each) with 0.1 N HCL and washed with dH_20 once.

2.3.1.5 Alizarin Red staining

This stain binds calcium ions in mineralised bone. This was made from 1% Alizarin Red powder (Sigma-Aldrich) in dH_20 with pH controlled (to range 4.1-4.3) using 0.5% ammonium hydroxide. Prepared stain solution was stored at room temperature away from sunlight. Cells were first fixed with 70% ice-cooled ethanol for an hour, washed three times with dH_20 and then stained with Alizarin Red stain for 30 mins at room temperature. Cells were then washed with dH20 again to remove excess stain solution.

2.3.1.6 Oil Red O staining

This was used to stain for lipid droplets and adipocytes. A stock solution was made from 0.35gm Oil Red O powder (Sigma-Aldrich) in 100ml isopropanol. For staining, a working solution was made from 6ml of stock solution diluted with 4ml dH_20 and then filtered.

Prior to staining, cells were fixed in 4% PFA for 15 minutes at room temperature, washed twice with H_20 and incubated with 60% isopropanol for 5 mins. Isopropanol was gently aspirated, and cells allowed to dry before application of the stain. Cells were then finally washed with dH_20.

2.3.2 Immunocytochemistry and Immunofluorescence

Immunocytochemistry was performed for cell lines in a range of experiments as detailed in the results chapter. This included cells on coverslips for monolayers, spheroids, Integra and on 3D bioprinted samples. Each protocol is briefly described. Details of all primary and secondary antibodies used are listed in Table 2.1.

2.3.2.1 Immunofluorescence protocol for ADSCs on cover slips

Cells were expanded on sterile coverslips in 24well plates until only approximately 40% confluent. Culture medium was removed from the wells and cells washed twice with 1X PBS – 200µl each time for 5 mins. The cells were then fixed with 4% PFA for 15 minutes at room temperature followed by 3x10 minutes washes in 1X PBS. The plate was either stored at 4°C in the cold room or stained immediately. Cells were incubated in a permeabilization and blocking solution (3% BSA, 10% FBS, in 1X PBS and 0.2% Triton X-100), for 30 mins at room temperature.

Blocking solution was then removed, and cover slips moved onto parafilm to allow primary antibody to be gently pipetted onto the cells (Fig. 2.3).

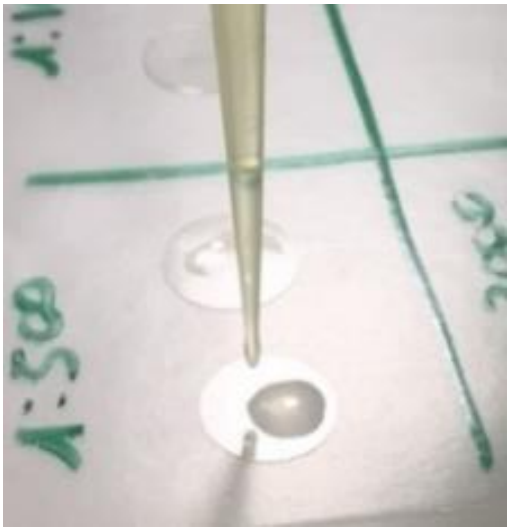

Figure 2.3. Antibody applied to cover slips. This method reduces the volume of antibody required. Total volume required for each cover slip was 50µl.

The primary antibody (mixed with diluted blocking/permeabilizing solution) was left for 2 hrs at room temperature or overnight at 4°C. Coverslips were then lifted off the parafilm and back into the 24 well plate where they were washed with PBS-T (1X PBS + 0.1% Tween 20) 3X for 10 mins. Finally, coverslips were returned onto the parafilm gently and incubated with fluorescent dye-conjugated secondary antibodies (including Hoechst nuclear counterstain) in blocking/permeabilizing solution for an hour at room temperature, moved back into the 24 well plate and washed again in PBS-T. The coverslips were then moved onto slides and mounted using Hydromount (National diagnostics, USA).

2.3.2.2 Immunofluorescence protocol for cells seeded in Integra

The standard protocol for Integra collagen sheet immunofluorescent staining was performed after 4% PFA fixation for 1 hour at room temperature on a shaker followed then by 3 washes with 1x PBS (3 x10mins washes of 200µl PBS). This was followed by overnight incubation with permeabilization/blocking (3% BSA, 10% FBS, and 1% Triton X-100 in PBS) at room temperature, on a shaker. Integra sheets were then incubated with primary antibodies for at least 24hrs at 4°C on a shaker and then extensively washed with PBS-T (0.5% Tween-20 in 1X PBS, 3 x 30 mins washes). Incubation with secondary fluorescent dye-conjugated antibodies and nuclei Hoechst counterstain (Hoechst 33258 Invitrogen, H1398) was undertaken with the samples covered with foil and left at 4°C on a shaker for at least 24hrs. Samples were then washed in PBS-T (3x30 mins) and stored at 4°C until imaging. Incubation times for each Integra experiment are specified for each sample within the Integra results chapter.

2.3.2.3 Immunofluorescence protocol for spheroids

The primary and secondary antibody incubation protocols were modified to enable optimal antibody penetration and is described in Table 2.2. Given the density of spheroids and previous unsatisfactory attempts at imaging with confocal microscopy, a tissue clearing protocol with BABB (1part benzyl alcohol to 2 parts benzyl benzoate) was found to be effective but required extended antibody incubation and increased concentration of Triton.

Antibody	Species	Types	Dilution	Source
Primary				
Human Collagen 2	Rabbit, polyclonal	IgG	1:200	Abcam, ab34712
Alpha tubulin	Sheep polyclonal	IgG	1:500	Cytoskeleton, ATN02
Human Vimentin	Mouse, monoclonal	IgG	1:500	Dako, M0725
Secondary				
Anti-sheep Alex Fluor®488	Donkey	IgG	1:400	Invitrogen A11015
Anti-mouse Alex Fluor®488	Donkey	IgG	1:400	Invitrogen A21202
Anti-mouse Alex Fluor®546	Goat	IgG	1:400	Invitrogen A11003
Anti rabbit Alexa Fluor® 633	Goat	IgG	1:400	Invitrogen A21070

Table 2.1 List of primary and secondary antibodies used for immunocytochemistry.

2.3.3 Tissue Clearing protocols

Different tissue clearing solutions were used for 3D spheroid tissue clearing. A detailed summary of the clearing protocols and whole mount immunostaining of spheroids is presented in Table 2.2. In experiment 1, three different protocols for tissue clearing were undertaken on undifferentiated spheroids. Following from this, all 3D spheroid tissue clearing was with BABB (1part benzyl alcohol to 2 parts benzyl benzoate), with increasing primary and secondary antibody incubation lengths and an increase of Triton from 0.2% to 2% as part of complete staining protocol optimisation.

2.3.3.1 BABB

BABB clearing of spheroids was undertaken in glass vials and dishes as the solution is corrosive to plastic material. The protocol involves an initial series of ascending 5-minute dehydration methanol solutions (25%, 50%, 75% and 100%) before clearing. Briefly, spheroids were placed in Eppendorf tubes and exposed to 5 mins of sequential methanol incubations (with rotation) at room temperature. The final incubation of 100% methanol was repeated 3 times. Finally a BABB:methanol 50:50 solution was added in sufficient volume to cover the spheroids and after 5 minutes replaced by 100% BABB. The spheroid was cleared with the final 100% BABB at the time of imaging as clearing was achieved within a minute and the spheroids become almost impossible to detect within the solution. Spheroid BABB clearing is described in detail in chapter 3 and the method developed to avoid microscope objective damage.

Cells	Spheroid size	Differentiation	Triton% & incubation	Ab incubation time	Clearing
Experiment 1					
ADSC H33	$1.0x10^5$	Undifferentiated	0.2% 90mins	Hoechst overnight	ScaleA2
ADSC H33	$1.0x10^5$	Undifferentiated	0.2% 90mins	Hoechst overnight	$Clear^{T2}$
ADSC H33	$1.0x10^5$	Undifferentiated	0.2% 90mins	Hoechst overnight	BABB
Experiment 2					
ADSC H33	$1.0x10^5$	Undifferentiated	2% 120 mins	Hoechst 24hrs	BABB
ADSC H33	$1.0x10^5$	Undifferentiated	2% 120 mins	Hoechst 48hrs	BABB
Experiment 3					
ADSC H33	$1.0x10^5$	Differentiated	2% 120 mins	*Primary:* 48hrs Vimentin 1:500 Collagen II 1:200 *Secondary:* 48hrs Hoechst 1:800 A546 A633	BABB
ADSC H33	$1.0x10^5$	Differentiated	2% 120 mins	Identical to above but 96hrs primary and secondary	BABB
Experiment 4					
ADSC H33	$3.0x10^5$	Undifferentiated	2% 120 mins	*Primary:* 96hrs Vimentin 1:500 Collagen II 1:200 Alpha tubulin 1:500 *Secondary:* 96hrs Hoechst 1:800 A546 A633 A488	BABB
ADSC H33	$3.0x10^5$	Differentiated	2% 120 mins	Identical to above	BABB
ADSC H33 (-ve cntrl)	$3.0x10^5$	Differentiated	2% 120 mins	*Primary:* Nil *Secondary:* 96hrs As above	BABB
Experiment 5					
ADSC H37 $eGFP^+$	$1.0x10^5$	Differentiated	2% 120 mins	*Primary:* 96hrs Vimentin 1:500 Collagen II 1:200 *Secondary:* 96hrs Hoechst 1:800 A546 A633	BABB
CSPC CH32 mCherry+	$1.0x10^5$	Differentiated	2% 120 mins	*Primary:* 96hrs Vimentin 1:500 Collagen II 1:200 *Secondary:* 96hrs Hoechst 1:800 A546 A633	BABB

Table 2.2. Summary of antibody immunostaining and clearing for whole mount spheroids. All spheroids were cultured for 6 weeks and then fixed with 4% PFA. Ab:Antibody, -ve cntrl: Negative control.

2.3.3.2 ClearT^2

Briefly, this protocol involved the use of sequential incubations of formamide (Merck Sigma-Aldrich) and Polyethylene glycol (PEG wt 8000 powder- Merck) as described by Kuwajima et al in 2013 (Kuwajima et al., 2013). Spheroids were incubated for an hour on a shaker at room temperature each time at solutions of 25% formamide/10% PEG and then 50% formamide/20% PEG. A final incubation of 50% formamide/20% PEG for 12 hours.

2.3.3.3 SCALEA2

This protocol was adapted from Hama et al publication on optical clearing (Hama et al., 2011). Sca*l*eA2 solutions were made using 4M urea, 0.1% (wt/vol) Triton X-100, 10% (wt/wt glycerol) to make a final volume of 1000ml solution stored at room temperature. This was achieved by dissolving urea crystals 800ml of Milli-Q water by stirring, adding 10ml of 10% (wt/vol) Triton X-100 solution, 100g of glycerol and finally adding further Milli-Q water to make up a total volume of 1000ml. Spheroids were incubated in ScaleA2 for 12 hours at room temperature on shaker then new solution added and further incubation for 7 days.

2.3.4 Microscopy

Tissue histology samples were imaged using Zeiss Axioplan 2IE microscope (Carl Zeiss, Germany in combination with Axiovision software (Carl Zeiss).

Large tissue samples (eg CAM grafts) were imaged using a Leica MZ FL III stereomicroscope (Leica).

Monolayer culture imaging of live and fixed cells with and without fluorescence were acquired on an Olympus Inverted IX71 (Carl Zeiss) microscope and HCImage software (Hamamatsu Corp).

2.3.4.1 3D imaging

Spheroids, bioprints and Integra samples were imaged using a Zeiss LSM 880 upright confocal (Carl Zeiss) microscope using two-photon excitation (unless stated otherwise) with ZEN software. Integra sheets were placed in petri dishes and immersed in PBS and were imaged using a 20x/NA1.0 Plan Apochromat Water dipping objective with correction collar (WD 2.4mm) or a 10x/NA0.5 W-Plan Apochromat Water dipping objective (WD 3.7mm). The technical details of spheroid imaging are described in chapter 3 (section 3.2.3.4).

3D video rendering and Z-stack reformatting were performed using Imaris cell imaging software (Oxford Instruments).

2.4 Integra Dermal Regeneration template

Both Integra single layer and double layer sheets were used for cell seeding experiments (Integra® Dermal Regeneration Template two-layer code 34101, and Integra® Dermal Regeneration Template single layer code 64101). Both were supplied in a sterile pocket with plastic reinforcement that is peeled away. For each experiment, Integra was cut using either sterile hole punches of the required diameter or sterile scissors (Fig. 2.4).

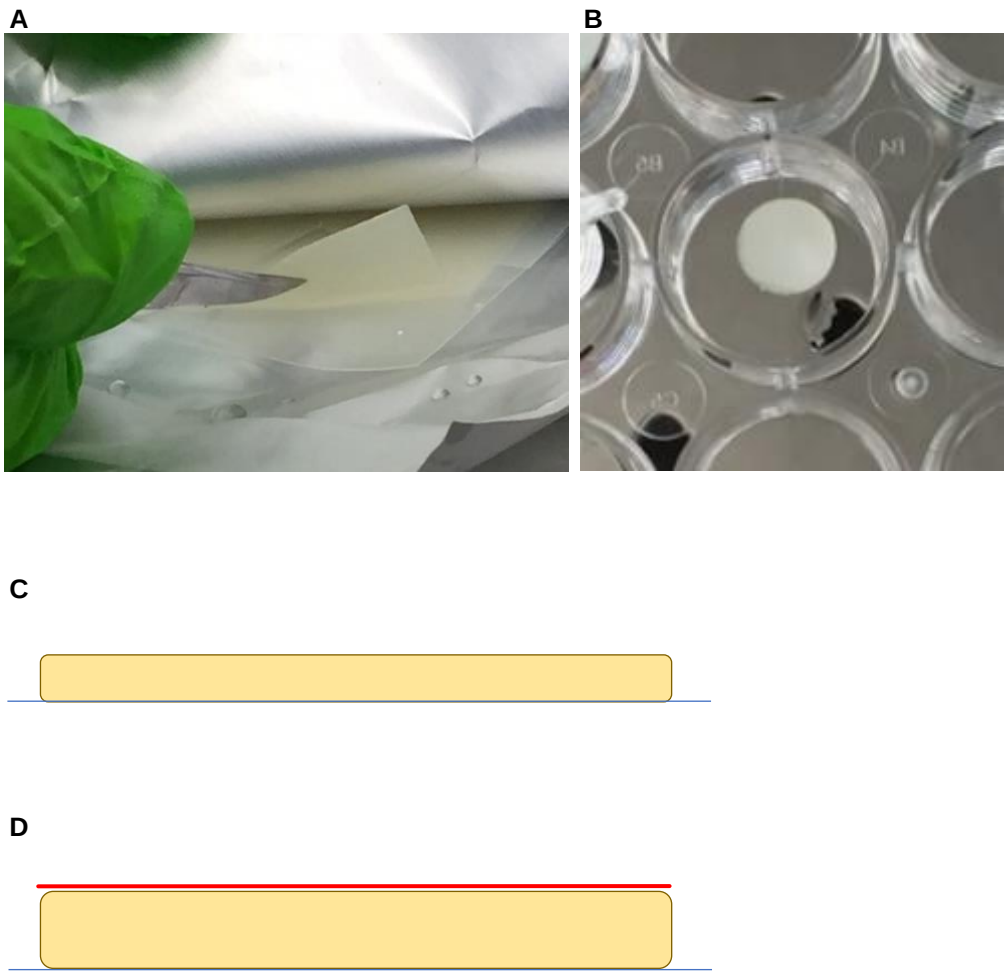

Figure 2.4. Integra Dermal Regeneration template (IDRT). (A) Integra is supplied as thin sheets, the single layer being approximately 800µm thick and is by a thick plastic sheet which is removed. **(B)** Integra samples were cut into desired shapes and sizes using sterile scissors or 8mm diameter surgical hole punch biopsy instrument. This was done under aseptic technique in a tissue culture hood. **(C, D)** Single layer and bilayer Integra. The bilayer Integra is supplied with a silicone sheet (red layer in D) attached to the Integra and is intended to be removed after 3 weeks. The bilayer Integra is up to 2mm thick.

2.4.1 Integra cell seeding

Cells were seeded onto Integra in a culture hood using aseptic techniques.

2.4.1.1 Integra single layer sheet

Cells were suspended in expansion medium at a concentration of $1x10^6$ cells/100µl and directly seeded onto Integra slowly using a pipette to allow gentle diffusion of the mix into the Integra. Cells were seeded at density of $1x10^6$cells/$1cm^2$ Integra unless stated otherwise. Study samples were either cut using sterile scissors or 8mm tissue punch instruments. Samples were left in an incubator for 2 hrs to allow cell attachment before further expansion medium was added to completely cover the samples.

2.4.1.2 Integra bilayer sheet

The silicone layer that is attached the sheet was left in situ throughout experiments using this Integra type. Disposable single use 8mm tissue punch instruments were used to cut 8mm discs from the bilayer Integra sheet. Cells were seeded by pipette from the top and allowed to diffuse into the Integra for 2 hrs prior to further expansion medium being added.

2.4.1.3 High cell density seeding protocol

An 8mm disc was cut from single layer Integra sheet using a tissue punch and placed into a transwell cell culture insert (Corning®, pore size 8µm) and was seeded with $6x10^6$ cells (CSPCs Ch90 mCherry+ labelled) suspended in 100µl of expansion media using a pipette. This was transferred into a 15ml conical centrifuge tube (Falcon™ Fisher scientific) so that it rested at the bottom and was centrifuged for 30 seconds at 500rpm. The transwell was removed after 30 minutes and placed in a 24 well plate with expansion media. The pellet at the bottom of the centrifuge tube was resuspended in expansion media and cells counted using an automated cell counter (TC20 ™Bio-Rad). Media was changed every 2-3 days and at day 7 was changed to chondrogenic differentiation media for a further 22 weeks (Fig 2.5).

A

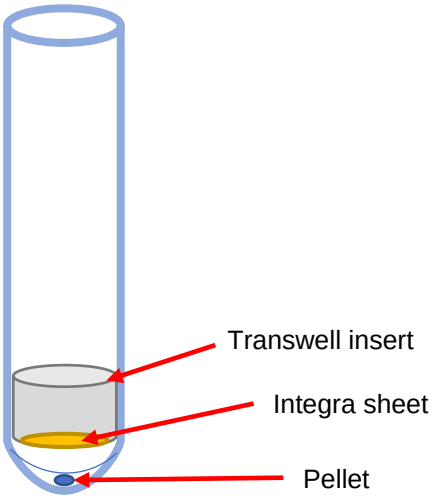

B

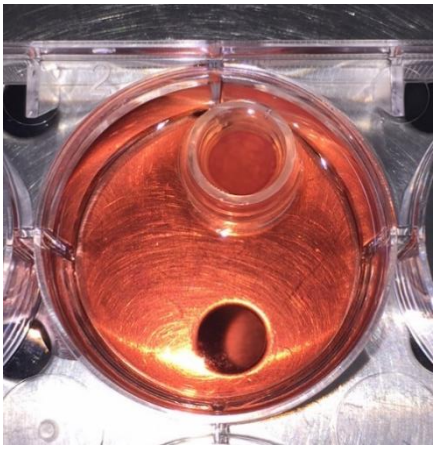

Fig 2.5 Integra seeded with 6x10^6 Ch90 mCherry cells. **(A)** The transwell was placed into a 15ml centrifuge tube and centrifuged for 30 seconds. **(B)** Transwell with cell seeded Integra in static chondrogenic culture medium.

2.5 Chick Chorioallaotic Membrane Assay

Chick Chorioallaotic Membrane (CAM) assay was used for in-vivo experiments for 3D bioprinted constructs, Integra sheets and fibrin constructs.

2.5.1 CAM Preparation

2.5.1.1 Licence and storage of eggs

CAM procedures were performed in accordance the guidelines and regulations of the Animals Act 1986 under Home Office approval. Fertilised Bovans brown eggs were supplied by Henry Stewart & Co (Norfolk, Uk). Eggs were initially stored at a temperature of 12-18°C (no longer than 10 days) prior to incubation at 37.5°C.

2.5.1.2 CAM windowing

At day 1, eggs were wiped clean with 70% ethanol and labelled with the date and sample number and then placed in a disinfected incubator (temp 37.5°C, >60% humidity). At 72hrs the eggs were taken out, wiped clean with 70% ethanol and 2-3ml of albumin was aspirated through a small hole made using a sharp 16G needle and syringe pointing down into the base of the egg. This created an air pocket which allowed a 2x2cm square window of shell to be cut and removed using a size 11 scalpel in a controlled manner (Fig 2.6). Both the window and albumin aspiration sites were then sealed with clear adhesive tape and returned to the incubator.

Eggs were inspected for growth and viability every day. At day 7 incubation, study samples were inserted onto the CAM and surrounding small vessels were agitated (to initiate gentle minor bleeding) using a sterile 21G needle. New adhesive tape was applied to the window and the eggs incubated for a further 7 days until embryonic day 14. At day 14, eggs were imaged using a Leica Zoom tissue microscope MZFLIII, then samples harvested but excising a small cuff of the CAM around the sample graft. Chicks were terminated at this point.

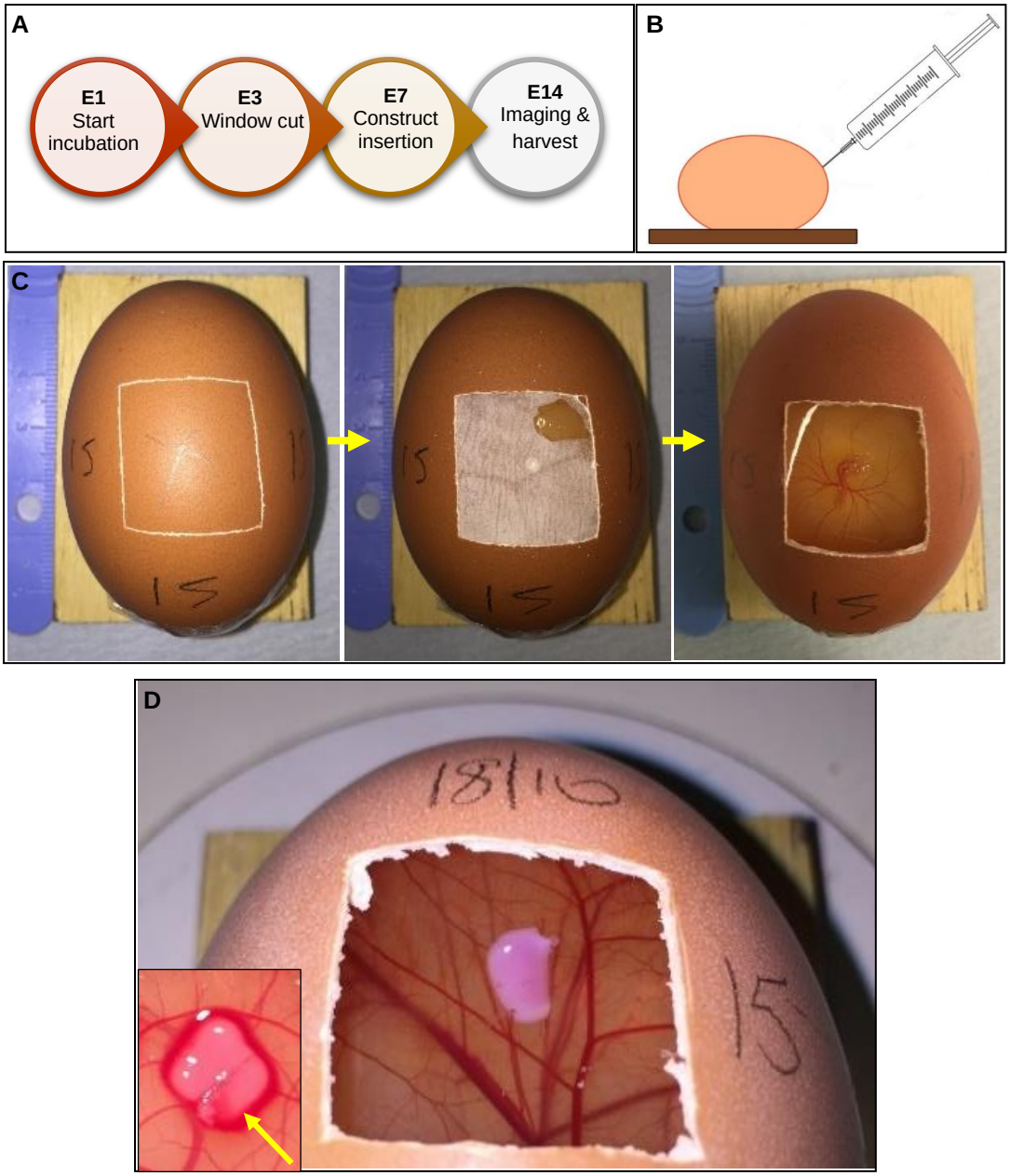

Figure 2.6. CAM experiment. (A) Main time points for experiment. Day 1 of incubation represents the start of embryonic day 1 through to the end of the experiment at E14 when the grafts are imaged and harvested. **(B)** Albumin aspiration. 2-3ml of Albumin is aspirated gently from each egg using a syringe pointed downwards to create an air pocket superiorly within the eggshell. **(C)** Egg windows**.** Gentle scoring of the eggshell using a number 11 scalpel blade is performed until the outer hard shell can be easily removed. The underlying membrane is then peeled away to reveal the CAM. **(D)** Construct applied to CAM. Constructs were applied to the CAM using sterile forceps. Local bleeding was encouraged by stroking surrounding small vessels with a sterile 21G needle (yellow arrow).

2.6 Three dimensional Bioprinting

A pneumatic-based micro-extrusion 3D bioprinter with dual print heads (CELLINK INKREDIBLE +, CELLINK Life Sciences) was used to print cells. The bioprinter extrudes cell laden bioink in a layer by layer fashion to generate a 3D print.

2.6.1 Printing preparation

All surfaces within the bioprinter were disinfected with 70% ethanol and the in-built fan set to maximum speed to create positive air pressure to reduce the risk of sample contamination. The print set up involves calibration of the print heads and the print platform in the y, x, and z axes. A sterile petri dish is placed and secured onto the print platform.

2.6.1.1 Cell preparation

The large number of cells needed for 3D bioprinting required upscaling of standard cell culture protocols. Cell expansion was upscaled using a 5-layer cell culture multi-flask (Corning™ 353144), with cells seeded at a density of $5x10^5$ per layer in 25ml of DMEM media supplemented with 5% human platelet lysate (HPL STEMCELL technologies 06962). For a print density of $1x10^6$/100ul bioink, 10million cells were required for ten prints. This was easily obtained from the 5-layer multi-flask after approximately 10 days of cell culture. Cells were then passaged with 0.05% trypsin solution, counted (TC20 automated counter-Bio-rad) and resuspended in 200ul of DMEM media and transferred to a 1ml syringe using a pipette under sterile conditions.

2.6.1.2 Bioink preparation

Bioink was purchased from CELLINK, alginate/cellulose bioink (CELLINK BIOINK S-20014-001) and Sodium alginate RGD (CELLINK A-RGD S-20012-001)**.** Under sterile conditions in a culture hood, 1ml of the required bioink was aspirated into a 2.5ml luer locking syringe using a luer lock connector. This volume of bioink was sufficient to print 10 constructs at a dimension of 10x10x1mm cubes.

2.6.1.3 Cell/bioink mixing technique

Once the bioink and cells were prepared and ready in individual syringes, the mixing protocol developed during this thesis can begin. The mixing device that was supplied with the bioprinter was found to waste significant volume of cells and bioink and therefore all 3D bioprinting was undertaken using my mixing protocol that eliminates this problem. Using a luer lock connector, both syringes (one with cells, the other with the bioink) are attached tightly at which point the cells are injected into the bioink.

It was important at this stage to avoid injecting air bubbles into the bioink and this was achieved by only injecting the cell mixture. The syringe containing the cells was then carefully removed and a new 1ml luer locking syringe attached (TERUMO 1ml, Japan). The cells were gently mixed with the bioink by numerous passes from one syringe to the next until the mix appeared homogenous. Approximately 12-15 transfers from one syringe to the next was required to achieve this. The cell/bioink mix was then transferred to the print cartridge (supplied with the bioprinter) in a similar manner using the luer lock connector to obtain the final ready-to-print mix. This mixing protocol was used for both types of ink, Bioink and RGD in an identical manner. The final cell/bioink cartridge syringe was kept cool in ice and all printing was undertaken within an hour of preparation. A 410µm wide nozzle was attached to the cartridge and together loaded into the printer and attached to the extrusion pressure tubing (Fig 2.7).

2.6.1.4 Cell printing protocol

Print designs for cell printing were either 5x5x1mm or 10x10x1 mm 3D cuboids and were generated using Blender (open source www.blender.org) and saved as stl. files. The design file was then uploaded into Slic3r (open source www.slic3r.org) 3D bioprinting software to allow manipulation of printing parameters. Print parameters for cell bioprinting were set at construct 1mm layer thickness, with 100% infill density with a rectilinear infill pattern. Print speed setting were set as 50 mm/s. The final design was transferred onto a SD card as a G-code file format and inserted directly into the printer.

The cell laden bioink cartridge was mounted onto the print head and a 410µm width nozzle attached. Print pressure set to 15-30kPa which was controlled directly at from the printer. Constructs were bioprinted onto sterile petri-dishes.

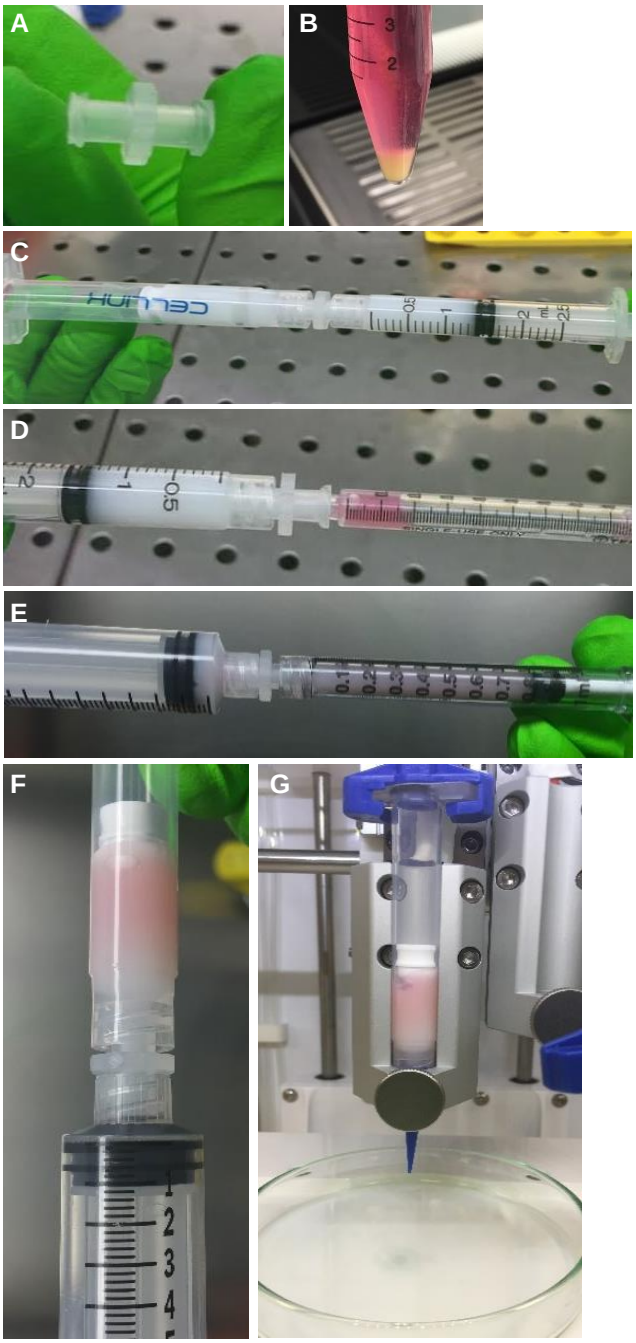

Figure 2.7. Cell/Bioink mixing protocol. (A) A sterile female-female Luer locking connector is required to enable mixing of bioink with cells to eliminate risk of accidental extrusion and loss of either the bioink or cells. **(B)** Cells are spun down and resuspended in 200µl of control media per 1ml of bioink. Using a Gilson 1000µl pipet, cells are gently placed into a Luer locking 1ml syringe by removing the plunger and pipetting directly into the syringe chamber. Care should be taken here to not lose the cells through the syringe tip. **(C)** Required volume of bioink is withdrawn from the stock bioink syringe using a 2.5ml syringe coupled to the Luer connector. **(D)** The 2.5ml syringe is connected to the 1ml syringe containing the cells. **(E)** Cells and bioink are mixed by gently transferring the contents of both syringes from one to the other until the mix appears homogenous. **(F)** Cell laden bioink is transferred to the printer cartridge. **(G)** The cartridge is mounted onto the print head and a 410µm width nozzle attached. Print pressure set to 15-30kPa.

2.6.1.4 Bioink cross linking

After each print, samples were immediately cross-linked with sterile calcium chloride solution. Briefly, the protocol for this was immediate direct application of 300µl of 100mM $CaCl_2$ per print ensuring the entire construct was immersed in solution, followed by incubation for either 10 minutes or 60 minutes at 37° C in a 5% CO_2 incubator. The crosslinking solution was then aspirated from the printed constructs and washed with DMEM (ThermoFisher Scientific 11965092) control medium once before finally incubating in fresh expansion medium. Medium was changed every 2-3 days and switched to chondrogenic medium where required.

2.6.1.5 Bioprint cell viability

Cell viability and mortality following bioprinting were assessed by using a Live/Dead™ assay (Invitrogen, Bioscience, United State). This Live/Dead™ viability assay discriminates live from dead cells by staining with green fluorescent calcein-Am to indicate intracellular esterase activity and red -fluorescent ethidium homodimer-1 to indicate loss of plasma membrane integrity. Both intracellular esterase activity and intact cell plasma membrane are important features of live cells. Bioprinted constructs were washed in serum-free DMEM medium and then 200µl of assay solution was added to samples, followed by incubation in a 37°C and 5% CO_2 incubator for 1 hour. Bioprinted constructs were then washed again in serum-free medium for a further 1 hour. Images were taken by using inverted fluorescent microscopy (IX,73, Olympus) with FITC and Texas Red filters, digital colour camera (XC10) and Fiji imaging software (Fiji 2). For each sample, three randomly selected regions were imaged at 10X magnification and the cell viability/death counted. Counting was performed using the particle analyses of ImageJ (1.44p, National Institutes of Health, Bethesda, Maryland, USA) and analysed using GraphPad Prism 8 software (GraphPad software, San Diego, CA, USA).

2.7 Three-dimensional printing of Polycaprolactone

Printing PCL shared many of the protocols already described for printing bioink. Construct shape was designed using Blender software in a similar way to the 3D bioprinted constructs. Constructs were designed and saved as stl. files and then converted into G-code using Slic3r open source 3D printing software.

2.7.1 Printer setup

In contrast to 3D bioprinting ink, printing PCL required high pressures and control of the nozzle and syringe temperature. To determine optimal printing conditions, the print speed, extrusion pressure, infill design and percentage infill for a basic rectangular shape were all manipulated using Slic3r software. PCL was printed on a 3D printer (CELLINK Inkredible+) using high molecular weight (Mn 50,000) beads (CELLINK TP605050001 50g) inserted into an aluminium 3ml cartridge (CELLINK CSA000011012).

PCL beads were placed into the cartridge and inserted into the printer chamber which has a built-in heated element. A 500µm or 600µm metal nozzle tip (CELLINK 000000020884) was attached to the aluminium cartridge and an external compressor pump connected to the printer provided pressure to drive the extrusion. Prior to initiating a print, the PCL was given 15 minutes to melt at 120°C and the pump pressure allowed to reach 600kPa. Printing was undertaken on either a glass surface (back of petri-dish) or onto plastic mounted onto the printer platform. Kapton tape (temperature heat resistant polyimide) was used to allow the PCL to adhere to either the glass or plastic surface (Fig 2.8). At the end of a print, samples were immediately placed in a 4°C fridge to allow rapid cooling and setting.

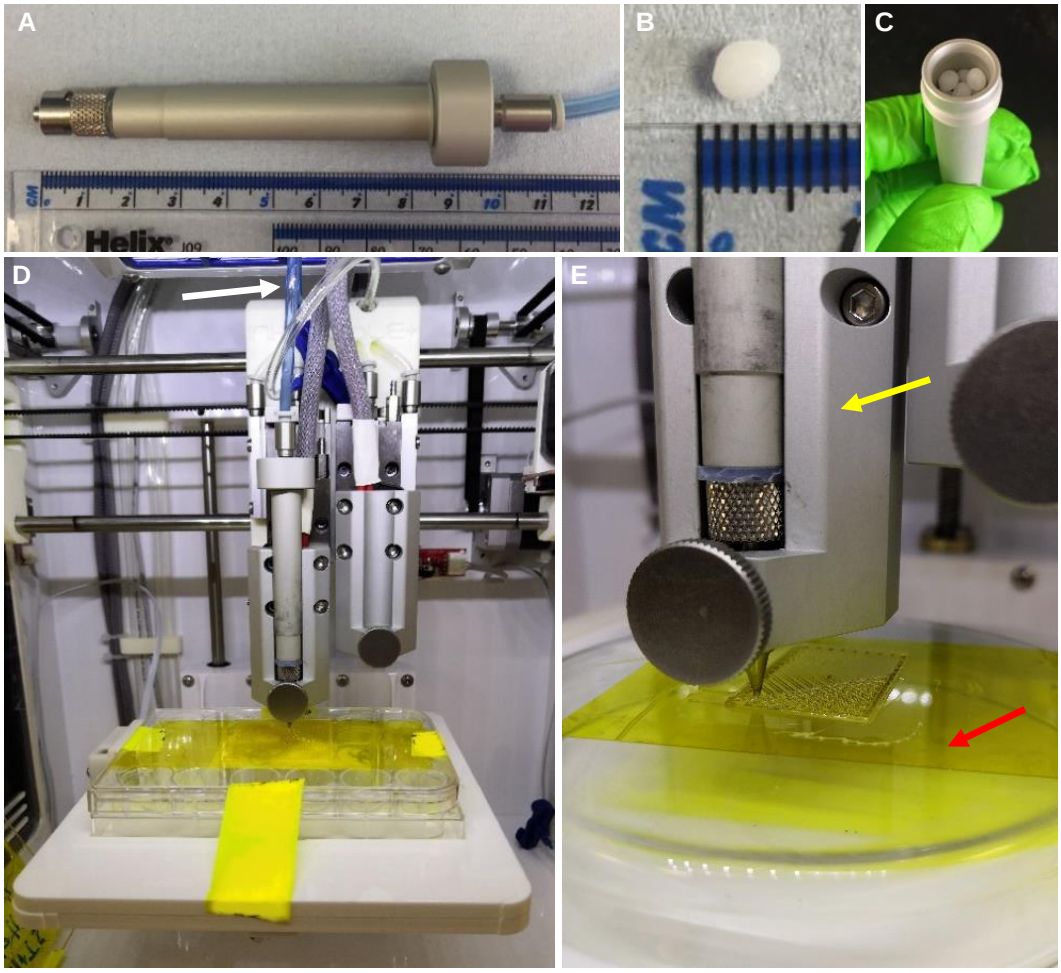

Figure 2.8. 3D printing of PCL. (A) Aluminium cartridge with pressure tubing attached. **(B)** PCL beads are packed into the syringe from the top end **(C). (D)** The cartridge is mounted into the printer and connected to the pump tube (white arrow). The print surface (the lid of a 24 well culture plate in this example) is firmly attached to the platform with adhesive tape. **(E)** Kapton tape (red arrow) is applied to the print surface to allow PCL to adhere during the printing process. The cartridge is heated to 120°C via the heating mechanism surrounding it (yellow arrow).

2.8 Fibrin experiments

2.8.1 Fibrinogen/thrombin experiment protocols

Fibrin was used as a hydrogel for 3D cell culture in 2 sets of experiments. Preliminary studies used cell line H103 (ADSCs) then later CH105 (CSPCs) for the PCL/Fibrin sandwich constructs. All samples were generated in triplicates.

2.8.1.1 Fibrin preparation for preliminary studies

Tisseel Lyo (two component fibrin sealant, Baxter, USA) consisting of 360-550mg of human fibrinogen and human thrombin 2500 I.U key components, were prepared to the following concentrations:

1500µl fibrinogen (500µl + 1000µl PBS)

1500µl Thrombin (1500 µl PBS+ 3µl thrombin)

These concentrations provided optimal handling and mixing consistencies that allowed easy manipulation of the product to allow enough time to mix cells (Fig 2.9).

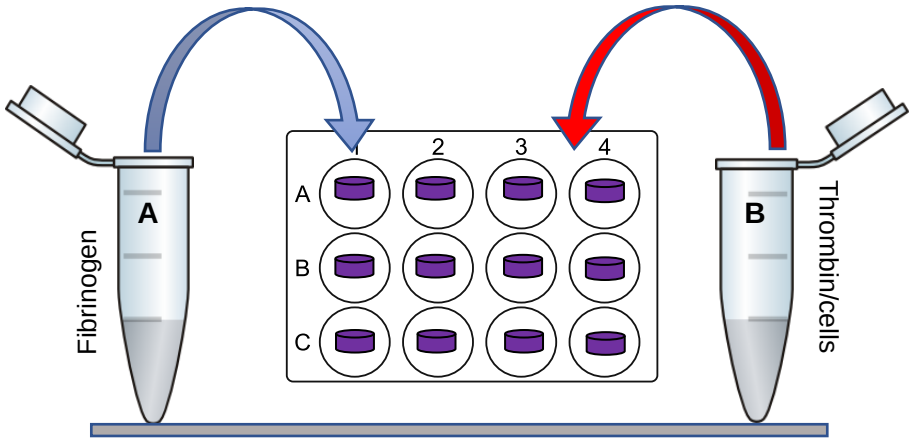

Fig 2.9. Fibrin constructs. (A) Fibrinogen at a volume 25µl was pipetted into a tissue culture plate. **(B)** A 25µl mix of thrombin and cells at a concentration of $20x10^6$ cells/ml thrombin was then mixed into each well of fibrinogen to create constructs of total volume 50µl each having $5x10^5$ cells. Wells were then flooded with growth medium after 2 minutes.

2.8.1.2 PCL and fibrin sandwich construct

PCL sandwiches were fabricated using printed PCL mesh with a cell laden fibrin centre. The sandwiches were generated by layering fibrin onto a PCL disc using a pipette then covering this layer with another layer of PCL. Petri dishes (10mm) were coated with 2% agarose in DMEM, allowed to cool and then 8mm holes punched out using an 8mm tissue punch biopsy instrument. The PCL discs were cut using an 8mm tissue punch, disinfected with 70% ethanol for 30 minutes, dried and placed into the bottom of each well in the agarose. To make constructs at a cell density of $10x1^6$ per ml, expanded CH105 P4 CSPCs ($36x10^6$ cells) were trypsinised, spun and resuspended in 1800µl of dilute thrombin (3.6µl of thrombin in 1800µl sterile PBS). A total volume of 1800µl dilute fibrinogen (600µl fibrinogen in 1200µl PBS) was warmed and placed into 36 individual wells of a 96 v-bottom well plate (50µl per well).

A volume of 50µl cell/thrombin mix was then added to a sample of fibrinogen from each well (to make total volume 100µl per construct with $1x10^6$ cells), mixed gently then pipetted into the PCL discs at the bottom of the agar plate and then covered with another layer of PCL mesh. This was repeated for every sample. This method was developed to permit controlled cell seeding into the PCL discs without loss of cells into surrounding spaces. The completed sandwiches were incubated for 40 minutes at 37°C. The agarose around each construct was pulled away to allow the constructs to be transferred into wells of a 12 well plate coated with 3-4% Agarose (low melting point agarose Gibco) in DMEM (Fig 2.10). Coated wells were used to limit cell migration out of the sandwiches. Sandwich constructs were cultured in two groups, a control group in expansion medium and a chondrogenic group, medium was changed every 2 days for both. A parallel fibrin experiment was prepared with fibrin only (not within a PCL sandwich) as a control and again was cultured in expansion and chondrogenic medium.

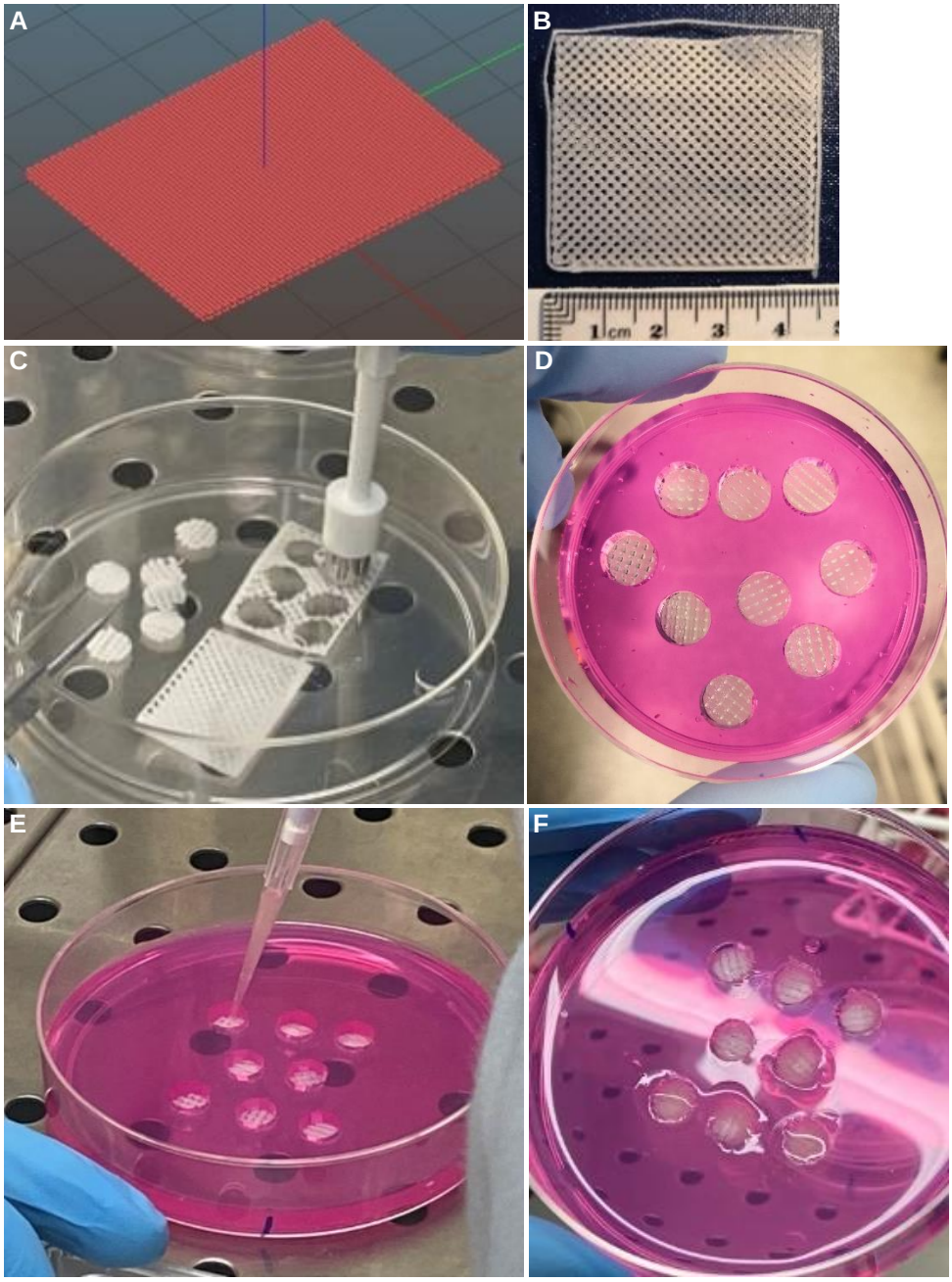

Figure 2.10. PCL/Fibrin Sandwich construct fabrication. (A) PCL sheet 2-layer rectangle, 90% rectilinear infill design. **(B)** PCL printed using 600kPa pressure, 130°C print head temperature and 500µm nozzle. **(C)** Tissue punch size 8mm used to cut discs. **(D)** Discs of similar size were punched out of 2% low melting point agarose poured into 10mm petri dish. PCL discs were gently pushed to into these cavities**. (E)** Fibrin/thrombin/cell mix pipetted gently onto the surface of the PCL discs. **(F)** The second layer of PCL disc was placed on top of the cells to form the completed sandwich construct.

2.8.1.3 Experimental design.

Fibrin sandwich proof of concept experiment was designed to compare cell behaviour in PCL/fibrin sandwich constructs cultured in expansion medium versus chondrogenic medium. Furthermore, replicates were cultured in either static medium or grafted onto chick CAMs. Control fibrin only constructs were also generated with the same number of cells. Constructs cultured in static medium were removed at time points 0, day 7 and day 21 for RNA extraction and histological analysis. Constructs that were used in CAM grafting were cultured and pre-differentiated in an incubator with static medium for 14 days first. A summary of the experiment is shown in Fig 2.11.

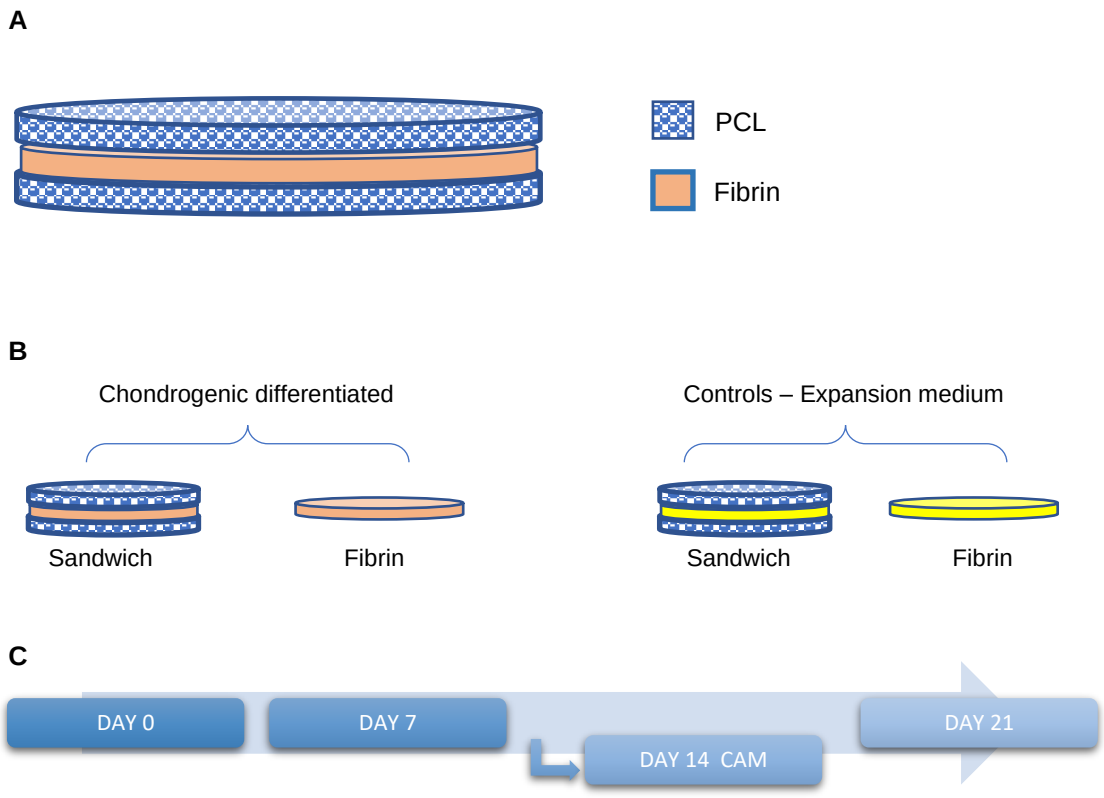

Figure 2.11 PCL fibrin sandwich and controls. (A) PCL/Fibrin sandwich design. Cell seeded fibrin hydrogel is sandwiched between 2 thin layers of printed PCL mesh. **(B)** Two different constructs (PCL/fibrin and fibrin only) cultured in two different conditions. Sandwiches were cultured in chondrogenic medium and expansion medium. The same mix of fibrin with the same cells were also used to generate fibrin only constructs that acted as controls. Samples were removed from culture at day 0, day 7, and day 21 (n=3 of each construct) for analysis at each time point. **(C)** At day 14, samples from all constructs (n=3) were grafted into chick CAM and then incubated for a further 14 days.

2.9 PLA pocket 3D printing

2.9.1 Design software

The PLA polymer pocket was designed using Blender software package which is a free and open source 3D creation suite (Dutch public-benefit corporation). Files were saved as STL (STereoLithography) and then either printed directly or processed using Slic3R open source 3D printing software to manipulate printing conditions.

2.9.1.1 PLA printing

Designs were 3D printed using a Makerbot replicator 3D printer (MakerBot Industries, Brooklyn, NY 11201 US) by fused deposition modelling (FDM) in collaboration with Professor Wenhui Song research team at the Royal Free Campus, UCL Centre for Biomaterials in surgical reconstruction and regeneration, London, UK. PLA filament was fed through the printer head and allowed to reach print temperature of 210°C. Blue 3D printer printing bed masking tape was used to allow PLA filament to adhere to the print bed. PLA square shaped constructs for initial Integra experiments were printed as 2-layer thickness 10x10x1mm dimension, 80% infill density.

2.9.1.2 PLA construct disinfection

All PLA prints were rinsed in PBS for 5 mins then immersed in 70% ethanol for 2 hours on a room shaker, rinsed again in PBS (5 washes).

2.10 Mechanical testing of lamb septum

As a proof of concept study to establish a protocol and experimental design to determine tensile elastic moduli of cartilage samples, a three-point bending study was undertaken using fresh frozen lamb nasal septum. Nasal septum was obtained by dissection of soft tissue and perichondrium off the septum. The septum was then cut and released of the maxillary crest (Fig 2.12).

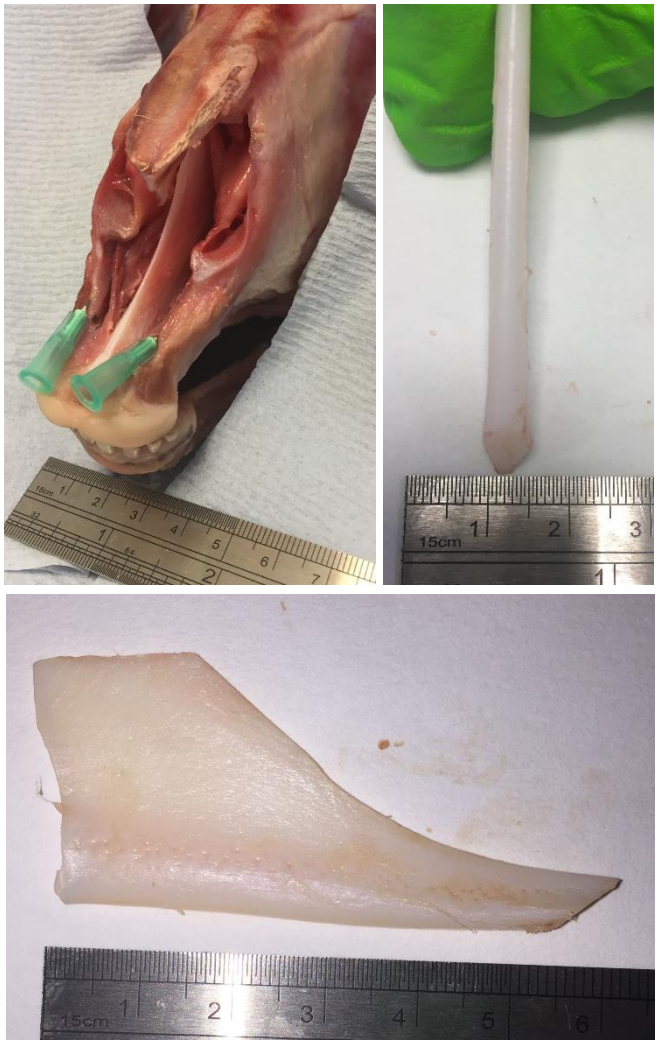

Figure 2.12. **Lamb nasal septum harvesting**. Nasal septum was dissected out following excision of overlying perichondrium.

2.10.1 Mechanical testing – Three-point bending

The lamb septum was cut into strips 15x2mm strips from the posterior superior edge as this region of the septum was the most consistent in thickness (1.5mm). Each strip was measured for thickness using callipers at the two ends and the centre of each strip. The cartilage strips were mounted on a custom-made jig attached to a single-column uniaxial Zwicki-line mechanical testing machine (Zwick/Roell, Germany). Samples were tested using this three-point bending setup, where load (mN) and displacement (mm) were measured and recorded. A load applicator was positioned above the centre of the strip being tested (Fig 2.13). Initial analysis of the data confirmed that the experimental design was suitable for cartilage sample testing and matched closely published results of testing cartilage in other species (Roy et al., 2004). Raw data is presented with initial analysis in Appendix, Fig A1 and Fig A2, as this protocol was not required further in the thesis.

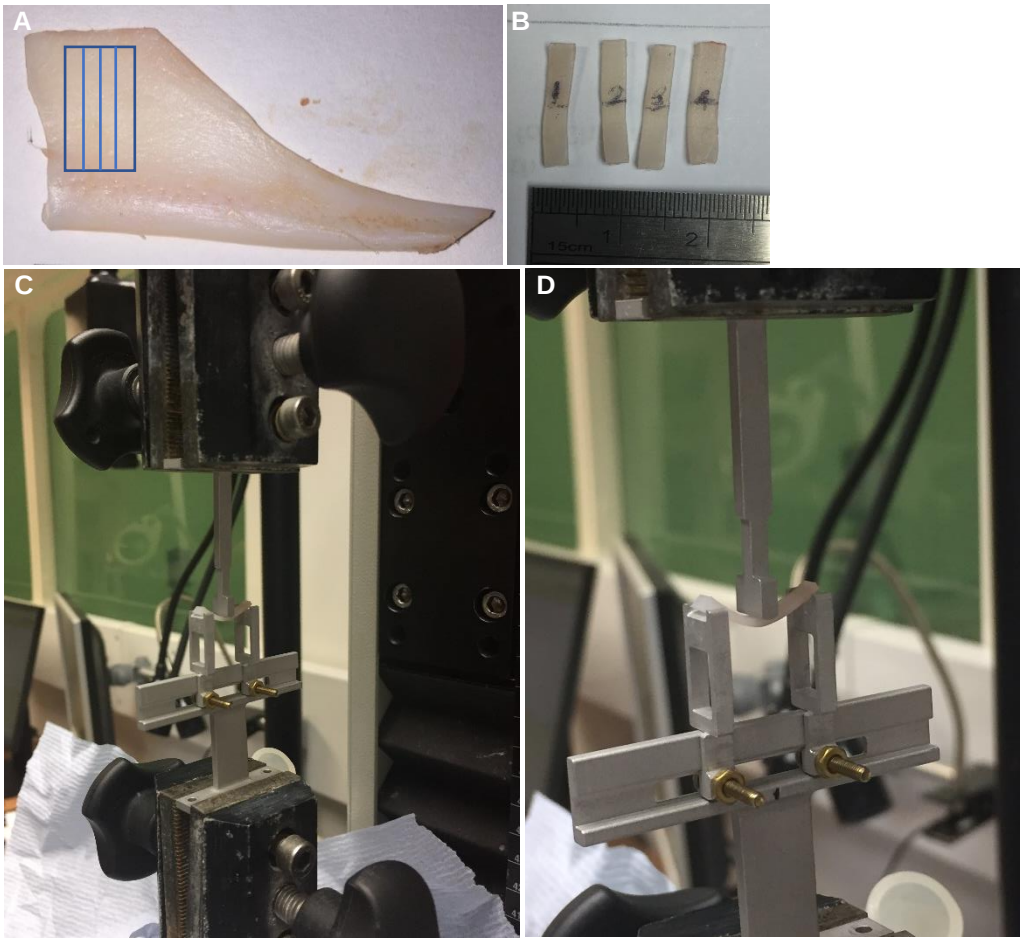

Figure 2.13. Three-point bending test. (A) Four strips were cut using a scalpel from the superior posterior aspect of the septum. **(B)** Each strip was measured for thickness using callipers at three points. **(C)** Custom made jig was attached to the uniaxial testing machine. **(D)** Sample being tested with load applicator positioned carefully in the middle of the strip.

2.11 Statistics

GraphPad Prism 8 software (GraphPad software, San Diego, CA, USA) was used for statistical analyses of data. Each experiment was undertaken in biological triplicates or quadruplicates unless stated otherwise. Differences in groups were analysed using analysis of variance (ANOVA) test. A p value of <0.05 was considered significant.

Chapter 3

RESULTS 1:

3D Spheroid cultures and whole mount analysis

3.0 Background

A step back from in-vivo experimentation, 3D cell culture models provide insight to cell organisation, ECM synthesis, cell death and survival likely to be more representative of natural tissue micro-environments when compared to 2D cell cultures. Learning from these systems to generate cartilage without a synthetic scaffold would be advantageous. With the aim of tissue engineering cartilage for a nasal septal product using stem cells, the ability of adipose derived stem cells (ADSCs) and cartilage stem progenitor cells (CSPCs) to deposit cartilage-like extra cellular matrix (ECM) in 3D in a scaffold free environment was studied. As the first step towards achieving the overall aims of the thesis, the behaviour of these two cell types in 3D without the potential restrictive influence of a scaffold or hydrogel was important to establish.

Pioneering studies of chondrocytes demonstrated their phenotype change from flattened to spherical when they are cultured in anchorage independent 3D systems compared to monolayer systems. This change in cell shape is also associated with increased collagen and proteoglycan synthesis as chondrocytes re-express their differentiated phenotype which can be lost during serial monolayer cultures (Benya and Shaffer, 1982). In the last 40 years, numerous studies have consistently demonstrated the dedifferentiation of chondrocytes when cultured on monolayers and the down regulation of the expression of type II collagen cartilage genes (Bonaventure et al., 1994; Stokes et al., 2001; von der Mark and Conrad, 1979). Since the natural micro-environment of cells is to be surrounded by other cells and ECM, 2D cell cultures will not predict accurately the in-vivo cellular behaviour. Three-dimensional tissue culture systems will therefore provide clues into cell interactions and development that more closely mimics in-vivo tissue. This had led to increased interest and development of 3D scaffold free culture systems for cartilage tissue engineering as they permit cell-cell interactions similar to those observed in embryonic development and produce their own ECM over time (Ahmad et al., 2020; Irie et al., 2008; Ong et al., 2018b; Zhang et al., 2010). There are numerous methods to prepare 3D spheroid cultures which include pellets (cell aggregation), spinner culture, hanging drop, rotating wall vessels and micromolded hydrogels. The most commonly used is the cell aggregation method (Edmondson et al., 2014; Lin et al., 2017; Olsen, 2014).

Such spheroid cultures can be prepared from numerous cell sources and can be generated from either single or multiple cell types (Olsen, 2014). Both ADSC and auricular cartilage-derived progenitor cells have been shown to easily expand and differentiate into the chondrogenic lineage in 2D and 3D cultures (Bernstein et al., 2018; Guasti et al., 2014; Zucchelli, 2018).

Both cell sources are easy to obtain with minimally invasive procedures. Cohen et al. 2018, demonstrated that suitable amounts of human auricular cartilage can be obtained from simple otoplasty procedures that can be used to isolate and expand chondrocytes at numbers averaging 8.3±2.3million/g of tissue (Cohen et al., 2018; Zucchelli, 2018).

A problem with the process of analysing 3D spheroids, however, is that they can be fragile, and their small dimensions makes them difficult to prepare for traditional histological methods. Zucchelli, 2018, demonstrated that chondrogenically differentiated ADSC and CSPCs cultured as 3D spheroids were difficult to section (undifferentiated spheroids in particular) and time consuming using traditional histological techniques given their small size and that such methods may result in processing artifacts caused by distortion of the spheroid tissue. Whole mount imaging that permits detailed analyses of the morphology of spheroids without having to section them would address these problems.

In this chapter my aim was to analyze the 3-dimensional organization and assess the expression of cartilage markers in both control (undifferentiated) and chondrogenic (differentiation) spheroids in whole mount preparations instead of standard histological sectioning techniques.

Specific objectives for this chapter included:

1. Identify the most effective tissue clearing method for chondrogenic spheroids that permits full depth imaging.
2. Optimize staining protocols for whole-mount immunofluorescent imaging of chondrogenically differentiation and undifferentiated spheroids.
3. To assess the expression of cartilage markers in sections of undifferentiated and differentiated spheroid cultures.
4. Develop a clearing protocol for BABB to allow its safe use in a 2-photon microscope.

3.1 Results

Cell lines used in this chapter are listed in table 3.0

ADSC	Microtic ear cartilage derived precursor cells
H33	**CH32**
H37	

Table 3.0. Cell lines used to generate spheroids in this chapter.

3.1.1 Spheroid cultures from ADSC and cartilage stem precursor cells (CSPCs).

Spheroids were generated from both ADSC and microtia ear cartilage derived precursor cells. Spheroids of different sizes were generated using either $1x10^5$ or $3x10^5$cells. All spheroids where incubated in either chondrogenic differentiation or control proliferation media over 6 weeks. Medium was replenished three times a week. Over the 6 week incubation, chondrogenically differentiated samples were consistently larger than the undifferentiated control spheroids in both the small and large spheroid groups. This was in keeping with work previously undertaken in our laboratory (Zucchelli, 2018).

3.2 Confocal microscopy analysis of whole mount spheroids

3.2.1 Determination of the most effective spheroid clearing method.

The protocols for each of the three optical clearing solutions tested (BABB, Sca*l*eA2, Clear^{T2}) are described in detail in section chapter 2 section 2.3.3.

This preliminary experiment was aimed at determining which clearing solution resulted in the most effective optical clearing of 6-week undifferentiated (in control media) ADSC spheroids of similar size ($1.0x10^5$ cells).

Spheroids incubated in different clearing solutions were whole-mount stained overnight with Hoechst nuclear staining prior to clearing. Effectiveness was defined by both macroscopic change in appearance of the spheroid and the depth of optical sectioning achievable using confocal and two-photon microscopy.

This initial pilot experiment (Fig. 3) demonstrated and confirmed that BABB was the most effective at clearing spheroids which was almost instantaneous. Macroscopically, Sca*l*eA2 spheroids appeared to enlarge and became softer with areas of early fragmentation noted (Fig. 3A). Despite a prolonged 2-week incubation on a roller, Clear^{T2} spheroid failed to demonstrate any significant macroscopic clearance (Fig 3B). Clear^{T2} was not investigated further given the obvious ineffective optical clearing.

BABB-cleared spheroids became transparent and almost impossible to detect within a minute. In a petri-dish, these spheroids felt firm and brittle when manipulated with forceps (Fig. 3C). They also appeared to have shrunk in size, consistent with known effects of BABB on tissue. Spheroids incubated in Sca*l*e*A2* for 4 hours also achieved a degree of clearing but not as effectively as BABB.

Hoechst dye-stained spheroids cleared with BABB and Sca*l*eA2 were then imaged using 2-photon microscopy to investigate the limit of imaging depth (Fig. 3.1A-C). Given the corrosive nature of BABB, the first attempt at imaging was undertaken with the spheroid placed in a depression slide and a cover slip to protect the microscope objective. Imaging of these two spheroids (BABB n=1, Sca*l*eA2 n=1) were similar with good detail of cells at the superficial regions but both suffered poor contrast and loss of cellular detail at deeper levels (Fig. 3.1B-C). Two-photon microscopy was significantly better than standard confocal imaging. By -90µm the Sca*l*eA2 spheroid lost significant detail compared to a deeper -120µm for the BABB spheroid (Fig 3.1).

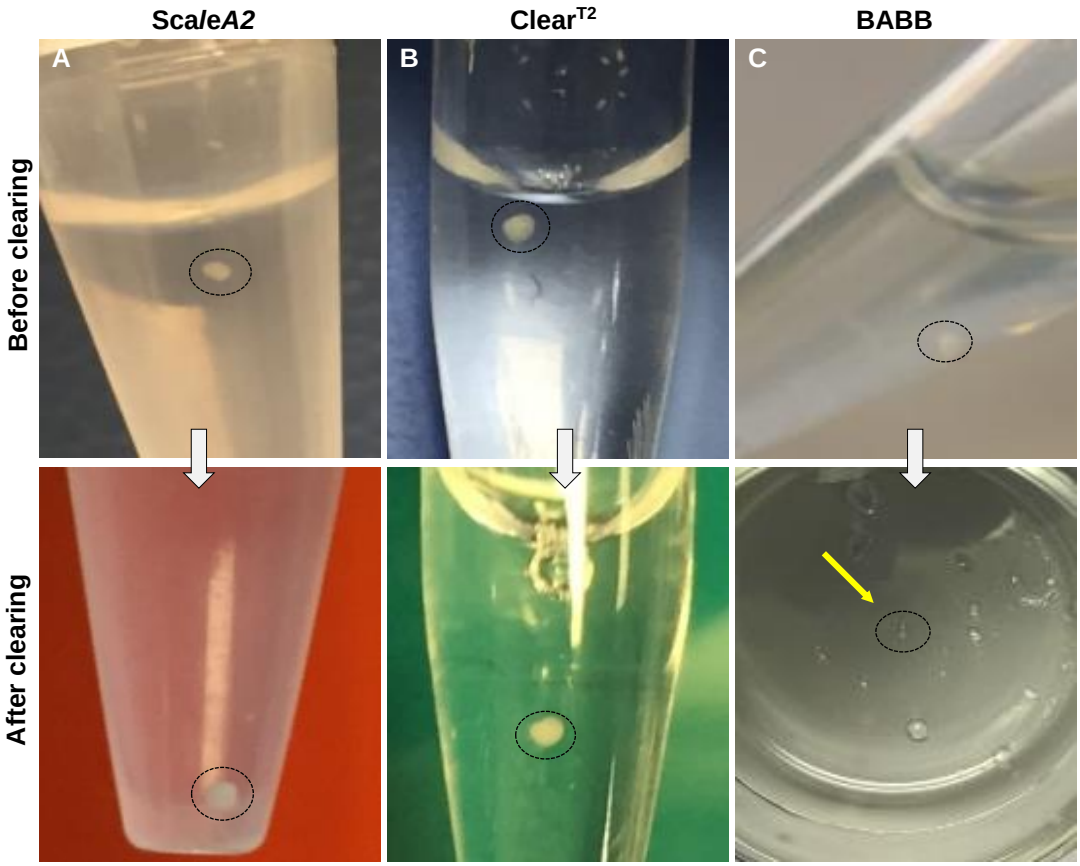

Figure 3.0. Spheroid macroscopic appearance after clearing with different protocols. Spheroids are highlighted within dotted circles before and after clearing. **(A)** Scale*A2* protocol resulted in moderate change with a degree of optical clearing and slight increase in size. **(B)** Clear^{T2} clearing protocol resulted in no visible change to the spheroid. **(C)** BABB was highly effective at clearing. Application of BABB to the spheroid was undertaken in a glass dish, resulting in total clearing. The micromass was just about visible to the naked eye as it became completely transparent (yellow arrow).

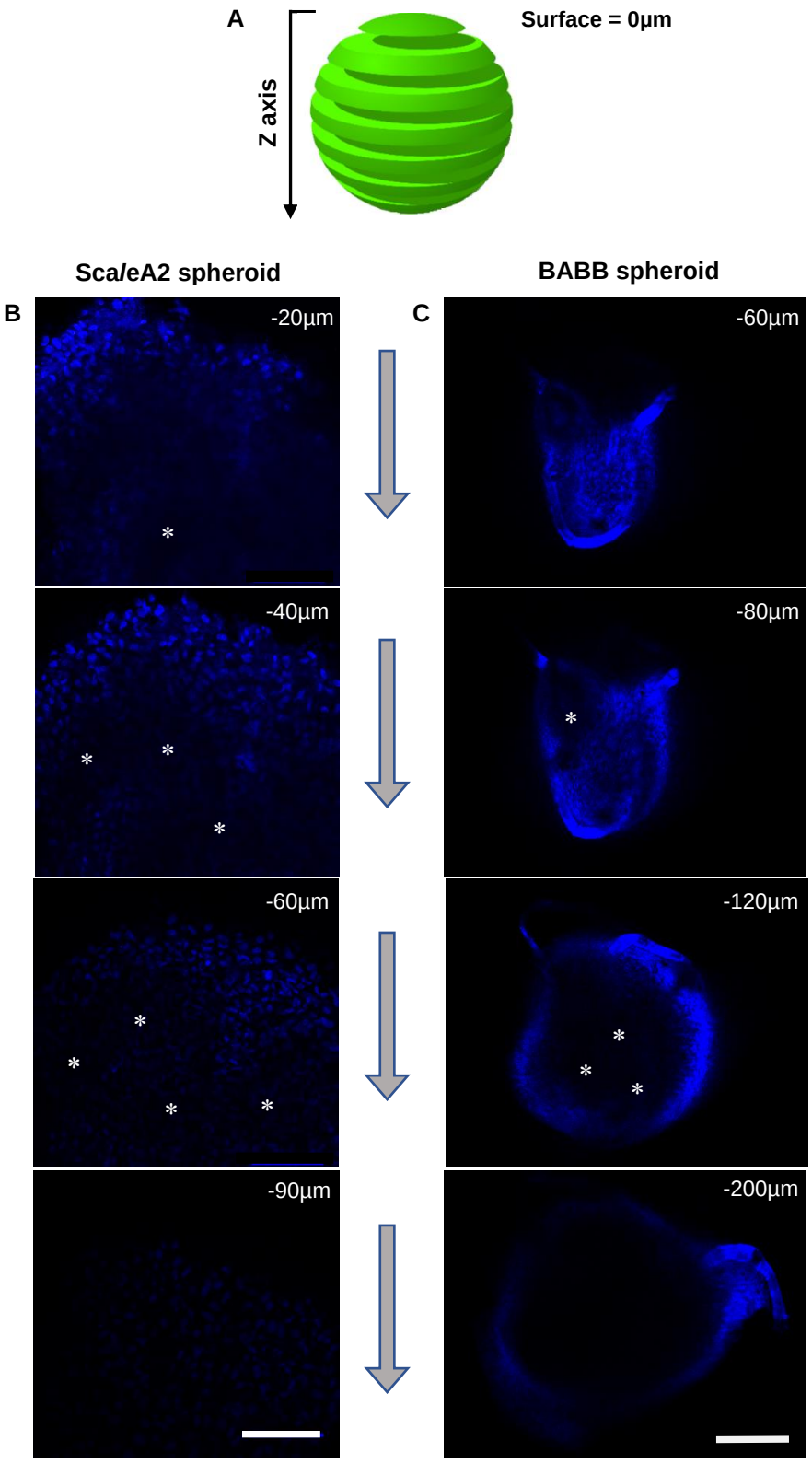

Figure 3.1. Two-photon microscopy optical sectioning of Hoechst dye-stained spheroids after clearing with different protocols. (A) Schematic of optical sectioning along the Z axis to create a "Z stack". As optical sectioning proceeds from the surface (taken as 0µm) into deeper levels loss of nuclear stain signal is observed. Hoechst nuclear staining of whole mount undifferentiated ADSC spheroids (1x10^5 cells) cleared with Sca*l*eA2 **(B)** and BABB **(C).** The depth of the image from the surface is shown in the top right corner of each image. Loss of signal is highlighted with asterix, seen in Sca*l*eA2 spheroid sooner than BABB. Scale bars: 100µm.

3.2.1.1 Spheroid imaging technique for BABB optical clearing

BABB clearing of spheroids was found to be effective (macroscopically and using confocal imagine) and quick in these initial experiments and was therefore selected as the clearing agent of choice. BABB cleared spheroids were imaged using a Zeiss LSM 880 upright confocal multiphoton microscope with Airyscan using the following objectives:

- 20x/NA1.0 Plan Apochromat Water dipping objective with correction collar. WD 2.4mm.
- 10x/NA0.5 W-Plan Apochromat Water dipping objective. WD 3.7mm.

A disadvantage of using BABB solution is that it is corrosive and can cause significant damage to microscopes and objectives. Two methods were developed during these experiments for BABB cleared spheroids.

3.2.1.2 Development of microscope safe techniques for imaging

Two techniques were developed during this thesis for imaging spheroids using BABB to avoid damage to microscope equipment, firstly the rubber ring technique secondly the inverted drop. We advocate the use of the rubber ring technique for larger samples and the inverted drop method for small spheroids although both can be used. The inverted drop technique was quicker and simple to carry out. This technique relied on the surface tension of the BABB to maintain the position of the spheroid on the “inverted” cover slip. Both techniques permitted safe use of BABB solution that avoided direct contact with the microscope objectives without distortion of the images produced.

3.2.1.3 Rubber ring on cover slip technique

This technique involved the use of a BABB resistant fluorocarbon ring Viton ®/FKM (Seals and Plastic Inc, TX, US) positioned onto a microscope slide with the spheroid placed in the center immersed in BABB solution. The rubber ring thickness must be more than that of the spheroid sample. The microscope slide is positioned onto a plastic or glass petri dish which can be secured into the microscope platform clamp. A cover slip is then gently placed onto the ring ensuring it contacts the underlying BABB solution, enough to mildly disperse it. The BABB solution and spheroid are effectively “sandwiched” between the microscope slide and the coverslip and using this technique both remain completely away from any microscope hardware. A 1ml-2ml drop of water is placed onto the second coverslip to allow an immersion objective to be used (Fig 3.2). For additional safety, the microscope slide which is positioned onto a petri dish can be placed in a further larger petri dish to catch any accidental spillage of BABB beyond the first petri dish.

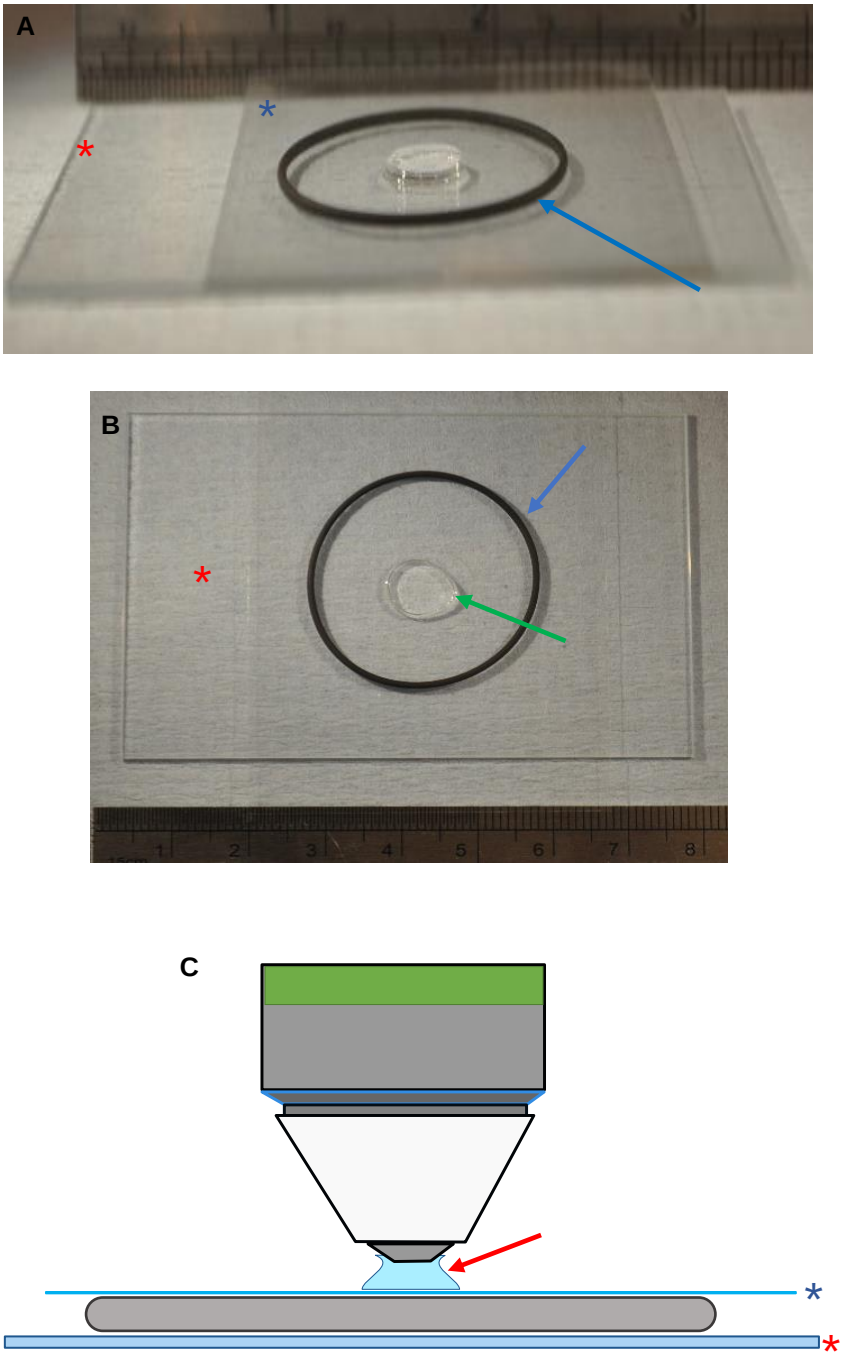

Figure 3.2. Spheroid confocal imaging with water dipping objective. (A) The spheroid in BABB is gently placed into the middle of a microscope slide (*) and a BABB resistant rubber ring (blue arrow) is placed around the spheroid/BABB sample. A coverslip (*) is placed on top of the rubber ring making sure that enough BABB is present to make direct contact with this coverslip. **(B)** Top view of (A) showing mild dispersion of underlying BABB solution (green arrow). **(C)** Diagrammatic representation of technical set up. Using this technique, the BABB sample remains safely away from the immersion objective. Sufficient volume of water is placed onto the coverslip to an allow immersion objective to be used (red arrow).

3.2.1.4 Inverted drop technique

In this technique, the spheroid being imaged is carefully and gently placed into the center of a glass cover slide with just enough BABB added to cover the spheroid. This is approximately 50µl. The cover slip is then flipped over so that the spheroid is now on the undersurface and is placed on to a Petri dish with the spheroid covered in BABB away from the microscope objective. A large drop of water can be safely placed onto the superior surface of the coverslip to allow the dipping objective to be used without risking potential corrosive damage from the BABB solution (Fig 3.3).

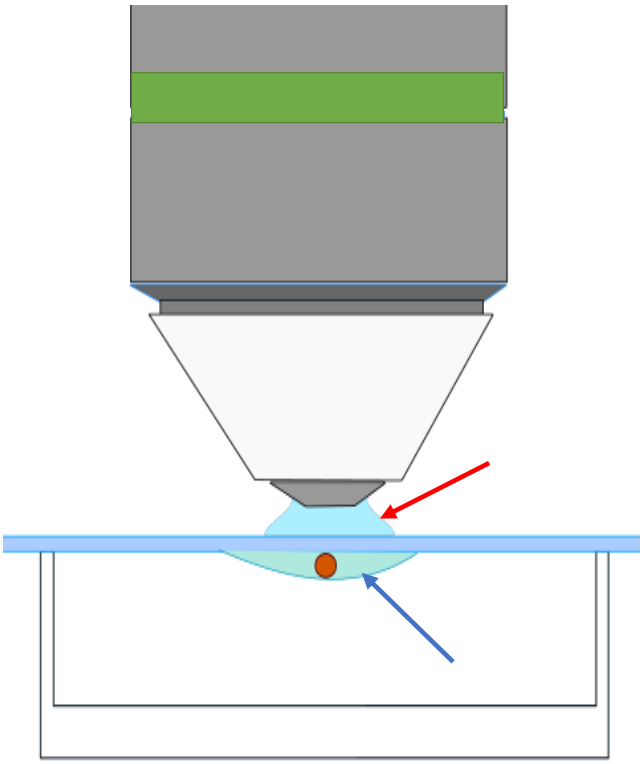

Fig 3.3. Inverted drop BABB cleared spheroid technique. BABB cleared spheroid can be effectively and safely imaged by leaving the spheroid in BABB solution (blue arrow) and carefully flipping the coverslip over to allow a water dipping objective to be used (red arrow). The coverslip is placed onto a petri dish to prevent BABB solution coming into contact with any microscope parts.

3.2.2 Whole mount immunostaining and optical clearing of spheroids.

The effectiveness of BABB on clearing chondrogenically differentiated spheroids to assess cartilage ECM development, and cell morphology was investigated. Spheroids cleared using BABB were incubated with primary and secondary antibodies for different lengths of time as well as with increasing concentrations of Triton x-100 detergent to improve antibody penetration. The details of the following spheroid experiments are described and summarized in table 2.3 chapter 2.

3.2.2.1 Small undifferentiated spheroids

Despite BABB being better than Sca*l*eA2 at optical clearing, significant central regions of the spheroids remained poorly visualized. As a starting point to identify how to improve on this, further small spheroids cultured in control medium over a 6 weeks period (identical to spheroids in first experiment) were stained wholemount with Hoechst over 24 hours and 48 hours respectively and then cleared with BABB (experiment 2 in table 2.3, section 2.3.3). Triton x-100 concentration within the permeabilizing solution was increased from 0.2% to 2% to improve Hoechst penetration. This was done to assess if poor diffusion of the Hoechst through the spheroid was resulting in the loss of signal identified in the first experiment. After BABB clearing, the spheroids were imaged using identical laser set up configuration on the same two-photon microscope. Z-stack optical slicing demonstrated very little change in the 24 hour-stained spheroids in comparison to the first experiment with similar reduced detail of nuclear staining in deeper regions. However, the 48 hour spheroid demonstrated significantly improved nuclear Hoechst detection throughout the entire spheroid (Fig 3.4).

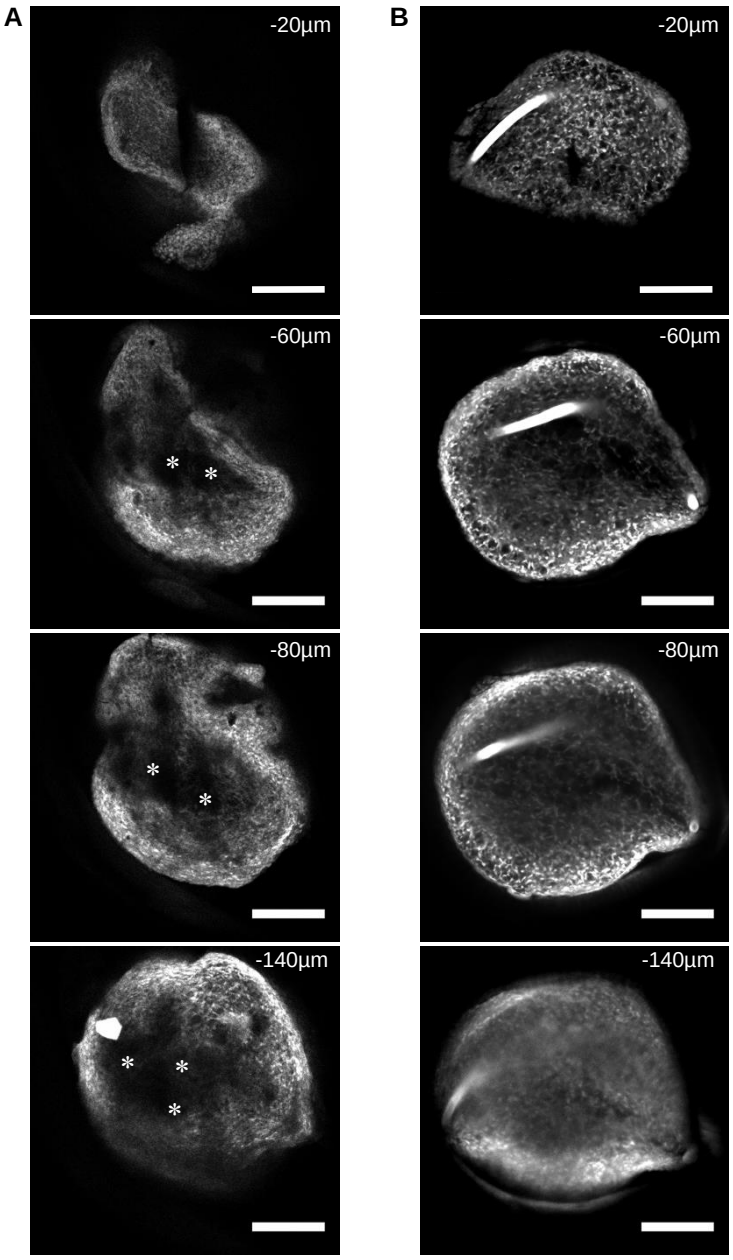

Figure 3.4. Undifferentiated ADSC-derived spheroids (6 weeks, 1x10^{5}cells) stained for 24 (A) and 48 (B) hours with Hoechst nuclear dye and cleared with BABB. Two-photon microscopy optical sectioning of whole mount spheroids. At progressive depths from the surface, the signal from the 48 hour spheroid is maintained whereas the 24 hour (A) demonstrates patchy regions of no signal at deeper core regions (asterisks). Scale bars: 100µm.

3.2.2.2 Small chondrogenically differentiated spheroids

Having demonstrated improved imaging with a prolonged nuclear staining protocol, the next experiment involved the addition of collagen II (Col2) and vimentin (Vim) immunofluorescence staining in chondrogenically differentiated ADSC derived spheroids of similar cell numbers $1x10^5$. These spheroids were found to be larger in size than undifferentiated controls despite being incubated for the same 6-week period, an observation previously noted and explained by the deposition of ECM. For this experiment, one group of spheroids were stained with the 48 hours protocol; 48 hour primary antibody followed by 48 hours secondary antibody and Hoechst dye incubation (Fig 3.5) and a second group for the extended 96 hours protocol (Fig 3.6) with antibodies to Col2 and vimentin and counterstained with Hoechst dye (experiment 3, table 2.3). Triton x-100 2% was used in both groups.

Antibody penetration appeared superior in spheroids stained with the 96 hour protocol and enabled detailed assessment of the core morphology. The nodular nature of deeper sections within the spheroid were visible in both protocols but clearer in the 96 hour staining and are characterized by regions of high Col2 signal. The 96 hour staining protocol was repeated to confirm these findings and similar results were obtained. Some regions still appeared patchy at deep levels 250µm even for the 96hr protocol with reduced signal of vimentin and collagen II in areas where cells were clearly present as defined by the Hoechst nuclear staining. This may indicate poor antibody staining rather than laser penetration. Laser penetration was the likely problem at deeper levels because Imaging at surface levels (less than 50µm deep), demonstrated vimentin and collagen II signals that were strongly positive and demonstrated presence of extracellular collagen II and spindle shaped cells (Fig 3.7).

In both spheroids, small cracks were identified at deeper levels, either resulting from cell condensation or as an unwanted effect of BABB solution during clearing (Fig 3.5, 3.6 blue arrowheads).

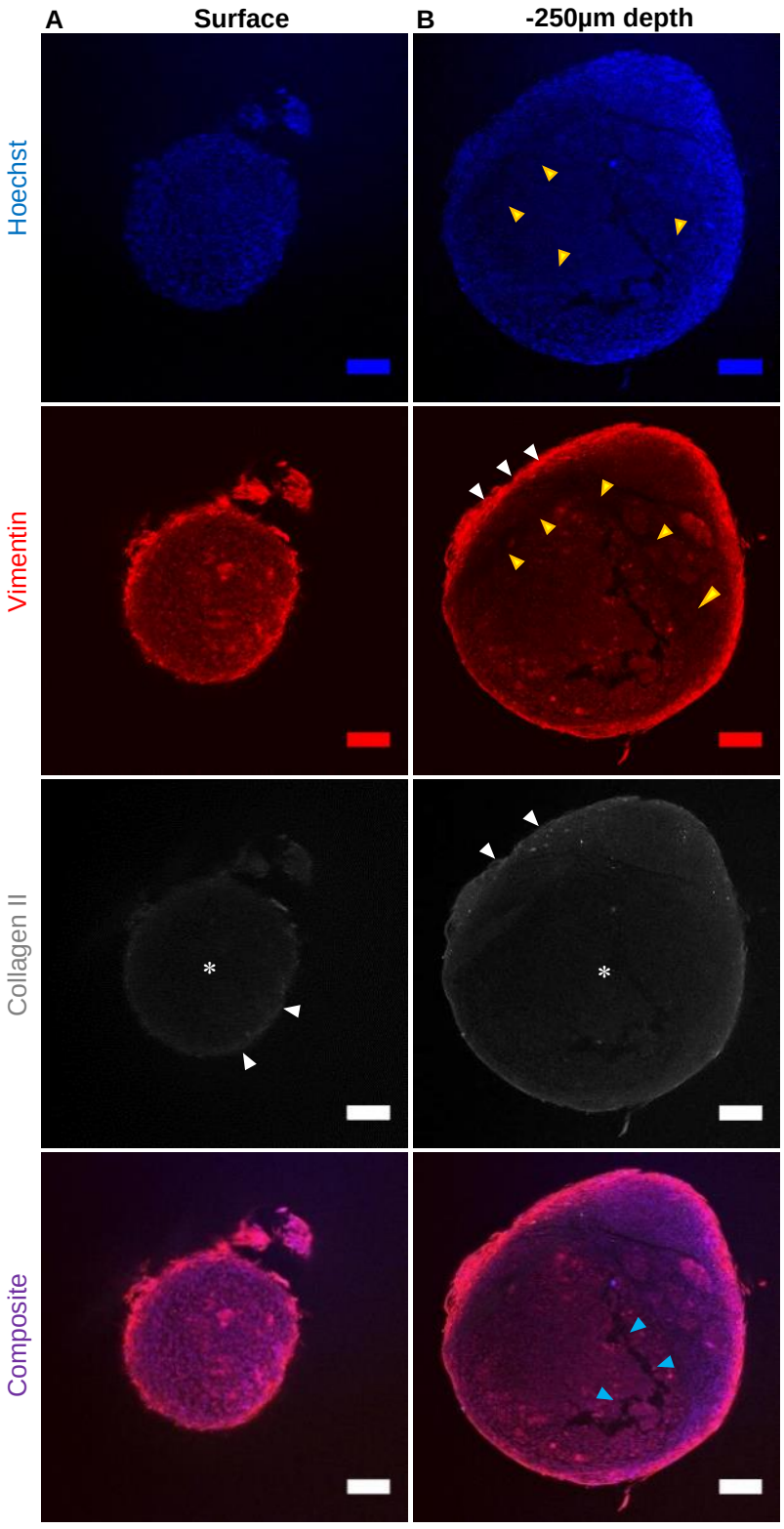

Figure 3.5. Immunostaining with the 48 hour protocol of BABB-cleared ADSC spheroids ($1.0x10^5$ cells, n=1) chondrogenically differentiated for 6 week. Two photon confocal images taken with a water immersion objective at the surface **(A)** and -250µm **(B)** Collagen II, vimentin, and nuclear staining at deeper levels has different staining intensity in different regions within the inner region. Hoechst and vimentin staining in central regions is patchy with lack of detail (yellow arrowheads). Peripheral regions are strongly labelled for vimentin and collagen II (white arrowheads). Collagen II staining is limited in central areas with poor signal (asterisk). Cracks are noted in central regions (blue arrowheads). Scale bars: 100µm.

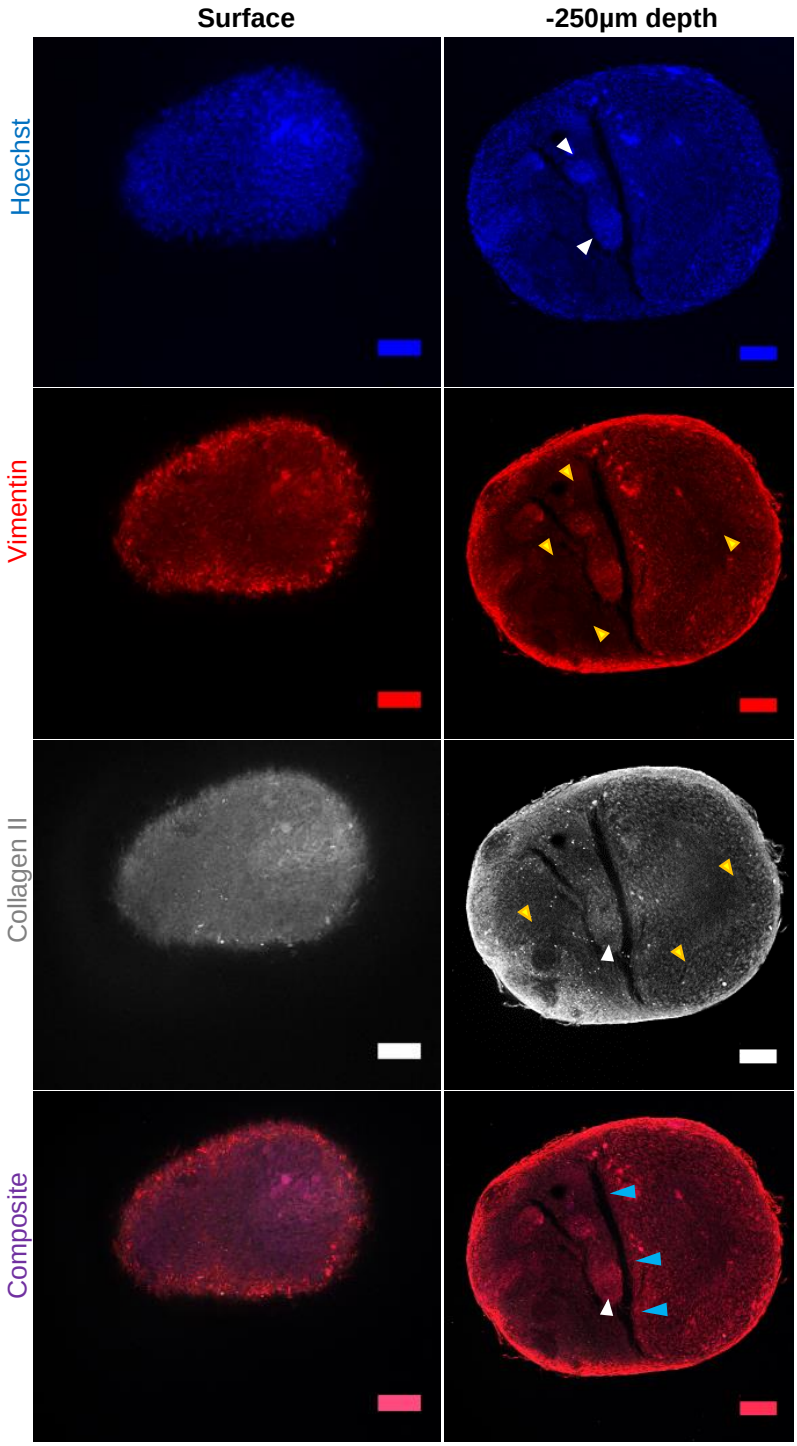

Figure 3.6. Immunostaining with the 96 hour staining protocol of BABB-cleared ADSC spheroids ($1.0x10^5$ cells, n=3) chondrogenically differentiated for 6 week. Two photon confocal images taken with water immersion objective at the surface after incubation for 96 hours with primary antibodies to collagen II and vimentin and for 96 hours with secondary antibodies and Hoechst dye following permeabilization with 2% Triton X-100. Hoechst staining is clearly visible even at the deeper level. Nodular morphology of deep sections within the spheroid are evident (white arrowheads). Immunofluorescent staining for collagen II, vimentin and is weak in some regions (yellow arrowheads). Cracks are noted in central regions (blue arrowheads). Scale bars: 100µm.

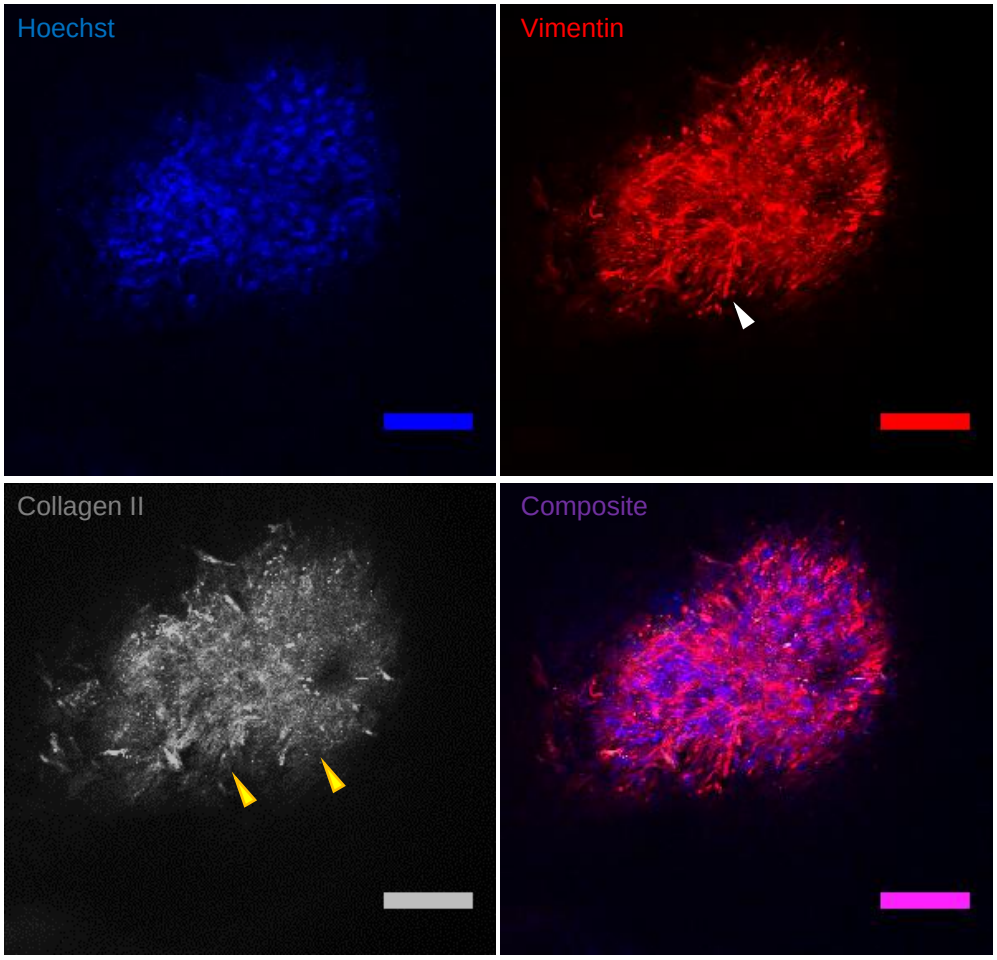

Figure 3.7. Confocal imaging with immersion objective at surface (-25µm) of spheroid in figure 3.6. Surface detail of spheroids is excellent with this immunofluorescence staining protocol. Extracellular secretion of collagen II (yellow arrowheads) and spindle like morphology of cells (white arrowheads) can be clearly identified. Scale bars: 100µm.

3.2.2.3 Large chondrogenically differentiated spheroids

Larger spheroids presented with further imaging challenges. Larger spheroids may be used in certain experiments to study cartilage ECM in 3D and therefore it was thought useful to analyze them as whole mount in a similar way to what has already been described for small spheroids. The ability of BABB solution to optically clear larger spheroids was investigated using spheroids of 3.0 $x10^5$ cells that had been maintained for 6 weeks either in control or chondrogenic medium. Spheroids were stained with primary and secondary antibodies using the extended 96 hour protocol (experiment 4, table 2.3).

Both chondrogenically differentiated and undifferentiated spheroids were investigated. Interestingly, it was observed that despite their size, undifferentiated spheroids cleared with BABB had strong Hoechst nuclear staining signal at both superficial and deeper (-250µm) levels. Vimentin and collagen II staining was variable although more intense for collagen II (Fig 3.8). In contrast, chondrogenically differentiated spheroids (despite BABB clearing) were difficult to image with two-photon microscopy and demonstrated very poor detail at deep regions with low intensity signal in central areas around -250µm depth for collagen II, vimentin and nuclear staining (Fig 3.9).

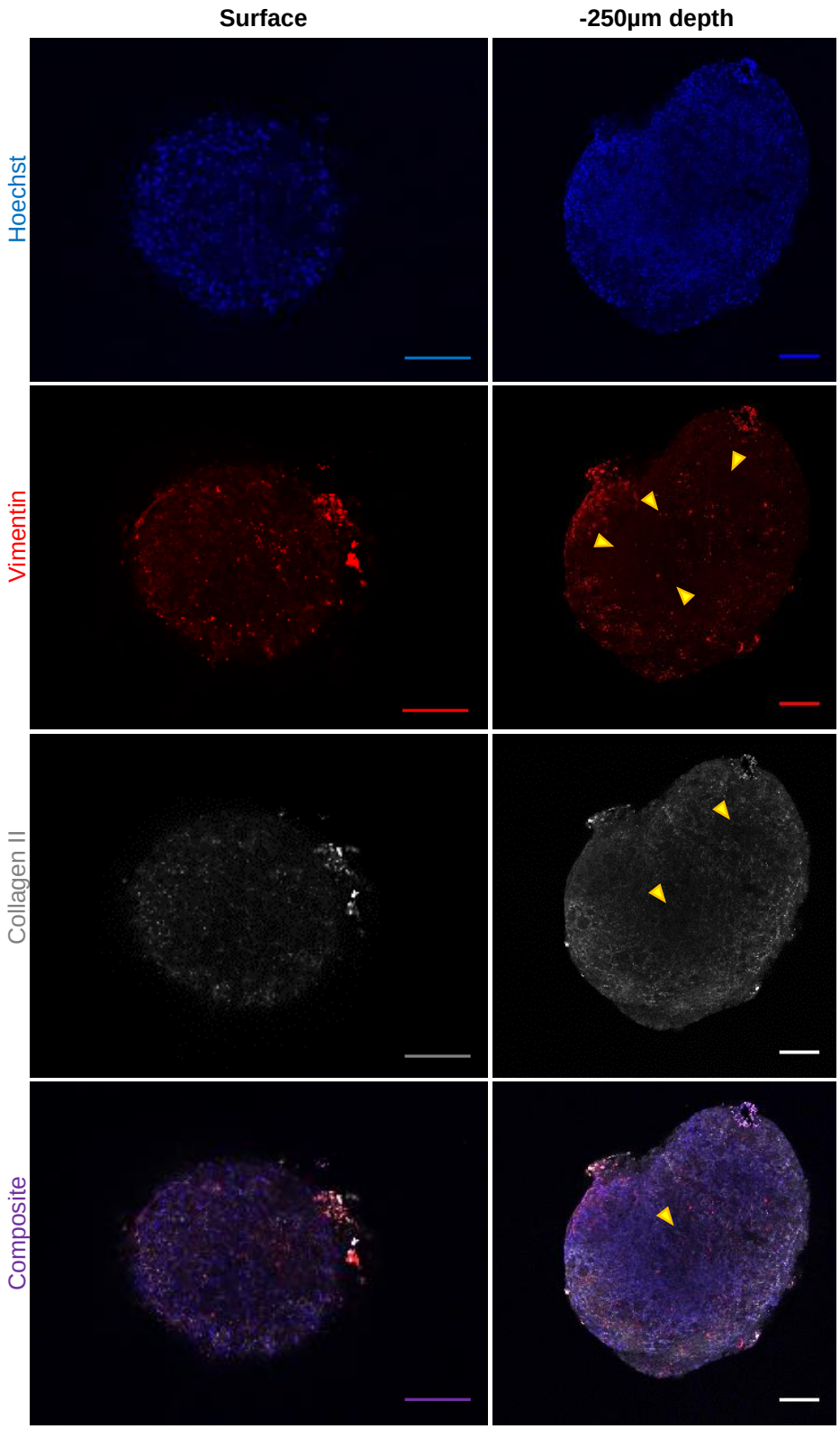

Figure 3.8. Immunostaining with the 96 hour staining protocol of BABB-cleared undifferentiated ADSC spheroids ($3.0x10^5$ cells, n=1). At both surface and -250µm depth, Hoechst nuclear staining is intense. Staining for vimentin and Collagen II in some core regions is of lower signal intensity (yellow arrowheads). Spheroid maximum depth approx. 600µm. Scale bars: 100µm.

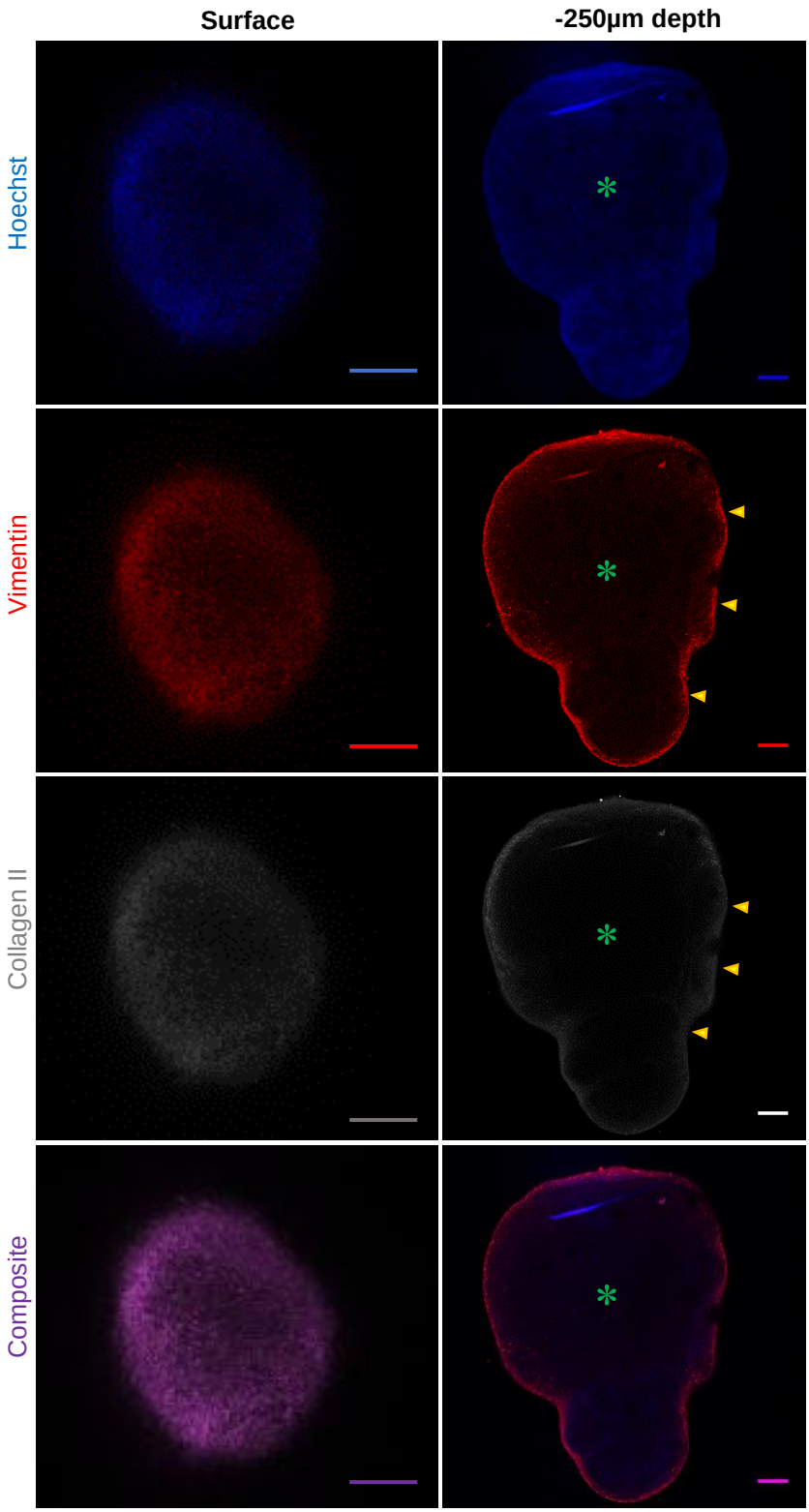

Figure 3.9. Immunostaining with the 96 hour staining protocol of BABB-cleared ADSC spheroids ($3.0x10^5$ cells, n=1) chondrogenically differentiated for 6 weeks. Two-photon optical sections demonstrate positive Hoechst and antibody staining at the surface but deeper core regions (*) very little antibody signal is detected. Staining is intense in peripheral areas (yellow arrows). Spheroid maximum depth 630µm. Scale bars :100µm.

3.2.2.4 Spheroids created with genetically labelled paediatric ADSCs and cartilage-derived precursor cells

To determine if regions of low intensity signal at deep levels of optically sectioned spheroids were due to poor laser penetration, BABB solution clearing or antibody penetration, genetically labelled cells were used to generate spheroids. This allowed fluorescent imaging of whole cells without the need for antibody staining and therefore any reduced signal noted with these spheroids could either represent a true acellular zone or explained by poor laser penetration.

Two lines were used (ADSC H37 line eGFP$^+$ and microtic ear cartilage derived cell line CH32 mCherry$^+$) that had already been generated in our laboratory by Dr Eleonora Zucchelli. Briefly, these lines were generated using eGFP$^+$ and mCherry$^+$ lentiviral vectors to transduce the cells lines. Cells were selected and expanded for fluorescence activated cell sorting with final cells appearing intensely fluorescent (Fig 3.10). These cell lines were tested to confirm that they had retained their ability to differentiate along the three mesenchymal lineages: adipogenic, chondrogenic and osteogenic. All lines retained this ability.

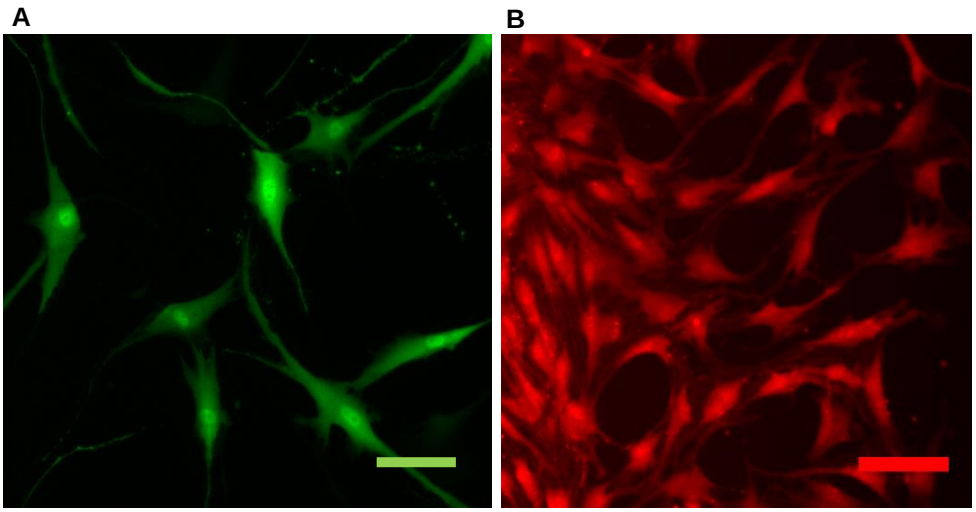

Figure 3.10. Genetically labelled ADSCs and CSPCs. (A) Fluorescence microscopy of ADSC eGFP$^+$ labelled H37 cell line and (B) mCherry+ labelled ear cartilage derived precursor cell line CH32. Both cell lines retained normal morphology following transduction and were intensively fluorescent. Scale bars: 100µm.

3.2.2.5 Preliminary imaging of genetically labelled spheroids

Before genetically labelled spheroids were stained for Col2 and vimentin to analyse the level of chondrogenesis, they were stained with Hoechst to enable a rapid initial view of the spheroid morphology. Initial experiments were undertaken with small ($1x10^5$, 6 weeks incubation) BABB cleared $eGFP^+$ ADSC chondrogenically differentiated spheroids (n=3), that were stained with Hoechst dye (for 96 hours). Prior to 2-photon confocal z-stack imaging of these BABB cleared spheroids, the spheroid was scanned to ensure that there was no surface debris that was interfering with laser penetration. Transmitted light from the 800nm laser was detected with a Photon Multiplier Tube (T-PMT), using a linear polariser to enhance contrast. Small particles and fibers had been noted in previous spheroid imaging but their impact on the signal had not been fully appreciated. What was observed is that small particle debris on the surface was indeed a potential problem and so they were gently removed with a sterile 23g needle under a tissue microscope prior to 2-photon imaging (Fig 3.11).

After careful removal of as much surface debris as possible without damaging the spheroid (some debris could not be detached off the spheroid), two-photon optical sectioning of these $eGFP^+$ spheroids demonstrated excellent detail and intense fluorescent signal throughout the entire depth (370µm). Furthermore, the internal morphology of the spheroid and the presence of cartilage nodules were easily identified. These nodules appear as dense foci of tissue with intense Col2 signal (Fig 3.12).

Merged images of optical sections of $eGFP^+$ cells stained with Hoechst of the same spheroid at all depths (more than -300µm) demonstrated intense nuclear staining and the $eGFP^+$ cells (Fig 3.13). Three dimensional images were obtained using z-stack data and enabled further investigation of spheroid morphology (Image shown in Fig A1 Appendix I).

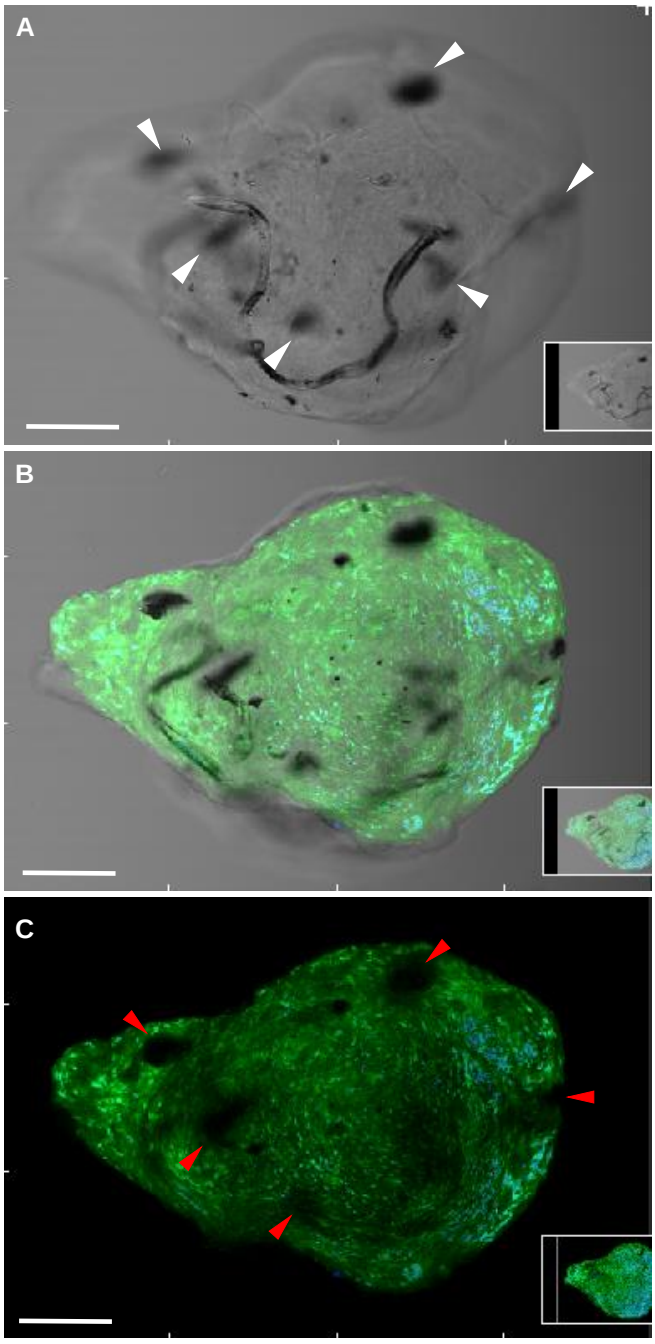

Figure 3.11. Surface debris on BABB cleared chondrogenically differentiated GFP+ ADSC spheroids (1x10^5, 6 weeks incubation, n=3) stained with Hoechst dye. (**A)** Brightfield imaging with numerous small foreign body debris and fluff identified on the surface (white arrowheads) following BABB solution clearing. **(B)** Superimposed and cellular images demonstrate the impact of the debris on the final image **(C)** which shows regions of absent signal as laser penetration is restricted by the debris (red arrowheads). Scale bars: 100µm. (3D media file on DVD, file M1).

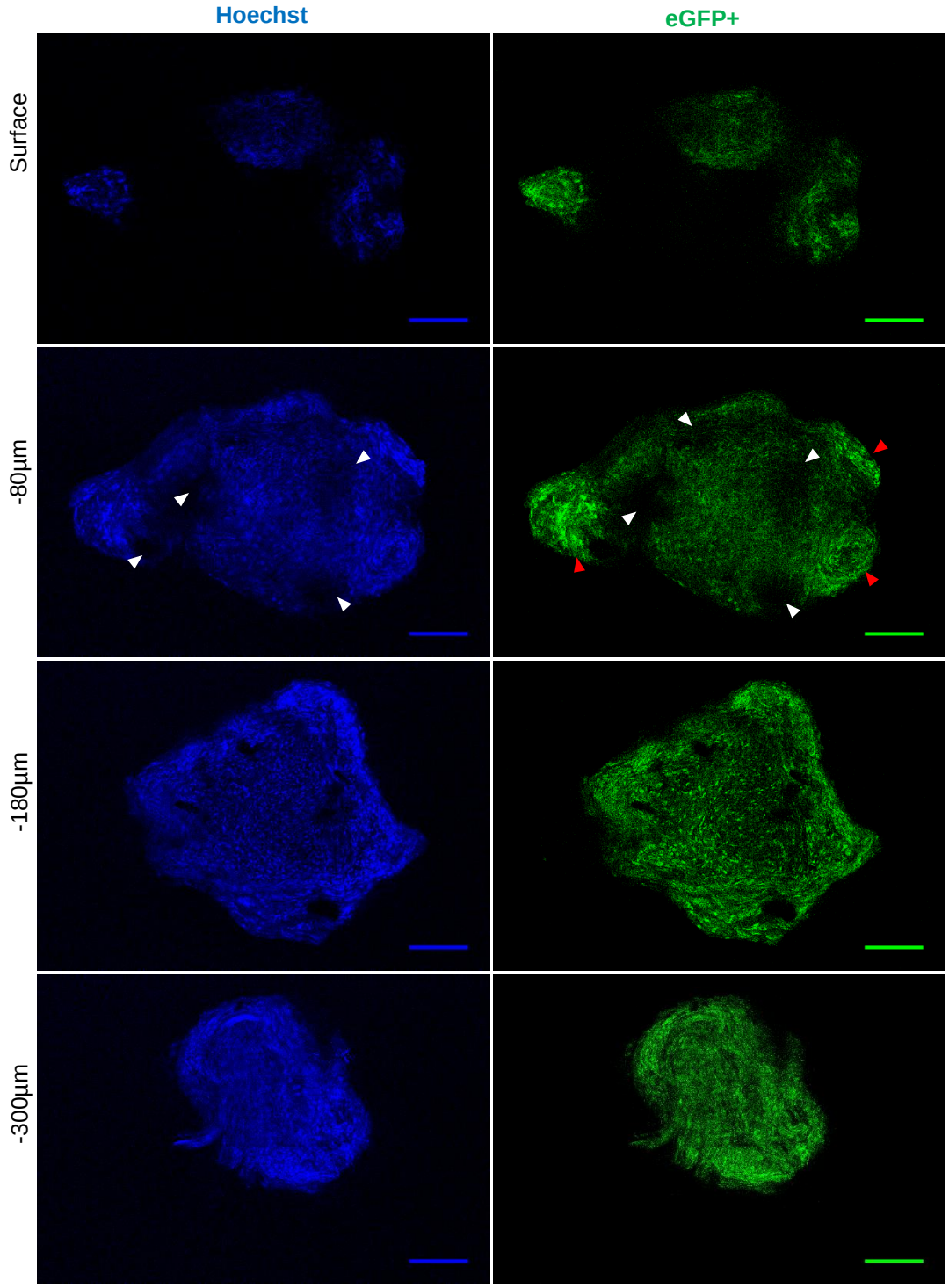

Figure 3.12. Whole-mount Hoechst staining for 96 hours of BABB cleared ADSC eGFP^{+} labelled spheroids 1x10^{5} cells, 6-week incubation in chondrogenic medium. Both Hoechst and eGFP+ signal from the cells is intense throughout the depth of the spheroid. Patchy regions (white arrowheads) are not acellular but represent surface debris that is interfering with laser penetration. Red arrowheads indicate regions of cartilage nodules. Scale bars: 100µm.

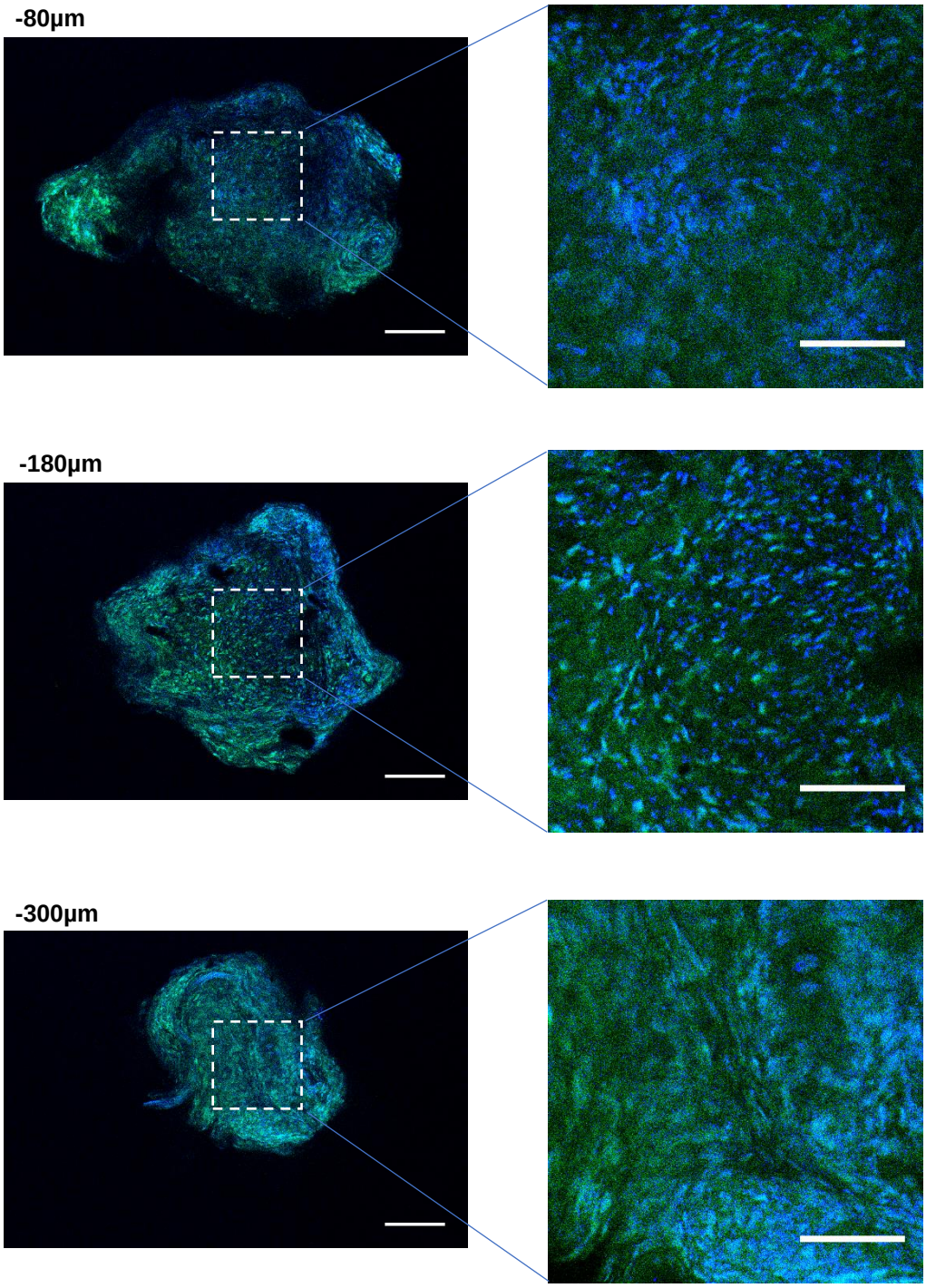

Figure 3.13. Core regions of the spheroid Fig 3.10. Two photon confocal imaging at increasing depths with merged channels of Hoechst and eGFP^{+} images. Core regions magnified (scale bars 50µm) demonstrate excellent signal with clear cellular regions and cell nucleus even at deeper optical sectioning. Scale bars: 100µm.

3.2.2.6 Imaging of genetically labelled ADSC and CSPC spheroids

In the final series of spheroid experiments, chondrogenically differentiated eGFP$^+$ ADSC spheroids stained with vimentin, collagen II and Hoechst (experiment 5, table 2.3) were investigated using the 96 hour staining protocol. The aim here was to determine the nature of cell behaviour in 3D in relation to cartilage ECM deposition given that cells appear to be present in core regions. Furthermore, chondrogenically differentiated mCherry$^+$ cartilage stem precursor cell (CSPCs) spheroids were also analysed at the same time to confirm that the 96 hour staining protocol used for ADSC can also be applied effectively to CSPCs. Following BABB clearing, multiphoton imaging of these spheroids demonstrated excellent visualization throughout the full depth of the spheroid (image of non-cleared eGFP$^+$ ADSC spheroid appendix I, Fig A3 for comparison).

eGFP$^+$ labelled cell distribution within the deeper levels was readily observed (to full 515µm depth) with intense vimentin and Hoechst staining and eGFP$^+$ cells. This provided further evidence that laser penetration was adequate, and that previous limited visualization of deeper spheroid regions was related to inadequate antibody penetration. Collagen II staining intensity remained patchy in some regions and this may reflect accurately the lower levels of chondrogenesis in core regions. At the periphery of the spheroid, intense Col2 signal is observed in regions which appear to represent nodules of cartilage that surround the inner region of the spheroid (Fig 3.14).

Similarly, mCherry$^+$ labelled CSPC spheroids stained with the same 96 hour protocol demonstrated strong Hoechst, vimentin and mCherry$^+$ signal throughout the full depth (330µm) of the spheroid. At the periphery, a small cartilage nodule is identified and a peripheral layer with intense collagen II signal is detected, distinct from the inner regions (Fig 3.15).

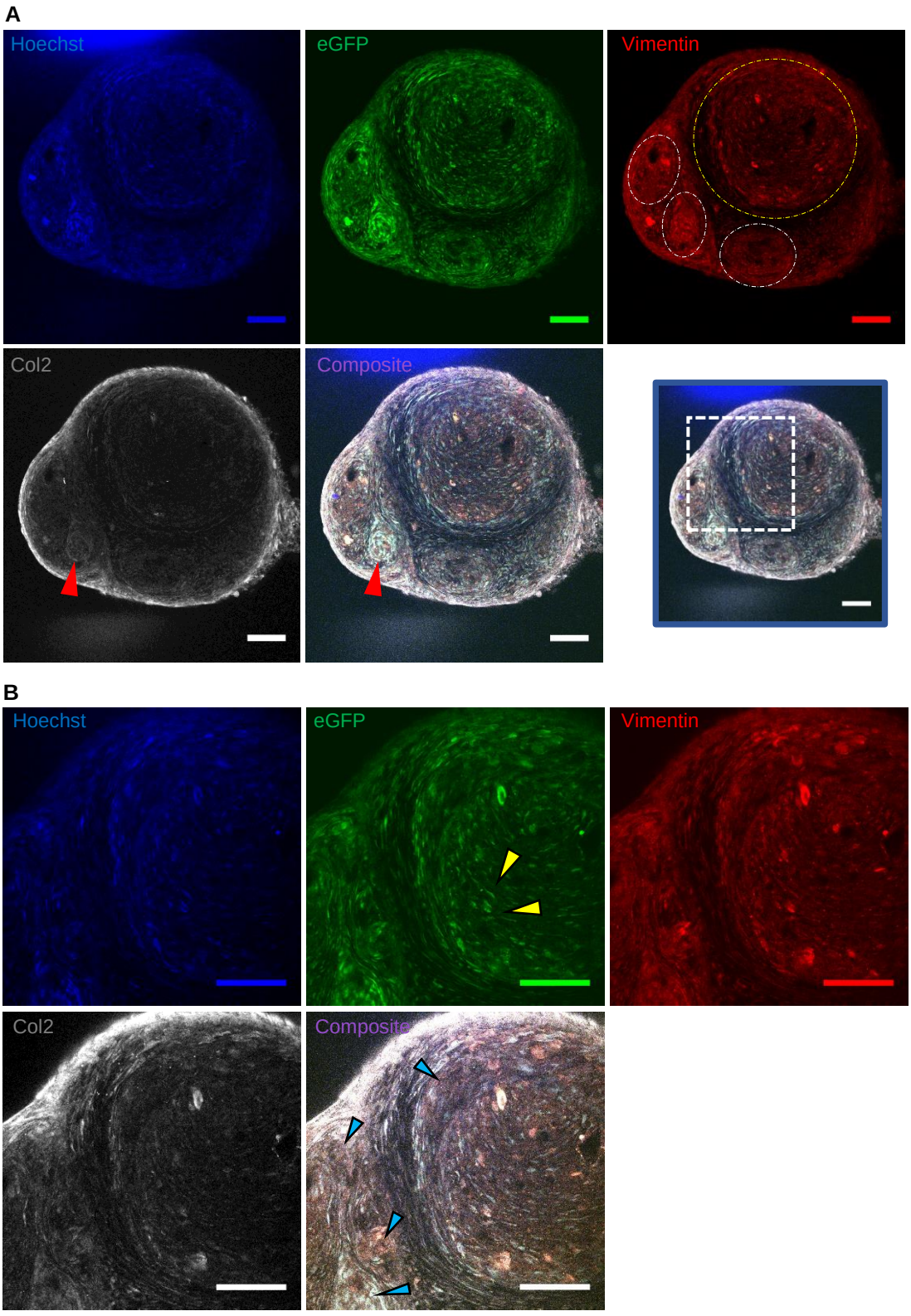

Figure 3.14. Immunostaining with the 96 hour protocol of BABB-cleared eGFP^{+} labelled ADSC spheroid (1.0x10^{5} cells, n=3), chondrogenically differentiated for 6 weeks. (A) Images taken with immersion objective at -160µm from surface. Intense staining is demonstrated throughout the spheroid. Cartilage nodules are identified (dashed white circles) with regions of intense Collagen II signal (red arrows) surrounding the main inner region of the spheroid (dashed yellow circles). **(B)** At higher magnification (Dashed box region within spheroid**)** Hoechst, vimentin and eGFP^{+} cells signal is intense and individual cells are easily identified (yellow arrowheads). Cartilage nodule condensations are also easily identified (blue arrowheads). Scale bars: 100µm.

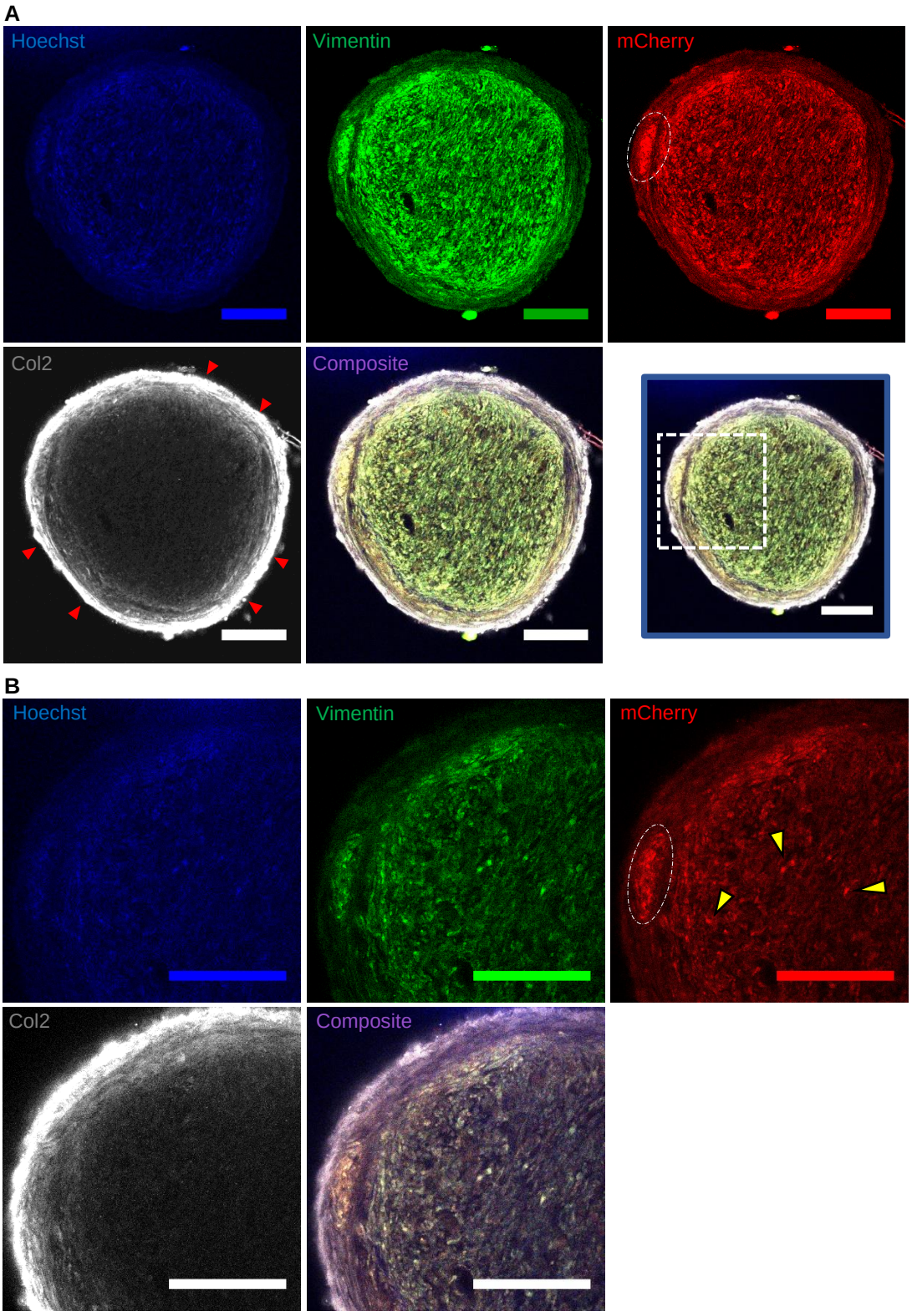

Figure 3.15. Immunostaining with the 96 hour protocol of BABB-cleared mCherry^{+} labelled CPSC spheroid (1.0x10^{5} cells, n=3), chondrogenically differentiated for 6 weeks. (A) Images taken with immersion objective at -200µm from surface. Intense vimentin and Hoechst staining is demonstrated throughout the spheroid. A cartilage nodule is identified (dashed white circle) at the periphery and intense Col2 signal surrounding the inner region is detected (red arrowheads) **(B)** At higher magnification (Dashed box region within spheroid**)** Hoechst, vimentin and mCherry^{+} cell signal is intense and individual cells are easily identified (yellow arrowheads). Cartilage nodule condensations are also easily identified (blue arrowheads). Scale bars: 100µm.

3.3 Discussion

Three dimensional culture systems such as spheroids have been extensively studied in relation to tissue engineering allowing characterization of cellular differentiation, proliferation and organization in 3D. Tissue optical clearing protocols for 3D culture systems have been widely published for spheroids generated from breast, liver, prostate cancer cells as well as neural stem cells, dermal fibroblasts, colon, liver, lung and heart cells (Costa et al., 2019; Dekkers et al., 2019; Kuwajima et al., 2013; Nürnberg et al., 2020). However, optical clearing of dense cartilage spheroids has not been extensively studied. Calve et al 2015, demonstrated optical clearing of bovine cartilage tissue using a fructose based clearing agent with fluorescently labelled probes with low MW and achieved optical clearing of cartilage tissue to 307µm thickness. In this study, chondrogenically differentiated spheroids were imaged to depths over 500µm and 600µm for undifferentiated spheroids. The use of BABB solution to achieve optical clearing of chondrogenically differentiated ADSC and CSPCs spheroids, is to our knowledge unreported. Furthermore, the use of genetically labelled cells to avoid the pitfalls of slow diffusing high molecular weight primary and secondary antibodies to optimize imaging of cartilage spheroids is novel.

3.3.1 Clearing solutions

Several clearing solutions are widely used for tissue optical clearing. Initial experiments revealed that although BABB solution was the most effective, it was challenging to use given its irritant nature and the risk of damaging microscopic objectives. In this study, all spheroids were cleared on glass dishes or slides and direct contact with microscope objectives was avoided. The imaging techniques developed during this thesis and described, proved to be safe without impact on the quality of images obtained. For small tissue samples such as small spheroids, the inverted drop technique was easy and quick to set up. Studies using BABB solution for optical clearing have attempted to design a safe imaging protocol using a ring of dental cement, glue and a metal ring around the sample with mixed levels of success (Azaripour et al., 2016). The inverted drop technique for safe imaging of BABB cleared tissue appears unreported and novel.

Further challenges of BABB clearing relate to its effect on tissue samples. It was difficult to move cleared spheroids from one slide to another as they were almost impossible to see with the naked eye. This problem was overcome by moving spheroids from petri dish to cover slip using a tissue microscope. BABB solution has been reported to reduce fluorescence signals due to quenching (Azaripour et al., 2016; Kuwajima et al., 2013). This was not observed in the spheroids and furthermore, some spheroids were imaged after 2 months with no obvious loss of fluorescence signal.

Another potential problem with BABB clearing is increased brittleness that risks fracturing the spheroid, therefore handling with tissue forceps should be done with caution.
BABB solution however was very quick to achieve effective clearing of dense cartilage spheroid. Clearing was almost instantaneous. Luo et al. 2019, described a highly effective clearing solution Poly(Ethylene Glycol) Associated Solvent System (PEGASOS) to effectively clear mice calvarial bone but the whole process appears to take at least 2-3 days, much slower than BABB (Luo et al., 2019).

3.3.2 Optimization of whole mount immunostaining protocol and optical clearing for inner-tissue imaging in small and large spheroids

Antibody staining protocols were developed with increasing incubation times and by increasing Triton x-100 concentration. In this study, there was improved immunofluorescent staining with increasing antibody incubation times between 24, 48 and 96 hours. At the extended 96 hour incubation protocol, Hoechst, collagen II and vimentin staining throughout the smaller spheroids was consistently better providing excellent imaging at all depths with stronger signals.

3.3.2.1 Antibody penetration versus laser penetration

Initial experiments with spheroids generated from unlabelled cells demonstrated limited signal within inner regions of spheroids. To maximize staining signal, antibody incubation periods were increased and Triton concentration. BABB clearing and two-photon laser configuration was kept constant and signal strength in similar sized spheroids increased. This would suggest that crucially, an effective clearing protocol and importantly the level of antibody penetration is critical. Some inner regions of chondrogenically differentiated spheroids were still poorly imaged. To establish whether this was still related to antibody penetration or laser penetration, $eGFP^+$ and $mCherry^+$ labelled spheroids were BABB cleared and optical sectioning at core levels clearly demonstrated the presence of cells in inner regions. This suggests that poor antibody penetration (e.g. collagen II and vimentin) in previous spheroid staining experiments was likely to explain the loss of signal in deep regions.

Variation in collagen II staining amongst the spheroid samples was consistent with other studies that shows a peripheral layer of collagen tissue that envelopes the outer surface of cells pellets (Lewis et al., 2016; Tare et al., 2005). This may be related to differing medium nutrient penetration and is critical on the spheroid size. Chondrogenically differentiated spheroids demonstrated cartilage nodules with regions of intense collagen II staining.

Zucchelli. 2018 demonstrated similar cartilage nodules in spheroids stained and sectioned with traditional paraffin embedding and microtome sectioning or with cryoembedding and frozen sectioning. Cell distribution and identification of nodules within small spheroids ($1x10^5$ cells) derived from labelled cells (both ADSC and CSPC) was clear and in great detail at both surface and core levels and resembled spheroids stained and imaged with conventional histological techniques.

In this study, spheroids were no larger than 600µm in depth which is well within the maximum possible imaging depth of multiphoton microscopy. For standardization, all micromasses were imaged with identical microscopy laser strengths and gain settings. Improvements in imaging depths can be made by higher laser setting but at the expense of fluorophore photo-bleaching and cellular autofluorescence. The limited imaging of larger sized (and higher cell numbers $3x10^5$) chondrogenically differentiated spheroids despite using BABB clearing, suggests that cells density and production of cartilage like ECM may limit adequate imaging. This is particularly relevant to chondrogenically differentiated spheroids. This suggests that initial cell numbers and density of the sample is an important consideration when planning spheroid studies with the intention of wholemount imaging and optical sectioning rather than traditional paraffin sectioning. The limits of imaging therefore appear to be dependent on tissue density rather than size.

3.4 Conclusion

In summary, I have shown that multiphoton microscopy of BABB cleared spheroids is a reproducible and effective alternative to traditional histology sectioning techniques in the investigation of chondrogenically differentiated 3D spheroids. Larger differentiated spheroids with higher cell densities may be more challenging to image. The results suggest that experimental models using small micromasses and with labelled cells where possible, will provide excellent visualisation of cellular morphology and ECM. This study addressed key variables which may impact on spheroid two-photon imaging. Notably these were, the antibody incubation period required for satisfactory penetration, the selection of an effective tissue clearing solution and to assess the ability of confocal laser to penetrate spheroids to the required depths.

Through development of the staining and optical imaging protocols, an optimal method is described that permits excellent imaging throughout full depths of spheroids well over 500µm in thickness.

This presence of cartilage nodules and intense collagen II staining in chronologically differentiated spheroids also provides detail into the pattern of cell assembly and ECM deposition within a scaffold free environment, critical to understanding cell behavior in upscaled 3D tissues.

Chapter 4

RESULTS 2:

Attachment and cell expansion in Integra Dermal Regeneration Template

4.0 Background

As highlighted in chapter 1 section 1.5.2.6, several studies have used Integra dermal regeneration template (IDRT) as a scaffold to generate an enhanced dressing for wound healing, increased angiogenesis on skin wounds and to improve scar formation. Based on such studies, I have explored the potential for Integra to be used as the core element within a “pocket” design product comprising of chondrogenically differentiated cells seeded into Integra as the cartilage core, sandwiched between a resorbable material.

Integra is available in both a single layer and a bilayer (a sheet of silicone attached to it) and is already widely used in clinical practice (chapter 1 section 1.5.2.6). In clinical use, it is used as artificial skin for burns and skin cancer reconstruction and forms a neo-dermis. Given that cells are able to migrate into the integra and deposit collagen in skin wound healing, its ability to permit chondrocyte migration and deposition of cartilage-like extracellular matrix is of interest and the reason for choosing Integra in this design.

The resorbable material will provide temporary mechanical support for the Integra core, so that by the time the material has fully resorbed, the Integra would have sufficient cartilage extra-cellular matrix to support itself. Many novel graft designs for nasal reconstruction have been investigated and published that involve 3D printed materials. A popular material for tissue engineering is polylactic acid (PLA) as it has been widely researched and is an FDA approved polymer. Rippy et al. 2018 examined the biocompatibility and absorption of PLA nasal dorsal implants in sheep and found no infections or tissue rejection up to 24 months post implantation. Grafts were fully encapsulated through 12 months and had completely resorbed by 24 months (Rippy et al., 2018). Furthermore, it is also known that PLA induces a low host response that only increases during the higher rate of resorption that occurs between 12-18 months following implantation. The main cellular response at this stage is macrophage infiltration that allows phagocytosis of degrading PLA debris. At this time, there is also an increase in collagen deposition at the graft site (Gogolewski et al., 1993). Furthermore, its 24-month resorption time would be excellent for the pocket design concept as this is sufficient time to allow the core cartilage component of the graft to mature. These properties make PLA an ideal material for custom made nasal grafts.

Historically in regenerative medicine cells are seeded directly onto hard scaffolds. If the scaffold material is biodegradable, then the final tissue generated may be heterogeneous given the unpredictability and variation in degradation rates. The advantage of the pocket design construct is that the central core region which will ultimately form cartilage tissue is mechanically supported by the outer hard PLA polymer scaffold.

Since cells are not directly seeded onto the hard scaffold this eliminates the unpredictability of the effect of resorption on cartilage formation since this is only achieved in the central core region. PLA has variable degradation relating to vascularisation and will degrade faster in areas under stress possibly related to crack formation (Athanasiou et al., 1998). In addition, the advantage of PLA is its ability to be readily printed into custom shapes using a 3D printer by fused deposition modelling (FDM) which is widely available and simple (Tiersch and Monroe, 2016). Production of PLA is also eco-friendly as it is derived from renewable sources such as corn, wheat, and starch.

Importantly for clinical translation is that PLA is already FDA approved and therefore easier to translate any novel medical products to clinical practice. PLA mechanical properties can also be modified to range from soft and elastic to stiff and high strength. The main concern with PLA is the build-up of acidic by products of degradation causing tissue irritation (Farah et al., 2016). This may present a problem given that the nasal septal product will be inserted between mucosal layers in the septal region which are relatively not highly vascular.

In this chapter my aim was to investigate the ability of Integra dermal regeneration template to support stem cell adhesion, expansion and their chondrogenic differentiation in order to generate cartilage like ECM and tissue within the Integra. This would serve as a possible suitable scaffold for the core element of the pocket design product. The second aim was to determine if the pocket design consisting of the integra core inserted into a PLA pocket was practical and reproducible.

Specific objectives for this chapter include:

1. Assess the survival, expansion, and migration of ADSC and cartilage derived precursor cells (CSPCs) within Integra sheets.
2. Assess the ability of ADSCs and CSPCs to deposit cartilage like ECM in Integra following chondrogenic induction by detection of collagen type II protein in both *in vitro* and *in vivo* models.
3. Histological analysis of Integra sheets to determine presence of cartilage like tissue morphology.
4. Assess the suitability of Integra sheet for the core element of a novel pocket nasal septal design utilising PLA biodegradable material.

4.1 Results

Cell lines used in this chapter are listed in table 4.1. Both ADSC and cartilage derived chondroblast cells were used. The terms Integra matrix, sheet or membrane are used interchangeably in this chapter and refer to the same product.

ADSC	Microtic ear derived precursor cells
H20	**CH32**
H37	**Ch90**
H20	**Ch105**

Table 4.0. **Cell lines used in Integra experiments.**

4.1.1 Analysis of ADSCs seeded on Integra bilayer membrane

Initial experiments were undertaken to assess the behaviour of ADSCs on Integra membranes. Initially Integra® membrane that consists of an outer silicone layer and an inner thick matrix layer was used (bilayer Integra) to seed ADSCs (line H20) labelled with $eGFP^+$ and $mCherry^+$ fluorescent proteins generated using a lentiviral system (Fig 4.0A). This allowed visualisation of cells during the experiment. Experiments were undertaken using bilayer Integra cut into 8mm discs (600µm thick) and seeded directly with $1x10^4$ ADSCs (n=2 for both groups). Macroscopic appearance of chondrogenically differentiated and undifferentiated (control) discs for both $eGFP^+$ and $mCherry^+$ groups showed a subtle but definite physical difference after 18 weeks in culture, with the differentiated discs appearing more compact and having increased their rigidity, as evident when handling them with forceps (Fig. 4.0B). The undifferentiated disc was fragile, soft and retained a spongy consistency similar to unseeded Integra.

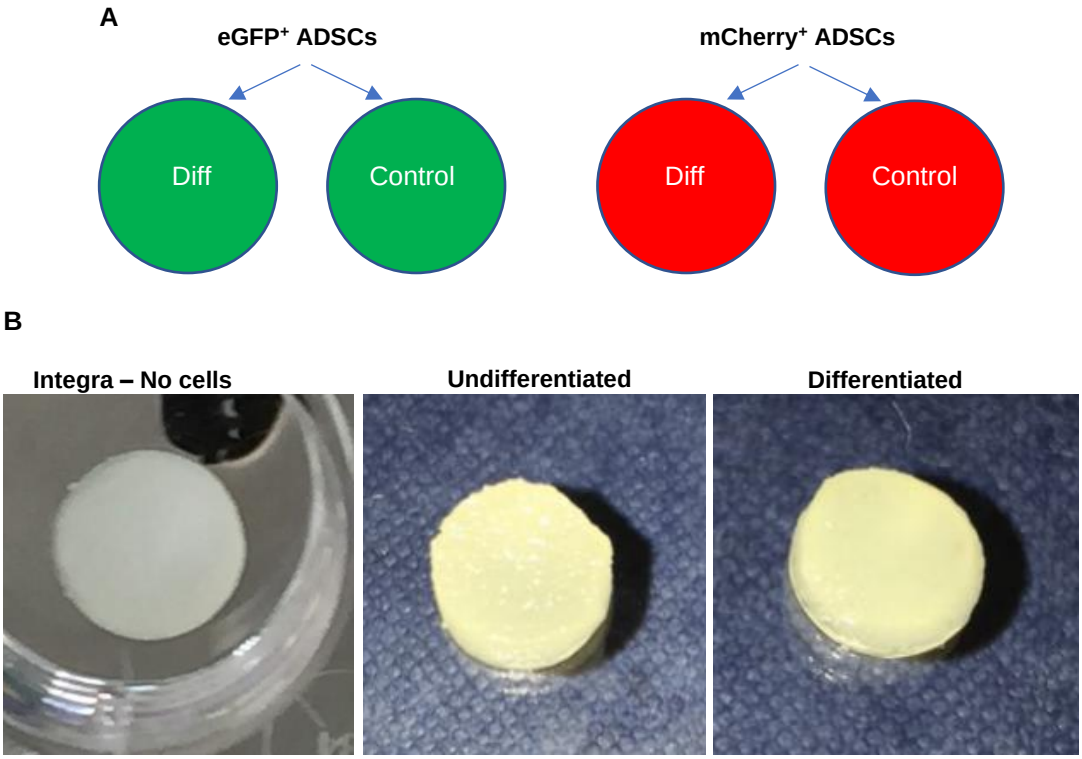

Figure 4.0. Initial Integra experiment using bilayer Integra cut into 8mm discs seeded with eGFP$^+$ and mCherry$^+$ labelled ADSC. (A) Each Integra disc seeded with either eGFP$^+$ or mCherry$^+$ cells were cultured in chondrogenic differentiation or control medium. **(B)** Macroscopic appearance of 8mm bilayer Integra discs. Integra at the start of the experiment without cells is opaque. Integra seeded with eGFP$^+$ ADSCs ($1x10^4$) and maintained in either control or chondrogenic medium for 7 months in static cultures (n=2). The differentiated disc has a compact appearance. Disc thickness 600µm, scale bars:8mm. mCherry discs demonstrated identical appearance.

The initial analysis of cell seeded in Integra over time with a Brightfield inverted fluorescent microscope showed that, notwithstanding Integra had a degree of autofluorescence, both labelled cells were identifiable. Interestingly, in mCherry$^+$ and eGFP$^+$ labelled discs chondrogenically differentiated in static cultures, fluorescence appeared to increase between 1 and 10 weeks (Fig. 4.1). Discs in control medium did not show any significant change over time. These initial experiments suggested that ADSC survive and can expand within the matrix of Integra. Having established that cells could be detected under a standard fluorescent microscope and that cells appear to survive; further analysis was done using confocal microscopy.

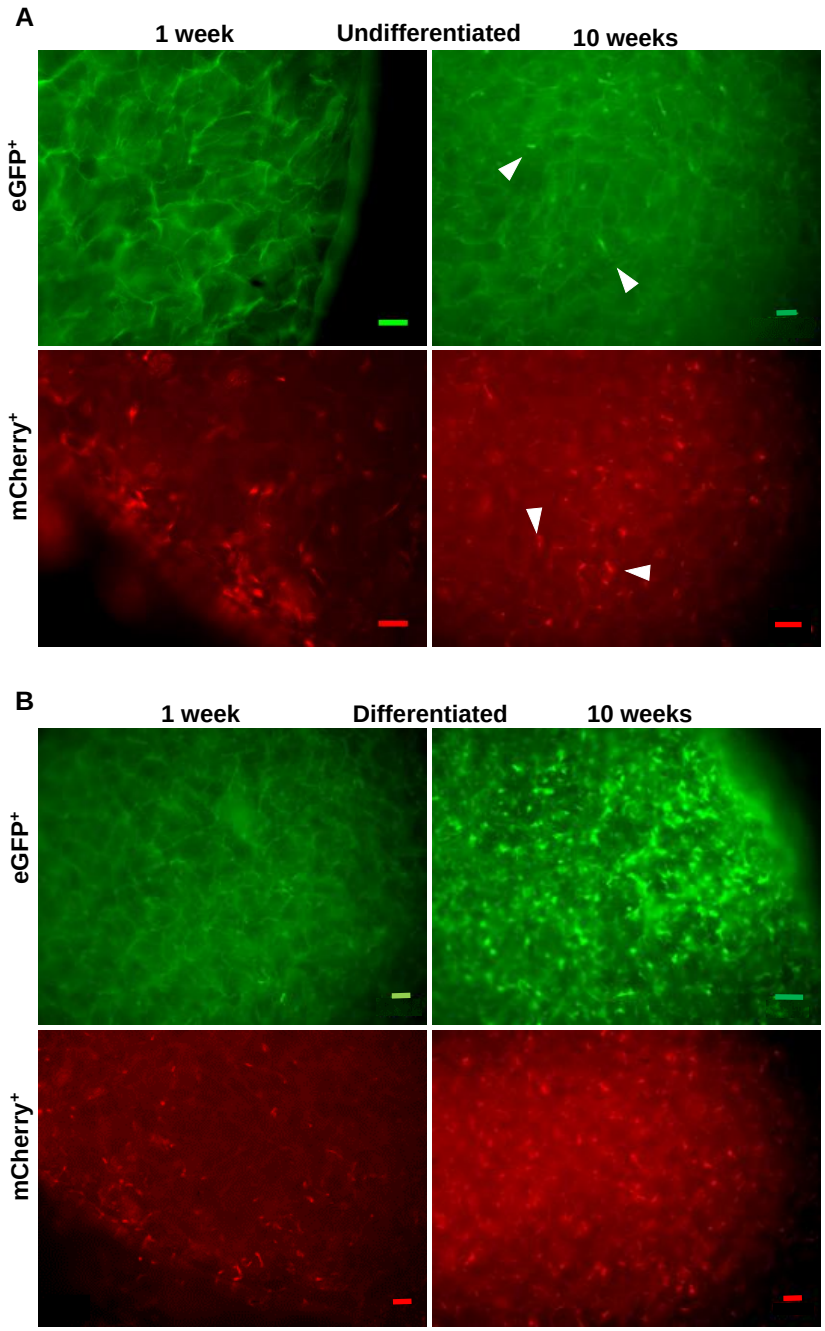

Figure 4.1. Fluorescent inverted microscope images of eGFP$^+$ and mCherry$^+$ labelled ADSCs (1x10^4 cells) seeded onto Integra membrane in control (A) and chondrogenically differentiated (B) medium. Images at 1 week and 10 weeks culture. (A) Undifferentiated discs demonstrate constant appears with minimal changes in cell density between weeks 1 to 10 (red arrowheads). **(B)** Over 10 weeks there is marked a change in cell density in both cell types with increased fluorescence intensity over time. Images taken of surface of each disc. Scale bars: 100µm.

4.1.1.2 Confocal imaging of bilayer Integra

As cells in 3D systems are more difficult to visualize using standard fluorescent microscopy than cells in 2D, subsequent analysis was carried out by confocal microscopy. To assess potential interference of Integra autofluorescence, prior to immunohistochemical staining, Integra sheets without cells were imaged by fluorescent confocal microscopy (Fig. 4.2). This demonstrated a significant level of autofluorescence from the Integra matrix throughout, detected in blue (485 SP), green (500-550 BP), red (575-610 BP) and far red (640-710 BP) channels using a single excitation at 800nm.

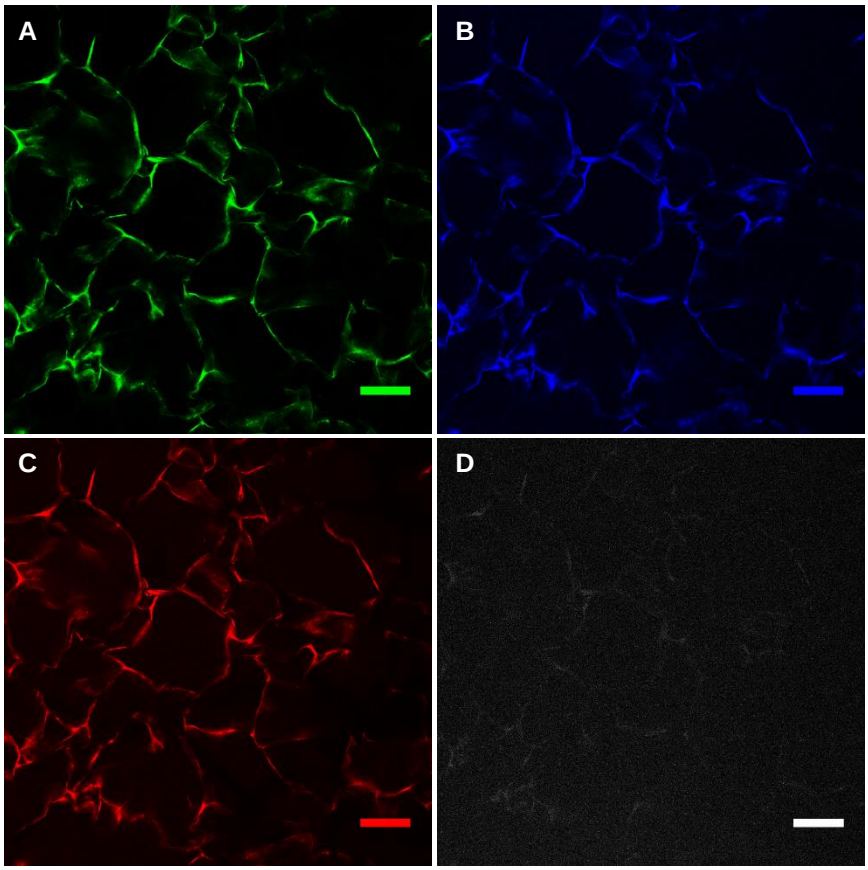

Figure 4.2. Two-Photon confocal fluorescent imaging at the centre of an Integra disc without cells. Autofluorescence is detected in all channels using 800nm excitation. The far red (640-710 BP) channel (D) autofluorescence is less than the other channels. Scale bars: 100µm.

4.1.1.3 Immunohistochemical staining of bilayer Integra discs

Immunohistochemical staining of the discs described in section 4.1.1 was carried out using the staining protocol described in chapter 2 section 2.3.2.2, to analyse cell distribution in the Integra 3D environment as well as the expression of collagen type II (as a marker of chondrogenesis). A 3D image created from confocal microscopy of a $mCherry^+$ disc detected ADSCs throughout the bilayer (Fig 4.3). Further confocal imaging of Integra with both cell lines ($eGFP^+$ and $mCherry^+$) demonstrated differences between deep and surface regions. Cells appear to have migrated through the entire depth of the Integra matrix but evidently, there are less cells at deeper levels of the Integra. (Fig 4.4). At a depth of 100µm of Integra from the surface, confocal imaging demonstrated deposition of collagen type II within the chondrogenically differentiated disc which was strongly positive compared control discs. However, collagen II expression is still observed in deep regions of the chondrogenically differentiated discs to 200-300µm from the surface. The results were consistent for both cell types (Fig. 4.5, Fig 4.6). Undifferentiated Integra discs were negative for Collagen II staining.

The problem of autofluorescence from Integra impacting on image interpretation was reduced by using composite images which made it easier to identify fluorescent stain and cells from the Integra matrix.

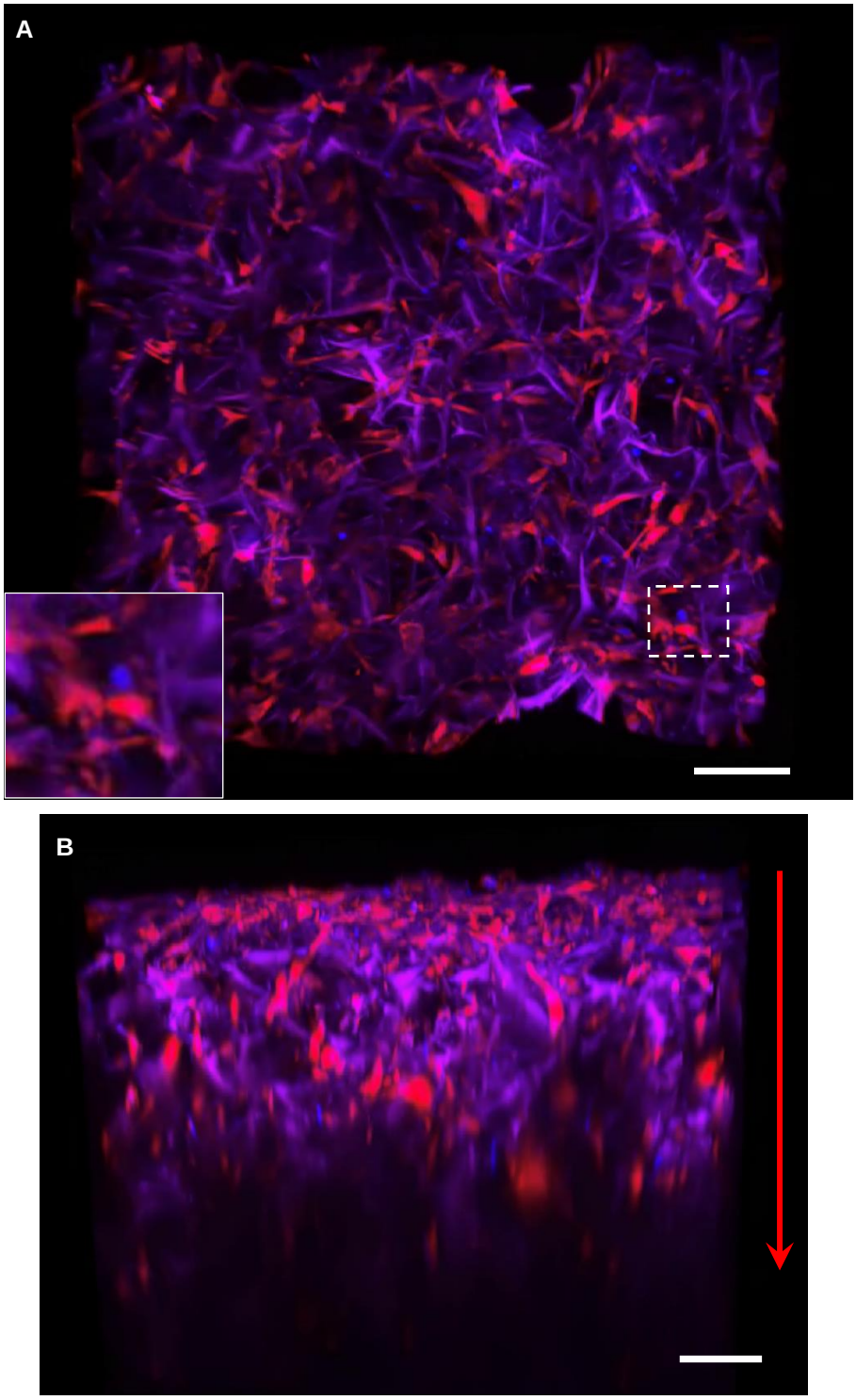

Figure 4.3. Confocal microscopy of Integra bilayer matrix disc seeded with mCherry labelled ADSCs ($1x10^4$) stained with Hoechst nuclear stain in chondrogenic medium at 18 weeks culture. (A) Analysis of the surface demonstrates easily detectable cells (magnified inset from dashed white box) widely distributed. **(B)** From the surface down (red arrow direction), mCherry cells are detected throughout the entire 600µm depth of the disc. Scale bars: 150µm. 3D media file on supplementary DVD-file M2.

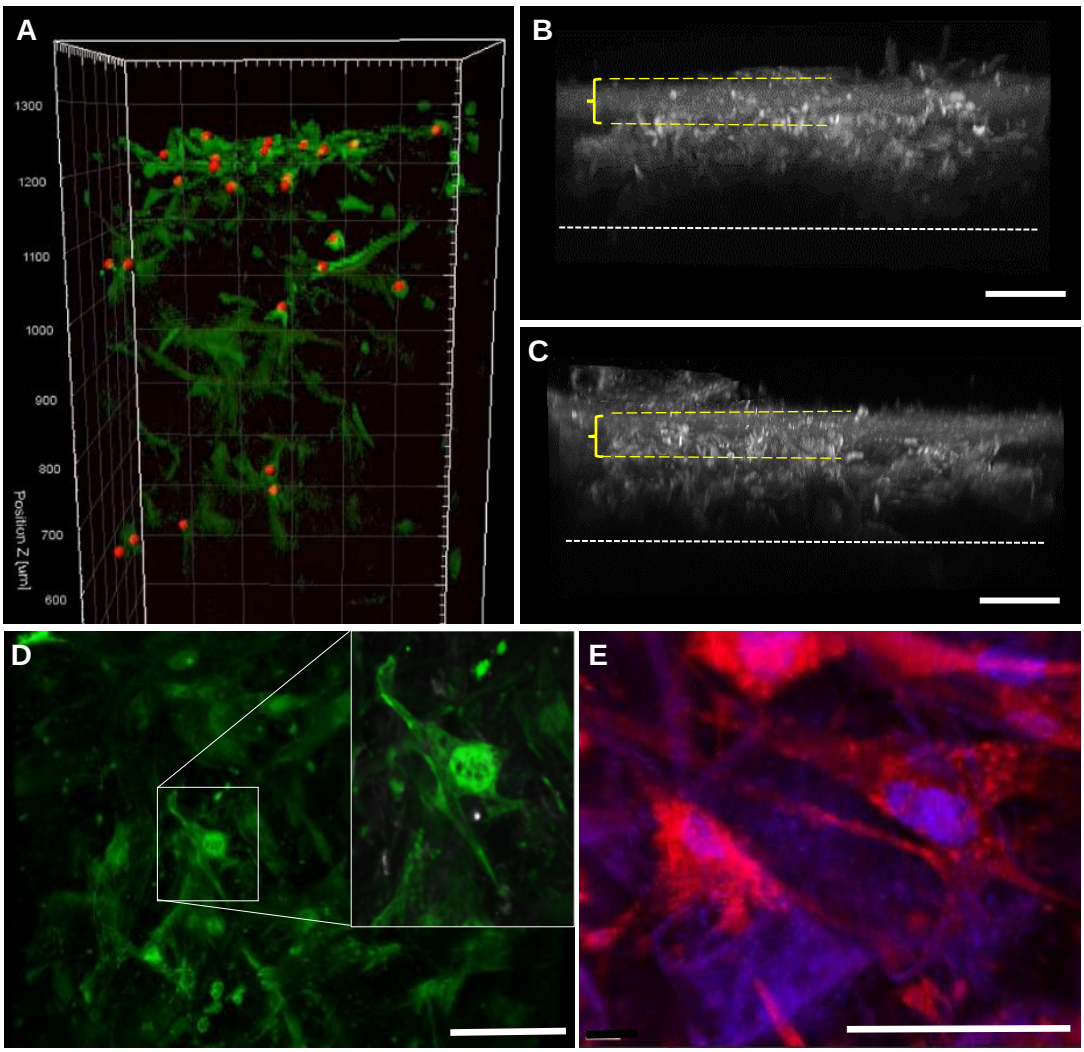

Figure 4.4. Confocal imaging of chondrogenically differentiated Integra bilayer discs. (A) 3D image (z-stack) of eGFP$^+$ Integra. Red dots highlighted using Imaris software (Oxford Instruments) with auto cell detection showing higher cell density at the first 100µm surface. Total depth of Integra approx. 600µm. **(B)** Z-Stack confocal image of eGFP$^+$ ADSC Integra disc with collagen II immunofluorescence. The top (within yellow brackets) demonstrates high expression of collagen II. **(C)** Z-stack confocal image of mCherry$^+$ ADSC. Similar appearance to (B) with higher collagen II expression at the surface. (**D)** eGFP$^+$ ADSC Integra surface. Cell morphology appears to be maintained. **(E)** Immunofluorescence staining of mCherry$^+$ ADSC Integra disc surface. Normal cell morphology with Hoechst counter staining. Scale bars: 100µm.

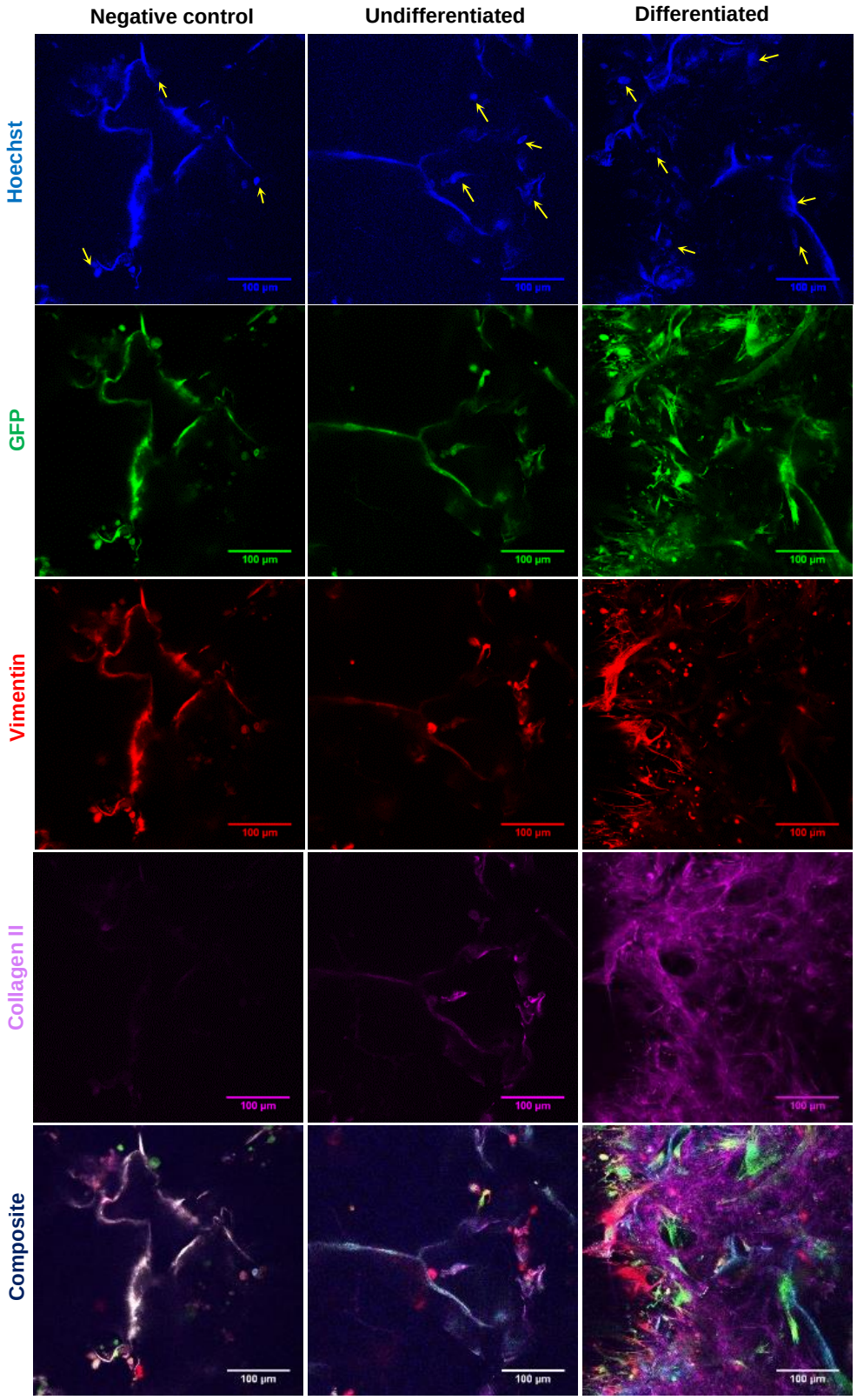

Figure 4.5. Two-photon confocal imaging at the middle depth of Integra discs seeded with eGFP^{+} labelled ADSC. Chondrogenic differentiation and undifferentiated control. Hoechst staining showing sparse cell numbers in all samples (yellow arrows). Expression of COL II demonstrated in the differentiation group. Scale bars: 100µm. (COL II image – secondary antibody Alexa Fluor 633 changed from grey to purple).

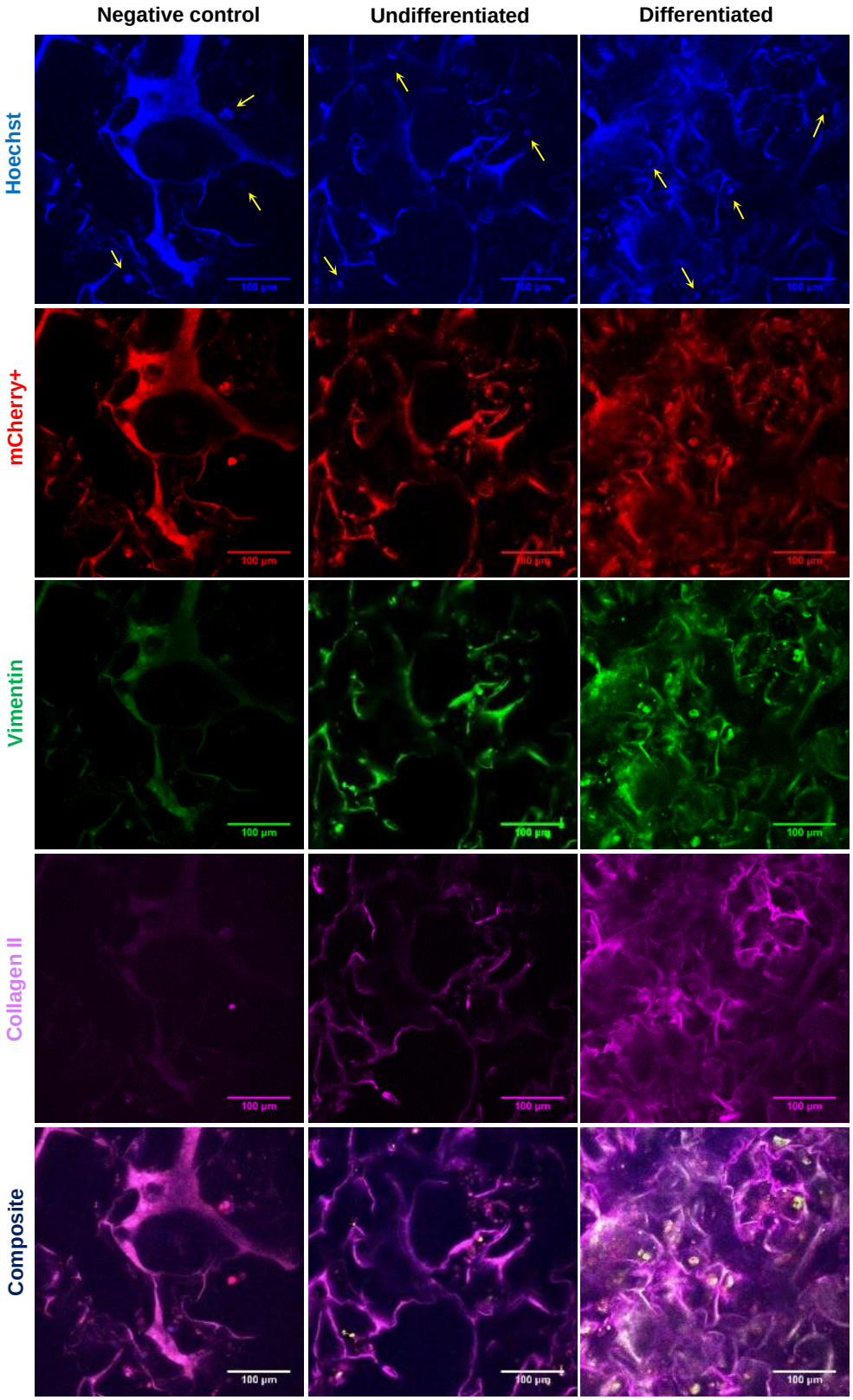

Figure 4.6. Two-photon confocal imaging at the middle depth of Integra discs seeded with mCherry^{+} labelled ADSC. Chondrogenic differentiated and undifferentiated control. Yellow arrows highlighting cell nucleus. Expression of COL II in differentiation group is high compared to controls. Scale bars: 100µm. (COL II image – secondary antibody Alexa Fluor 633 changed from grey to purple).

4.1.2 Analysis of ADSCs seeded on single layer Integra

While the silicone layer of Integra offers additional protection when used in the clinic as a skin-substitute, it may affect access of nutrients in the culture system. Therefore, the single layer Integra, that consists of the matrix layer only and is thinner than the bilayer might be more suited for cartilage generation. Hence, $5x10^5$ ADSCs (line H37 $eGFP^+$, n=2) were seeded onto 1x1cm squares of Integra single layer and cultured for a total of six-weeks in either control or chondrogenic differentiation medium. As a comparison, ear CSPCs were also seeded onto Integra at an identical density (line CH90 $mCherry^+$, n=4).

Integra matrix seeded with both ADSCs and CSPCs and cultured in control media for three weeks appeared very similar to Integra without cells. These samples remained soft, flexible and did not change macroscopically in any significant way (Fig 4.7A, B). The chondrogenically differentiated Integra single sheet appeared much more cartilage-like than the bilayer Integra seeded with $1x10^4$ cells and had changed from an unstable sheet to a rigid structure in just six weeks. Interestingly, the Integra sheet seeded with CSPCs demonstrated a significant physical change in appearance with a higher degree of contraction observed in all biological triplicate samples (Fig 4.7C). The contraction and change in shape was striking and may relate to rapid deposition of ECM and formation of an organised collagen network by CSPCs. A similar macroscopic change to the chondrogenically differentiated ADSC Integra sample was observed, with a clear change to the surface appearance (Fig 4.7D). Both chondrogenically differentiated samples were rigid enough to be held with forceps.

4.1.2.1 Live dead assay of CSPCs in Integra

Live dead assay of low passage ear cartilage derived precursor cells incubated in control medium for 7 days demonstrated high cell viability and low cell death numbers when seeded at $5x10^5$ cells in single layer Integra (Fig 4.8). Live dead assay with Integra seeded with ADSCs at identical numbers demonstrated similar results with no significant difference between the cell types (data not displayed due to covid access restriction to laboratory).

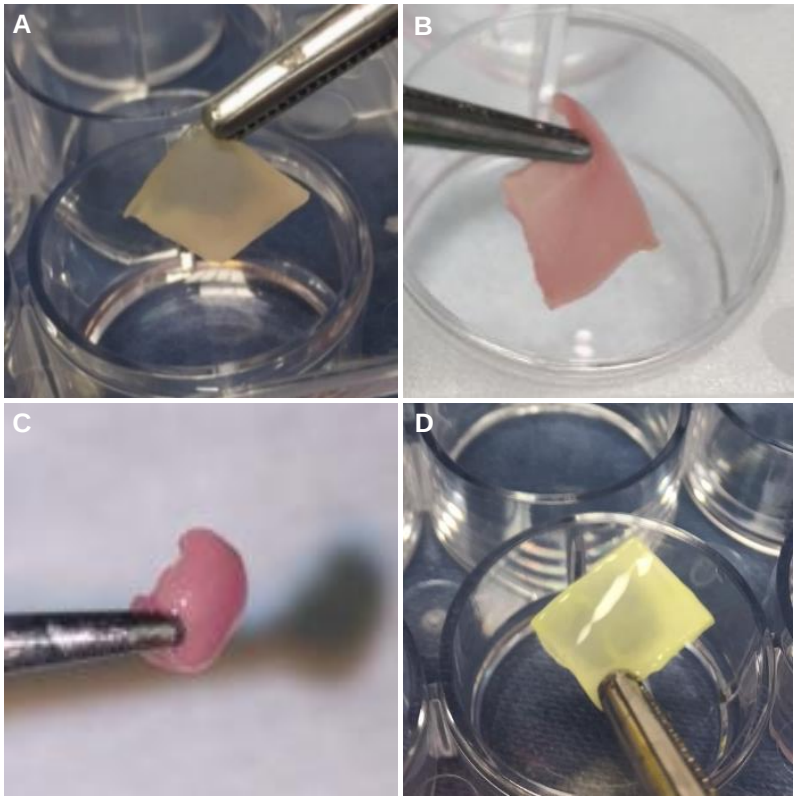

Figure 4.7. Macroscopic appearance of Integra (1x1cm squares) with and without ASDCs or CSPCs and either maintained in control or chondrogenic medium. (A) Integra without cells. Integra sheet in control culture medium remains soft and sponge like and retains its transparency. (**B)** Integra seeded with $5x10^5$ CSPCs incubated in control culture media, there is no significant change to the Integra sheet. Integra seeded with ADSC incubated in control media were identical in appearance to this CSPCs sample. **(C)** Integra seeded with $5x10^5$ CSPCs. Over a similar 6-week chondrogenic differentiation, the Integra shows significant contraction and can be easily handled with forceps without distortion **(D)** Integra seeded with $5x10^5$ ADSCs. Following chondrogenic differentiation in static medium for 6 weeks, the sheet appears opaque, feels rubber like and can be picked up with surgical forceps without distortion.

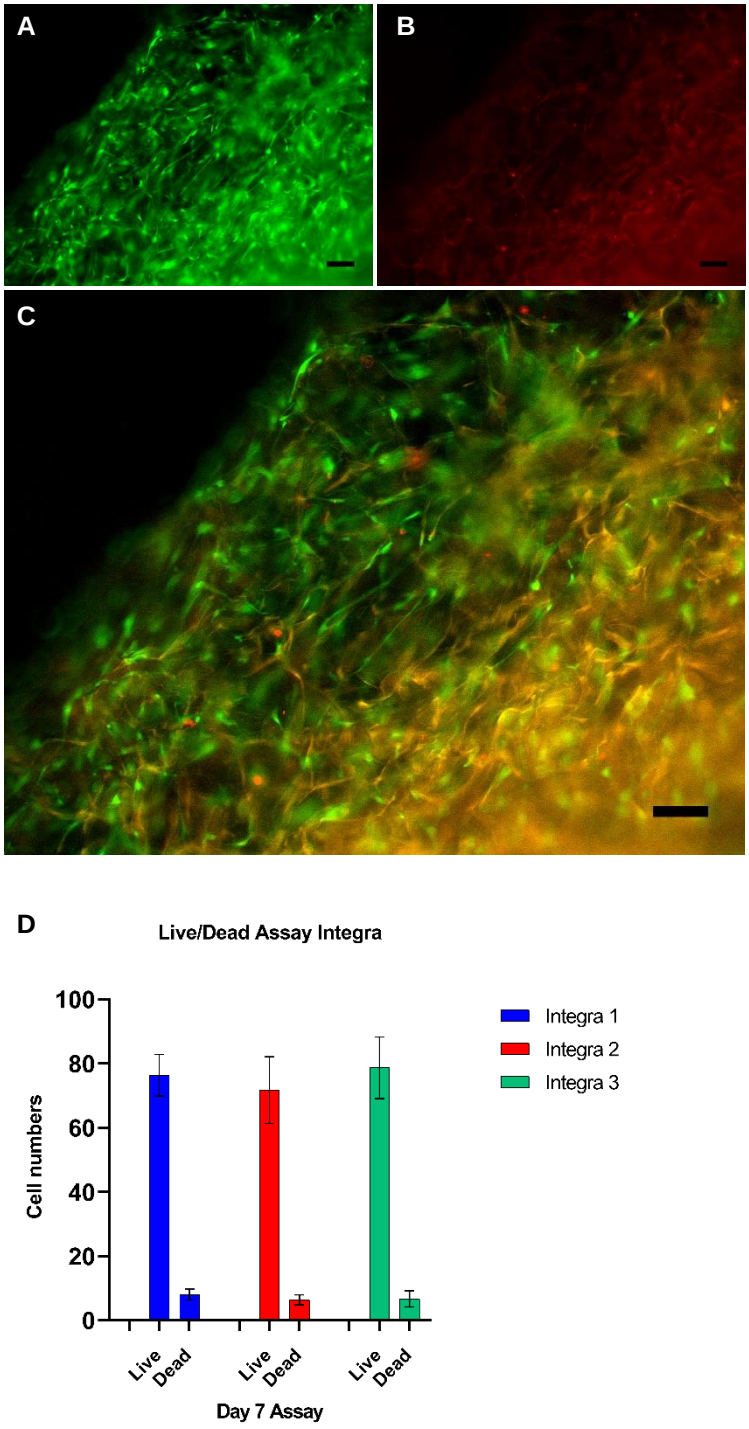

Figure 4.8. Live dead assay of ear cartilage derived precursor cells in Integra matrix at day 7 incubation in control medium. Fluorescent microscopy of surface of Integra matrix using live green **(A)** and red dead cell assay **(B)**. **(C)** Composite image showing cell viability and cell distribution at the surface. **(D)** Cell viability at day 7 from 3 different replicates at 3 random surface areas (1cmx1cm) from each. Scale bars: 100µm.

4.1.2.2 Detection of cells seeded in single layer Integra by immunofluorescence

The Integra discussed next are the same as those described in section 4.1.2, imaged at 3 weeks incubation. Confocal imaging just below the surface, at a depth of -50µm demonstrated high expression of collagen type II within the Integra matrix with both endogenously labelled cell lines ($eGFP^+$ and $mCherry^+$) cultured in chondrogenic medium (Fig. 4.9 and Fig 4.10). Despite the problem of autofluorescence within the Integra matrix, collagen II expression was clearly detected. Furthermore, individual cells were readily identified and easily distinguishable against the degree of Integra autofluorescence. Composite images enabled further easy cell detection.

As shown by imaging Integra seeded with chondrogenically differentiated cells, fewer cells are detected at depths greater than 100 µm (Fig 4.11). In contrast, at the surface there is almost a continuous network of cells. It is unlikely that the reduced cell numbers in deeper regions is due to insufficient laser penetration as the Integra matrix is still easily observed.

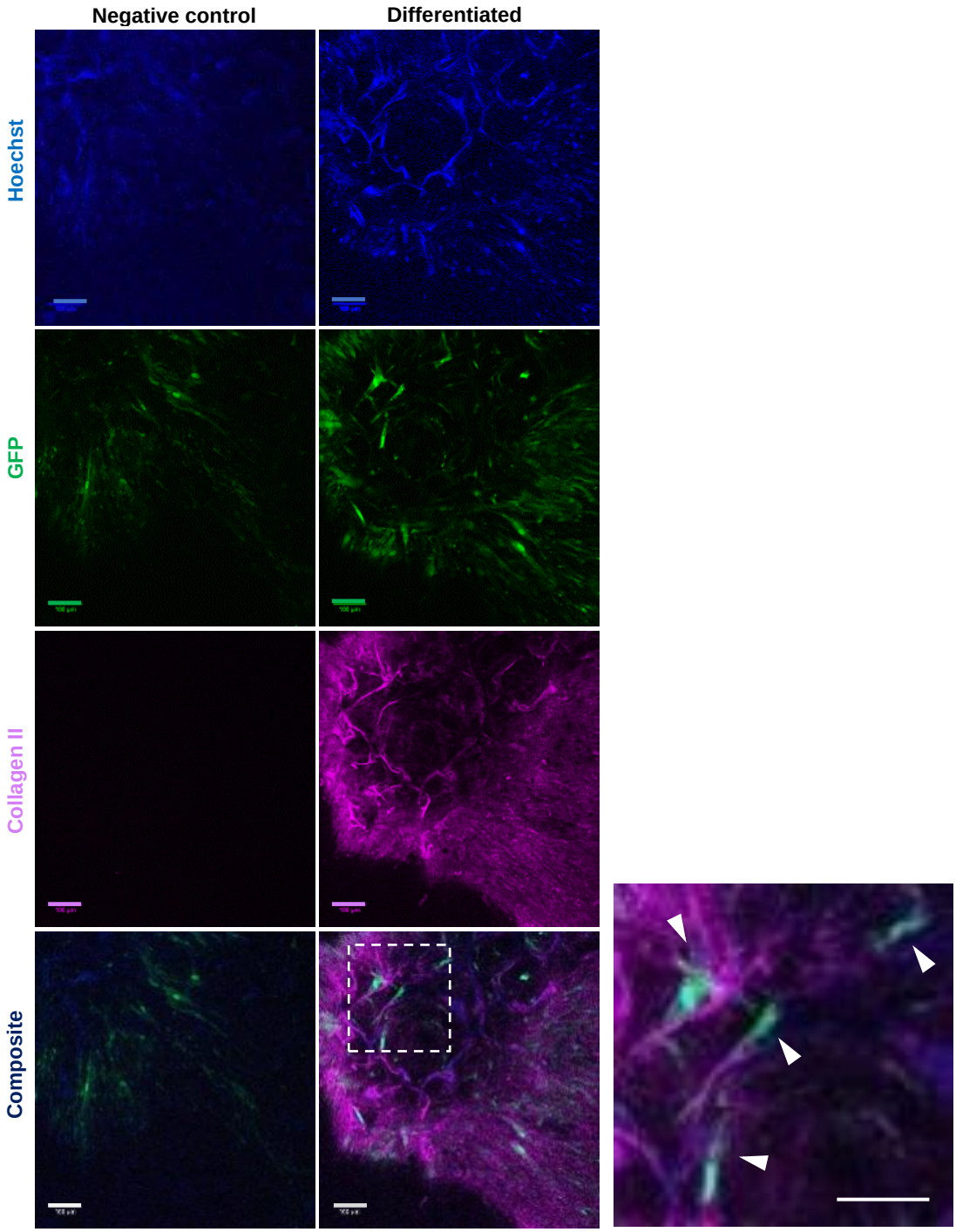

Figure 4.9. Confocal images of Integra seeded with eGFP-labelled ADSCs (H37). Immunofluorescent staining of 3 weeks static control and chondrogenically differentiated samples. Cell seeding was at density of $5x10^5$ cells/$1cm^2$. Compared to the undifferentiated control, the differentiated cells show high expression of collagen II. Cells (white arrowheads) can be identified within Integra, as more easily seen at high magnification of the dotted square within the composite image. (Collagen image-secondary antibody Alexa Fluor 633 changed from grey to purple). Scale bars:100µm.

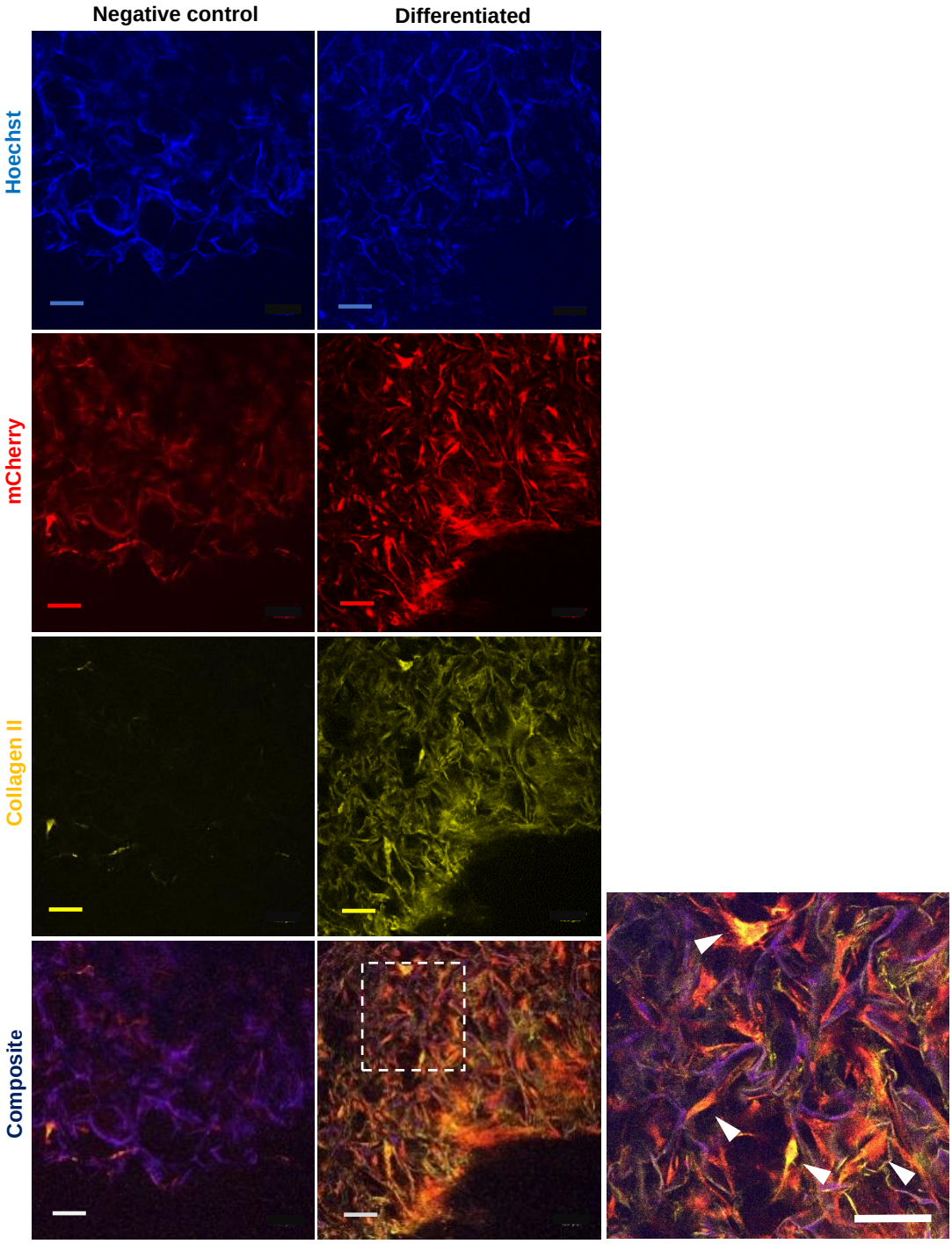

Figure 4.10. Confocal images of Integra seeded with mCherry-labelled CSPCs (Ch90) stained for collagen II. Immunofluorescent staining of 3 weeks static control and chondrogenically differentiated samples. Cell seeding was at density of $5x10^5$ cells/$1cm^2$. High expression of extracellular collagen type II is observed throughout the Integra sheet upon differentiation. Cells (white arrowheads) can be identified within Integra as seen in magnified image of dotted square within the composite image. (Collagen image-secondary antibody Alexa Fluor 633 changed from grey to purple to yellow). Scale bars: 100µm.

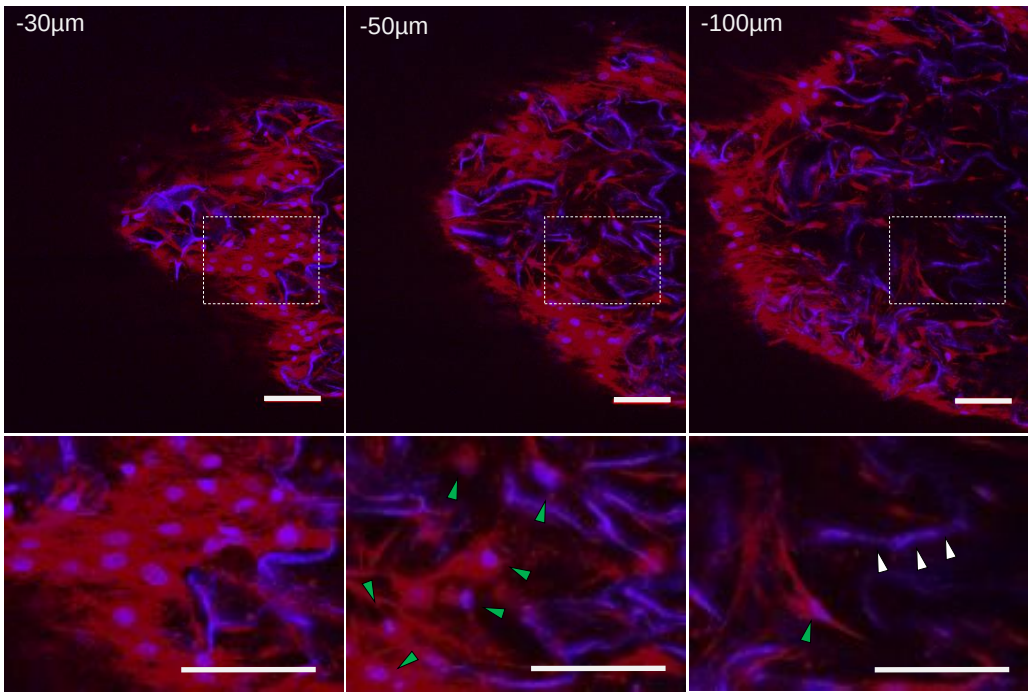

Figure 4.11. Confocal images of chondrogenically differentiated mCherry-labelled CSPCs in Integra. Cells incubated in chondrogenic medium in static cultures for 10 weeks are counter-stained with Hoechst dye (blue) to detect nuclei. Increasing depths of -30µm, -50µm and -100µm from the surface demonstrates reduced cell numbers (green arrowheads). Lower images are higher magnifications of dashed boxes. At -100 µm depth, some cells and the Integra matrix can still be seen (white arrowheads) but at deeper levels almost no cells are detected. Scale bars: 100µm.

4.1.2.3 Integra seeded with a high number of chondroblast stem/precursor cells

A further experiment was setup to investigate the effect of seeding a much higher numbers of cells ($6x10^6$, n=1) than in the previous experiments into Integra (Fig. 4.12). To aid cell penetration into the Integra after pipetting the cells onto it, the Integra disc was briefly centrifuged in a Falcon tube (see methods section 2.4.1.3 for details; Fig. 4.12A). Approximately $8.5x10^4$ were counted in the pellet at the bottom of the tube (Fig 4.12B). Therefore, the majority of the cells seeded were retained within the Integra membrane, and possibly some at the top surface of the transwell membrane. This Integra disc was then incubated in static chondrogenic media for 22 weeks.

The purpose of this experiment was to push cells deep into the Integra sheet to enhance cell distribution. Over this extended incubation, the Integra shrunk from 8mm to 5mm in diameter and a dense thickening began to develop at its surface that resembled a spheroid. This was observed after 6 weeks and by 22 weeks incubation the thickening had enlarged to approximately 2 mm in diameter (Fig 4.12C-E). This was not noted in any previous Integra experiments.

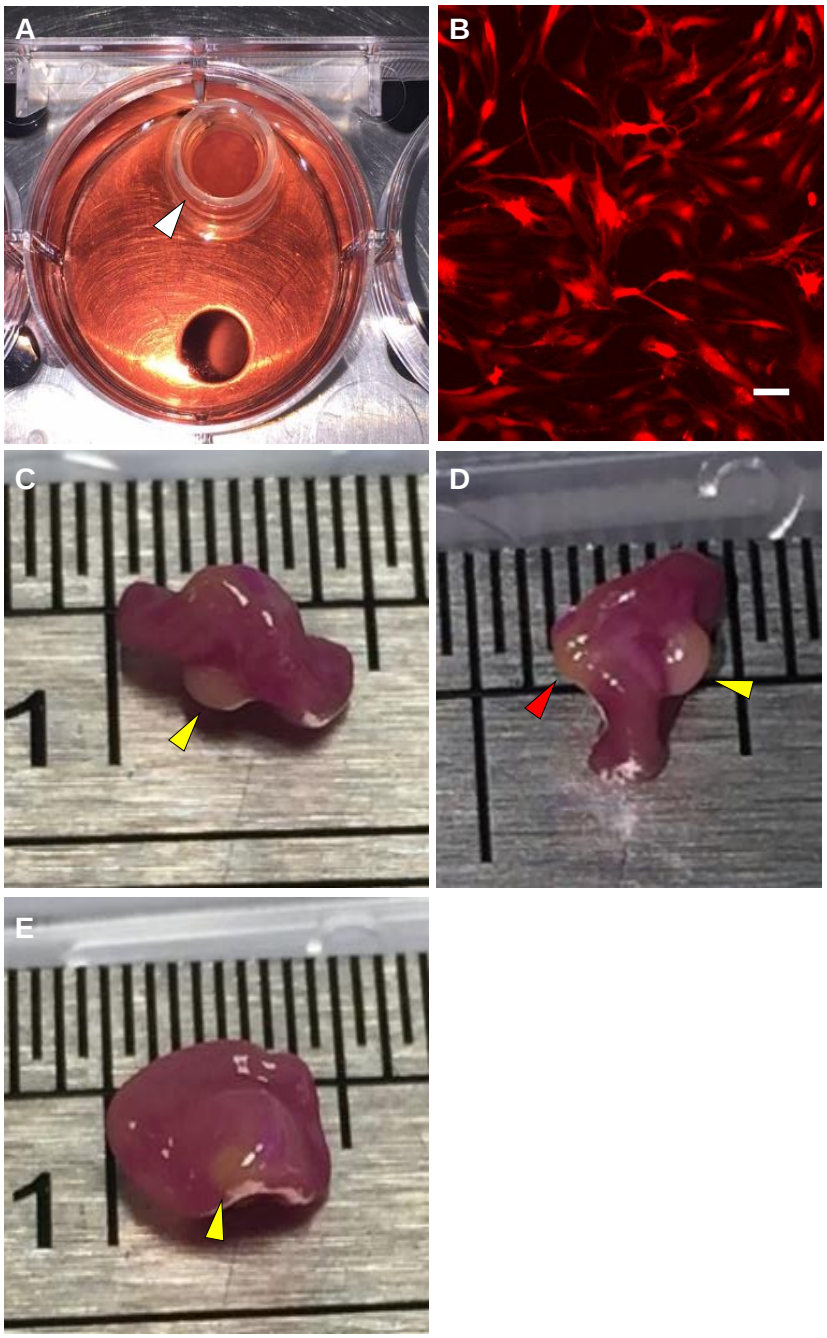

Figure 4.12. CSPC (Ch90 p13) mCherry labelled cells seeded at 6million onto Integra and spun for 30 seconds at 5000rpm. (A) 8mm Integra disc remains flat (white arrowhead) after cell seeding and rapid centrifugation within a transwell. **(B)** Inverted microscope bright field image of mCherry^{+} collected after centrifugation. **(C, D, E)** Same disc after 22 weeks incubation. The disc has contracted by approx. 40-50% and a well-formed tissue mass (spheroid-like) is noted on the surface (yellow arrowhead). A smaller second mass has also developed (red arrowhead). Scale bar in (B): 100µm. Ruler spacing is 1mm each.

4.1.2.4 Histological analysis of Integra seeded with $5x10^5$ CSPCs

From these initial Integra experiments and immunofluorescence imaging, the results suggested that Integra matrix had limitations for cell penetration, expansion and to support chondrogenesis throughout its entire thickness. The CSPCs seeded onto single layer Integra demonstrated the most contraction and physical change and therefore it appeared that these cells would be more suitable for cartilage tissue engineering than ADSCs. With this in mind, the Integra seeded with CH90 CSPCs (same samples described in section 4.1.2) were paraffin embedded and sectioned to further analyse the distribution of cells and the presence of cartilage like ECM in the differentiated and undifferentiated samples (n=4 of each) after 6 weeks incubation. Integra without cells was also paraffin embedded and sectioned as a negative control.

The appearance of native Integra matrix without cells appears as a loose matrix. There was little difference in the presence of GAG between the Integra without cells and Integra with undifferentiated cells with AB staining. H&E staining of undifferentiated cells in Integra demonstrated scanty cell number distributed mostly in superficial layers (Fig 4.13). In the differentiated CSPCs in Integra, both H&E and Alcian blue staining was mainly restricted to the superficial layers and no differentiation is observed within the Integra matrix (Fig 4.14A-D). Many more cells have been retained in the differentiated Integra compared to the undifferentiated samples. Cells appear to have condensed and formed small foci of cartilage-like ECM with increased Alcian blue staining only where the Integra has contracted and folded. The superficial regions also demonstrate increased cell density in keeping with results from immunofluorescent studies (Fig 4.14).

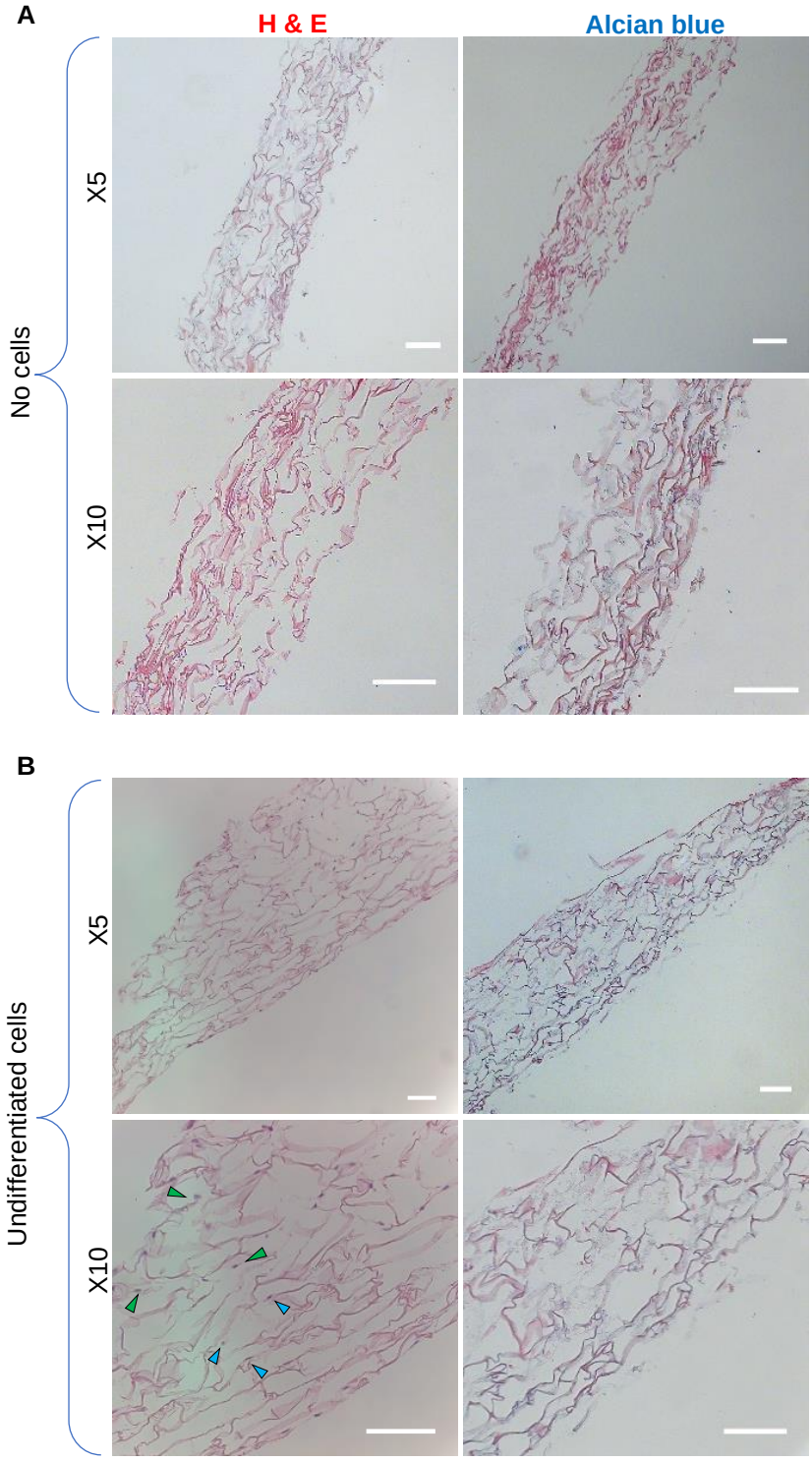

Figure 4.13. H & E and Alcian blue staining of paraffin embedded sections of Integra without cells and with undifferentiated CSPCs. (A) Integra without cells kept in control medium for the same amount of time as the seeded Integra samples. Integra appears as a loose matrix with numerous spaces. **(B)** CSPCs ($5x10^5$ cells) in Integra cultured in control expansion medium for 6 weeks. H&E detects cells throughout the thickness of the membrane, but they are rather sparse; cell in superficial regions (green arrowheads) but at greater depths (blue arrowheads) are indicated. Alcian blue staining is negative for GAGs. Scale bars: 500µm.

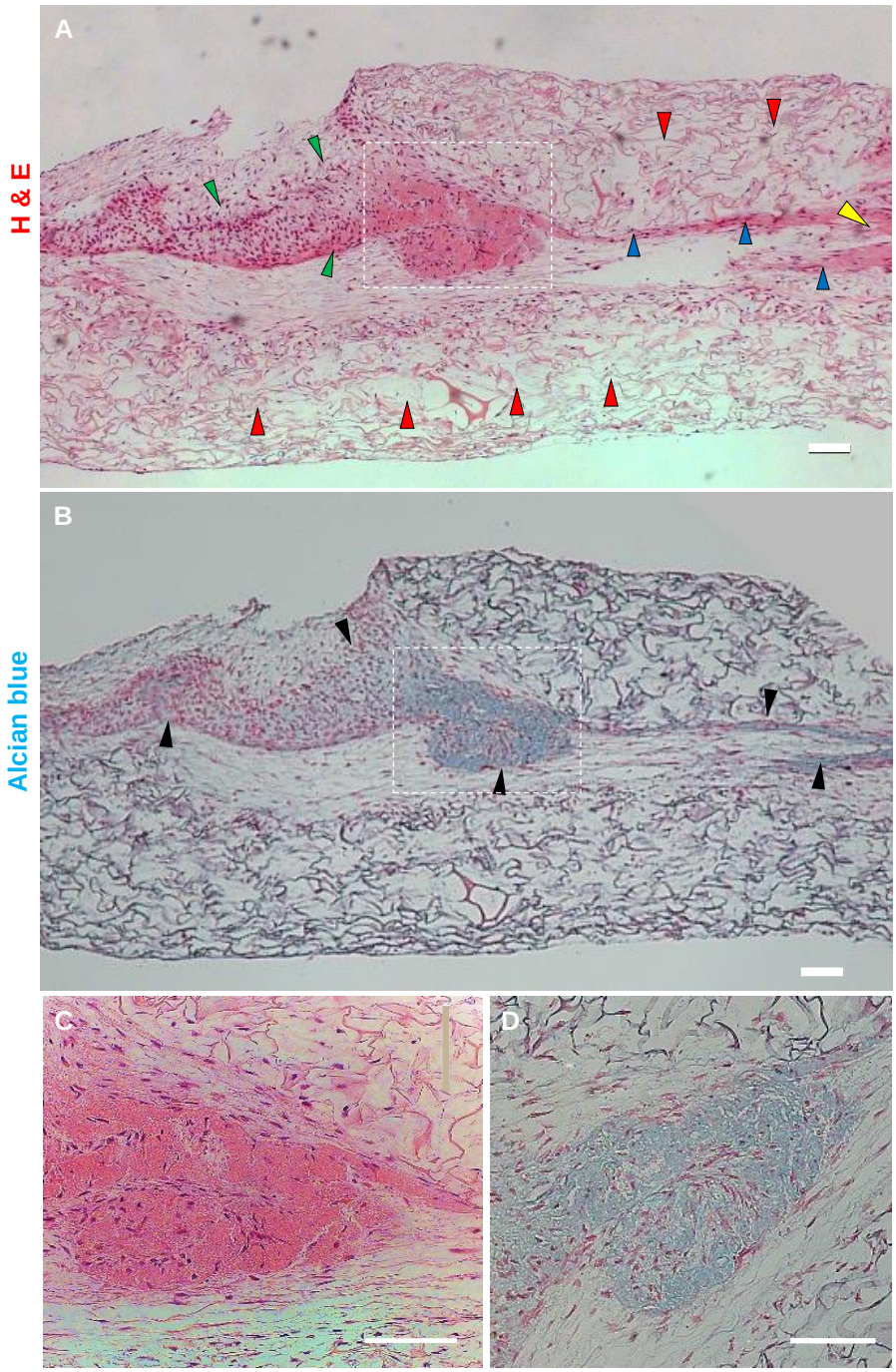

Figure 4.14. Paraffin embedded sections of Integra seeded with 5x10^5 CSPCs (Ch90) in chondrogenic medium. (A) H&E staining after 6 weeks of chondrogenic differentiated. The sheet has contracted and folded over (yellow arrowhead), the superficial regions of Integra have folded inwards and are highly cellular (blue arrowheads). Inner regions appear largely acellular (red arrowheads). High cell density appears at the inner surface where the two surfaces have become approximated and indicating a possibly enhanced environment for cell expansion and differentiation (green arrowheads). **(B)** Alcian blue staining of an adjacent section from the same Integra sample demonstrating increased GAG`s (black arrow heads) at the surface and core regions. **(C, D)** Magnified images of dotted boxes in (A) and (B). Scale bars: 100µm.

4.1.2.5 Histological analysis of Integra seeded with $6x10^6$ CSPCs

The experiment with $6x10^6$ CSPCs seeded onto integra and spun in a centrifuge demonstrated interesting histological appearance after 22 weeks in chondrogenic medium. Consistent with all other Integra samples seeded with cells and chondrogenically differentiated in other experiments, the cells here preferentially coalesce/attach on the surface to form a clear band of tissue around the Integra (Fig 4.15). In this experiment, the mass noted macroscopically appeared similar to a spheroid when stained with H&E and Alcian blue staining. Within this spheroid, the cell morphology and histology appeared very cartilage-like with organised ECM resembling that of native hyaline cartilage with expression of GAG at the deeper regions surrounding the mature chondrocytes. A clear difference is observed in central regions with mature chondrocytes within lacunae. In some areas, the periphery of the cell condensation as well as the edges of Integra demonstrated a well-defined layer of cells that appeared akin to perichondrium (Fig 4.16).

Unfortunately, this expression of GAG was not seen in any deep regions within Integra itself and again provided some further evidence of the limited cell expansion and differentiation within Integra despite seeding high cell numbers and extended incubation period.

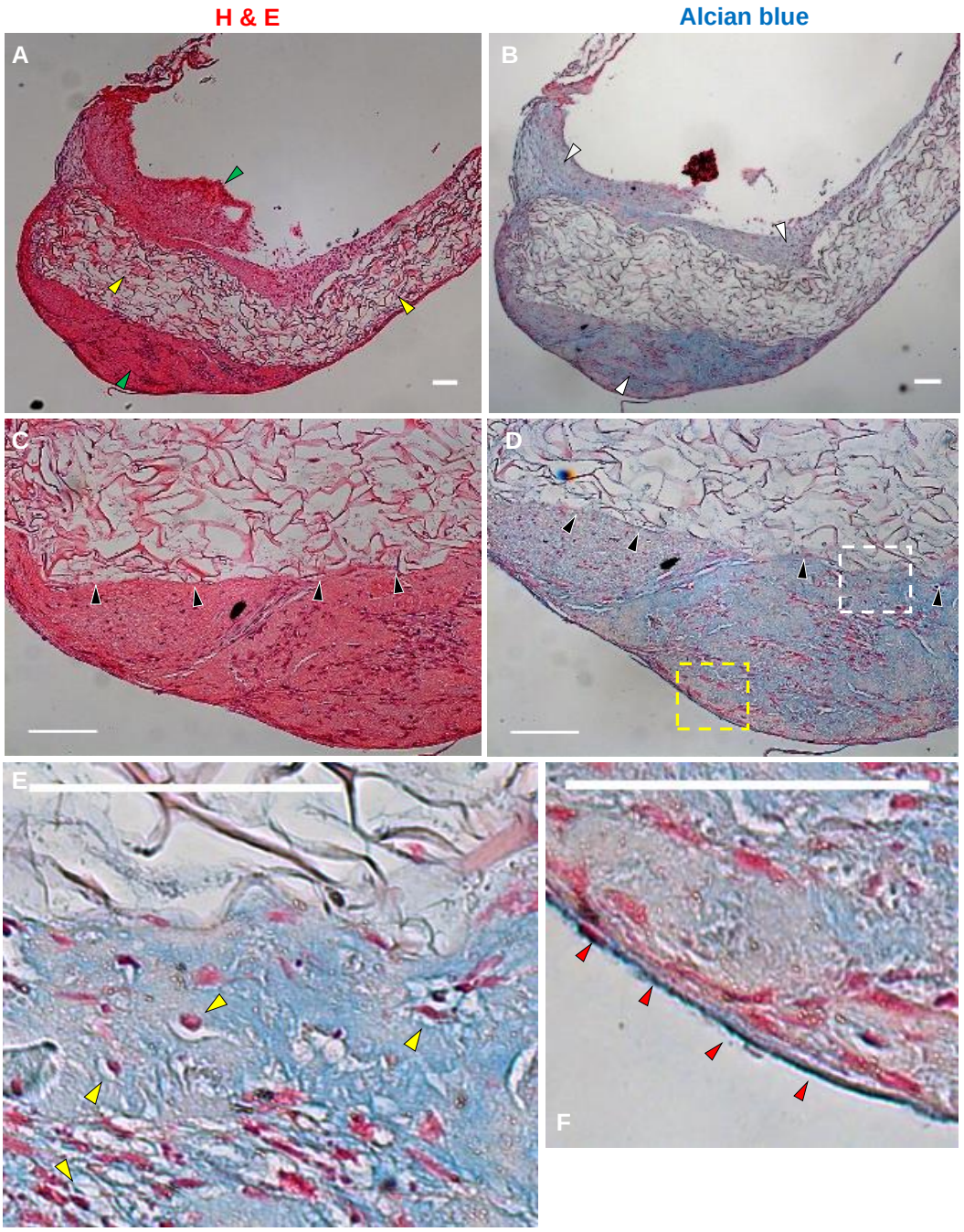

Figure. 4.15. Integra with CH90 CSPC. Paraffin embedded section stained with H&E and Alcian blue. (A) Low magnification of integra showing high cell density attached to the Integra (green arrowheads), the deeper Integra matrix remains to be sparsely cellular (yellow arrowheads). **(B)** Alcian blue staining demonstrating expression of GAG within the cellular regions (white arrowheads). **(C, D)** Higher magnification demonstrating clear distinction between cell condensation regions and Integra (Black arrowheads). **(E)** Magnification of white dotted square in (D) showing cells with lacunae. **(F)** Magnified image of yellow box in D showing cell alignment mimicking perichondrium at the periphery of dense cellular regions (red arrowheads). Scale bars: 100µm.

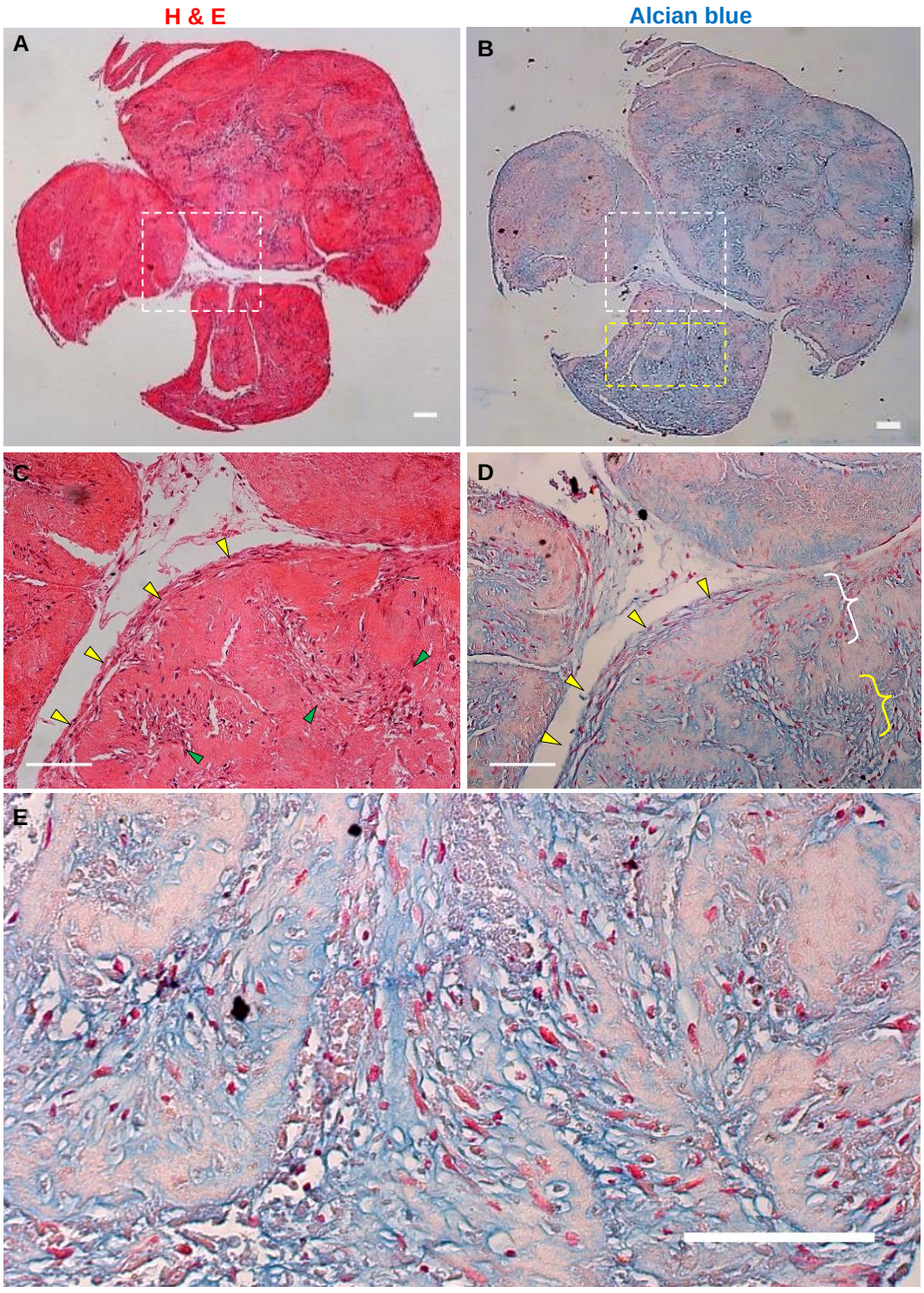

Figure 4.16. Spheroid-like masses at the surface of an Integra matrix with CH90 CSPC in differentiation medium incubated for 22 weeks. Paraffin embedded sections stained with H&E and Alcian blue. (A, B) Low magnification of spheroid like tissue growth on Integra. **(C)** Magnified images of dashed boxes in (A). The separate and well aligned layer of cells surrounding the cell mass appears almost perichondrial like and is clearly identified (yellow arrowheads), also observed in (D)**. (D)** Magnified image of white dotted square in (B)**.** Two distinct layers are observed with difference in cell morphology with mature looking chondrocytes in deeper layers (yellow bracket) compared to the flat cells found in the superficial regions (white bracket). **(E)** High magnification of yellow dotted box in (B). Mature chondrocytes with lacunae are easily identified in this region surrounded by positive GAG staining. Scale bars: 100µm.

4.2.3 Characterisation of Integra grafts on CAM in-vivo model

Clinically, Integra matrix in situ is replaced by granulation tissue and epithelium around 3 weeks' time post operatively. In this experiment I wanted to assess broadly whether native chick cells infiltrate the Integra sheet and increases its degradation as compared to maintenance in static media.

4.2.3.1 Integra on CAM – macroscopic appearance

Integra sheet samples (n=3) were grafted onto chick chorioallantoic membrane (CAM) as 2mmx2mm samples using the standard protocol (chapter 2 section 2.5). The aim was to use the CAM as an experimental platform to study blood vessels formation into and around the Integra and to characterise any morphological changes within the Integra. Integra matrix with (CSPCs mCherry^{+} CH90) and without cells were grafted. Eggs grafted with Integra seeded with cells did not survive and the specific cause of the chick death was undetermined. The CAM grafts with acellular Integra were harvested at day 14 development, washed in PBS, fixed in 4%PFA overnight (Fig 4.17). In all samples (n=3) Integra sheets were encircled by blood vessels. In regions were the Integra had not adhered to the CAM they were dark and visibly dry.

4.2.3.2 -Integra on CAM – histological analysis

Paraffin embedded blocks were cut into 5µm sections and stained with toluidine blue and picrosirius red staining. Native Integra matrix stained intensely with toluidine blue and picrosirius red (both brightfield and polarised). At high magnification, dense cellular infiltrate was demonstrated with strong nuclear toluidine blue staining. Picrosirius red staining of the same region demonstrated absent collagen fibres but intense yellow staining which is often found in picrosirius red myocyte staining. They may also represent monocytes or macrophages, but further cell specific staining would be required to identify these cells (Fig 4.18). Interestingly, the region above this cellular infiltrated shows patchy collagen staining in both brightfield and polarised microscopy suggesting that the either the Integra sheet has been fragmented or possibly new collagen deposition has been deposited by host cells, or a combination of the two (Fig 4.19). Despite this, the majority of the grafted Integra retained its normal appearance after 7 days in the CAM and very few cells were seen within the Integra sheet.

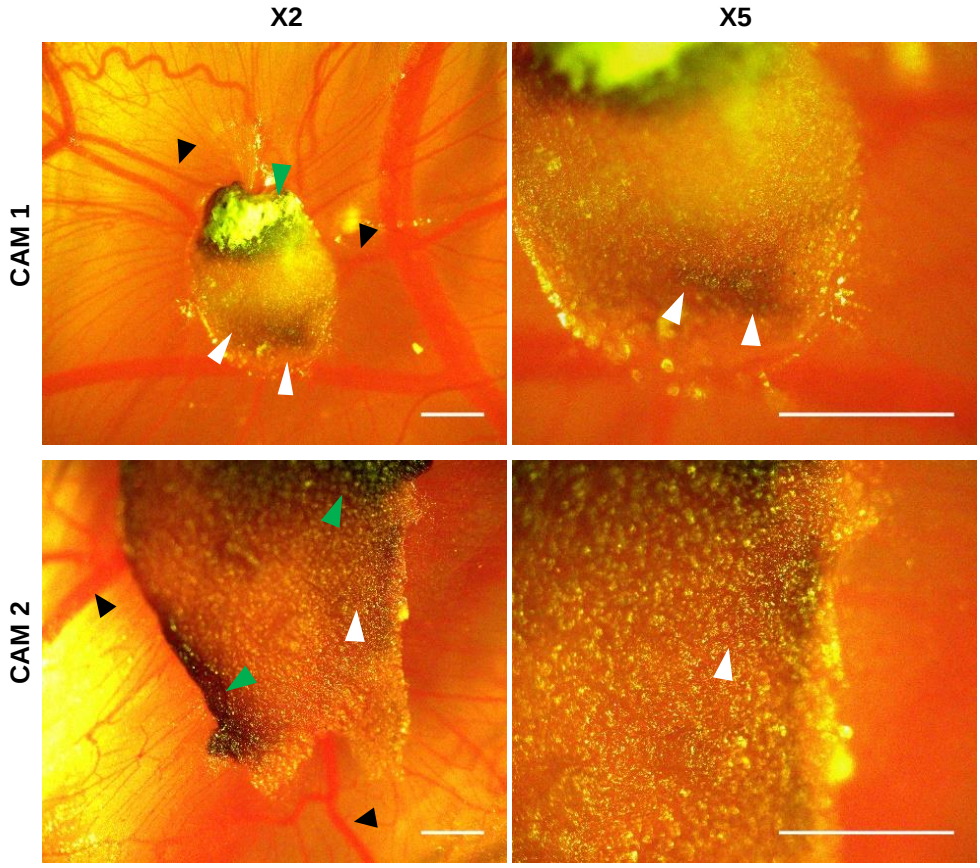

Figure 4.17. In ovo images of Integra CAM grafts at day 7 implantation at low and higher magnification. Well-developed vasculature surrounding the Integra is observed (black arrowheads) in all samples. Integra regions deeply embedded in the CAM appear darker and highly adherent to it (white arrowheads). Some peripheral regions that are not stuck to the CAM appear dry and black (green arrow heads). Scale bars: 1000µm.

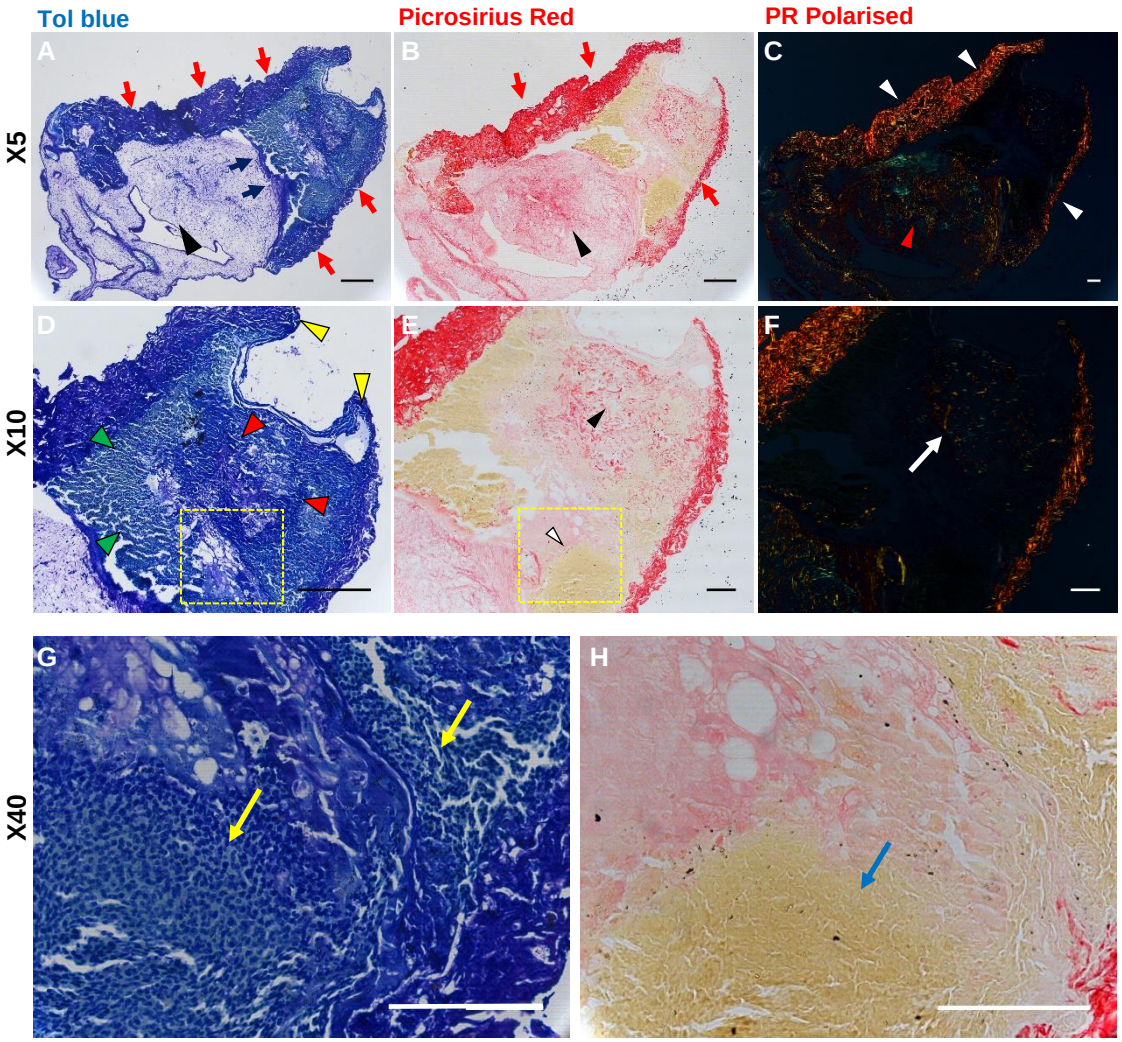

Figure 4.18. Brightfield polarised microscopy of CAM grafted Integra sheet without seeded cells stained with toluidine blue and picrosirius red. (A) Low magnification image of Integra (red arrows) with underlying CAM (black arrows). **(B)** Picrosirius red staining demonstrating collagen within the Integra (red arrows) and the CAM (Black arrowhead). **(C)** Polarised light microscopy showing yellow-orange birefringence of collagen fibres of Integra (white arrowheads) and deeper areas within the CAM (red arrowheads) which also demonstrate green collagen birefringence. **(D)** An apparent break in the Integra at the surface (yellow arrow heads) with remnants at deeper levels still present (red arrowheads) beneath which a dense cellular infiltrate is observed. **(E)** A region of collagen fibres is demonstrated on picrosirius red staining representing either the remnants of the Integra or new collagen deposited, also confirmed by polarised microscopy (F). **(G, H)** High magnification images of boxed region in (D, E) demonstrating dense cellular infiltration (yellow and blue arrows) above the CAM and within what should be the native Integra. Scale bars: 100µm.

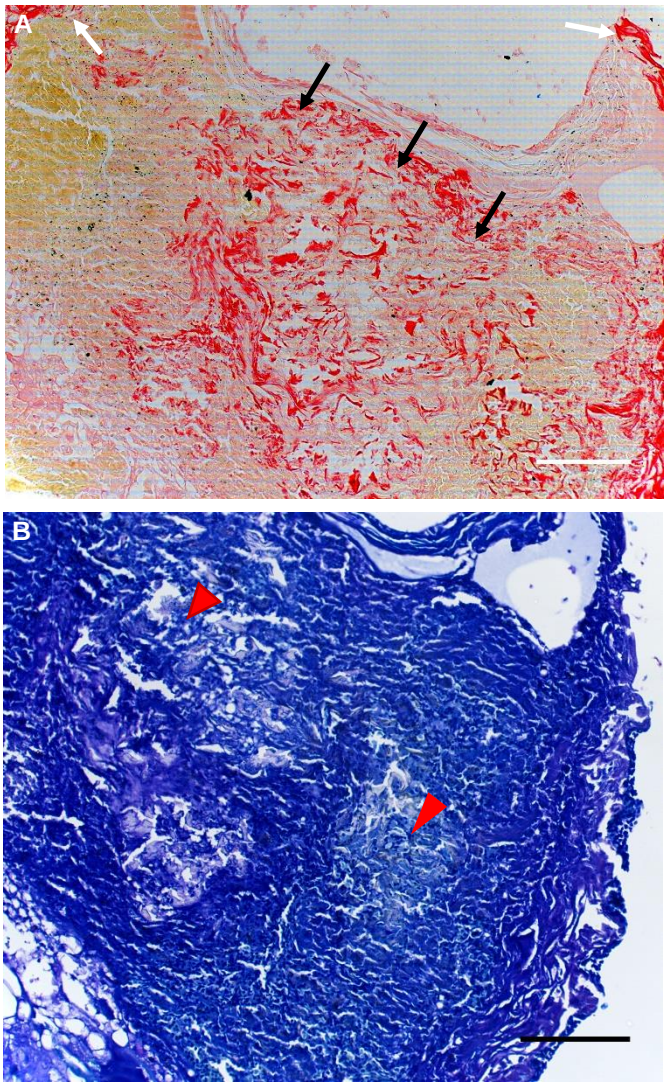

Figure 4.19. Brightfield polarised microscopy of CAM grafted Integra sheet without seeded cells stained with toluidine blue (A) and picrosirius red (B), (magnified image Fig 4.21). Black arrows highlighting presence of collagen between the two ends of Integra (white arrow) suggesting that Integra has fragmented in this region with cellular infiltration (red arrowheads). Scale bars: 100µm.

4.2.4 Pocket design and printing

The concept of the pocket design relies on a tissue engineered cartilage central region which has been pre-differentiated and matured in vitro to a degree that will allow it to be inserted into a “pocket” which would provide purely mechanical support once inserted between the 2 mucosal layers of the nasal septum (Fig 4.20A-D). Once grafted into the patient, the central cartilage region will mature further in time as it becomes integrated and has a supply of nutrients through vascularisation. The size of the pocket design can be estimated clinically or ideally based on CT or MRI imaging. The dimensions of the cartilage product can then be custom made and patient specific, but fabrication of a pocket graft could also be easily processed without any imaging and made available in a small range of sizes based on average septal dimensions.

4.2.4.1 Three-dimensional printing of PolyLacticAcid (PLA) scaffold.

The initial pocket design was based on septal anatomy so that the pocket width was at least 1.5mm in thickness with 1mm thick abutting walls resulting in a total thickness of 3.5mm. This would allow surgeons to handle the product easily and provide enough rigidity to support overlying soft tissue drape. Further design considerations were the inclusion of holes in the walls of the pocket to allow vascular perfusion to the central engineered cartilage core. The easiest and most predictable method of doing this was to incorporate a mesh design rather than pores. Mesh style printing would be achievable with a 3D printer. Preliminary designs are shown in Fig 4.21A-D. Designs were then 3D printed using a Makerbot replicator 3D printer (MakerBot Industries, Brooklyn, NY 11201 US) as described in chapter 2, section 2.6.2. Printing with PLA even at low resolution produced good shape print fidelity and mesh holes (Fig 4.22).

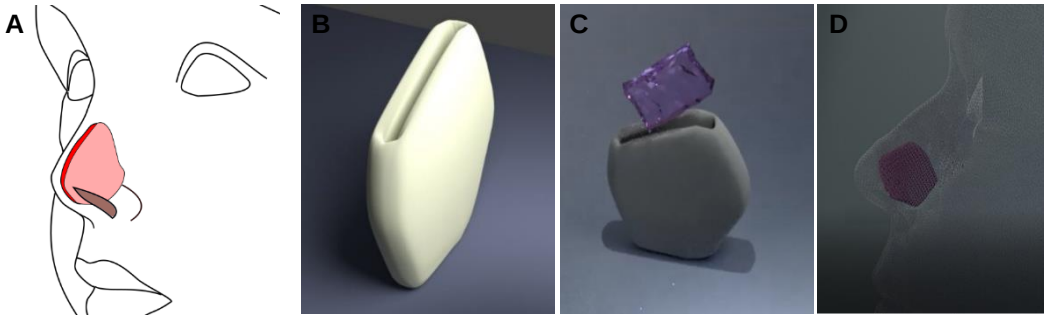

Figure 4.20. Pocket design concept. (A) The septal cartilage product dimensions can be estimated clinically or ideally by CT. **(B)** Pocket is then 3D printed using a biodegradable material. **(C)** The bioengineered cartilage core (Integra sheet) is inserted into the pocket following pre-differentiation in vitro**. (D)** The product is then inserted into the nose to reconstruct the missing septum.

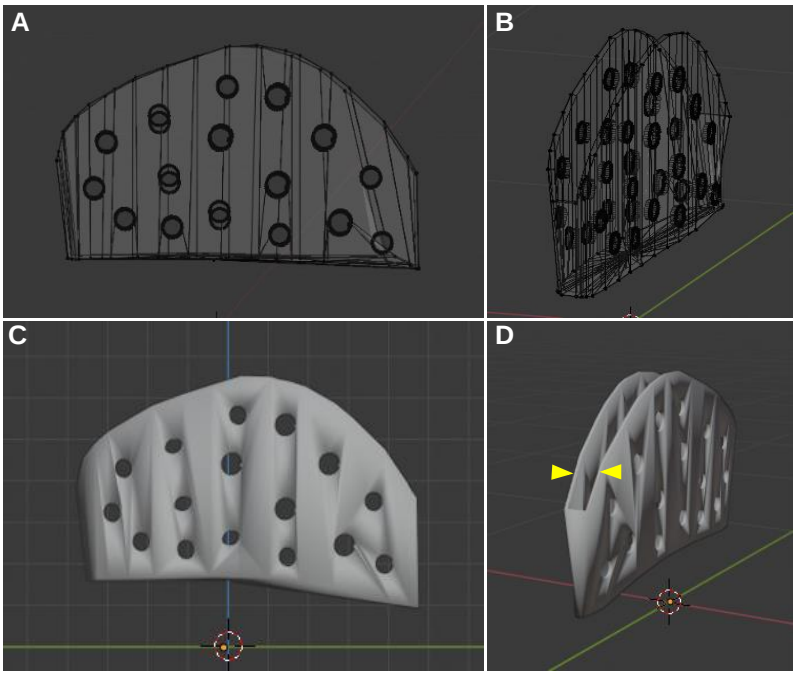

Figure 4.21. Pocket designs with holes. (A, B) Wireframe image**.** The shape and size of the pocket can be designed to be custom made for individual patients' septal size. **(C, D)** Solid object view. The mesh hole sizes can be adjusted easily in any random or organised pattern. The width is a maximum of 3mm to allow easy insertion in between septal mucosa (yellow arrowheads).

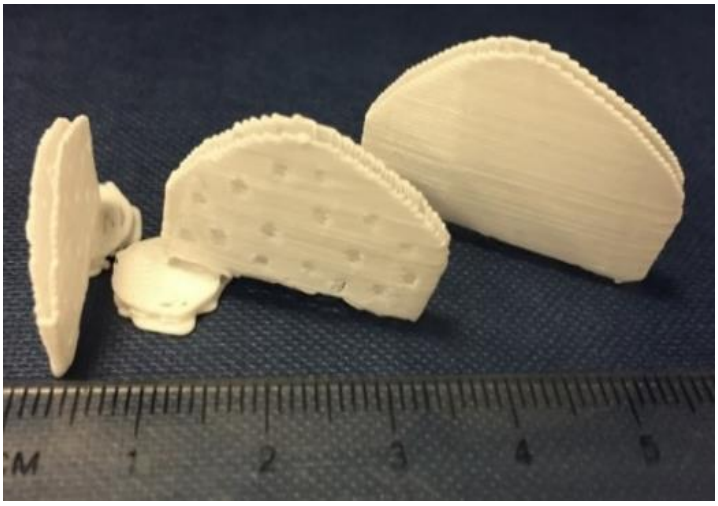

Figure 4.22. Photograph of PLA septal pockets printed with PLA filament to full scale. Pockets with and without holes were printed with good fidelity.

4.2.4.2 Assessment of ADS behaviour in combined PLA and Integra sheet

Initial experiments with PLA were undertaken to analyse how cells seeded into the integra would interact with the PLA (3D printed square shaped constructs) and to observe if cells would migrate through the integra and through the meshed PLA or solid print PLA. This would give an indication if cells would migrate out through the PLA into surrounding native tissue even without pores or a meshed surface. PLA squares were printed in the method described (chapter 2 section 2.9.1.1) at 80% infill density with solid walls. Twelve constructs were printed at the same time to achieve many samples of the same print quality. Even at 80% infill, there appeared to be clear channels between the PLA printed filament of approximately 100µm width but with areas of variation (Fig 4.23). To enable easy identification of cells, eGFP+ labelled ADSC (H37 p8) cells were seeded onto the Integra at $5x10^5$ number of cells. As described in section 2.9.1.2, PLA squares were disinfected with ethanol 70% and then washed with PBS before the Integra was applied on top Fig 4.24A-B). Cells were then seeded onto the Integra and each construct moved to the well of a 6 well plate.

After 24 hours, the Integra, the PLA square and the plastic beneath were imaged to assess cell attachment and migration (Fig 4.24C). Cells were detected within the Integra and attached to the PLA in all regions. Furthermore, some cells had migrated through the PLA holes and had attached and expanded on the culture plate plastic.

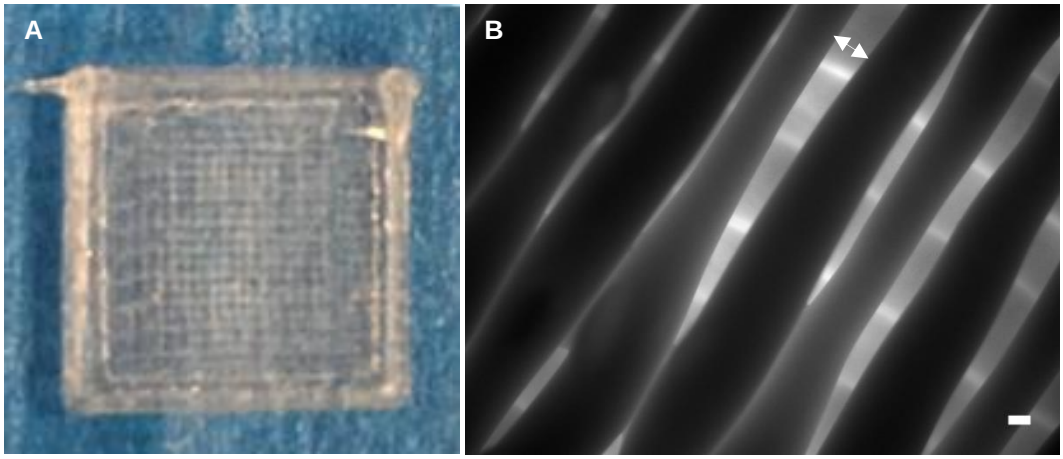

Figure 4.23 PLA squares printed at 10x10x1mm dimension with 2-layer print at 80% infill density. **(A)** Macroscopic appearance **(B)** Brightfield microscopy showing variable sized spaces between PLA printed filament some of which are over 100µm (white arrow) which should allow cells to move into and out of the PLA surface. Scale bar: 100µm.

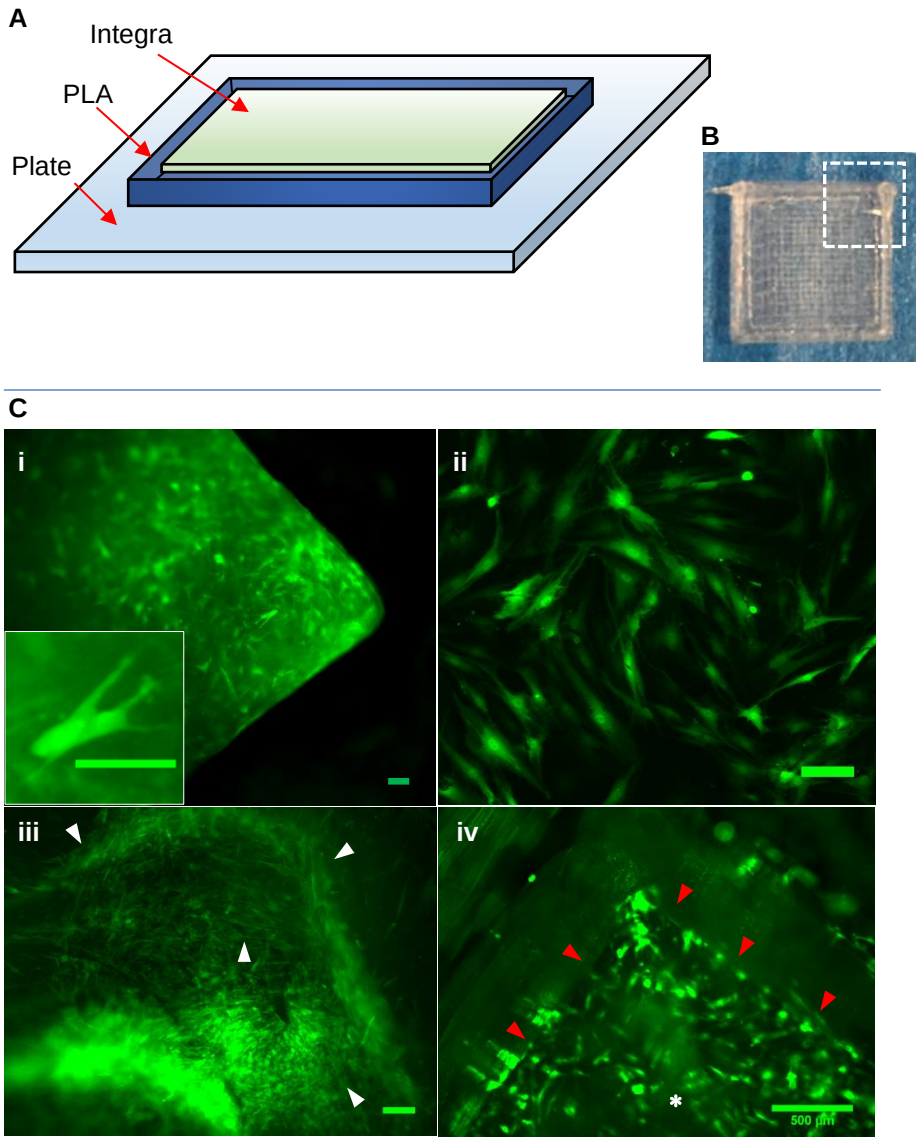

Figure 4.24. Assessment of eGFP-labelled ADSC (H37 P8) migration through Integra and PLA square 24 hours after seeding. (A) Schematic drawing of the position of integra in relation to the PLA. **(B)** Printed PLA construct; the white dotted box highlights the corner of the PLA that represents the images in (C). **(C)** Fluorescent microscopy (live images) of the Integra sheet seeded with eGFP^{+} cells showing homing of cells in the sheet (i). Image of the bottom of the well shows cells that have migrated through the Integra and the PLA have attached and expanded onto the plastic (ii). Image of the corner of the PLA square shows presence of cells attached to the PLA (white arrowheads) (iii). Cells have attached at central regions of the PLA construct (red arrowheads) (iv). All scale bars 100µm except C iv which is 500µm.

The next step was to establish as proof of concept how easily Integra sheets seeded with cells could be placed into PLA pockets.

Integra was seeded with ADSCs (H37) or cartilage derived precursor cells (CH90) both at $1x10^6$ cells and were inserted into PLA 3D printed pockets after 3 weeks incubation in chondrogenic medium. Insertion of Integra into these pockets proved to be very difficult as manipulation of the Integra sheets into a small narrow (1-2mm) pocket was not easy and resulted in some damage to the sheet. Uniform flat placement of Integra into the pocket was not reliably achieved. Insertion of the Integra sheet into the pocket proved to be difficult as the pre-differentiated Integra had curled at the edges and therefore could not be laid flat and inserted down to the floor of the pocket. A further problem was regions of voids where the Integra was not in direct contact with the PLA pocket wall. Horizontal contraction of the Integra resulted in horizontal deficiency within the pocket even when it was inserted fully. This was the same problem in the vertical dimension.

If the Integra achieved a higher level of mechanical stability and cartilage maturation, then it may be possible to withstand the manipulation into the pocket. However, with the tendency of Integra to curl up once ECM has been deposited at the surface (with chondrogenic differentiation medium), insertion into the PLA pocket was unsatisfactory (Fig 4.25). Integra sheets seeded with cells incubated in control medium remained flexible and attempts to insert them into PLA pockets were also difficult as the integra began to tear.

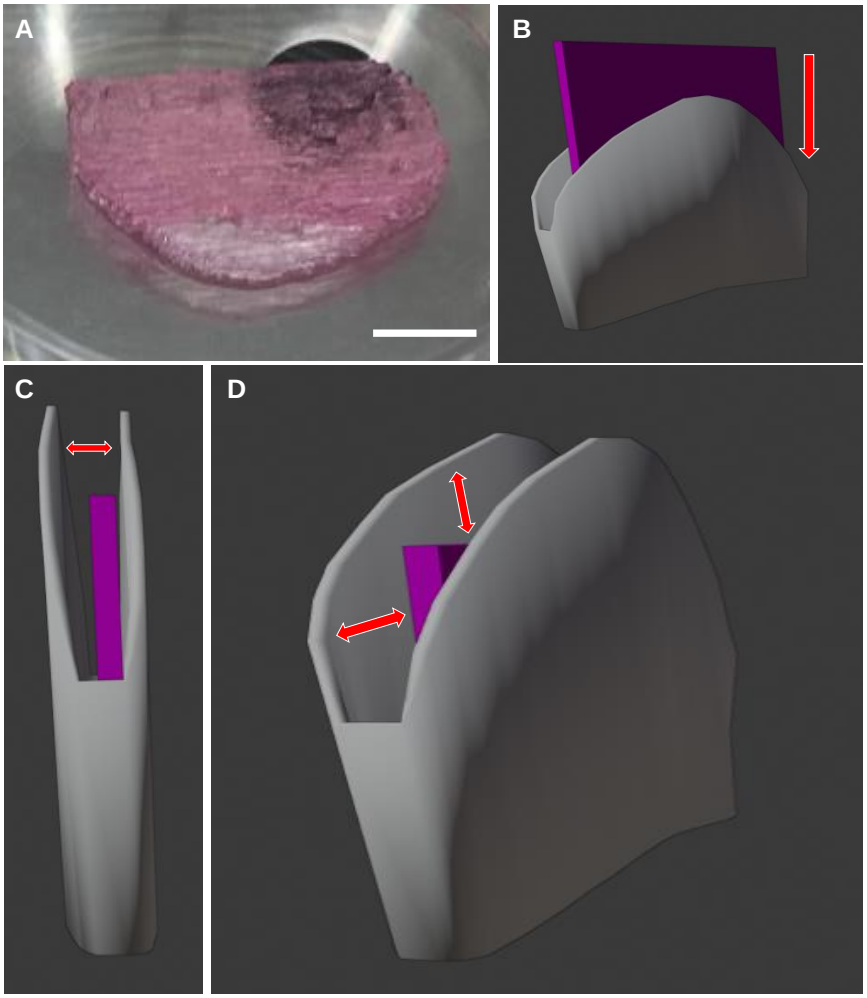

Figure 4.25. Integra insertion into PLA pocket. (A) PLA pocket in 6 well plate- the cavity width is 1.5mm. **(B)** Drawing showing the technique used to insert the Integra sheet into the pocket. **(C)** Drawing showing regions of voids that form where Integra is not in direct contact with the PLA pocket wall. **(D)** Drawing showing contraction of the Integra and consequent incomplete filling of the pocket. Scale bar: 1cm.

4.3 Discussion

Integra dermal regeneration template has been successfully used in clinical practice for over 30 years for wound healing in burn patients (FDA approved in 1996) and for skin cancer reconstruction. In patients, studies have shown that Integra is slowly replaced by fibroblasts, vascular channels, and collagen bundles (Lee et al., 2015). As a novel approach to generating cartilage, I was interested in exploring the potential of Integra to support cell viability, expansion and ultimately provide a chondrogenic inductive environment for cartilage ECM deposition.

To my knowledge this is the first study that has characterised the behaviour of human ADSCs and CSPCs in Integra dermal regeneration template, and their ability to produce cartilage like tissue within Integra matrix. The results indicate that human ADSCs and CSPCs can produce cartilage like tissue when incubated in chondrogenic medium when seeded into Integra matrix. This was evaluated after short 6 week and extensive (up to 7 month) incubation times and assessed by histology for GAG and collagen content and immunofluorescent staining for collagen II expression. Chondrogenically differentiated Integra samples all displayed increased collagen II expression when compared to controls. However, immunofluorescent staining with confocal microscopy demonstrated higher cell densities at the surface of samples and collagen II deposition limited to upper regions of the Integra. Even at higher cell density seeding ($6x10^6$), similar distribution of cells, collagen and GAG was observed histologically.

Bornes et al. 2016, study on optimal seeding densities for in vitro chondrogenesis of Integra matrix (sponge 3.5mm thick, 6mm diameter), seeded bovine whole bone marrow aspirates (containing populations of bone marrow-derived mononucleated cells, and bone marrow derived MSCs) at very high cell densities of up to $50x10^6$ cells (Bornes et al., 2016). In a similar method to what is described in this thesis for Integra cell seeding, they pipetted cells onto each scaffold, incubated for 30 mins followed by additional 1ml chondrogenic medium, cultured for 21 days. In their study, seeding at $50x10^6$ BMSCs/cm^3 produced the highest deposition of GAGs when compared to lower densities of $1x10^6$ and $0.5x10^6$ BMSCs. However, even at these high cell numbers, it appears that cells do not remain within deep levels of the Integra and the majority of chondrogenesis is at the surface as identified by safranin-O staining on histological analysis. These are similar findings to what has been demonstrated in this thesis. In this thesis however, I have also shown the formation of chondrogenic spheroid-like masses forming on Integra surface which are convincing of cartilage tissue not previously reported.

Furthermore, I have shown that Integra seeded with ADSCs and CSPCs changes in appearance over time when incubated in chondrogenic media and acquires a translucent cartilage like appearance with increased stiffness.

Several challenges were met in using Integra for generating a nasal septal product. Autofluorescence from Integra made it difficult to identify seeded cells easily, even when labelled cells were used but this was mostly an issue with live imaging rather than confocal microscopy. Autofluorescence was problematic when imaging Integra using confocal microscopy to detect proteins by immunofluorescence. Labelled cells imaged with confocal microscopy were identified easily on merged channel images.

The deposition of collagen within Integra was convincing in both single layer and bilayer sheets but was limited to a minimal depth on the same side that cells were seeded. Both immunohistochemical staining and paraffin sections demonstrated this. An observation found in both cell types was their inability to penetrate, migrate and attach into deeper layers of Integra. Despite integra pore size being up to 150µm (Dagalakis et al., 1980), cell penetration into deeper levels of Integra was very limited. It appears that undifferentiated cells do migrate within Integra but fail to expand and their density remains low possibly due to failure to attach to the Integra matrix. Cells at the surface, however, do not have that constrain, can expand, and possibly because of higher numbers can more easily remodel the Integra matrix and have a more favourable environment to undergo differentiation and deposit extracellular matrix. Cells seeded into Integra and chondrogenically differentiated are rarely seen deep in the matrix with higher numbers detected on the surface where they deposit extracellular matrix in an unconstrained favourable environment. Cells at deeper regions may be lost due to lack of attachment, for technical reasons or have migrated and coalesced with other cells towards the surface.

Although SEM was not undertaken, the morphology of Integra on paraffin embedded samples gave some indication to the morphology of the Integra matrix. Although pore size was sufficient to allow cells to migrate through, it appears that the density and pattern of the Integra cross linked type I collagen and GAG was too dense to permit easy cell movement.

Both ADSCs and CSPCs seeded into Integra could deposit ECM components as indicated by positive collagen II expression, and positive GAG histological staining. CSPCs seeded into Integra in all replicates appeared to affect a more significant change on the physical appearance of Integra compared to ADSCs. It was difficult to quantify the difference in ECM deposition between the two different cell types, but this result was not surprising since in 2D, CSPCs expand at a faster rate than ADSCs of a similar passage. Furthermore, chondrogenesis in 2D is also more rapid in CSPCs.

The nasal septal pocket design is novel and has not been previously reported. Unlike other delicate cartilages of the nose, the nasal septum must withstand considerable forces of overlying tissue and skin drape, tissue contraction after surgery and to maintain its dimensions to avoid aesthetic failure. For this reason, a tissue engineered cartilage graft must have suitable mechanical strength. The benefit of a pocket design is that it can be fabricated to meet satisfy such criteria and can be easily changed to the desired dimensions. The 3D PLA pocket construct was rigid and thin and was easy to handle. Insertion of the Integra into the pocket was challenging as described.

4.4 Conclusions

The concept of a core cell seeded hydrogel (or Integra) mechanically supported by a rigid polymer remains useful for nasal septal cartilage reconstruction. Although chondrogenesis appears limited within Integra, it certainly appears to support cartilage ECM deposition on the surface, and I have demonstrated that mature cartilage like microtissue develops over extended periods of differentiation. As a strategy for producing a nasal septal graft product, an alternative technique for generating cartilage would be to use Integra as a cell support for cartilage deposition on its surface. The advantage of Integra is that it easy already FDA approved, widely available, easy to handle and resorbs with breakdown of the matrix over time. Seeding stem cells into Integra is also a simple process. In this manner, it would still be viable to use Integra within the novel pocket design if a predicable layer of mature cartilage can develop on its surface.

The pocket design tested in this chapter has limitations as described and an alternative design to support the inner core region such as that highlighted in Fig 4.26 may be advantageous.

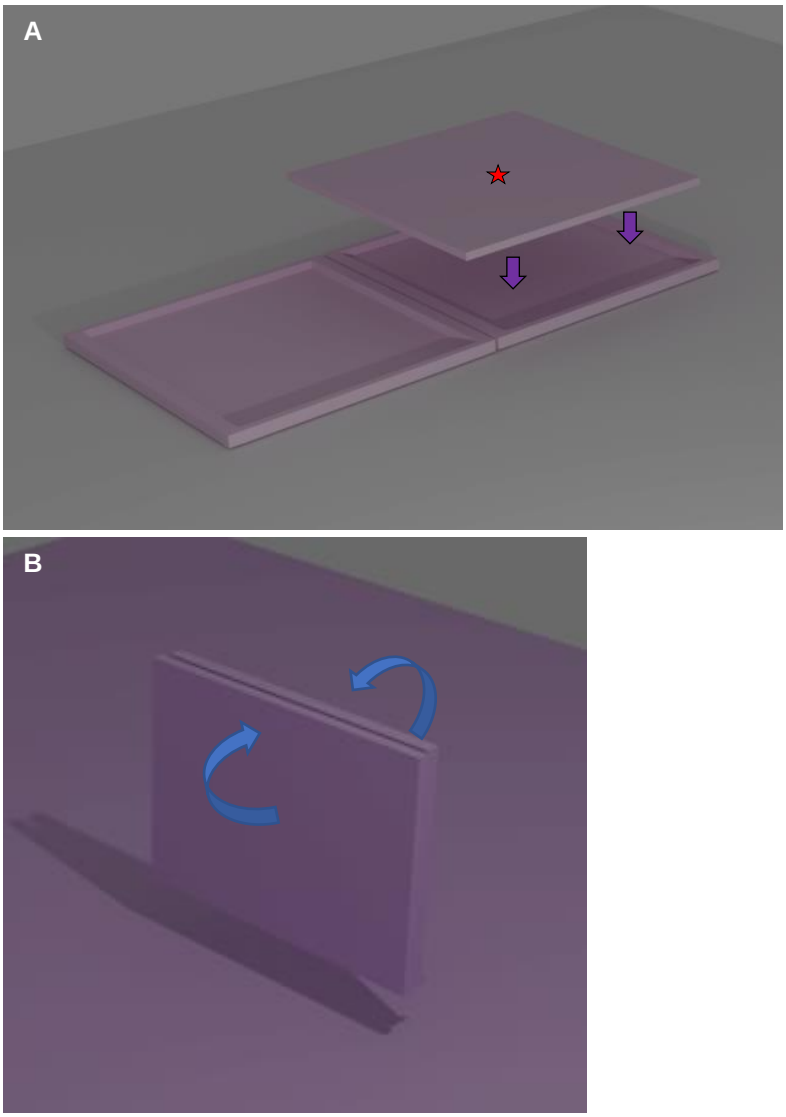

Fig 4.26. PLA modification. **(A)** “Clam shell” PLA print would allow insertion of Integra (*)in the centre, laid flat and even. **(B)** The construct would then be folded and secured closed with either a stich or glue to secure the two sides together.

Chapter 5

RESULTS 3:

Analysis of bioprinted ear cartilage derived precursor cells and polycaprolactone constructs

5.0 Background

3D bioprinting technology is a rapidly emerging branch of tissue engineering that has the potential to address the complications and challenges of facial reconstructive surgery. Bioprinting will enable fabrication of custom made and patient specific cartilage grafts to accurately reconstruct nasal defects requiring cartilage. The morphology of native nasal cartilage can be easily reproduced using CAD software and printed using a 3D bioprinter (Murphy and Atala, 2014). This is also applicable for ear cartilage where an entire ear cartilage framework can be designed and printed and similarly tarsal plates. (Chen et al., 2020; Zhou et al., 2018). Typically, protocols are required that facilitate the expansion of millions of cells for 3D bioprinting and various cell sources and cell types (stem cells & induced pluripotent stem cells) have been studied extensively (Ong et al., 2018a). Adipose derived stem cells, human nasal septal chondrocytes and human bone marrow-derived stem cells (hBMSCs) have been studied in relation to cartilage tissue engineering (Fisher et al., 2017; Shafiee et al., 2011). Bernstein et al demonstrated that human auricular chondrocytes encapsulated in type I collagen hydrogels can generate a rich proteoglycan matrix with cellular lacunae when implanted in nude mice and at variable passages (P3,P4,P5) (Bernstein et al., 2018). Other studies have also demonstrated the ability of auricular derived chondrocytes mixed with collagen and injected into ear moulds to create ear constructs resulting in tissue similar to native cartilage(Cohen et al., 2018). However, the behaviour and ability to form cartilage like tissue of these auricular cartilage stem/precursor cells (CSPCs) in 3D bioprinting is very limited. No publications were identified using ear cartilage derived precursor cells in 3D bioprinting.

In the previous chapter, it was demonstrated that Integra seeded with Adipose derived stem cells (ADSCs) and cartilage derived precursor cells failed to produce significant glycosaminoglycans (GAGs) and cartilage ECM proteins in deeper regions in both in-vitro static cultures and in CAM models. The concept of the pocket design whereby the cell seeded Integra was inserted and sandwiched inside a pocket of PLA proved to be technically tricky. Regardless of the ability of Integra to provide a microenvironment conducive to chondrogenic tissue growth, the technical challenges of inserting the Integra sheet into the pocket would make clinical translation of the concept very difficult. Therefore, in the pursuit of generating nasal septal cartilage using autologous mesenchymal stem cells, an alternative approach was taken that utilises pneumatic extrusion bioprinting technology with a 3D printer.

To avoid the potential mismatch in the rate of new tissue formation and scaffold degradation, a scaffold free approach is preferable. A hydrogel would still be required to provide the environment required for 3D cell-cell interactions, but cells are not directly seeded onto a hard polymer scaffold. In fabricating a nasal septal graft, the role of a hard polymer scaffold as described in chapter 4 is to provide mechanical stability. Polycaprolactone (PCL) appears to be an attractive scaffold material as offers some advantages compared to PLA that has been described in chapter 4. PCL is a linear synthetic biodegradable aliphatic polyester that is biocompatible, cheap and easy to produce, and is also already FDA approved.

There are several 3D printing/bioprinting methods such as extrusion printing, stereolithography, inkjet, laser assisted bioprinting and powder fusion printing/selective laser sintering. Extrusion based bioprinting is the most common type of printing and involves layer by layer deposition of cell laden bioink to fabricate 3D patient specific grafts. Advantages include the ability to print in a wide range of materials including synthetic polymers PCL and PLA, the ability to print different bioinks cells via multiple print heads and at high cell densities. The main disadvantage is the pressure strain on the cells during printing process which may affect cell viability (Gillispie et al., 2020; Panwar and Tan, 2016).

Tissue engineering by 3D bioprinting therefore requires careful consideration of the appropriate printing technology (e.g. inkjet or microextrusion) and the appropriate selection of a bioink that has the required viscosity, biocompatibility, degradation, and mechanical properties. To achieve physical properties required for clinical use, printed constructs may require maturation in a bioreactor system under chondrogenic inductive conditions to enhance cartilage maturation (Gharravi, 2019; Gupta et al., 2018; Yeatts et al., 2013)

The aim of this chapter was to isolate and culture auricular cartilage derived stem/precursor cells for 3D bioprinting in an alginate/cellulose bioink using a pneumatic based micro extrusion printer. An alternative approach to developing the nasal septal graft product would not rely on the “pocket” design but instead a “sandwich” design whereby a core cell seeded hydrogel would be sandwiched between a resorbable polymer scaffold that would be in direct contact with the hydrogel. Having considered the potential benefits of 3D bioprinting, the aim now was to print cells onto a 3D printed polymer scaffold in a tri-layer approach comprising of a polymer-hydrogel-polymer sandwich. In a similar way to the original pocket design, the polymer scaffold would provide mechanical stability for the inner layer while the hydrogel is slowly replaced with cartilage tissue. Alginate/ cellulose bioink (requires cross-linking with calcium chloride) and a pneumatic based extrusion printer where chosen for this investigation as they are both widely available and the properties of this bioink (biocompatible and mechanical strength of cellulose nanofibrils) are advantageous for cartilage tissue generation. The pneumatic extrusion printer is also able to 3D print PCL via a secondary print head simultaneously.

Specific objectives of this chapter include:

- To generate a new healthy human auricular cartilage precursor cell (CPSC) line and characterise it.
- To assess the viability of CSPCs when mixed in a commercially available alginate/cellulose bioink using a novel mixing protocol both before and after 3D bioprinting and crosslinking with calcium chloride.
- To assess the expression of cartilage markers GAG and collagen in 3D bioprinted CSPCs laden alginate/cellulose bioink cultured in static chondrogenic media and in CAM graft models.
- To optimise PCL printing parameters to achieve a mesh suitable for the sandwich design.
- To compare Collagen and GAG expression between CSPCs mixed in alginate/cellulose bioink and a fibrin-based hydrogel.

5.1 Results

5.1.1 Isolation of human auricular CSPCs and assessment of their differentiation potential

Newly isolated CH105 CSPC line was obtained during this PhD thesis. Cartilage was resected from a 14yr old male patient undergoing pinnaplasty for otapostasis and processed for CSPCs isolation as described in chapter 2 section 2.1.3. A section of harvested cartilage is shown in Fig 5.1 Ai.

5.1.1.1 Cell isolation

Cells were identified migrating out from the explants after a minimum of 5 days incubation and began to become confluent by day 15. Isolated cells appeared fibroblast like in their morphology with large flat and elongated spindle appearance (Fig 5.1 Aii). Cells were isolated and expanded from all 12 explant cartilage samples cultured. Generating new cell lines from the auricular cartilage explant was easy and predictable. Consistent with other cell lines generated, the key determining step was to ensure direct contact between the explant and the well floor which was simply achieved by the addition of culture media with gentle pipetting at the time of initial explant placement into the well.

5.1.1.2 Trilineage differentiation

CSPCs were cultured for 3 weeks in adipogenic, osteogenic and chondrogenic differentiation medium (Fig 5.1 B). Over the 21 days incubation, cell morphology changed in all 3 groups. The adipogenic differentiated cells demonstrated clear areas of lipid droplet formation as seen on brightfield images. The osteogenic differentiated cells became highly condensed at small foci of calcium crystals developed. Chondrogenically differentiated cells also changed to the typical morphology of being highly condensed and forming square/rectangular zones. Control cultures did not demonstrate these changes identified in all three groups. At the end of 3 weeks, the three differentiated cell groups were stained with Oil-red-O for lipid droplets, Alizarin red to identify calcium deposition and Alcian blue staining for GAG deposition all of which were strongly positive.

These results, which are consistent with other CSPC lines isolated by other members of the laboratory demonstrated that normal auricular CSPCs can be reproducibly differentiated towards all three mesenchymal lineages.

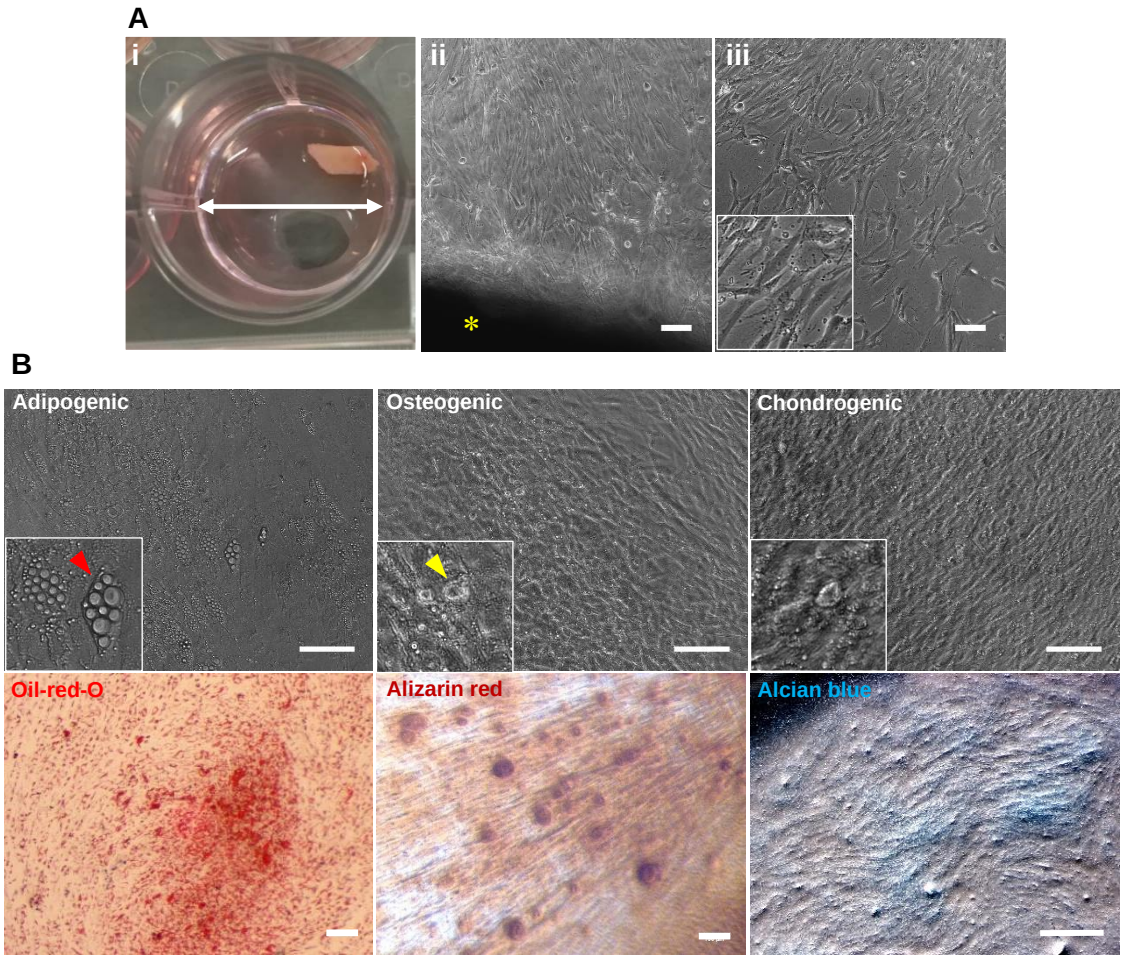

Figure 5.1 Ear cartilage explant (CH105) stem cell isolation, expansion and trilineage differentiation. (Ai) Ear cartilage explant. Ear cartilage explant in 24 well plate (arrow 15.6mm) incubated for approx. 2 weeks. **(Aii)** Precursor cells migrating out from explant (*). **(Aiii)** P0 explant cells exhibited mostly fibroblast like morphology. **(B)** Bright field images of three-week trilineage differentiation in adipogenic, osteogenic and chondrogenic media; note lipid droplets (red arrowhead) and calcium deposition (yellow arrowhead) in adipogenic and osteogenic differentiated cells. Oil red O, Alizarin and Alcian blue staining of differentiated CSPCs. Trilineage differentiation was done with 4 biological replicates. Scale bars: 100µm.

5.1.1.3 Histological analysis of normal ear cartilage – CH105

Soft tissue attached to the harvested cartilage was gently excised and the sample cut into 2mm sections. Macroscopically the cartilage looked entirely normal. Sections were paraffin embedded and stained with Haematoxylin and Eosin (H&E) and Alcian Blue (AB). Histological examination confirmed the typical appearance of a highly cellular central mature cartilage with abundant chondrocytes (found in pairs or in isolation) within lacunae throughout (Fig 5.2). Numerous isogenous groups are observed surrounded by their territorial matrix which stains positive with H&E. Expression of GAGs is evident on positive AB staining. Covering the chondrium is the dense fibrous perichondrium with two identifiable layers – the outer fibrous and inner chondrogenic cellular layer. In this chondrogenic layer, CPSCs are noted as well as chondroblasts in the deeper (transitional layer) region adjacent to chondrium.

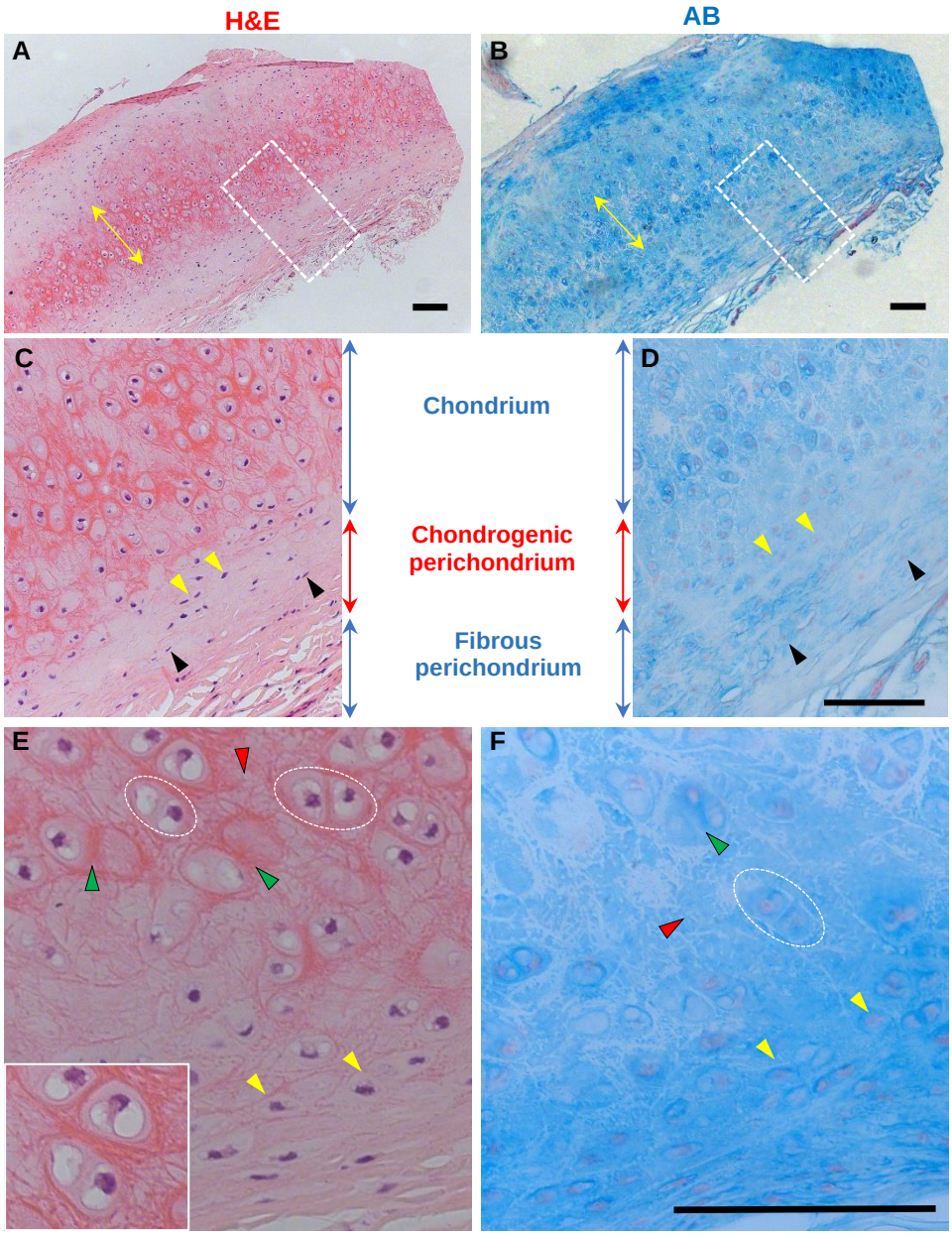

Figure 5.2 Histology of normal ear cartilage (CH105) stained with H&E and AB. (A&B) Low magnification of 5µm section. Elastic cartilage zone (yellow arrow). **(C&D)** High magnification images of zonal architecture. Chondrogenic perichondrium contains CSPCs (black arrowheads) and chondroblasts (yellow arrowheads) in the deeper layers (transitional layer). **(E&F)** Higher magnification of mature Chondrium layer**.** Dashed circles highlight isogenous groups. Red arrow heads=interterritorial matrix and green arrowheads= territorial matrix. Chondroblasts highlighted again (yellow arrowheads). Inset box in (E) highlighting chondrocytes within lacuna. Scale bars: 100µm.

5.1.2 Viability of CSPCs in alginate/cellulose bioink

All experiments reported in this section were carried out using CSPCs (line CH105) isolated and expanded during this PhD thesis. All printing was undertaken using the same pneumatic extrusion 3D bioprinter as described in chapter 2 section 2.6. Given that this was the first 3D bioprinting undertaken in the laboratory, there were no previous result to compare too and therefore no existing protocols to follow. Therefore, the initial challenge was to develop cell/bioink mixing protocols to maximise homogeneity of the suspension and minimise bioink waste. The mixing of cells with bioink had numerous critical aspects. Firstly, achieving a homogenous cell laden bioink mix was important to achieve predictable, reproducible, and equal (as much as possible) cell numbers in each 3D bioprinted construct. Secondly, the mixing protocol had to be simple in order to minimise the stress on the cells hence limiting cell injury and death. Finally, the protocol described should result in negligible waste of cell laden bioink as very little is lost in dead spaces within commercially available mixing devices. The technique developed and described in detail in chapter 2 section 2.6.1.3 achieved all these goals as shown by the data described in the following sections.

5.1.2.1 CSPC distribution in alginate/cellulose bioink using novel mixing protocol

Cell distribution of cells within bioink using the developed mixing technique was assessed using mCherry^{+} labelled CSPC (CH90). This permitted easy identification of cells within the bioink. The resultant mix was imaged using 2-photon confocal microscopy to determine cell distribution in 3D. The results showed an even distribution of cells throughout the mix in all dimensions with no clumping or large voids observed (Fig 5.3).

5.1.2.2 Cell viability of printed and non-printed CSPC in bioink

Analysis of 3D bioprinted constructs to determine cell viability was carried out at day 1, 7 and 21 after bioprinting CSPCs (CH105) either with the alginate/cellulose bioink or a similar bioink with additional RGD functionalization as described in chapter 2 section 2.6.1.5. For comparison, cell viability was also assessed in cells mixed with bioink but not printed. Each analysis was performed on triplicate constructs. The results demonstrated that cell death in the RGD bioink was low at 1 day but increased over time and was significantly higher by day 21 (Fig 5.4). The alginate/cellulose bioink CSPCs in contrast, appeared to recover from the bioprinting at day 1 where a lower percentage of live cells were measured that then increased and fewer cell death was observed by day 21 when compared to the RGD group (Fig 5.5).

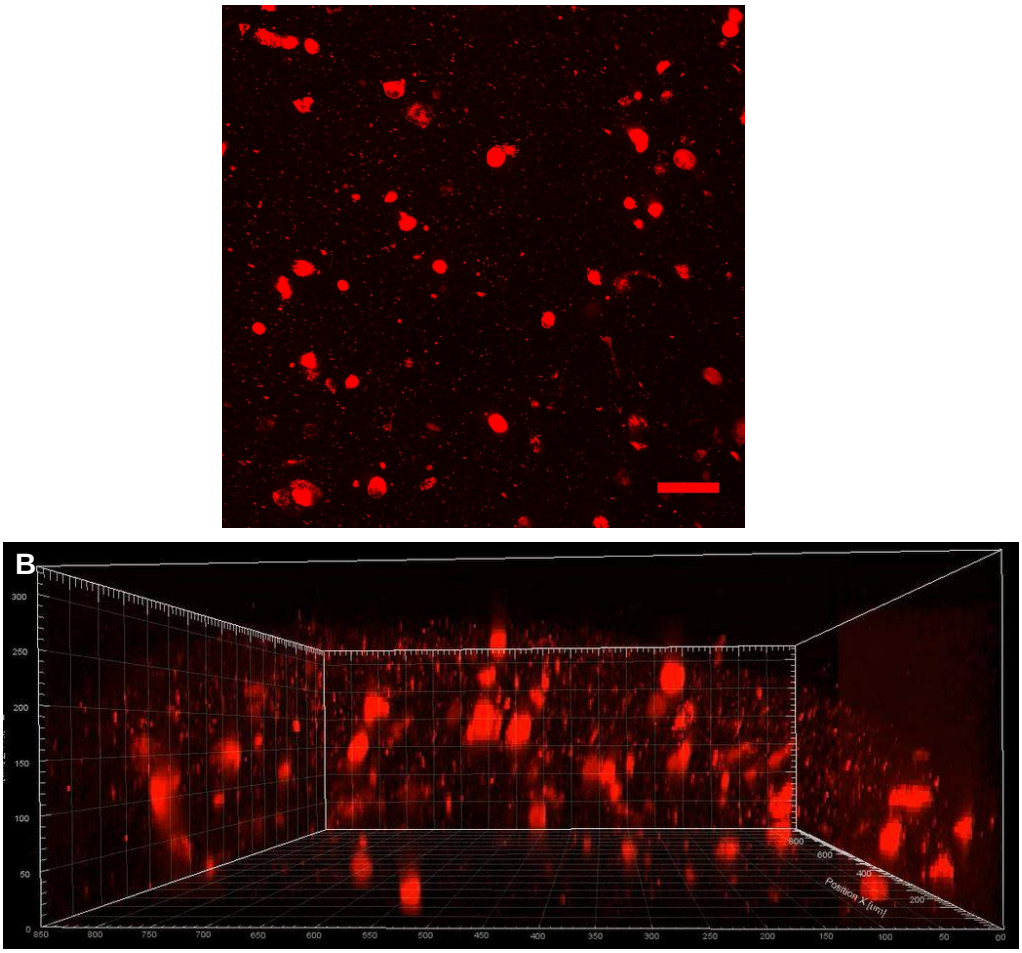

Figure 5.3. Two-photon confocal imaging of mCherry^{+} labelled CSPCs within alginate/cellulose bioink. **(A)** Cells at a density of 10x1^{6} cells/ml imaged in z-stack overlay. **(B)** The same z-stack highlighting 3D distribution of cells along the z axis. Three biological replicates were imaged showing similar results. MP4 3D moving image of z-stack is provided on supplementary DVD. Scale bar: 100.

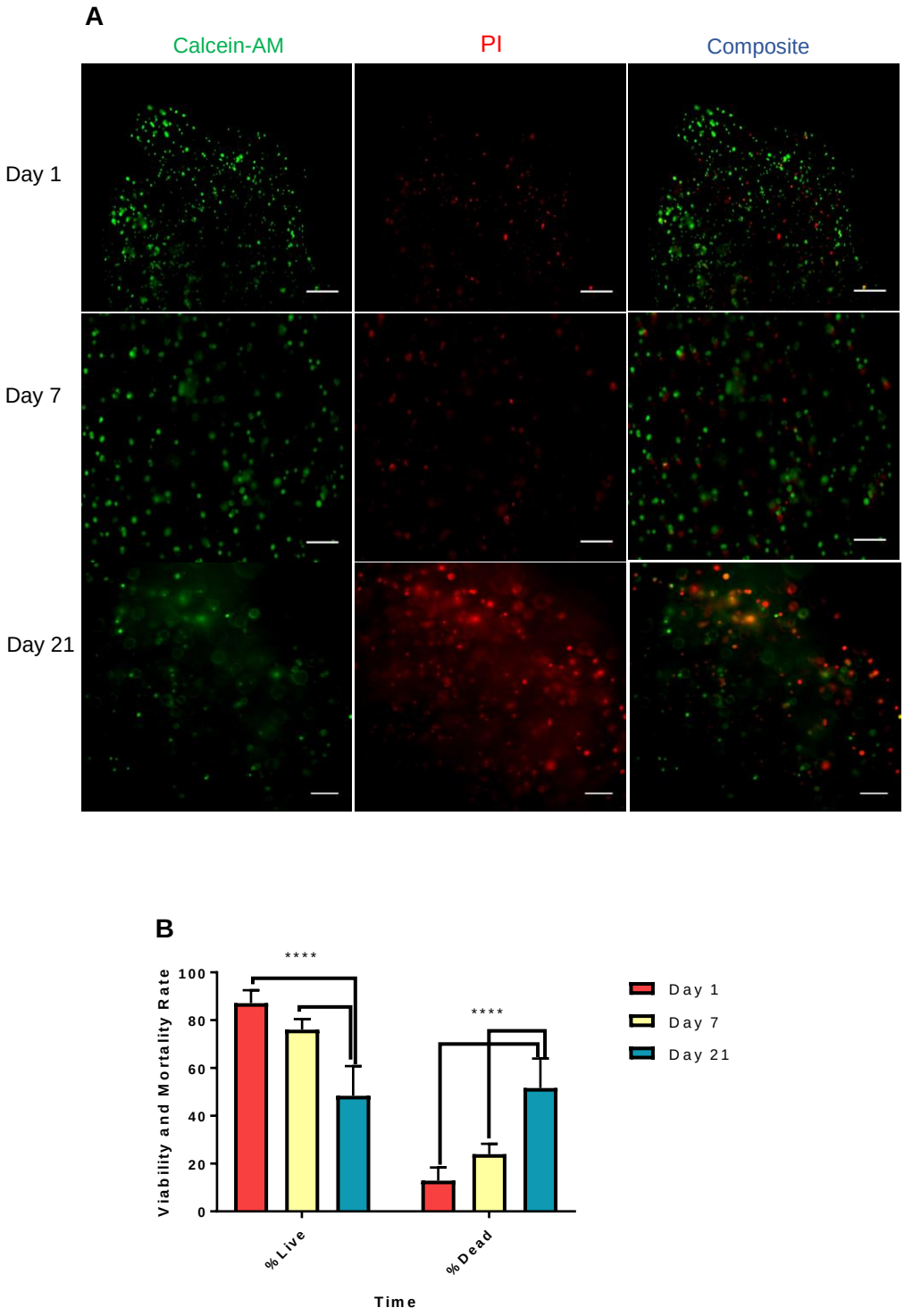

Figure 5.4. Fluorescent microscopy images of CSPCs viability and mortality in 3D bioprinted cell laden RGD bioink. **(A) Calcein-AM/PI staining**. Live cells (green) and dead (red) at day 1, days 7 and day 21. Cell death is observed throughout the time course and increases. **(B) Quantitative data of cell viability during the different time points (Day 1, 7, 21) post-printing.** As a total percentage, cell death numbers appear to increase with time. Scale bars:100μm. *p<0.05, **p<0.01 and ***p<0.001, ****p<0.0001 indicates the significant different amount of the experiment by the different days of evaluation (Results from MSc student Estephania Candelo Gomez, supervised by me).

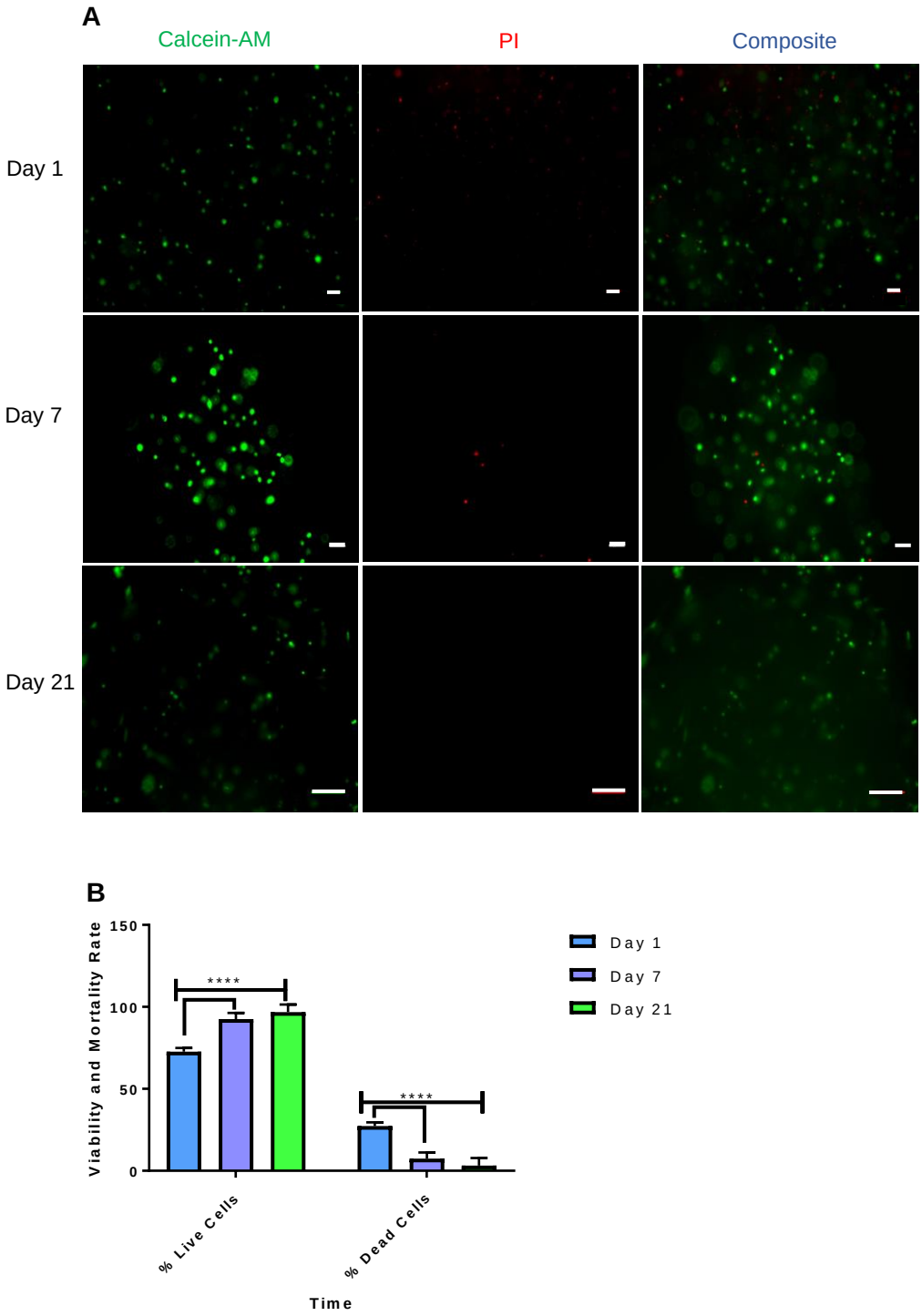

Figure 5.5. Fluorescent microscopy images of CSPCs viability and mortality in 3D bioprinted cell laden alginate/cellulose bioink. (A) Calcein-AM/PI staining. Live cells (green) and dead (red) at day 1, days 7 and day 21. This demonstrates stable cell survival within this ink and almost no cell death detected by day 21. **(B) Quantitative data of cell viability during the different time points (Day 1, 7, 21).** Cell death appears to decrease with time. Scale bars: 100μm. *p<0.05, **p<0.01 and ***p<0.001, ****p<0.0001 indicates the significant different amount of the experiment by the different days of evaluation (Results from MSc student Estephania Candelo Gomez, supervised by me).

Live/dead assays on non-printed CSPCs laden bioink using the same mixing protocol was also undertaken to assess cell viability and mortality as a control for the printing process. Only the standard alginate/cellulose bioink was studied (Cellink without RGD functionalisation). After 1-day post-mixing cell viability rate was 73% (IQ 71.7-73.2) and mortality 26.9% (IQ 26.7-28.2%). No significant differences in mortality and viability rates were observed between printed and non-printed constructs at day 1 and 7. After day 21 a significantly higher cell viability and lower mortality were observed in both groups (printed and unprinted) compared with day 1 and 7 (Fig 5.6).

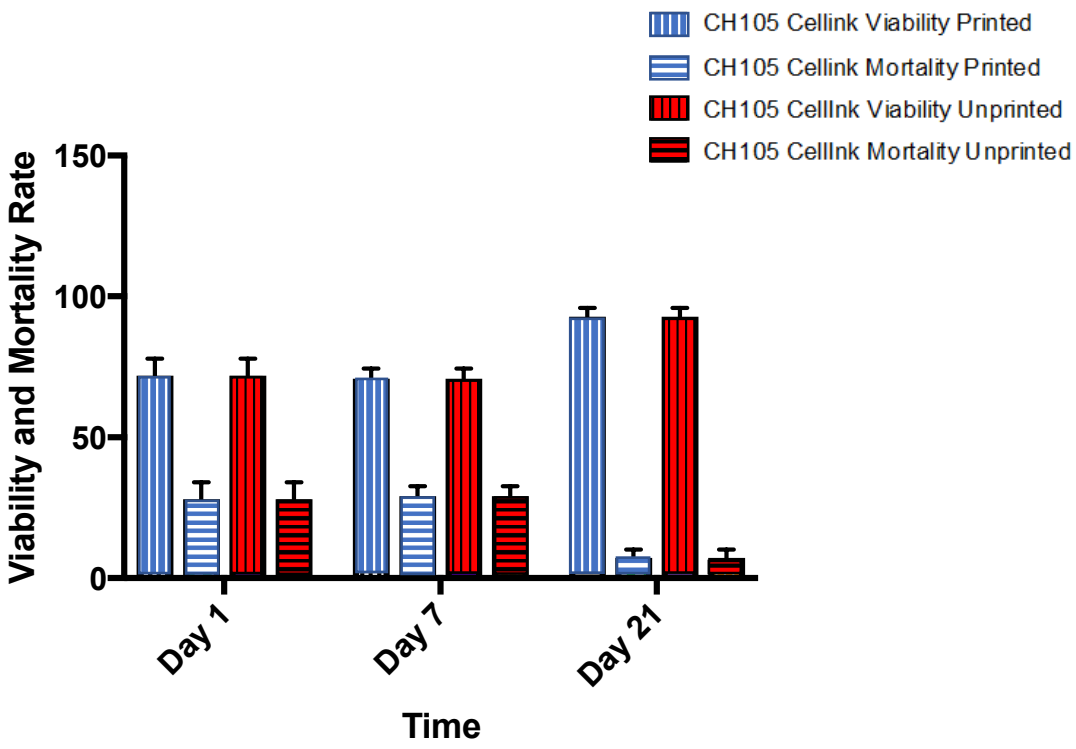

Figure 5.6. A comparison of CSPC viability and mortality in non-printed and printed cartilage constructs. Over 1, 7 and 21 days, cell survival and mortality of printed constructs was identical to non-printed controls. The process of printing appears to have no detrimental effect on cell survival (Results part of joint work with MSc student Estephania Candelo Gomez).

5.1.2.3 Cell viability of printed CSPCs after crosslinking with calcium chloride

The effect of Calcium Chloride ($CaCl_2$) crosslinking on cell survival was investigated to determine $CaCl_2$ cytotoxicity. Cell survival was analysed following 3D-printing and application of $CaCl_2$ to constructs for 10 minutes and 1-hour (Fig 5.7). Cell viability assay was undertaken after 24hrs. The 10-minute $CaCl_2$ crosslinking group had a cell viability of 84.4% (IQR 81.9-86.7) and cell death of 15.5% (IQR 13.2-18.1). The results demonstrate a higher rate of cell death by exposing cells to $CaCl_2$ cross-linking for 10 minutes, but after this longer treatment, cell survival was still high at 79.0% (Fig 5.7). Control group which was printed but not cross-linked demonstrated the highest cell survival (% live cells from total number of cells). Given that cross-linking printed constructs with $CaCl_2$ is a rapid process, there appears to be no reason to expose cells to if for longer than 10 minutes.

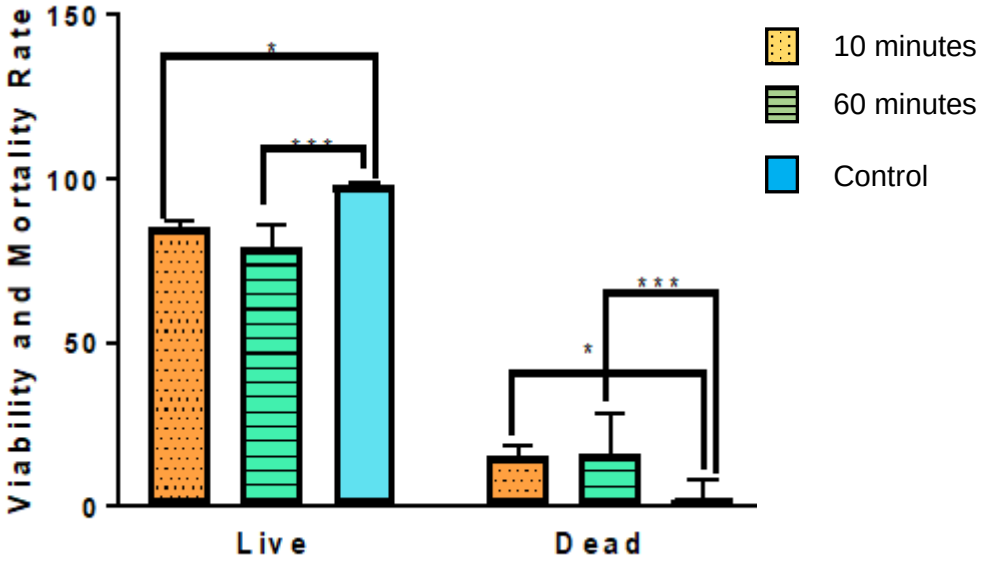

Figure 5.7. Live/dead assay of printed CSPC laden bioink crosslinked with calcium chloride for three different lenghts of time. Cell viability and cell death are comparable after 10 and 60 minute cross-linking, but lower and higher, respectively than in controls *p<0.05, ***p<0.001.

5.1.3 Expression of cartilage markers in 3D bioprinted CSPCs laden alginate/cellulose bioink

Next, the chondrogenic differentiation ability of CSPCs bioprinted in alginate/cellulose bioink was investigated by immunocytochemical and histological analyses. Given that the cell viability assay showed higher cell death in the RGD bioink, this bioink was not studied further.

Two time points were studied, 3-week differentiation and 6 months. At both time points, some regions within the chondrogenically differentiated bioprints demonstrated hypertrophic cells, but this was very sparse. Indeed, there was no observable difference in tissue staining between the chondrogenic and control groups. The chondrogenically differentiated bioprints demonstrated less fragmentation on handling with forceps subjectively. Interestingly, even the chondrogenically differentiated printed constructs in alginate/cellulose bioink over an extended period of 6 months demonstrated poor cartilage tissue-like morphology and ECM.

5.1.3.1 Histological analysis of paraffin embedded sections of 3D bioprinted constructs

Bioprinted constructs printed at the same time with identical print parameters were cultured in either chondrogenic or control medium. Macroscopically, over time (greater than 3 weeks) the chondrogenic differentiated bioprints developed small spheroid- like masses attached to the surface of the constructs; some isolated spheroids were also observed in the well. Paraffin embedded sections of 5µm thickness were stained with picrosirius red to identify collagen fibril networks and Toluidine blue metachromatic staining for proteoglycans as a representation of cartilaginous matrix deposition. Picrosirius stained sections were also studied under polarised light to detect collagen bundles (no differentiation between the types) of varying orientation and thickness detected as green and yellow-red birefringence.

Toluidine blue stain was very weak throughout the 21-day differentiated bioprinted constructs. Furthermore, only small numbers of cells were observed within the constructs, with only a few appearing to be enclosed within lacunae typically found in mature cartilage (Fig 5.8).

Three weeks differentiated bioprints demonstrated speckled regions of picrosirius red staining with brightfield microscopy but under polarised light no collagen birefringence was seen. As expected, areas with high cell condensations that generated small spheroids did show the presence of new collagen fibres under polarised light and positive staining of picrosirius red using brightfield microscopy (Fig 5.9).

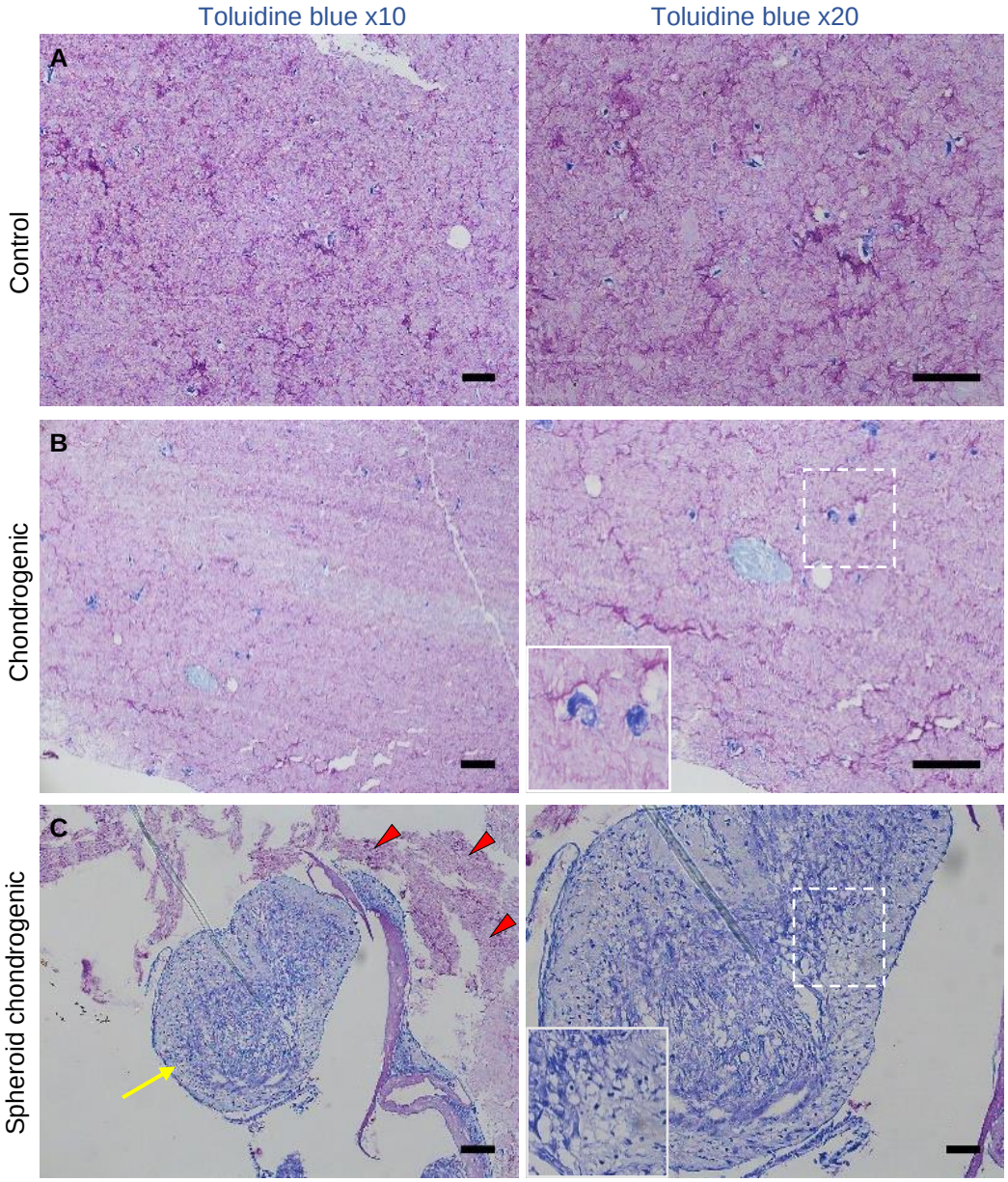

Figure 5.8. **Toluidine blue red staining of sections from CSPCs bioprinted in alginate/cellulose bioink and cultured in either control or chondrogenic medium for 21 days. (A)** Control and **(B)** chondrogenically differentiated bioprinted constructs appear to have similar low cellular content. In chondrogenically differentiated constructs some cells appear to be in lacunae (see magnified insert from dotted-line square). **(C)** Spheroid- like structure (yellow arrow) protruding from a chondrogenically differentiated construct (red arrowheads). Tissue morphology in this mass resembles cartilage like extra-cellular matrix with hypertrophic chondrocytes within lacunae (see magnified insert from dotted-line square). Scale bars:100µm.

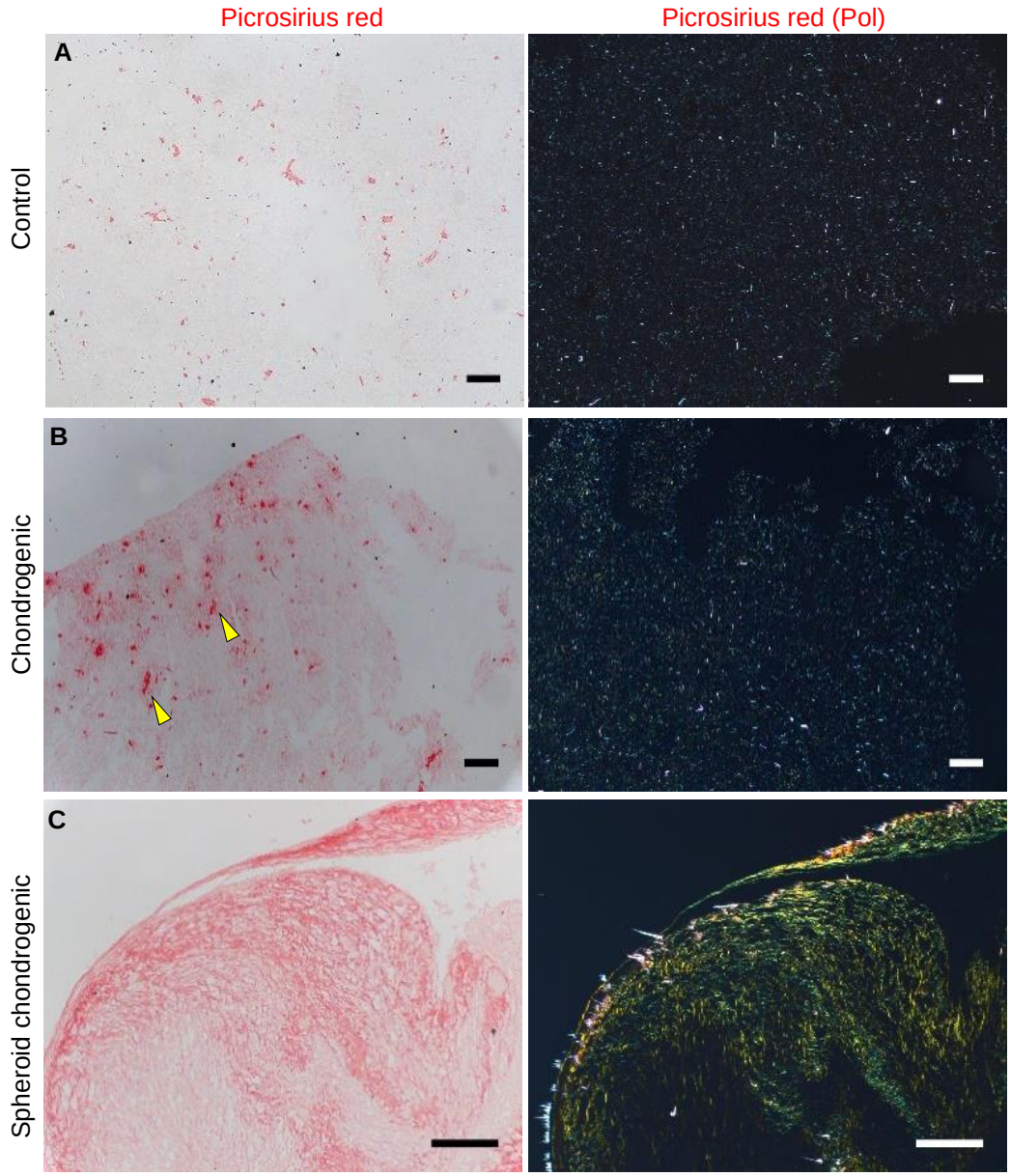

Figure 5.9. Picrosirius red staining of sections from CSPCs bioprinted in alginate/cellulose bioink and cultured in either control or chondrogenic medium for 21 days. After 3 weeks in culture there is little difference between **(A)** control and **(B)** chondrogenic differentiated constructs. Control group is negative for picrosirius staining. **(B)** Picrosirius red positive staining (yellow arrowheads) is minimal and patchy in the chondrogenic group. Polarised light microscopy showed no collagen fibres. **(C)** Spheroid like structure protruding from a chondrogenically differentiated construct were strongly staining for picrosirius red staining under brightfield and polarised light microscopy. Polarised light microscopy demonstrated green/yellow collagen birefringence throughout. Scale bars:100µm.

The 6 month cultured bioprinted constructs were paraffin sectioned and stained with Toluidine blue and Picrosirius red. Control bioprinted constructs were not stained by Toluidine blue, indicative of a lack of ECM proteoglycans, but numerous CSPCs within the bioink were identified. The chondrogenically differentiated group was almost identical in appearance. Within the print, Toluidine blue stain was again not positive except for cell nuclei. Like other constructs cultured in chondrogenic media (Integra), a peripheral layer of dense cells on the construct surface was noted. Furthermore, a highly cellular dense region of tissue had formed on the surface that resembles a chondrium was also observed. This spheroid-like tissue stained strongly for Toluidine blue indicating cartilage like ECM secretion of proteoglycans, with cartilage like cellular morphology (Fig 5.10).

Control bioprints at 6 months were almost identical to the 21 day control bioprints demonstrating similar Picrosirius red staining with brightfield microscopy and with no collagen birefringence on polarised light microscopy. The chondrogenic bioprints also demonstrated weak Picrosirius red staining. The spheroid-like tissue that had formed on the surface of the bioprint was strongly positive for Picrosirius red as expected. (Fig 5.11). Cell numbers within the 6-month bioprints for both groups counted in 3 biological replicates in three $1cm^2$ sections for each replicate were similar for both groups ($P=0.597$).

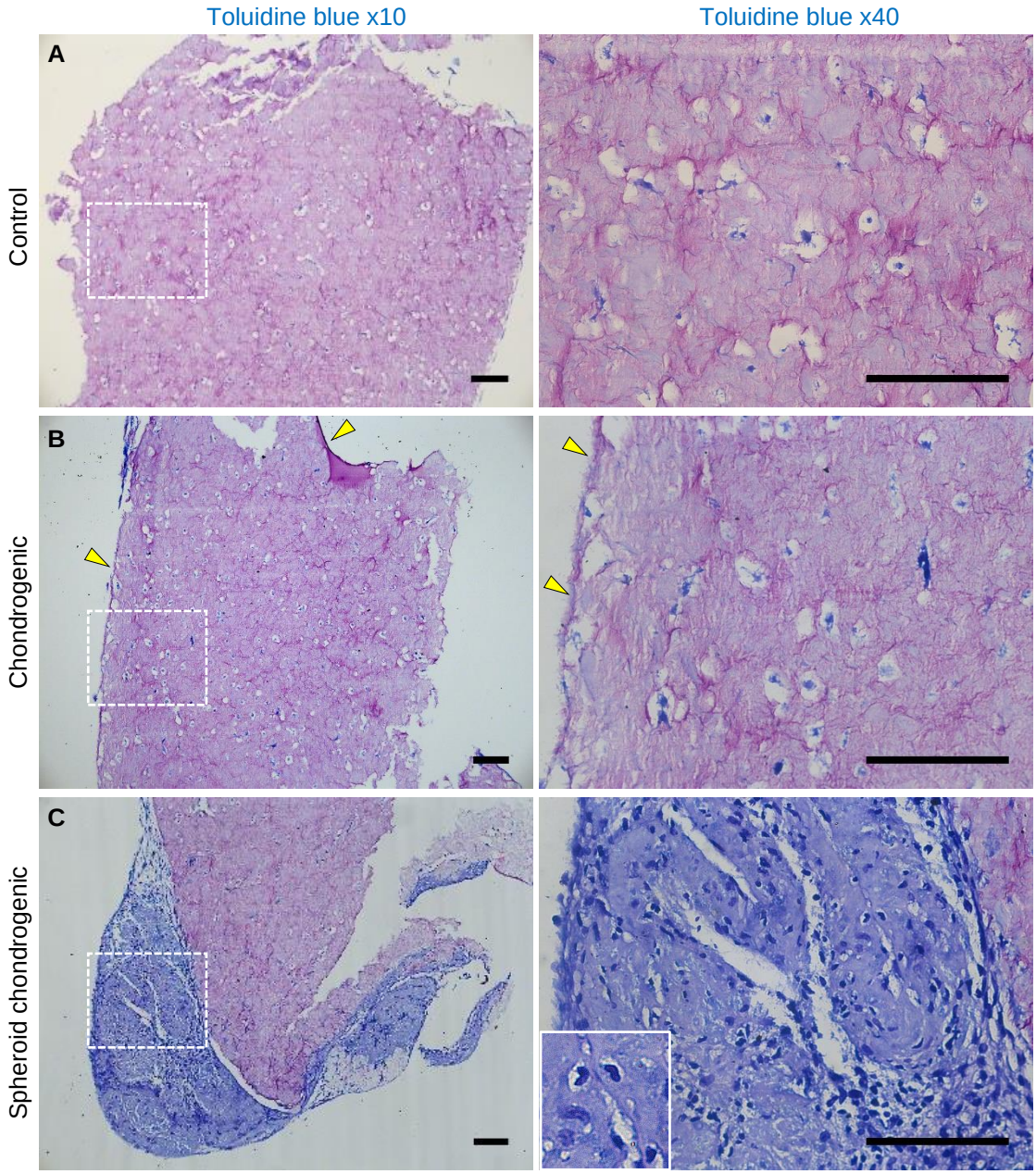

Figure 5.10. Toluidine blue staining of sections from CSPCs bioprinted in alginate/cellulose bioink and cultured in either control or chondrogenic medium for 6 months. (A) The control group appears to have an even distribution of cells throughout the bioprint. Higher magnification (of white dotted line box) demonstrates cells within lacunae with nuclei positively stained. There is no positive stain for extracellular proteoglycan**. (B)** The chondrogenically differentiated bioprints appear similar to the control group with identical cellular morphology. The only difference is the thin layer of cells that has formed on the surface around the entire construct (yellow arrowheads). **(C)** A strongly positive Toluidine blue stain of the cell condensation that has formed at one edge of the bioprint (not within it) with a spheroid-like appearance. Higher magnification (dotted line box) demonstrates high cell density and cells within lacunae surrounded by positively stained proteoglycan ECM. Scale bars: 100µm.

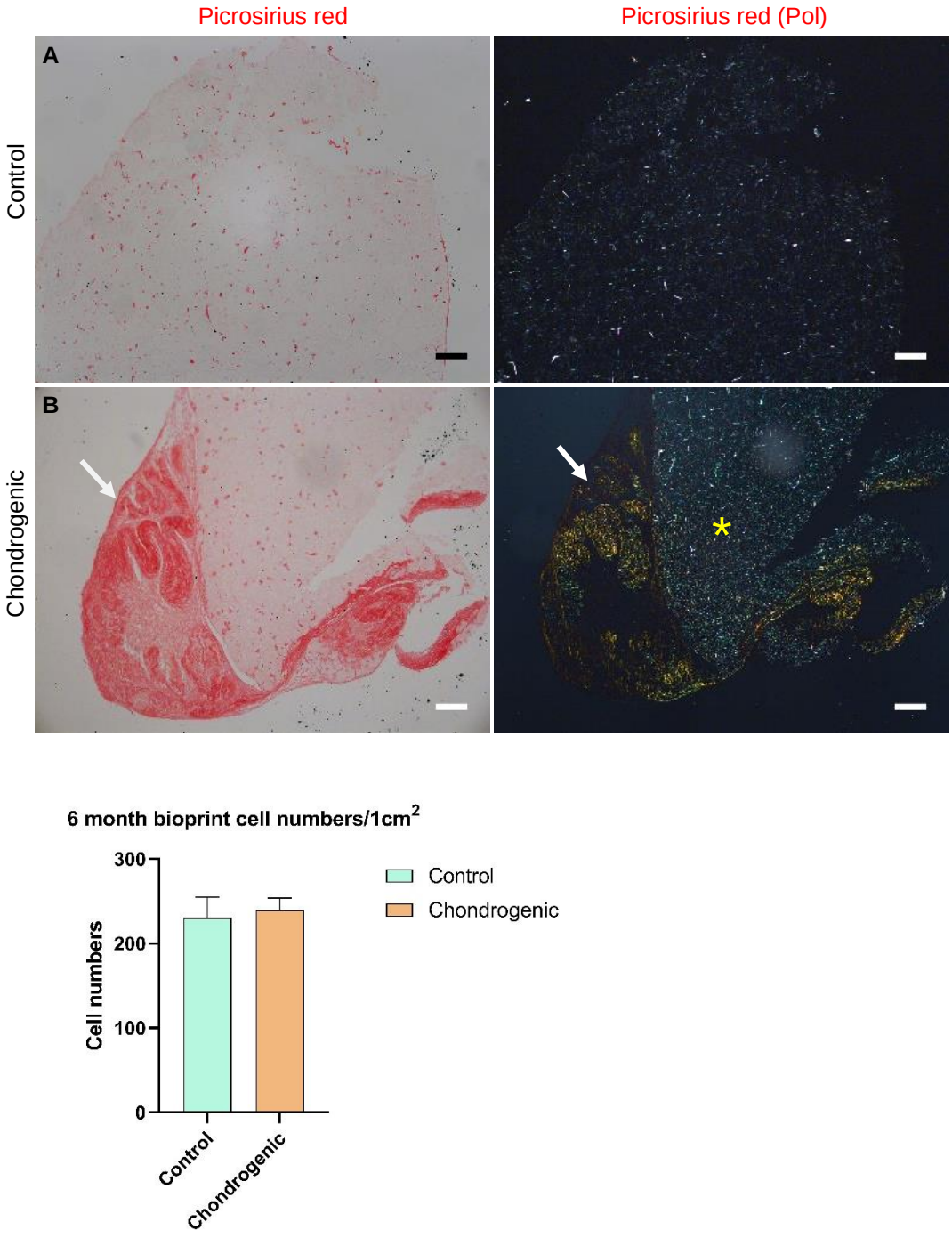

Figure 5.11. Picrosirius red staining of 6 months undifferentiated (control) and differentiated CSPCs bioprinted in alginate/cellulose bioink. The control group construct shows sparse speckles of positive Picrosirius red staining under brightfield microscopy. Polarised light microscopy demonstrates absence of collagen bundles. The chondrogenic differentiated construct displays a similar Picrosirius red staining pattern within the bioink (yellow Asterix), but associated spheroid-like tissue is strongly positive (white arrows). Cell numbers within the two constructs at 6 months are similar (averages of 3 replicates, no significant difference p=0.597). Scale bars: 100µm.

5.1.3.2 Immunohistochemical analysis of paraffin embedded sections of 3D bioprinted constructs

In order to provide further characterisation of 3D bioprinted CSPCs in alginate/cellulose bioink, samples were analysed by immunohistochemistry staining. Targets for staining were vimentin, a marker of mesenchymal stem cells, Hoechst staining to identify cell nuclear DNA and collagen II to assess for cartilage ECM. After staining, samples were imaged whole mount using 2-photon microscopy and a x10 dipping objective then processed as z-stacks of optical sections. The problems with interpreting the results were similar to that of Integra described in the previous chapter, namely the background autofluorescence that makes identifying cells more difficult. Importantly, collagen II staining in the far red (Alexa Fluor 647) was easier to image as this did not have the same background problem. The 21 day cultured bioprints were analysed with negative controls.

The bioprinted constructs maintained in expansion media were easily fragmented and even the staining protocol requiring gentle incubation of primary and secondary antibodies on a slow roller appeared to be damaging the samples and made them difficult to handle. Nuclear and Vimentin staining overlapped significantly with the native matrix of the bioink making cell identification difficult. However, at higher magnification, cells were seen distributed throughout the construct, as indicated by the nuclear staining, and displayed a flat and round morphology. The bioprint edges were irregular and fragmenting with large cracks transecting the sample. Staining for collagen II was negative with a negligible signal (Fig 5.12).

Chondrogenic differentiated bioprints at 21 days expressed Vimentin throughout the sample with higher levels focally at the periphery. This coincided with weak but positive collagen II expression at the surface of the sample. Collagen II expression within deeper regions of the bioprint was also very weak and nonspecific. CSPCs were identified at all levels of the sample (down to -215µm) and evenly distributed. At higher magnification, a tight network of dense flat round cells around the bioprint was observed (Fig 5.13). At deeper optical sections (-215µm) a similar pattern and level of expression of Vimentin and Collagen II staining was present. However, at this deeper section, there were focal patches of no signal, representing possibly poor laser penetration, genuine reduced cell numbers or poor antibody penetration (Fig 5.14).

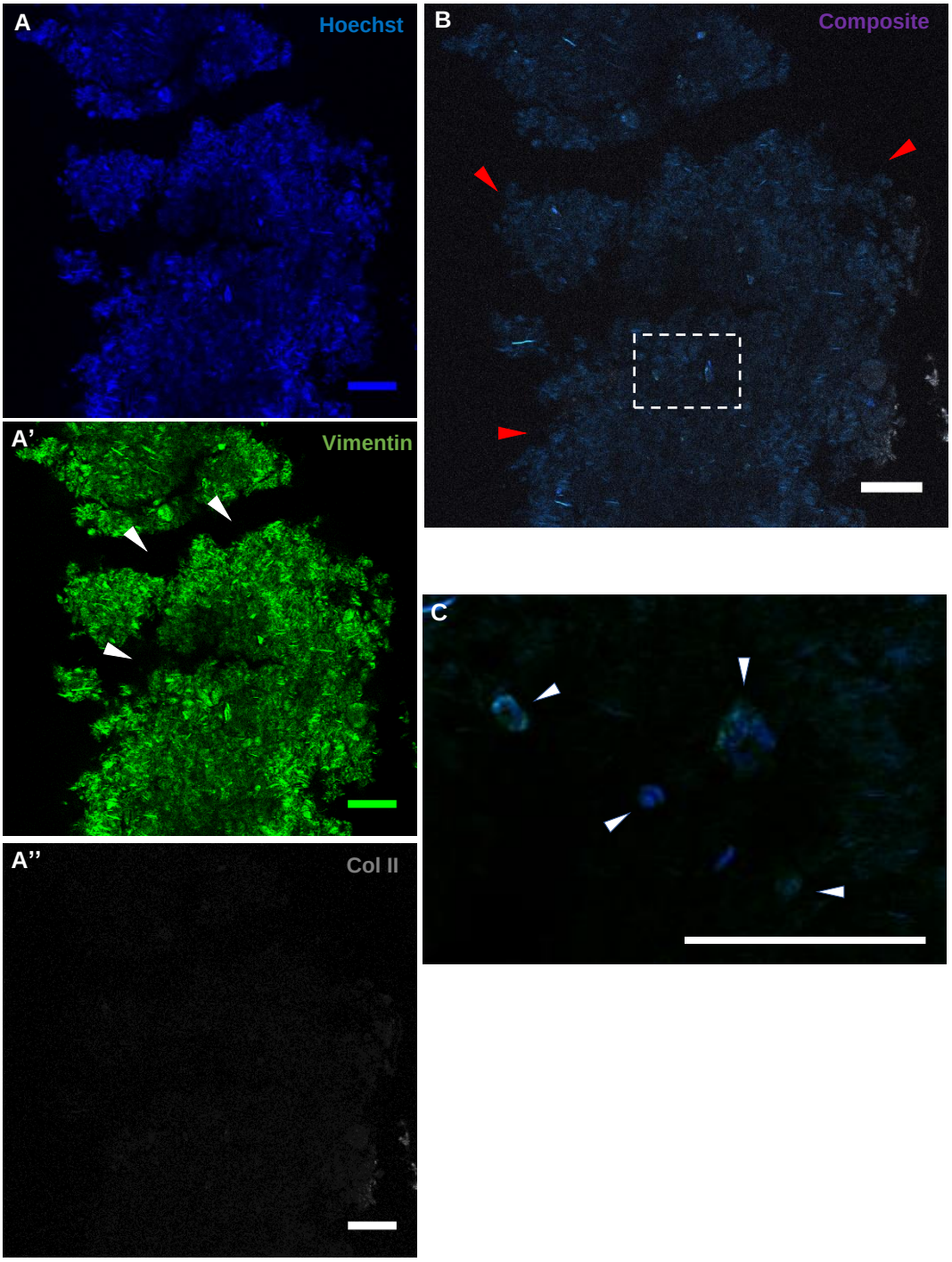

Figure 5.12. Expression of Collagen II and Vimentin at 21-day incubation in a section from a control bioprinted construct. (A-A'') Two-photon Confocal images of Ch105 CSPCs printed in alginate/cellulose bioink stained for Vimentin (green), Collagen II (red) and counterstained with Hoechst (blue). Control bioprinted constructs were fragile and easily fragmented (white arrowheads). **(B)** Composite image demonstrates cell distribution within the bioprinted construct. Edges of the sample are irregular (red arrowheads). **(C)** High magnification of dashed box in (B) showing cell morphology. Images taken at depth of 125µm. Scale bars: 100µm.

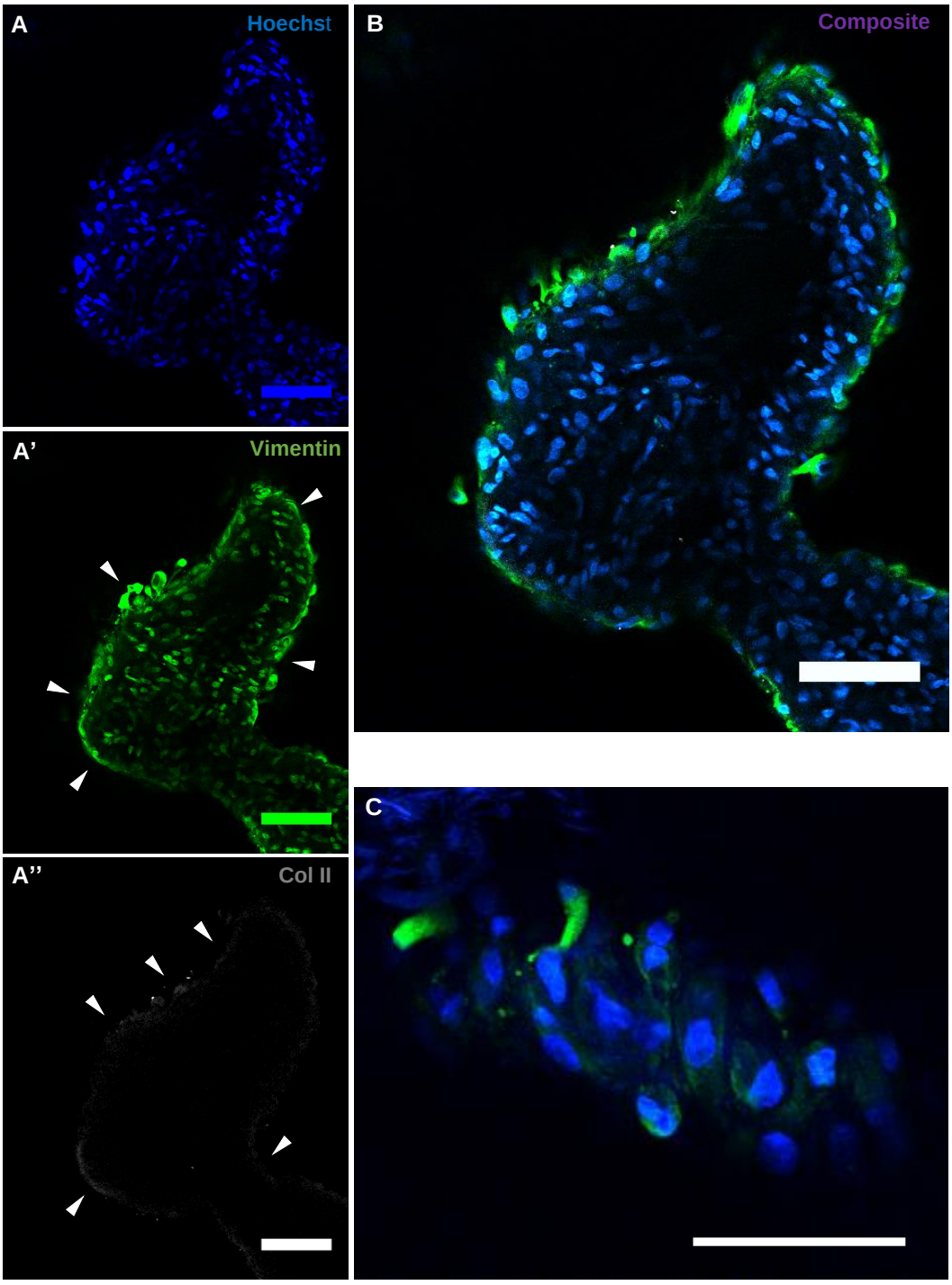

Figure 5.13. Expression of Collagen II and Vimentin at 21-day incubation in a section of chondrogenically differentiated CSPCs bioprinted in alginate/cellulose. (A-A'') Two-photon confocal images of a Ch105 construct stained for Vimentin (green), Collagen II (grey) and counterstained with Hoechst (blue) at depth -125µm. Stronger Vimentin and Collagen II staining around the surface of the bioprinted construct (white arrowheads). **(B)** Low magnification image of composite stain demonstrates cells distributed within the bioprint. The edges of the sample are well defined, and cells appear organised into a layer around the bioprint. **(C)** High magnification image of cell morphology within construct. Samples stained in triplicates. Scale bars: 100µm.

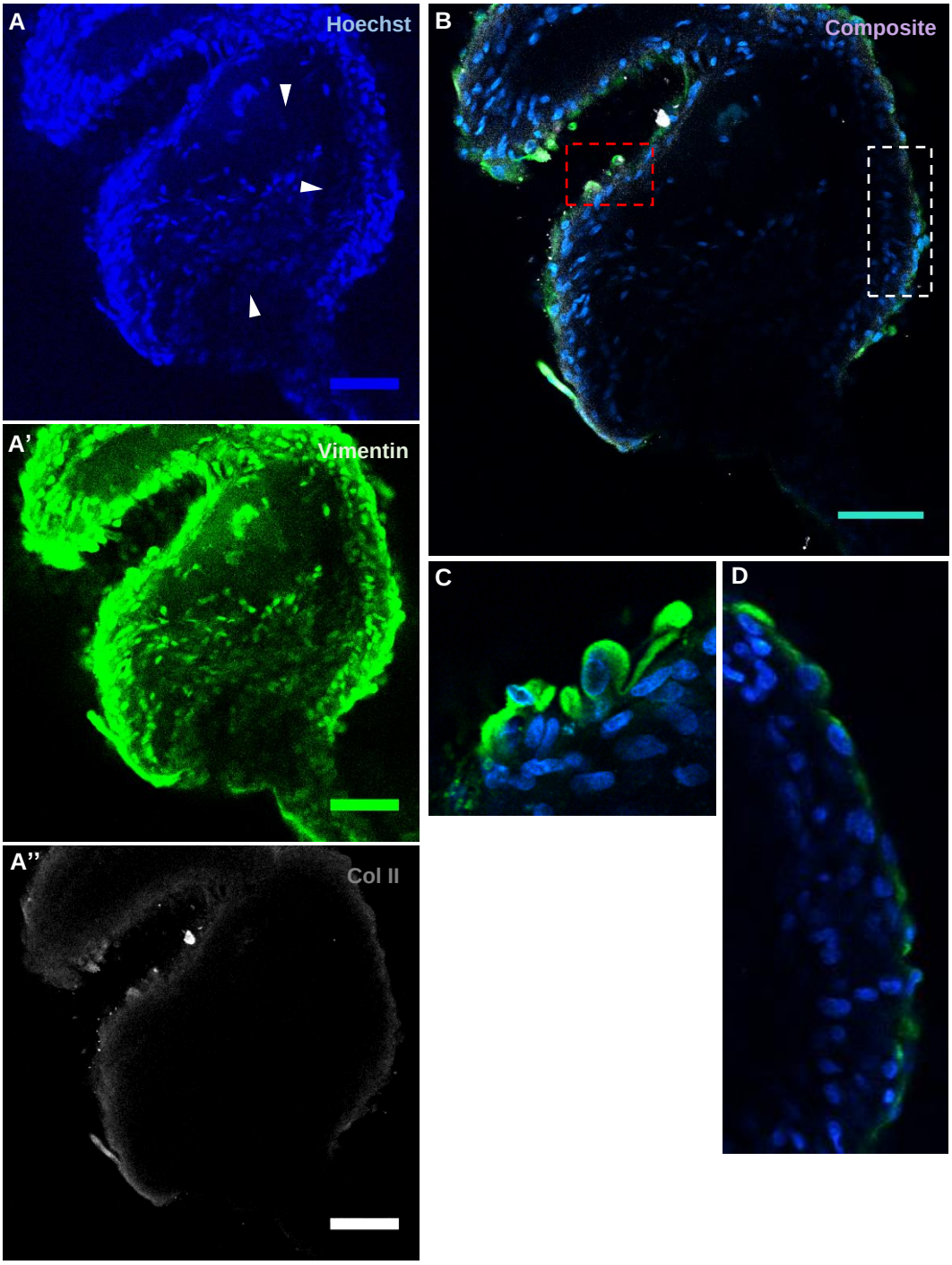

Figure 5.14. Expression of Collagen II and Vimentin at 21-day incubation in a section of a chondrogenically differentiated CSPCs bioprinted in alginate/cellulose. (A-A'') Two-photon confocal images of a CSPCs construct stained for Vimentin (green), Collagen II (grey) and counterstained with Hoechst (blue) at a depth of -215µm. Focal high expression of Vimentin and Collagen II staining around the surface of the bioprint like that seen at -125µm. Some regions of the bioprint at this depth are void of signal (white arrowheads). **(B)** Low magnification image of composite stain demonstrates well defined network of cells at the surface. **(C)** High magnification image (red dashed box in (B)) showing cell morphology. **(D)** High magnification (of white dashed box in (B)) demonstrating tight cellular network at the surface. Scale bars: 100µm.

5.1.4 Expression of cartilage markers in 3D bioprinted CSPCs laden alginate/cellulose bioink in a CAM in-vivo model

In vitro cultures of bioprinted CSPCs in alginate/cellulose bioink over both time points did not demonstrate cartilage ECM deposition. To assess this bioink further as a suitable hydrogel for chondrogenesis, the chick chorioallantoic membrane (CAM) system was used. Specifically, assessment of improved chondrogenic differentiation was the reason for using this model. This culture platform provides an easier and less cumbersome, efficient alternative to murine models. The CAM model allowed cell laden bioprinted constructs to be grafted without provoking a host immune response (chick embryo is immune deficient until late development) and importantly CAM vasculature development provided nutrient supply to the grafts.

For these experiments, another normal CSPC line, CH90, labelled with mCherry^{+} (P11) was used instead of CH105, as fluorescently labelled cells within the construct would be easier to identify by immunofluorescent microscopy and could be distinguished from host cells. The cell/bioink mixing protocol and cell density ($1x10^{6}$ cells/ml bioink), print speeds, print infill% and print pressure were identical to the in-vitro studies using CH105. Bioprints were cultured in control expansion media and chondrogenic media for 3 weeks prior to grafting on CAM (Pre-differentiated) at day 7 of egg incubation. CAM grafts were monitored daily and harvested after a further 7 days.

5.2.4.1 CAM graft macroscopic appearance

Bioprinted grafts appeared well attached to the CAM for both control and chondrogenic groups. After 7 days of incubation, CAM vasculature was well developed with a rich network of neo-vessels that had encircled the grafts in the typical wheel spoke pattern (Fig 5.15). All grafts adhered to the underlying CAM. Over the 7 day incubation, there were no obvious physical changes to any of the grafts.

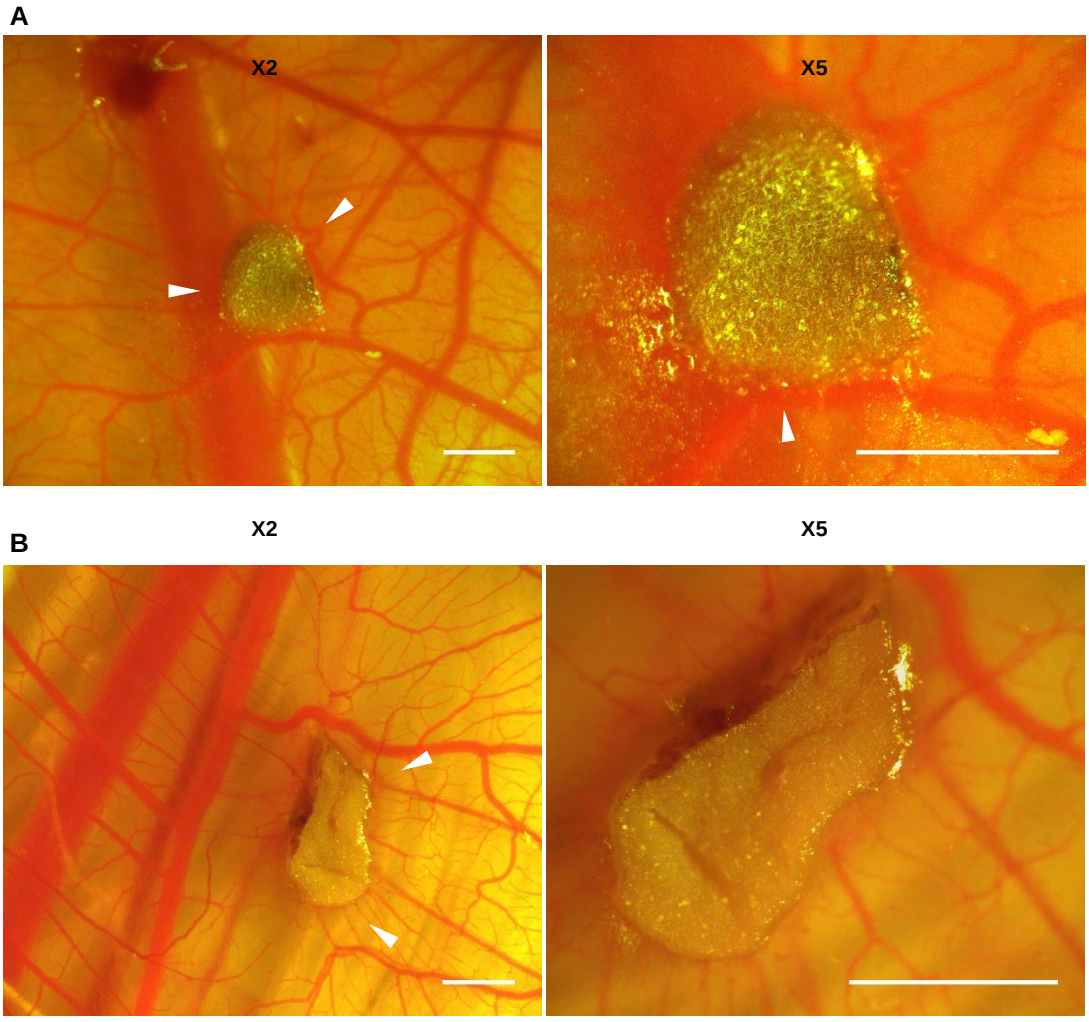

Figure 5.15. Macroscopic view of 21-day pre-cultured control and pre-differentiated bioprints of CH90 CSPCs in alginate/cellulose bioink. (A) Low and high magnification image of control bioprint placed on CAM 7 days after grafting. Note vascularisation of the CAM (white arrowheads) and adhesion to the graft. **(B)** Low and high magnification of chondrogenically pre-differentiated bioprint placed on CAM 7 days after grafting. CAM vascularisation and adhesions to graft are also present. Scale bars: 1000µm.

5.1.4.2 Histological analysis of paraffin embedded sections of 3D bioprinted constructs

In order to characterise and assess the CAM grafts for the presence of cartilage ECM markers – collagen, GAGs and proteoglycans, harvested grafts were paraffin embedded and sectioned to 5µm thick slices and stained with Picrosirius red and Toluidine blue.

Toluidine staining of control group bioprinted constructs demonstrated positive staining of cell nuclei throughout the sample with cells surrounded by loose matrix. The bioprinted constructs showed similar ragged edges with fragmented regions similar to control samples from in-vitro culture. Expression of collagen bundles was weak with negative Picrosirius red staining both under brightfield and polarised light microscopy. Blood vessel infiltration into the graft was not evident and the CAM had detached from the graft (during specimen paraffin embedding) in all control samples (Fig 5.16).

Surface regions of chondrogenically differentiated bioprinted constructs were moderately positive for Picrosirius red staining as were focal regions at central areas. The remaining bioprinted constructs expressed weak positive staining for collagen. Picrosirius red stain with polarised light demonstrated moderate collagen birefringence at surface regions and around central areas where there appears to be micro-cracks in the samples (Fig 5.17).

Chondrogenic differentiated grafts stained positive for Toluidine blue for cell nuclei (cells identified within lacunae) and for dense tissue surrounding the bioprint, but strong expression of ECM proteoglycans and GAGs was not evident within the main body of the sample (Fig 5.17). The CAM tissue remained intact and adherent to the bioprint. In central areas of the bioprint, strongly positive Toluidine blue staining was associated with focal cellular density with cells of different morphology to the surrounding embedded CSPC`s (Fig 5.18). These were also identified in other biological replicates (Fig 5.19).

In summary, alginate/cellulose bioink seeded with CSPCs failed to demonstrate significant cartilage like ECM and tissue in both in-vitro and in-vivo platforms. An alternative bioink more conducive to chondrogenesis would be required. The potential for fibrin as a suitable alternative bioink is discussed later in this chapter.

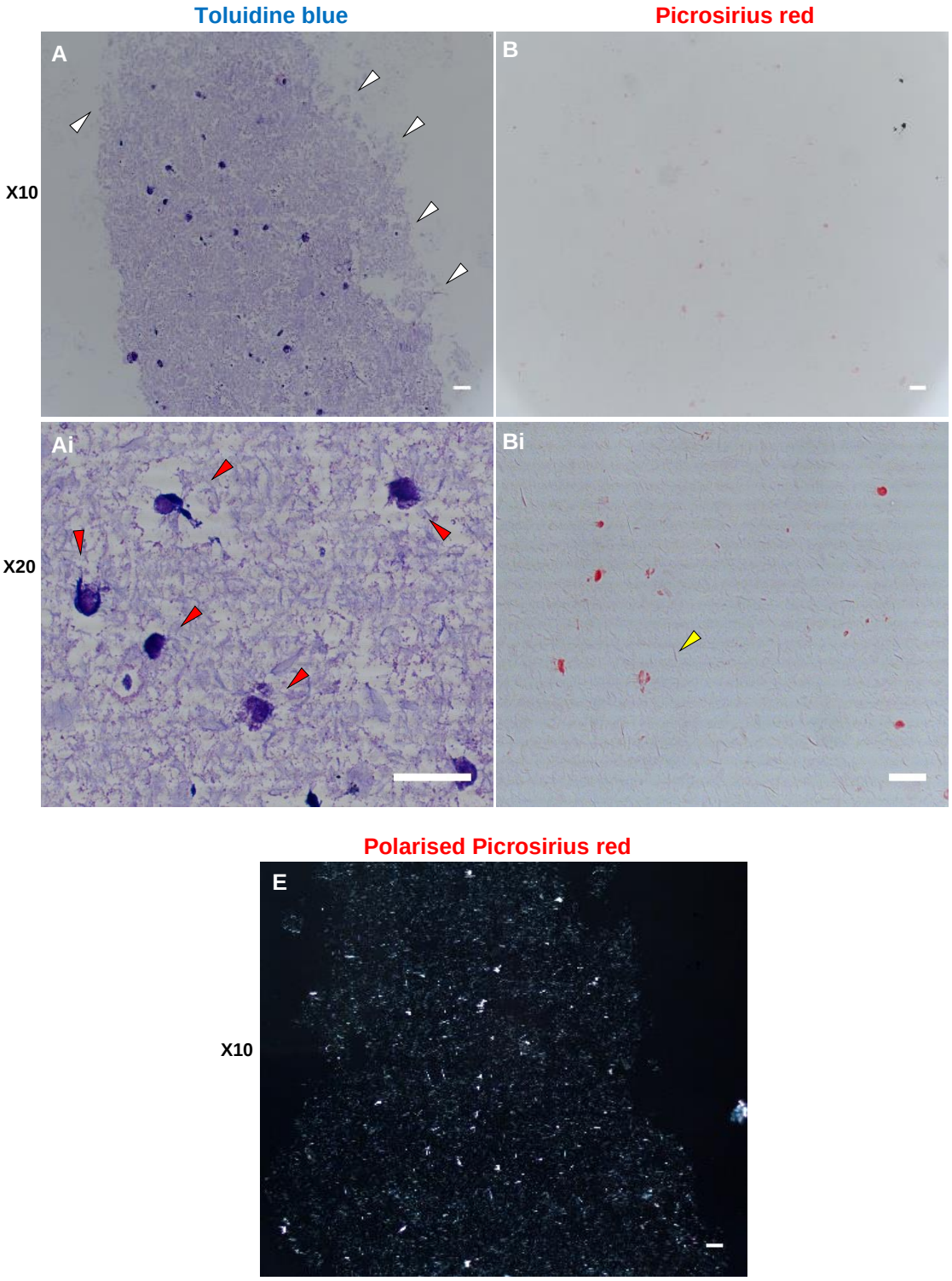

Figure 5.16. Toluidine blue and Picrosirius red staining of an undifferentiated (control) bioprinted construct grafted onto the chick chorioallantoic membrane (CAM). (A) CSPCs are positively stained for Toluidine blue and are found within a loose matrix which demonstrates fragmentation at the periphery (white arrowheads). (Ai) Higher magnification showing positively stained cells (red arrowheads). (**B)** Low magnification showing negative Picrosirius stain and at higher magnification (Bi) weakly positive collagen (yellow arrowheads). **(C)** Polarised light microscopy is also negative for collagen fibres. Scale bars: 100µm.

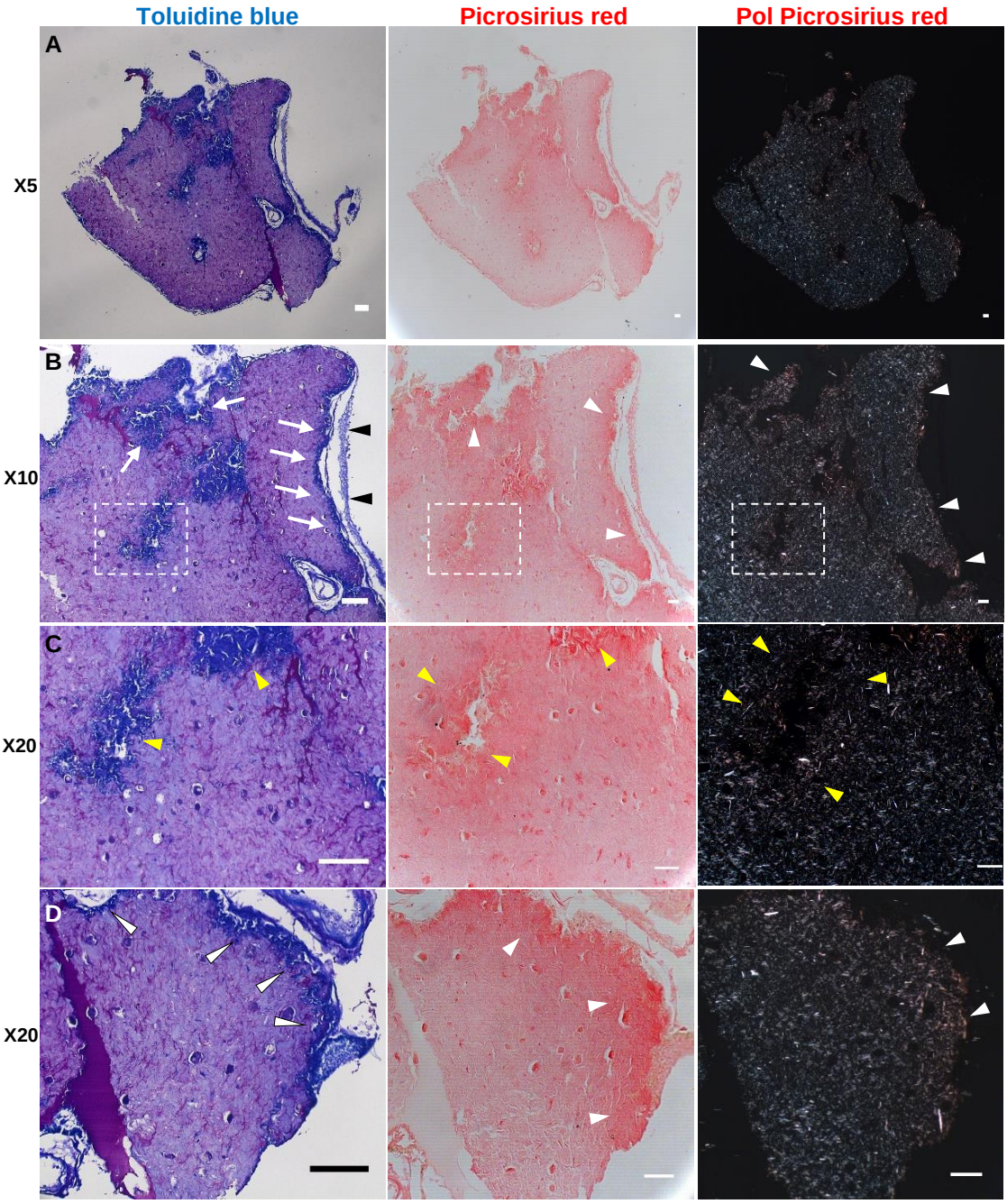

Figure 5.17. Toluidine blue and Picrosirius red staining of a chondrogenically differentiated bioprinted construct grafted onto CAM. (A) Section of a bioprinted construct showing dense matrix with well-defined margins and little fragmentation **(B)** Expression of GAGs at the construct surface by positive Toluidine blue staining (white arrows). The CAM has remained attached to the sample (black arrowheads). Expression of collagen is noted around similar focal points with moderate signal of Picrosirius red in brightfield and polarised light microscopy (white arrowheads). **(C)** High magnification of dotted box in (B), central samples areas express GAGs with Toluidine blue stain and collagen with Picrosirius red (yellow arrowheads). **(D)** High magnification of peripheral sample region further demonstrating expression of GAGs and collagen at the outer regions of the bioprint. Scale bars: 100µm.

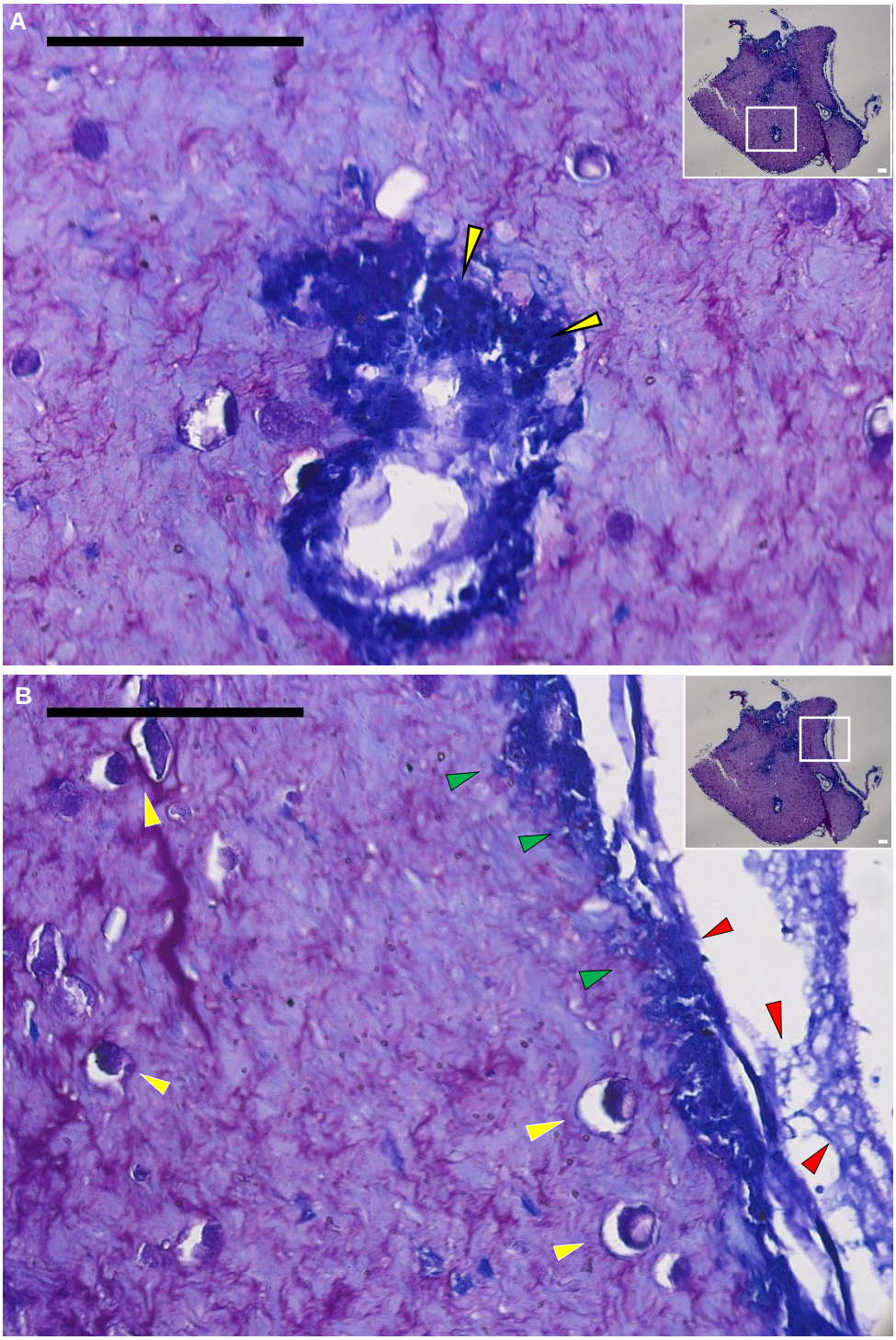

Figure 5.18. Toluidine blue staining of chondrogenically differentiated bioprints in CAM. Same sample as seen in 5.17**. (A)** High magnification of central region within bioprint (boxed region from inset image) with strongly positive Toluidine blue stain and dense cellular infiltrate (yellow arrowheads). **(B)** Attachment of CAM to sample (red arrow heads) surface which is positively stained for GAGs (green arrowheads). Round cell morphology is noted. Scale bars: 100µm.

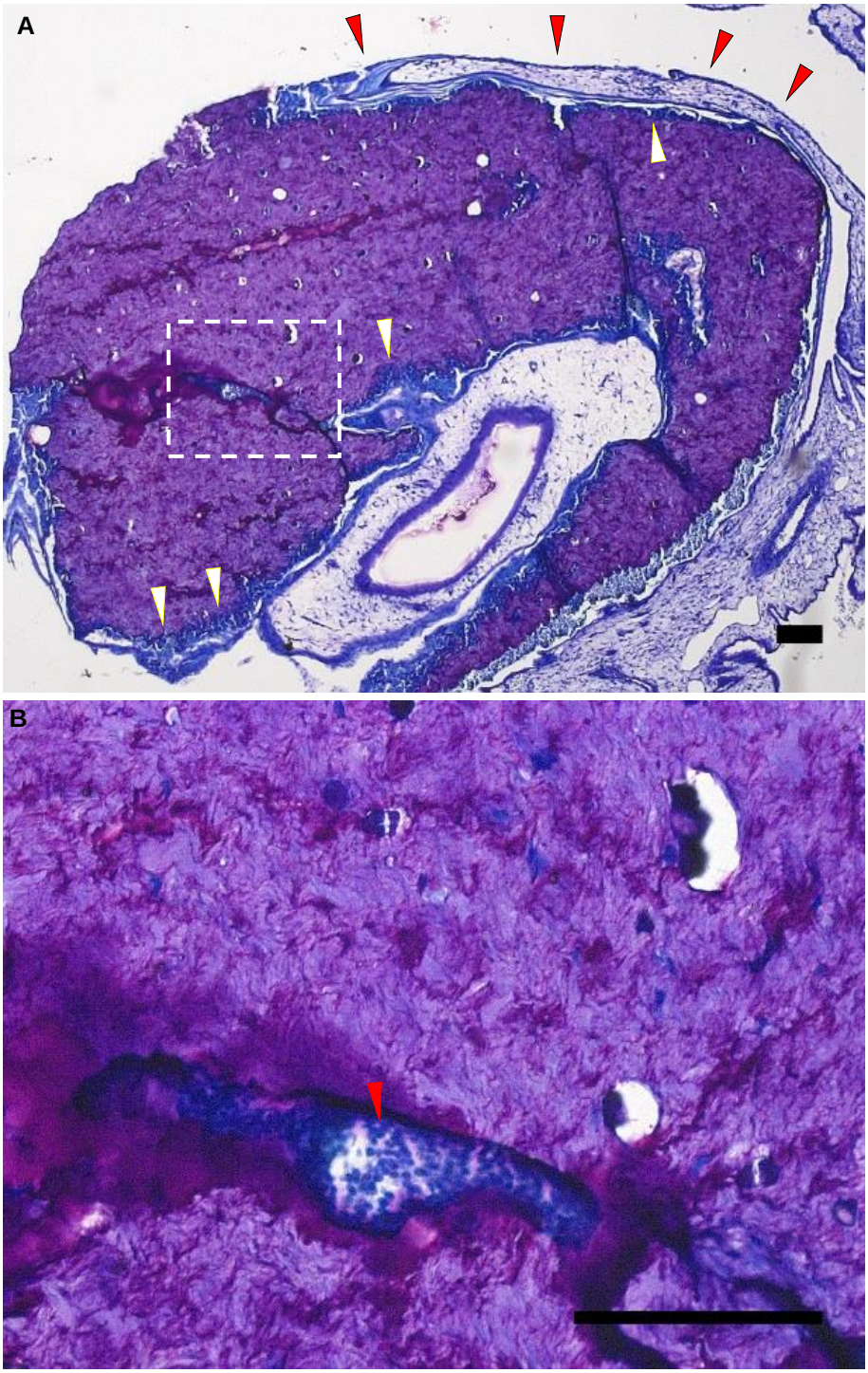

Figure 5.19. Toluidine blue staining of chondrogenically differentiated bioprints (2nd biological replicate) in CAM. (A) CAM graft is still adherent to bioink print (red arrowheads) and expression of GAGS at the surface of the print on positive Toluidine blue staining (yellow arrowhead). **(B**) High magnification of white dotted box in (A), cell nuclei of dense cellular infiltration in a well contained focal area are identified within a central region of the sample (red arrowhead). Scale bars: 100µm.

5.2.5 Optimisation of PCL printing for sandwich design septal graft

PCL polymer was chosen as a material for the sandwich design due to its excellent biocompatibility, mechanical strength, predictable degradation, and ease of print. Our laboratory 3D bioprinter with 2 print heads enabled an aluminium cartridge to be attached and heated to required temperatures. Given that there were no previous studies on PCL printing in our laboratory, new printing protocols were developed for this project. The process of printing PCL has many similarities with cell bioprinting. Briefly, this involves the design of the print as an object using 3D CAD software which is typically saved as an STL file which is then converted into a 3D print file (G-Code) that provides the specific instructions of print parameters to the printer. Converting STL files to G-Code was done using Slic3r printing toolbox software which was obtained from the manufacturer webpage (CELLINK) but is widely available for free.

Printing parameters were controlled by a combination of manipulation of printer software settings and physical options on the printer directly (Inkredible + Printer, CELLINK).

5.2.5.1 Optimisation of printing parameters – Software controlled

Important software (Slic3r) controlled parameters:

- Print speed mm/s
- Infill pattern
- Infill density
- Print head temperature

Printing PCL standardised for pressure and temperature (650kPa at 130°) at over 5mm/s resulted in poor layering of PCL bead. Higher print speeds did not allow extruded PCL to stick to the print bed or PCL layers beneath as the print nozzle movement exceeded the rate of PCL extrusion out of the metal micro tip. At 5mm/s the flow rate and print head movement were better matched.

Infill pattern options include rectilinear, line concentric, honeycomb, grid, Archimedean chords and spiral. Two infill patterns were tested that would result in mesh like prints, grid and rectilinear. At print speed of 5/mms, 500µm nozzle tip, 50% infill density, 650 kPa pressure and 130°C PCL temperature a 10x10x1mm square was printed using the 2 different infill patterns. Rectilinear infill pattern created the best construct mesh-like pattern and when infill density was increased to 90% this was improved further (Fig 5.20).

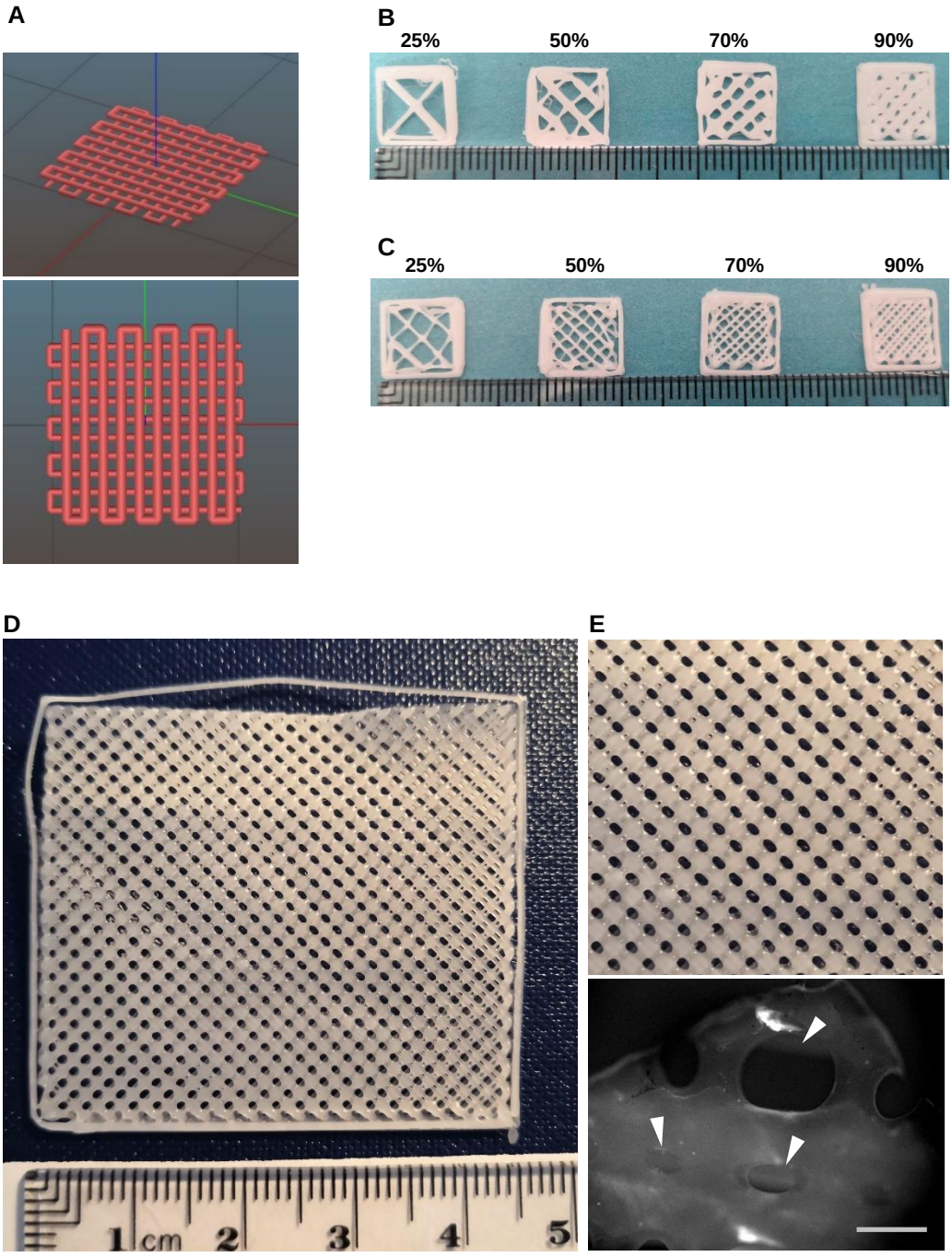

Figure 5.20. PCL printing Grid and Rectilinear infill patterns. (A) Print pattern can be manipulated with Slic3r software, Rectilinear demonstrated. **(B)** Grid infill pattern with increasing infill density. **(C)** Rectilinear infill pattern with increasing infill density up to 90% demonstrates mesh like result. **(D)** Large scale Rectilinear infill pattern at 90% density. **(E)** High magnification of (D) and brightfield image of print holes showing variable sizes (white arrowheads). Most sizes ranged from 600x550µm to 350x200µm. Scale bar: 500µm**.**

5.2.5.2 Optimisation of printing parameters – Printer controlled

Important printer-controlled parameters:

- Extrusion pressure in kPa – dependent on pump used – up to 700 kPa
- Live print head temperature adjustment 1-130°C
- Nozzle diameter – 500µm or 600µm micro metal precision tapered tip diameter for PCL printing

Initial PCL printing was performed at 130 kPa based on manufacturer (CELLINK) protocol. However, at this extrusion pressure, very little PCL flow was achieved. At nozzle diameters of 500µm and 600µm, optimal print pressure was found to be 650kPa. This resulted in a constant steady flow of PCL through both micro tip nozzles during printing.

Although PCL has a melting point of about 60°, optimal print head temperature was 130°C. By changing the print head temperature and keeping other parameters constant (print speed, nozzle diameter, extrusion pressure), PCL flow was found to be most consistent at 130°C. This higher temperature maintained the PCL at an appropriate viscosity to permit printing during. Cooling of the PCL through its passage from the aluminium cartridge (heated by the print head element) through to the micro-tip nozzle is a likely explanation of why the higher temperature is required to compensate for this heat loss.

Micro tip metal nozzle diameter was available at the time of this thesis only in 500µm and 600µm sizes. The 500µm nozzle resulted in more accurate prints with higher fidelity than the 600µm and therefore all PCL prints were undertaken using the smaller diameter tip (Fig 5.21).

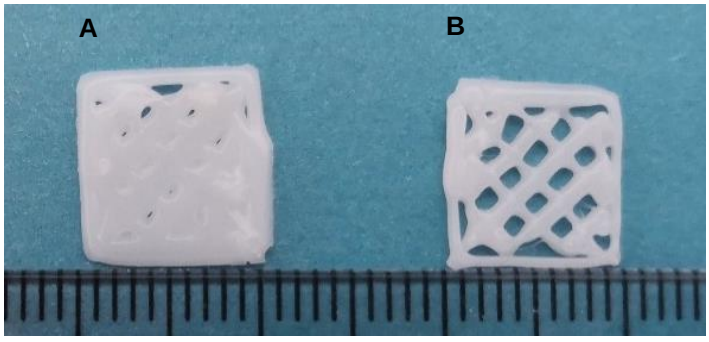

Figure 5.21. 10x10x1mm PCL prints using Grid infill pattern with 70%infill density. **(A)** 600µm metal tip print fidelity. **(B)** 500µm metal tip print fidelity.

The protocol for fabrication of the PCL mesh produced in Fig 5.20 (D), was deemed to be suitable for the preliminary sandwich experiments. Pore/hole size was assessed to be appropriate given that the primary role of the PCL polymer sheet was to provide strength for the inner hydrogel. For diffusion of nutrients and cells through the PCL mesh into the central hydrogel, these sizes were acceptable.

5.2.6 Analysis of CSPCs in a fibrin-based hydrogel.

The ability of alginate/cellulose bioink to provide a microenvironment that is inducive to cartilage tissue generation, despite demonstrating high CSPCs viability, appears very limited based on data presented. An alternative hydrogel was therefore investigated. Fibrin was considered favourably as it is already FDA approved and used clinically. The purpose of these initial studies was to analyse the behaviour of CSPCs in a 3D fibrin environment and their ability to form cartilage ECM within it. At the time of this thesis, fibrin as a commercially produced bioink was not available, so was prepared in the laboratory by myself but not in an injectable form that could be 3D bioprinted. The mixing protocol of the 2 components (fibrin with thrombin) and the details of the study design are described in chapter 2 section 2.9 but briefly, fibrin constructs were generated at a density of $1x10^6$/1ml fibrin/thrombin and incubated in chondrogenic and control media for 3 weeks. They were then paraffin embedded and sectioned for histological staining with Picrosirius red and Toluidine blue.

5.2.6.1 Histological analysis of CSPC laden fibrin hydrogel constructs

Fibrin constructs were analysed at two times points, day 0 and day 21. Day 0 control constructs under brightfield microscope demonstrated an even distribution of cells within the loose fibrin matrix, but a band like dense layer of cells was noted just under the surface. Cell morphology was mostly round throughout the sample. Toluidine blue stain for GAG expression was negative (Fig 5.22). As expected, there was no expression of collagen on picrosirius red straining either (Fig 5.23).

Toluidine blue staining for control samples at day 21 demonstrated a change of cell shape to more spindle like. The fibrin matrix appeared dense and stained more positively for Toluidine blue than at day 0. In some region of the sample, cells appeared to have begun to self-organise with an intimate network of cells (Fig 5.24). Picrosirius red stained positive for collagen in surface regions and confirmed the appearance of cells becoming organised.

Interestingly, Picrosirius red staining under polarised light demonstrated yellow-green collagen birefringence around the same regions indicating collagen deposition at these points (Fig 5.25).

By day 21, Toluidine blue staining was positive for the chondrogenic group with expression of GAGs in some regions of the constructs in a band-like orientation and in some focal areas of intense staining (Fig 5.26). Histological resemblance to cartilage however was not specifically noted. The orientation of the sample adds complexity to the staining interpretation as it appears the central region may reflect cells that have attached to the fibrin from the culture well plate rather than representing real changes within the fibrin. However, there are areas within the fibrin that are intensely staining that do appear to be originating from the fibrin matrix.

Picrosirius red staining viewed in brightfield and polarised light demonstrated high expression of collagen fibres in the chondrogenic differentiated group. A band like Picrosirius red stain was noted with focal points of yellow-red and green birefringence indicating different orientation of collagen fibrils (Fig 5.27).

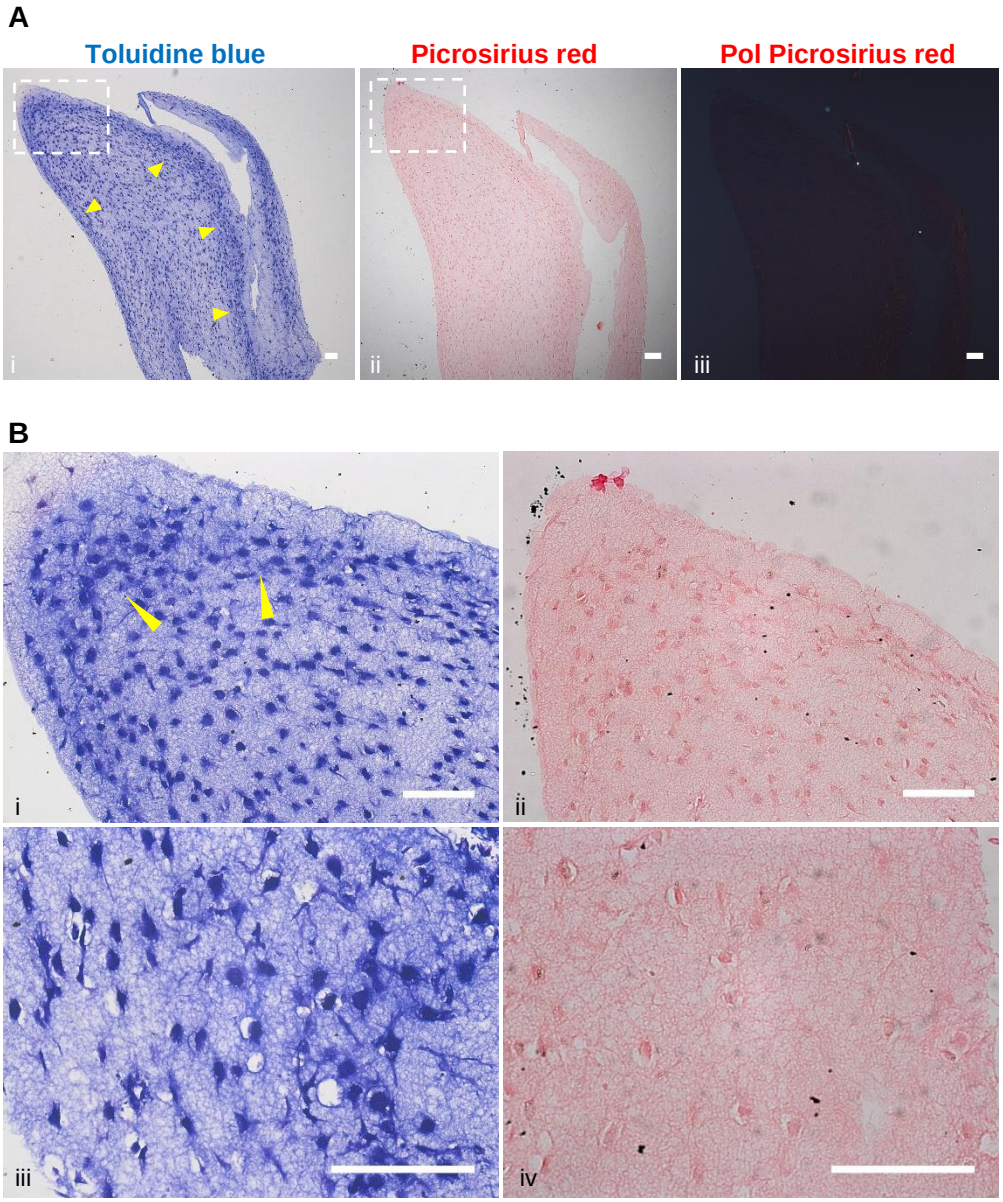

Figure 5.22. Toluidine blue and Picrosirius red staining of day 0 CSPC laden fibrin constructs. (A) Low magnification of the construct demonstrates a band of high cellularity with Toluidine blue staining (yellow arrowheads (Ai)). (Aii) Picrosirius red stain in brightfield and (Aiii) polarised light. **(B)** Higher magnification image of dashed line box in (A). Round cell and nuclear morphology, dense cells in the subsurface region (yellow arrowheads). Expression of ECM GAGs and collagen is negative on both stains. Scale bars: 100µm.

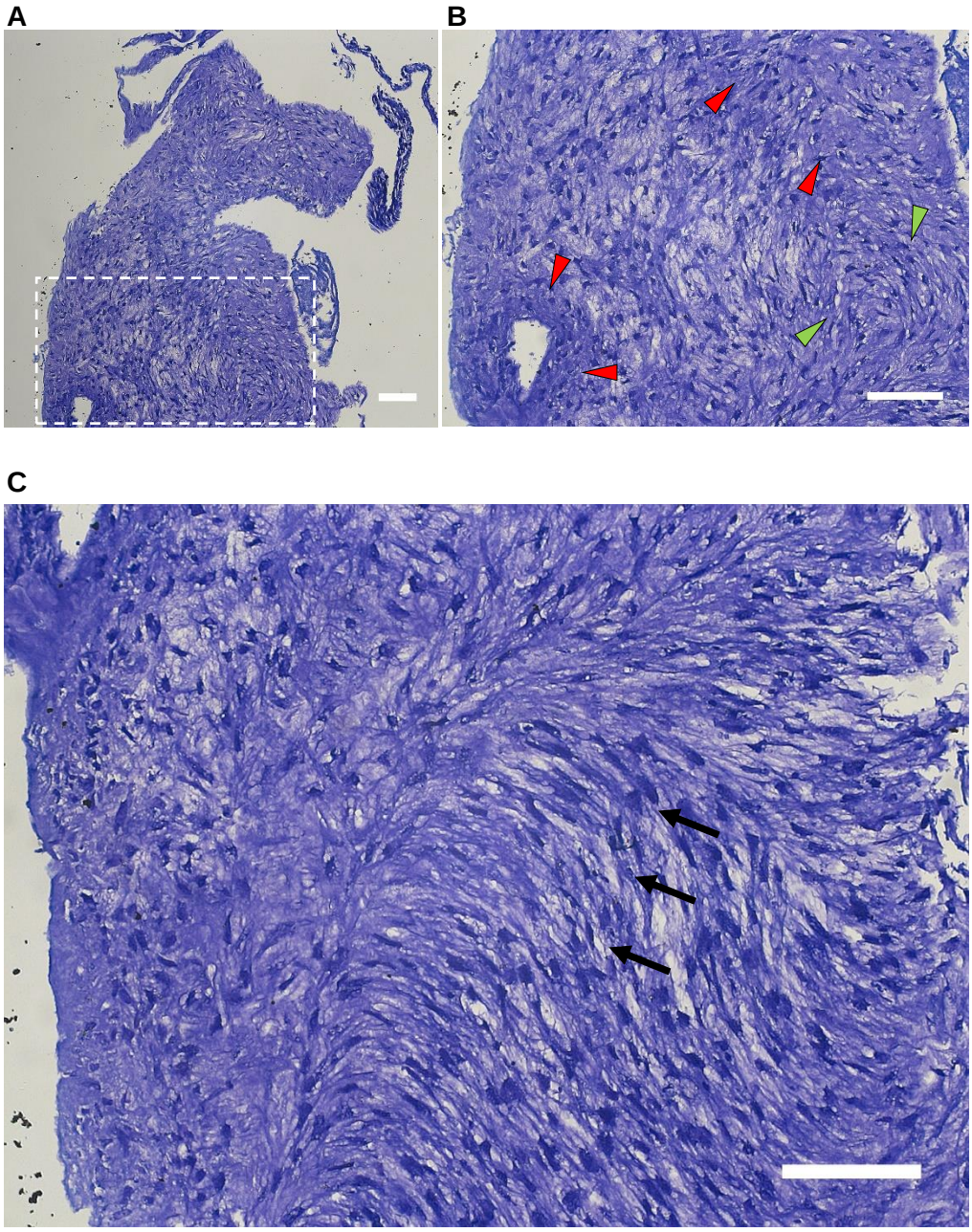

Figure 5.23. Toluidine blue stain of control CSPC laden fibrin constructs at day 21. (A) Low magnification image of construct. **(B)** Magnified image of dashed line box in (A), increased Toluidine blue staining is noted in some regions (red arrowheads). Cellular morphology more spindle like in areas (green arrowheads). **(C)** Cell orientation appears organised in some regions and different to cells closure to surface (black arrows). Scale bars: 100.

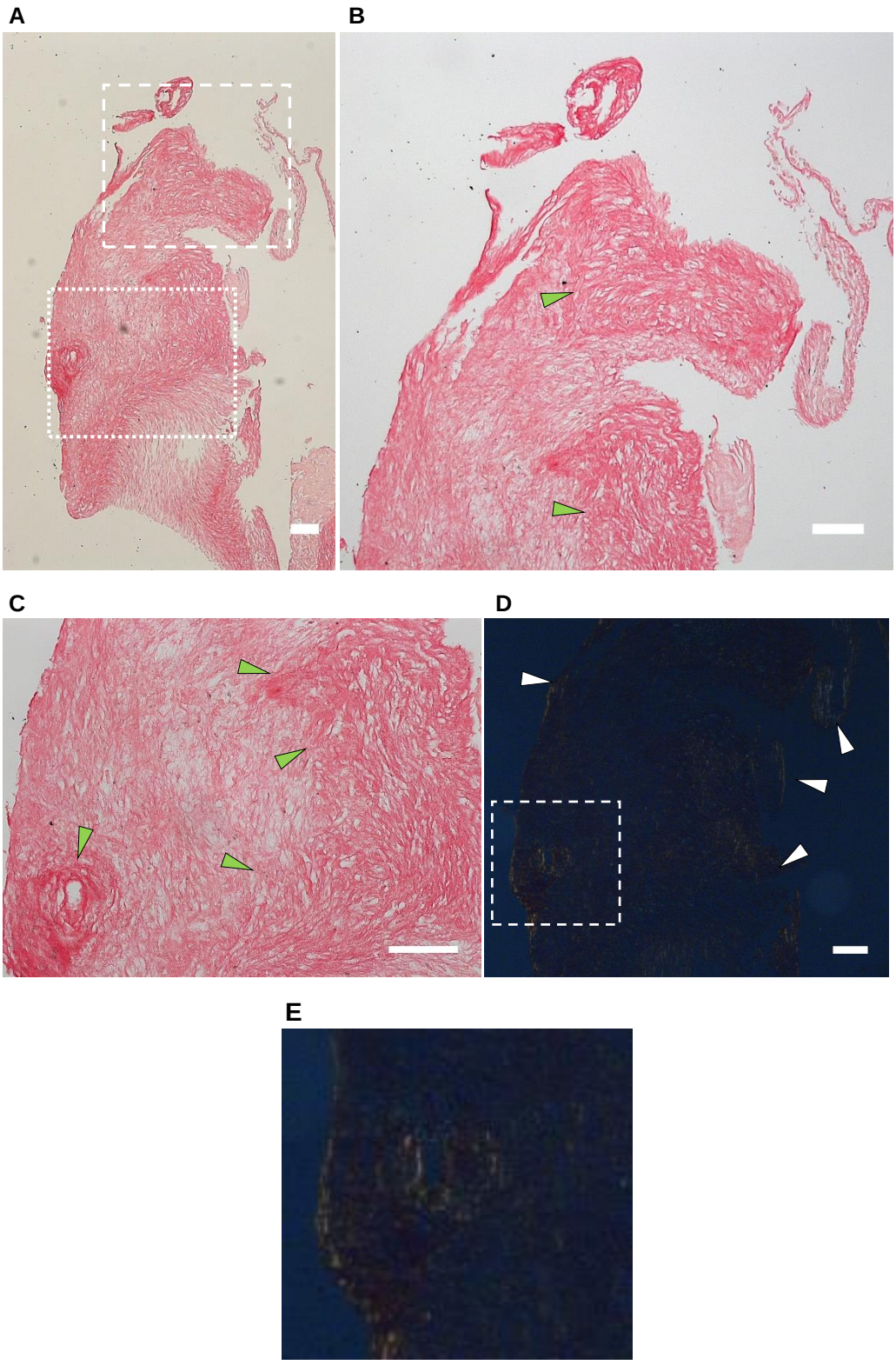

Figure 5.24. Picrosirius red stain of control CSPC laden fibrin constructs at day 21. (A) low magnification brightfield image of construct. (B) Higher magnification of dashed line box in (A). Variable staining of Picrosirius red, expression of collagen is higher in areas (green arrowheads). **(C)** High magnification of dotted line box in (A). Increased staining of Picrosirius red in marked regions (green arrowheads). Polarised light microscopy showing yellow collagen birefringence (white arrowheads). **(E)** High magnification of dashed box in **(D).** Positive Picrosirius red staining on polarised light microscopy. Scale bars: 100µm.

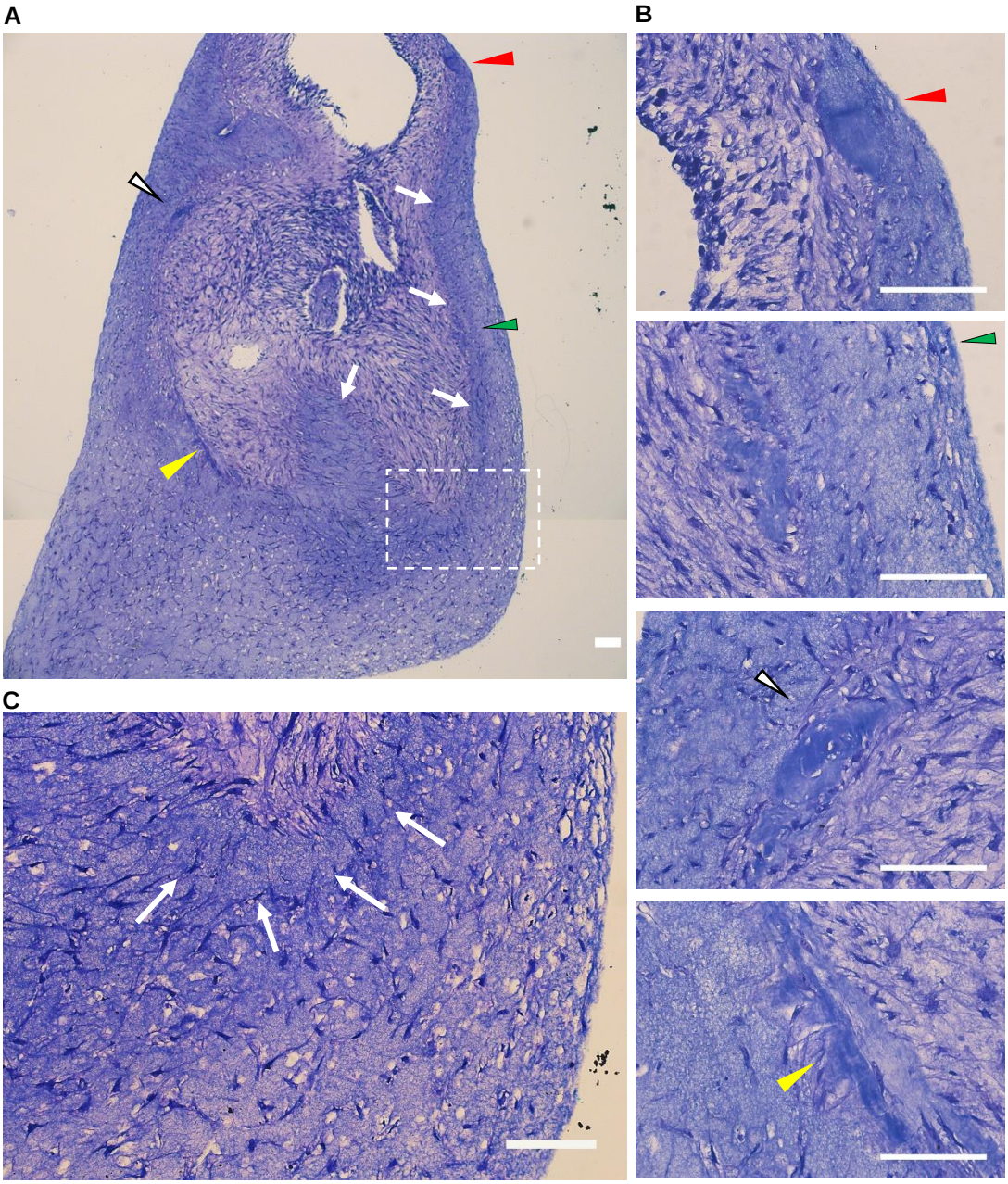

Figure 5.25. Toluidine blue stain of chondrogenic differentiated CSPC laden fibrin constructs at day 21. (A) Low magnification image of construct, intense focal staining highlighted with arrowheads, band-like intense staining (white arrows)**. (B)** High magnification of focal areas of intense Toluidine blue staining (arrowheads represent their matched arrowheads in (A). **(C)** High magnification of dashed box in (A), positive Toluidine blue staining region (white arrows). Scale bars: 100µm.

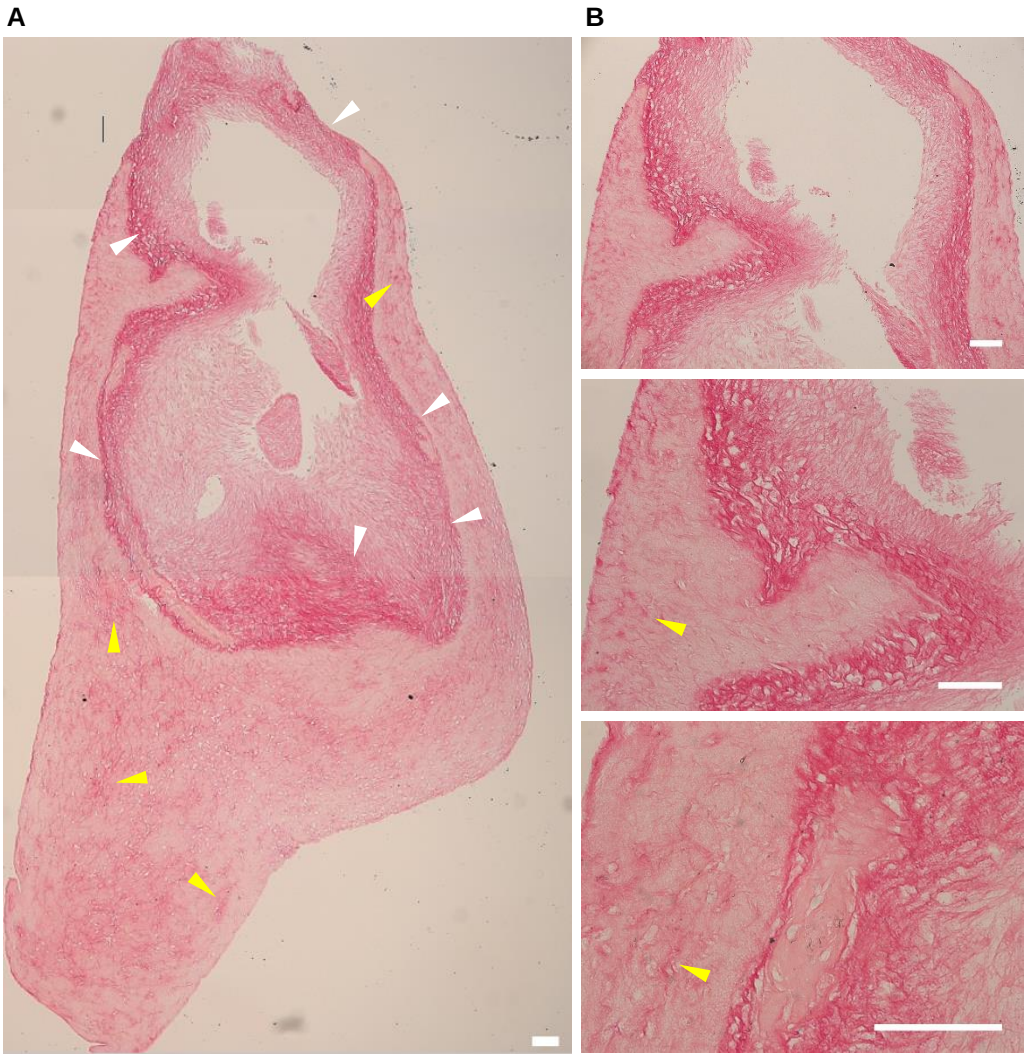

Figure 5.26. Brightfield images of Picrosirius red stain of chondrogenic differentiated CSPC laden fibrin constructs at day 21. (A) Low magnification image of construct. Expression of collagen appears intense in certain regions (white arrowheads) in a band like pattern and specular in others (yellow arrowheads). **(B)** High magnification of Picrosirius red positive staining within construct with speckled positive staining (yellow arrowheads). Scale bars: 100µm.

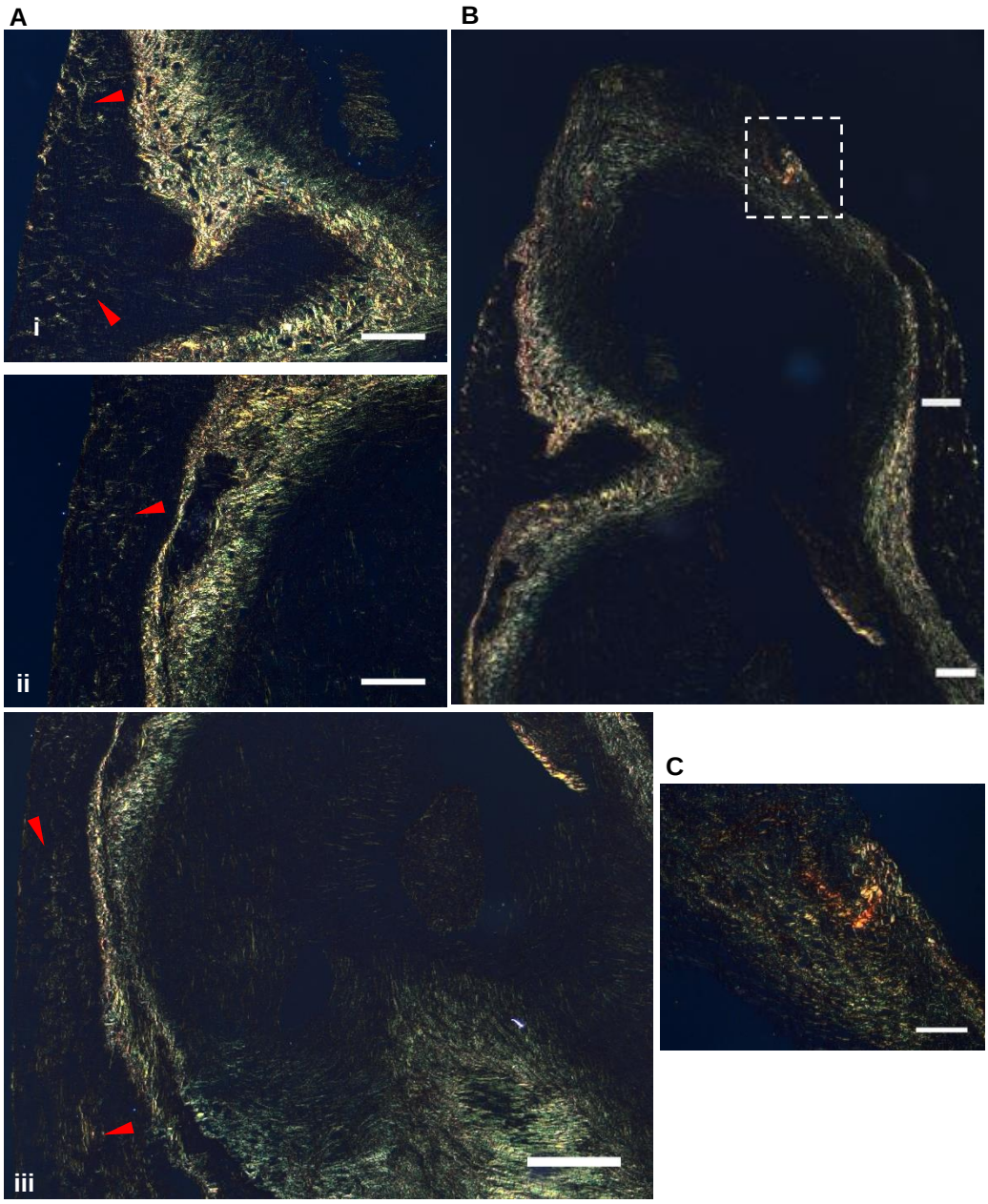

Figure 5.27. Polarised light images of Picrosirius red stain of chondrogenic differentiated CSPC laden fibrin constructs at day 21. (A) High magnification images of the left edge of the construct from top to bottom (i-iii). Speckled positive Picrosirius red stain (red arrowheads). **(B)** Expression of collagen fibres with yellow-green birefringence in band-like pattern as well. **(C)** Focal point of positive staining demonstrating red collagen birefringence (magnification of dashed box in (B)). Scale bars: 100µm.

5.2.6.2 Analysis of PCL fibrin sandwich construct in a CAM model

Staining of the 3 week chondrogenically differentiated fibrin constructs cultured in-vitro demonstrated deposition of collagen and GAGs by CSPCs. This fibrin once sandwiched between the two PCL layers will require enough nutrient supply to maintain cell viability and sustain chondrogenesis. To assess this, fibrin hydrogel was seeded with CSPCs at density of $1x10^6$/ml of fibrin and applied to a 1mm thick PCL disc (90% infill, rectilinear pattern)allowed to gel, then covered a by a second PCL disc to complete the sandwich design. This construct was then applied to CAM over 7 days and resulted in neovascularisation around the sandwich construct (Fig 5.28). These were harvested at day 7 egg incubation, paraffin embedded and sectioned for histological analysis *(analysis not completed due to COVID-19 closure of laboratory*).

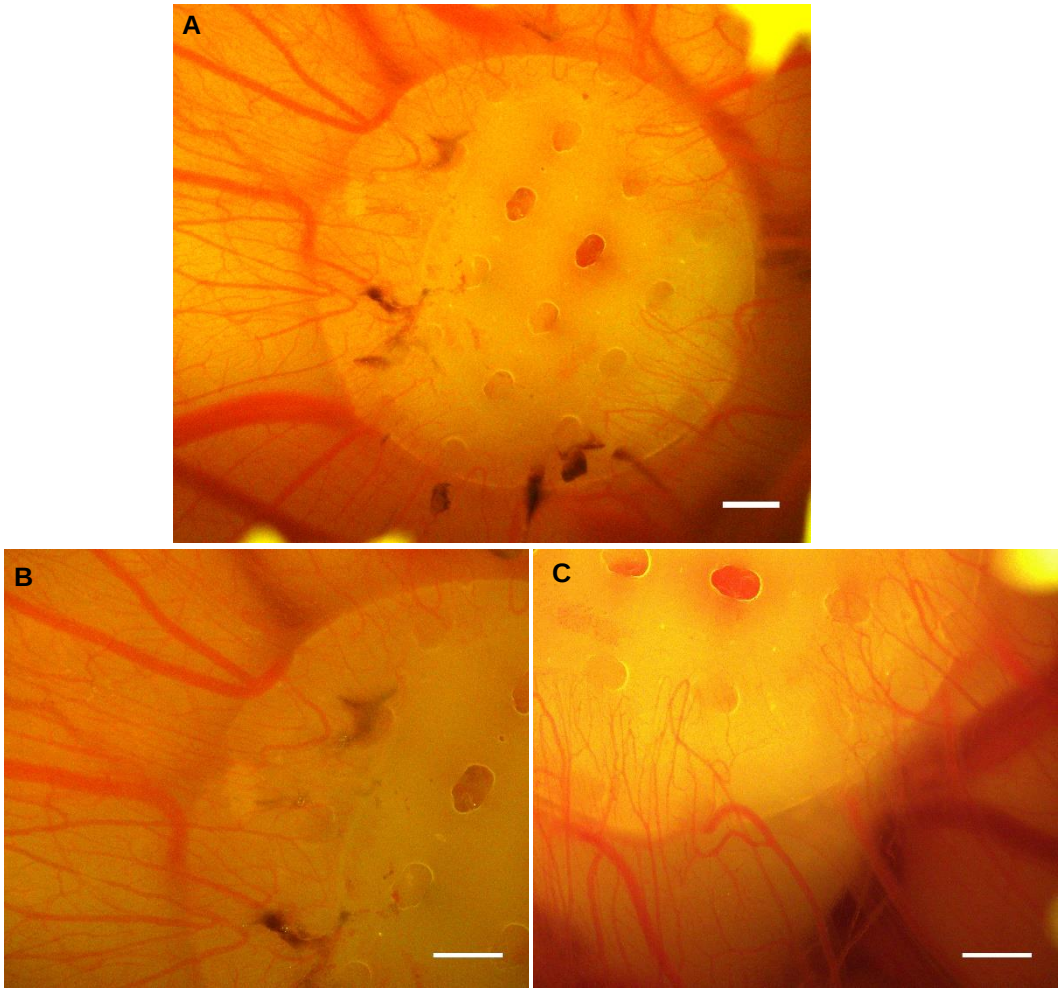

Figure 5.28. CAM grafts of PCL discs. PCL mesh printed with 500µm nozzle at 650kPa extrusion pressure and cut out with 8mm punch. **(A)** CAM response to graft with increase in vasculature and no sign of graft provoking an immune response or rejection macroscopically. **(B)** High magnification of top left corner of disc. **(C)** High magnification of bottom left corner of disc. Scale bars:100µm.

5.3 Discussion

The strategy for developing a nasal septal product using 3D bioprinting addresses some of the challenges faced with using Integra in a PLA pocket. In the previous chapter it was demonstrated that CSPCs and ADSCs seeded onto a collagen I matrix (Integra) deposited cartilage like ECM limited mostly to surface regions. Insertion of Integra into a PLA pocket also proved difficult. The use of 3D bioprinting technology as an alternative strategy to generate cartilage was then pursued, seeking to explore a different nasal product concept that does not require insertion of a hydrogel into a pocket, but that can be fabricated as a single construct. The objective in this chapter was to print cells in bioink directly onto PCL (for mechanical support), but analyses of differentiated bioprint constructs printed onto a sterile petri-dish first, failed to demonstrate any meaningful chondrogenesis. However, much has been learned from analysis of bioprinted constructs using these two cell lines.

During this thesis, commercially available alginate/cellulose bioink was used to print cells as developing a novel alterative bioink in our laboratory would have been incredibly time consuming and challenging. This study has for the first time, demonstrated that human auricular CSPCs can survive the stress of bioprinting and in this case the cross-linking required for alginate/cellulose bioink. Interestingly, contrary to what would be expected, RGD functionalised alginate/cellulose bioink resulted in reduced cell survival when compared to the non-functionalised bioink. However, bioink mixed with CSPCs failed to demonstrate any meaningful chondrogenesis in both in-vitro and in-vivo (CAM) models with insignificant deposition of collagen or GAGs. Given that bioprinted constructs were cultured over 6 months in-vitro, cartilage like ECM was expected but not observed. Alginate/cellulose bioink seeded with auricular CSPCs for cartilage tissue engineering appears to have limitations and does not offer an environment conducive to chondrogenesis. Possibly, alginate/cellulose biodegradability is mismatched with ECM deposition and therefore is restrictive on cells.

Markstedt et al. 2015, demonstrated that cell viability of human nasal chondrocytes printed with an alginate/cellulose bioink was 73% and 86% after 1- and 7-days 3D culture, this is consistent with results produced in this chapter (Markstedt et al., 2015a). Bioprinted constructs were also cross-linked using $CaCl_2$. In a further study by the same group, alginate/cellulose bioink printed with human nasal septum chondrocytes (final concentration $20x10^6$ cells mL^{-1}, lattice shaped constructs $4.8x4.8x1.0mm^3$) were cultured for 28 days in chondrogenic medium (Martínez Ávila et al., 2016).

Their study demonstrated that septal chondrocytes synthesized GAGs with accumulation of collagen fibrils within the pericellular space and territorial matrix surrounding the cells on transmission electron microscopy. Alcian blue staining for glycosaminoglycan appeared positive in many regions of their constructs.

The design for a septal product using 3D bioprinting was based on printing cells onto PCL using the same printer but given that the bioprinted constructs did not demonstrate cartilage ECM, printing cells onto PCL was not attempted. However, a PCL mesh printing protocol was still developed and optimised to aid in future attempts at printing cells onto PCL with an alternative bioink. This hybrid (bioink/polymer scaffold) design has many advantages and many recent studies by other authors share this approach. For example, Baena et al. 2020, printed human chondrocytes isolated from articular cartilage in alginate bioink, onto PLA by a volume by volume 3D fabrication procedure (Baena et al., 2019). They demonstrate that cells embedded in alginate bioink and printed onto PLA mesh survive the manufacturing process with 90% viability up to day 7 in culture. Using a printer that prints PLA by fused deposition modelling (FDM), they were able to print rigid PLA mesh scaffolds onto which cells could be printed on in a layer by layer fashion, allowing the PLA temperature to decrease before addition of the next layer. Kim et al.2016, also developed a hybrid approach to tissue engineering by simultaneous bioprinting of mouse embryonic fibroblasts in alginate hydrogels with PCL in direct contact with the cells and demonstrated excellent cell viability and proliferation over 14 days (Kim et al., 2016). Interestingly, Schuurman et al. 201, generated hybrid cell laden alginate PCL constructs and found similar high cell viability after printing (Schuurman et al., 2011). They suggested that there may be sufficient cooling of the PCL polymer as it is deposited and comes into direct contact with cells to allow cell survival in the hydrogel. In another similar method, Ruiz-Cantu et al. 2020, used sheep condyle chondrocytes printed in gelatine methacrylate (GelMA) into a PCL mesh to form hybrid constructs for nasal reconstruction and demonstrated cell proliferation and deposition of cartilage ECM within the constructs (Ruiz-Cantu et al., 2020). The interaction of chondrocytes with PCL did not interfere with their behaviour. However, despite all these studies demonstrating high viability of cells printed in contact with PCL, they all incorporate a mesh design that spans the full height of the construct. This is problematic as the resorption of PCL in central regions would be unpredictable and could lead to regions with a nasal product without cartilage. A design whereby cells are printed onto a sheet of PCL or mesh of PCL and then covered with another sheet or mesh is preferable as it avoids this problem.

Alginate/cellulose bioink did not provide a chondrogenic inductive environment for CSPCs to deposit cartilage like ECM. Therefore, fibrin was assessed as an alternative hydrogel. Fibrin bioink was not commercially available at the time of this thesis, so surgical grade fibrin (applied clinically for haemostasis) was used. The strategy for fabricating a nasal septal product depended on fibrin manually mixed with CSPCs then sandwiched between two-thin layers of PCL mesh sheets.

In a similar manner to the PLA pocket, a PCL polymer scaffold can provide mechanical support to a bioprinted construct until cartilage ECM is deposited by the cells to form mature cartilage. The advantage of PCL is that it can be printed by the same bioprinter and therefore a complete construct can be printed composed of cells directly printed onto PCL scaffold (latest 3D printers can also print PLA with cells). Initial experiments were designed to characterise CSPCs behaviour in fibrin and their ability to deposit cartilage-like ECM. Toluidine blue and picrosirius red staining demonstrated that CSPCs within fibrin deposited collagen and GAGs in both control and chondrogenic differentiated groups, but more in the later. However, although immediately after seeding cells were evenly distributed, differentiation occurred in patches and assessment of cell behaviour of fibrin over months was not done (compared to Integra and bioink). Extended differentiation time is likely to be crucial to fully characterise cell behaviour in fibrin.

In this study, fibrin was mixed with cells and then mixed with thrombin to begin gelation. The volumes of fibrin and thrombin were chosen purely to allow sufficient time to pipette the mixture and apply to the PCL sheet (about 10 seconds before the mix began to gel). However, the physical properties of this mix may have an influence on cell behaviour and viability. Kim et al in demonstrated that ADSC mixed with different ratios of thrombin and fibrin results in different deposition of collagen type II and therefore chondrogenic potential. Gel stiffness appears to play an important role in ADSC chondrogenic differentiation and behaviour with fibrin. Furthermore, high concentration formulations resulted in inhibition of hydrogel degradation (Kim et al., 2020). The effect of different fibrin and thrombin concentrations mixed with this auricular CSPC line would provide further understanding and development of a fibrin based bioink. Another variable that would be interesting to investigate is the effect of cell numbers on chondrogenesis. A standard $1x10^6$cells/ml hydrogel was used in this study but variation in cell numbers seeded may produce different significant results.

Printing PCL offers many advantages over PLA, in particular its lower melting point and therefore reduced heat injury to cells. Printing PCL by a pneumatic based microextrusion system involves control of several parameters including print speed, print density, PCL print temperature, nozzle diameter and print pressures. In this chapter it was demonstrated that PCL printing can be optimised to generate reproducible mesh sheets that can be predictably seeded with CSPCs seeded in a fibrin hydrogel. These constructs appeared to be biocompatible when grafted onto chick CAMs. Unfortunately, due to covid pandemic, complete analyses of these constructs were not done.

5.4 Conclusion

Results in this chapter demonstrate that over a 6-month incubation, bioprinted constructs in chondrogenic differentiation medium did not deposit any GAGs within the bioink. A cartilage like cellular mass resembling a spheroid was detected on the surface and stained intensely for toluidine blue GAGs and picrosirius red collagen staining. No other studies have cultured human auricular CSPCs in alginate/cellulose bioink in-vitro for this extended period.

Analysis of CSPCs seeded in fibrin appear to demonstrate that it supports cartilage differentiation and may be a more suitable hydrogel for generating bioprinted constructs using the “sandwich design”.

Chapter 6

FINAL DISCUSSION

6.0 Summary of findings

The main findings of this study are summarised in relation to the aims and objectives of this thesis.

To analyse cartilage 3D spheroids in vitro using non-destructive methods.

- BABB optical clearing was found to be highly effective and in combination with an extended 96 hour immunostaining protocol allowed enhanced imaging of deeper levels of cartilage spheroids using two-photon microscopy. A novel imaging method to permit safe use of BABB that avoids damage to microscope objectives was developed. Firstly, the use a BABB compatible rubber ring mounted onto a cover slip, or secondly the inverted drop method.
- Using genetically labelled human paediatric ADSCs and CSPCs to generate cartilage spheroids resulted in easier identification of cells and optimal imaging conditions in whole mount two-photon confocal imaging.
- Cartilage nodules were identified in all regions and depths of spheroids similar to those identified using traditional histological sectioning described in previous studies in our group.

Asses the degree of chondrogenesis in Integra matrix when seeded with ADSCs and CSPCs and analyse its suitability to be used within a 3D printed PLA septal pocket.

- ADSCs and CSPCs attach, expand differentiate in Integra matrix. Deposition of cartilage ECM is confined to surface layers, but mature cartilage does develop and furthermore, small cartilage spheroid like structures develop and are found attached onto Integra demonstrating high levels of GAG and collagen.
- These results do not preclude Integra as a potential useful scaffold for cartilage tissue engineering as this preference for cells to expand and deposit cartilage on the surface can still be exploited for cartilage tissue engineering.
- Integra matrix was difficult to insert into a custom-made PLA pocket. Inserting undifferentiated Integra sheets into the pocket resulted in small tears and damage to the matrix. Insertion of pre-differentiated Integra sheets into the pocket was complicated by the stiffness and contraction of the sheet. Laying the Integra flat into the pocket was impossible.

To assess the level of maturation of chondrogenically induced CSPCs in 3D bioprinted constructs and fibrin hydrogel.

- Bioprinted constructs of CSPCs in alginate/cellulose bioink demonstrated excellent cell viability. CSPCs printed in alginate/cellulose bioink with RGD motifs demonstrated increasing levels of cell death over 21 days incubation compared to alginate/cellulose without RGD motifs.
- Over an extended 6-month incubation, bioprinted constructs of CSPCs in alginate/cellulose bioink cultured in chondrogenic differentiation medium did not result in deposition of cartilage ECM.
- Bioprint constructs of CSPCs in alginate/cellulose bioink did not demonstrate significant cartilage like ECM in a chick CAM in-vivo model.
- CSPCs seeded in fibrin hydrogel were evenly distributed and regions of chondrogenesis were detected over a short incubation of 21 days.

To assess the level of chondrogenesis in a "Sandwich" construct of cell seeded Fibrin hydrogel within PCL mesh sheets. .

- PCL mesh sheets were printed using a reproducible protocol developed in this thesis. As a potential for a nasal product, these sheets were easy to fabricate and handled well.
- "Sandwich" constructs made from PCL mesh sheets with a CSPCs/fibrin hydrogel core were generated fairly easily, but fibrin as a bioink and printed onto the PCL mesh would have been easier.
- Due to corona virus pandemic, the levels of chondrogenesis in these sandwich constructs was not analysed.

6.1 Conclusion

Both adipose derived stem cells and cartilage stem precursor cells were easy to isolate and expand and there are advantages to each cell source. Adipose tissue is easy to harvest with a syringe and needle and can performed under local anaesthetic with very little morbidity. Isolating cells from ear or nasal cartilage is slightly more invasive but also relatively simple.

Since many patients with nasal deformity undergo several operations, there will be numerous opportunities to harvest adipose tissue or cartilage to isolate, expand cells and fabricate a tissue engineered construct. For example, patients with cleft lip and palate will have several surgical procedures throughout their childhood to correct the cleft lip, then the palate, then any jaw deformity (orthognathic surgery) to align their teeth and finally rhinoplasty when they are over 18 years old. Over the numerous procedures, several tissue samples could be harvested to isolate stem cells that can be cryopreserved to generate cartilage at a later stage. Even patients undergoing aesthetic rhinoplasty will often have more than a single procedure and tissue samples isolated from their primary surgery could be banked in similar way.

The challenges of generating cartilage is achieving a level of mechanical stability and maturity that will allow surgeons to manipulate and handle the cartilage in a predictable manner. Furthermore, tissue engineered septal cartilage grafts must be strong enough to support the framework of the nose. The use of polymer scaffolds will provide addition strength to any engineered cartilage but many studies either seed cells directly onto resorbable biomaterials or inject cells in a hydrogel into 3D constructs that predominantly contained a polymer scaffold throughout the construct. The strategies described in this thesis attempt to avoid this by pursuing a scaffold free approach whereby the polymer is only contributing to the mechanical properties of the construct almost like an exoskeleton protecting the inner core cell/hydrogel mix. All three strategies described have potential to generate cartilage, but the most convenient one is the use of a bioprinter that allows printing of both cells and polymer scaffolds. A rapidly developing branch of tissue engineering, the bioprinting industry now offers bioprinters with multiple print heads capable of printing several hydrogels and polymer thermoplastics simultaneously. Furthermore, the range of commercially available bioinks has expanded massively to include fibrin, hyaluronic acid, and collagen.

6.1 Future work

All the in-vitro studies discussed in this thesis involved static cultures. Repeating the Integra, bioink and fibrin experiments using a bioreactor would allow further characterisation of the behaviour of ADSCs and CSPCs and the level of chondrogenesis in a dynamic culture system. Furthermore, Integra seeded with chondrogenically differentiated CSPCs or ADSCs implanted subcutaneously into mice would provide further data on cell viability, migration and chondrogenic potential in an in-vivo model. This would also allow evaluation any potential risks and biological compatibility of the pocket design.

A modification to the Integra novel PLA pocket design would be to place Integra into a “Clam shell” design (described in Fig. 4.26), and therefore avoiding the problems of insertion of Integra into a tight pocket space. Such a design would be easy to 3D print.

Given that the availability of numerous different commercially available bioinks has now massively increased, future work would include generating bioprinted constructs of CSPCs or ADSCs in fibrin, hyaluronic or collagen hydrogels that are more representative of cells natural environment compared to alginate.

Unfortunately, due to covid pandemic and restricted access to our laboratory, fibrin/PCL constructs generated in-vitro and also grafted onto chick CAMs were not fully analysed. For future work, both chondrogenic differentiated constructs and controls (constructs in expansion medium) will be histologically stained for markers of chondrogenesis (GAGs and collagen). Furthermore, gene expression analysis of cartilage markers (Col2) will be carried out to quantify chondrogenesis in these constructs.

Scanning electron microscopy (SEM) of PLA and PCL will provide useful data on cell adhesion and cell morphology when seeded with ADSCs and CSPCs. SEM will also provide details of surface structures of these materials when 3D printed.

Lastly, mechanical testing of constructs, both the Integra pocket design and the fibrin PCL sandwich, cultured in both control and differentiated medium, will help optimisation of scaffold mechanical properties to match closely that of native septal cartilage. Three-point bending or nanoindentation protocols will be used.

APPENDIX

Figures

CONTROL	L	W1	W2	W3	Wavg	t1	t2	t3	t_avg	L/t	Fmax	K		stress	stress modified [Mpa]		**E**
1	14	3.1	2.6	2.8	2.8333	0.9	0.89	0.96	0.91666	15.27272	0.17	0.089473684		1.499504	1.4820932	1.516915	**28.12467081**
2	14	2.9	2.8	2.7	2.8	0.9	0.9	1.3	1.033333	13.5483	0.17	0.089473684		1.517355	1.499737	1.534973	**19.86735662**
3	14	2.5	2.8	3	2.7666	0.97	1	1.2	1.056666	13.24921	0.18	0.089473684		1.625968	1.6070890	1.644847	**20.10672236**
4	14	3.2	3.2	3.1	3.1666	0.94	1	1.3	1.08	12.96296	0.28	0.143589744		2.209795	2.184137	2.235453	**28.19186894**

Figure A1. Lamb nasal septum mechanical testing data. Youngs modulus = tensile stress/tensile strain.

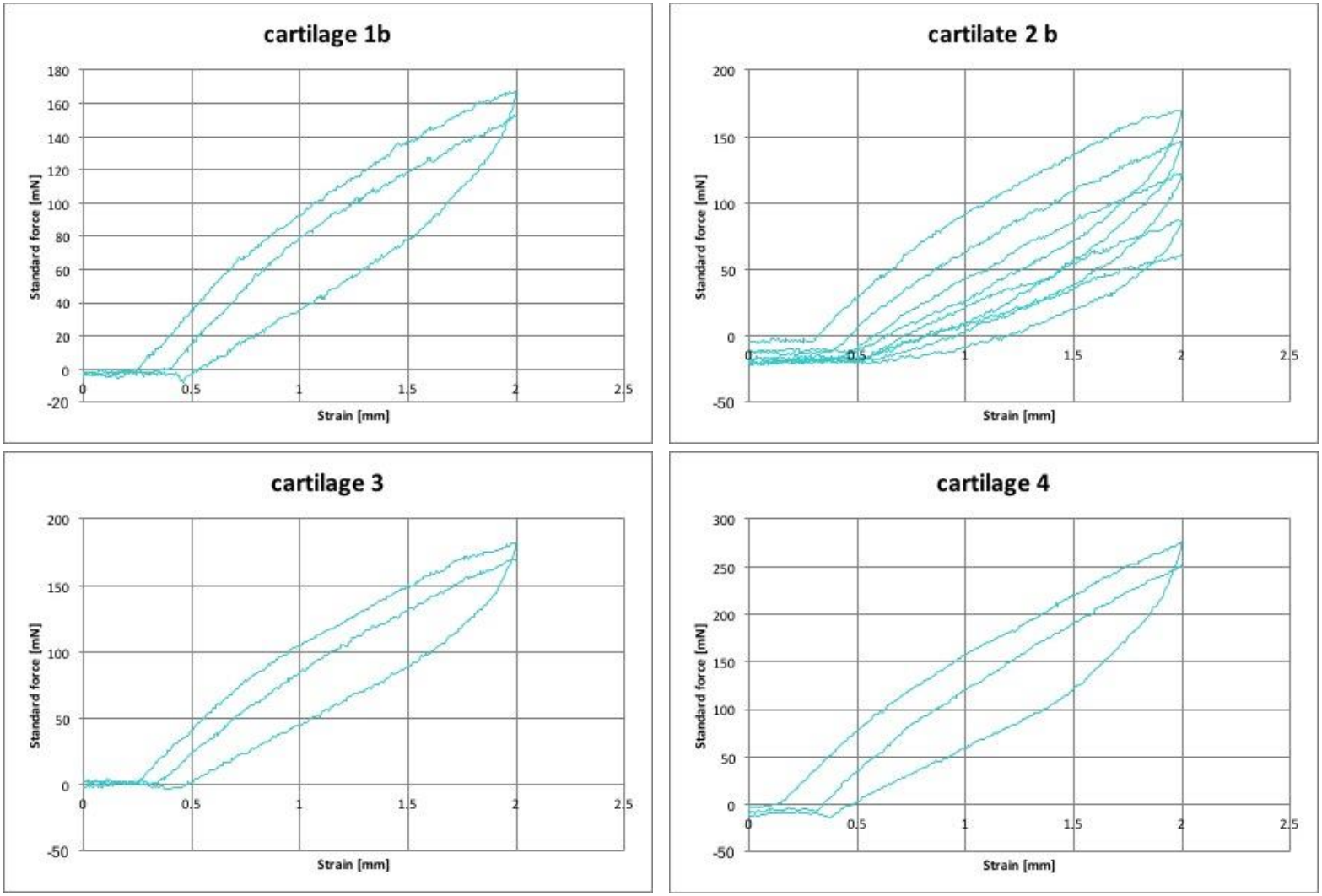

Figure A2. Graphs of results of lamb nasal septum mechanical testing. Youngs modulus = tensile stress/tensile strain.

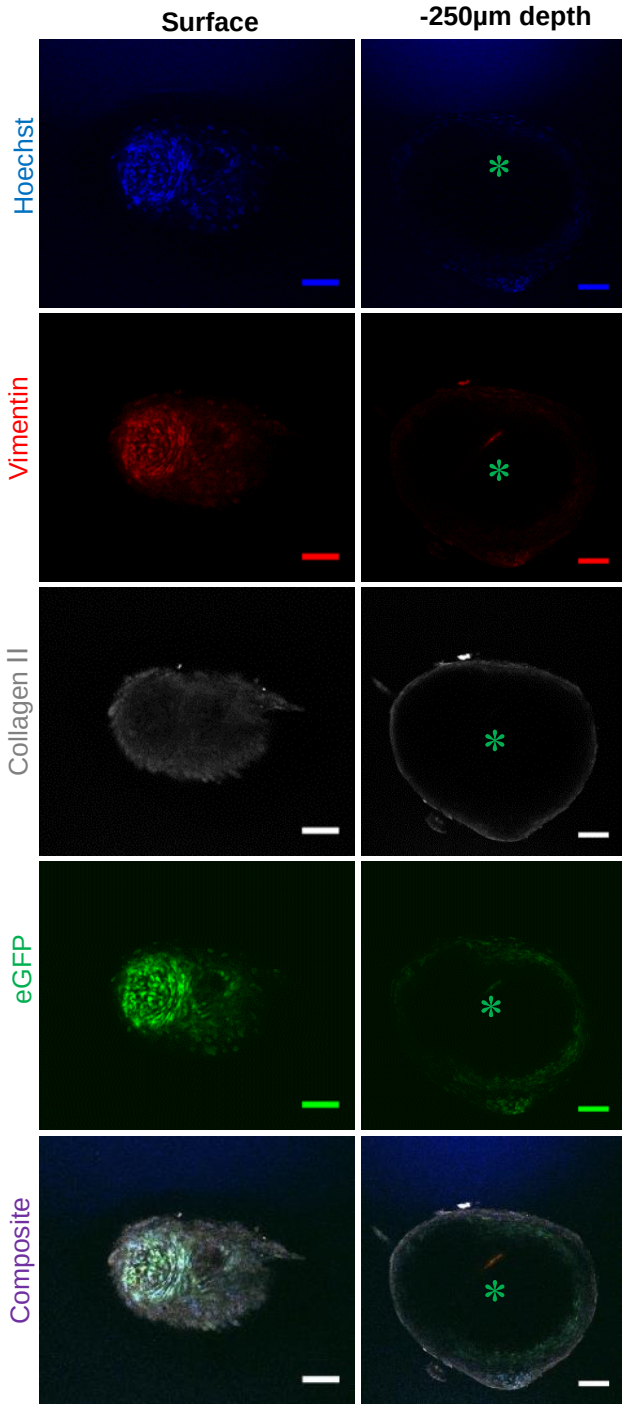

Figure A3. Confocal imaging of non-cleared, 6 week chondrogenically differentiated eGFP labelled ADSC spheroid (1.0x10^5 cells). Images taken with dipping objective at surface and -250µm. An extended 96 hour primary and secondary antibody incubation with a higher concentration of Triton (2%) was used. Immunofluorescent staining for collagen II, vimentin and Hoechst both at the surface and at deeper levels. As expected, imaging of the surface is possible, but becomes highly limited at deeper levels where central regions are not visible at all (*). At -250 µm depth, only staining at the peripheral edge of the spheroid was observed. Scale bars: 100µm.

Media files

Media 1: ADSC eGFP$^+$ labelled spheroid co-stained with Hoechst.

Media 2: Confocal microscopy of Integra bilayer matrix disc seeded with mCherry labelled ADSCs.

Media 3: 2-photon confocal imaging of mCherry$^+$ labelled CSPCs within alginate/cellulose bioink.

BIBLIOGRAPHY

Adamson, P A. (2000). Grafts in rhinoplasty: autogenous grafts are superior to alloplastic. *Archives of Otolaryngology--Head & Neck Surgery*, *126*(4), 561–562. https://doi.org/10.1001/archotol.126.4.561

Adamson, Peter A., & Gantous, A. (2019). Once Upon a Rhinoplasty: The History of the Queen of Facial Plastic Surgery. *Facial Plastic Surgery*, *35*(4), 322–339. https://doi.org/10.1055/s-0039-1693443

Adamson, Peter A. (1988). Rhinoplasty--our past. *Facial Plastic Surgery : FPS*, *5*(2), 93–96. https://doi.org/10.1055/s-2008-1064741

Ahmad, T., Byun, H., Lee, J., Madhurakat Perikamana, S. K., Shin, Y. M., Kim, E. M., & Shin, H. (2020). Stem cell spheroids incorporating fibers coated with adenosine and polydopamine as a modular building blocks for bone tissue engineering. *Biomaterials*, *230*(September 2019), 119652. https://doi.org/10.1016/j.biomaterials.2019.119652

Ahmed, T. A. E., Dare, E. V., & Hincke, M. (2008). Fibrin: A versatile scaffold for tissue engineering applications. *Tissue Engineering - Part B: Reviews*, *14*(2), 199–215. https://doi.org/10.1089/ten.teb.2007.0435

Akiyama, H., Chaboissier, M. C., Martin, J. F., Schedl, A., & De Crombrugghe, B. (2002). The transcription factor Sox9 has essential roles in successive steps of the chondrocyte differentiation pathway and is required for expression of Sox5 and Sox6. *Genes and Development*, *16*(21), 2813–2828. https://doi.org/10.1101/gad.1017802

Allareddy, V., Allareddy, V., & Nalliah, R. P. (2011). Epidemiology of facial fracture injuries. *Journal of Oral and Maxillofacial Surgery*. https://doi.org/10.1016/j.joms.2011.02.057

Amos, P. J., Kapur, S. K., Stapor, P. C., Shang, H., Bekiranov, S., Khurgel, M., … Katz, A. J. (2010). Human adipose-derived stromal cells accelerate diabetic wound healing: Impact of cell formulation and delivery. *Tissue Engineering - Part A*, *16*(5), 1595–1606. https://doi.org/10.1089/ten.tea.2009.0616

Angelos, P., & Wang, T. (2012). Revision of the cleft lip nose. *Facial Plastic Surgery*, *28*(4), 447–453. https://doi.org/10.1055/s-0032-1319838

Apelgren, P., Amoroso, M., Lindahl, A., Brantsing, C., Rotter, N., Gatenholm, P., & Kölby, L. (2017). Chondrocytes and stem cells in 3D-bioprinted structures create human cartilage in vivo. *PLoS ONE*, *12*(12), 1–16. https://doi.org/10.1371/journal.pone.0189428

Aremu, S. K., Alabi, B. S., & Omokanye, H. O. (2011). Dentogenic nasal septal abscess. *Ear, Nose and Throat Journal*, *90*(3), 27–28. https://doi.org/10.1177/014556131109000321

Asakura, T., Ishii, M., Kikuchi, T., Kameyama, K., Namkoong, H., Nakata, N., … Hasegawa, N. (2016). Disseminated mycobacterium marinum infection with a destructive nasal lesion mimicking extranodal NK/T cell lymphoma: A case report. *Medicine (United States)*, *95*(11), 1–5. https://doi.org/10.1097/MD.0000000000003131

Athanasiou, K. A., Agrawal, C. M., Barber, F. A., & Burkhart, S. S. (1998). Orthopaedic applications for PLA-PGA biodegradable polymers. *Arthroscopy*, *14*(7), 726–737. https://doi.org/10.1016/S0749-8063(98)70099-4

Aust, L., Devlin, B., Foster, S. J., Halvorsen, Y. D. C., Hicok, K., du Laney, T., … Gimble, J. M. (2004). Yield of human adipose-derived adult stem cells from liposuction aspirates. *Cytotherapy*, *6*(1), 7–14. https://doi.org/10.1080/14653240310004539

Azaripour, A., Lagerweij, T., Scharfbillig, C., Jadczak, E., Willershausen, B., & Noorden, C. J. F. Van. (2016). Progress in Histochemistry and Cytochemistry A survey of clearing techniques for 3D imaging of tissues with special reference to connective tissue. *Progress in Histochemistry and Cytochemistry*, *51*(2), 9–23. https://doi.org/10.1016/j.proghi.2016.04.001

Baena, J. M., Jiménez, G., López-Ruiz, E., Antich, C., Griñán-Lisón, C., Perán, M., … Marchal, J. A. (2019). Volume-by-volume bioprinting of chondrocytes-alginate bioinks in high temperature thermoplastic scaffolds for cartilage regeneration. *Experimental Biology and Medicine*, *244*(1), 13–21. https://doi.org/10.1177/1535370218821128

Becker, K., Jährling, N., Saghafi, S., Weiler, R., & Dodt, H. U. (2012). Chemical clearing and dehydration of GFP expressing mouse brains. *PLoS ONE*, *7*(3), 1–6. https://doi.org/10.1371/journal.pone.0033916

Beekman, B., Verzijl, N., Bank, R. A., von der Mark, K., & TeKoppele, J. M. (1997). Synthesis of collagen by bovine chondrocytes cultured in alginate; posttranslational modifications and cell-matrix interaction. *Experimental Cell Research*, *237*(1), 135–141. https://doi.org/10.1006/excr.1997.3771

Bellis, S. L. (2011). Advantages of RGD peptides for directing cell association with biomaterials. *Biomaterials*, *32*(18), 4205–4210. https://doi.org/10.1016/j.biomaterials.2011.02.029

Bennett, J. P. (1984). Sir William Fergusson and the Indian Rhinoplasty. *Annals of the Royal College of Surgeons of England*, *66*(6), 444–448.

Benya, P. D., & Shaffer, J. D. (1982). Dedifferentiated chondrocytes reexpress the differentiated collagen phenotype when cultured in agarose gels. *Cell*, *30*(1), 215–224. https://doi.org/10.1016/0092-8674(82)90027-7

Bernstein, J. L., Cohen, B. P., Lin, A., Harper, A., Bonassar, L. J., & Spector, J. A. (2018). Tissue Engineering Auricular Cartilage Using Late Passage Human Auricular Chondrocytes. *Annals of Plastic Surgery*, *80*(4 Suppl 4), S168–S173. https://doi.org/10.1097/SAP.0000000000001400

Bonaventure, J., Kadhom, N., Cohen-Solal, L., Ng, K. H., Bourguignon, J., Lasselin, C., & Freisinger, P. (1994). Reexpression of cartilage-specific genes by dedifferentiated human articular chondrocytes cultured in alginate beads. *Experimental Cell Research*, *212*(1), 97–104. https://doi.org/10.1006/excr.1994.1123

Bornes, T. D., Jomha, N. M., Mulet-Sierra, A., & Adesida, A. B. (2016). Optimal seeding densities for in vitro chondrogenesis of two- and three-dimensional-isolated and -expanded bone marrow-derived mesenchymal stromal stem cells within a porous collagen scaffold. *Tissue Engineering - Part C: Methods*, *22*(3), 208–220. https://doi.org/10.1089/ten.tec.2015.0365

Brain, D. J. (1993). The early history of rhinoplasty. *Facial Plastic Surgery : FPS*, *9*(2), 81–88. https://doi.org/10.1055/s-2008-1064600

Breasted, J. (1930). *The Edwin Smith Surgical Papyrus, Vol.1*. https://doi.org/10.1126/science.26.678.918

Burget, G. C., & Menick, F. J. (1985). The subunit principle in nasal reconstruction. *Plastic and Reconstructive Surgery*. https://doi.org/10.1097/00006534-198508000-00010

Caffrey, J. P., Kushnaryov, A. M., Reuther, M. S., Wong, V. W., Briggs, K. K., Masuda, K., … Caffrey, J. (2013). Flexural Properties of Native and Tissue Engineered Human Septal Cartilage. *Otolaryngol Head Neck Surg*, *148*(4), 576–581. https://doi.org/10.1177/0194599812474228

Calve, S., Ready, A., Huppenbauer, C., Main, R., & Neu, C. P. (2015). Optical clearing in dense connective tissues to visualize cellular connectivity in situ. *PLoS ONE*, *10*(1), 1–14. https://doi.org/10.1371/journal.pone.0116662

Caplan, A. I. (1991). Mesenchymal stem cells. *Journal of Orthopaedic Research*, *9*(5), 641–650. https://doi.org/10.1002/jor.1100090504

Castano, R., Thériault, G., & Gautrin, D. (2007). Categorizing nasal septal perforations of occupational origin as cases of corrosive rhinitis. *American Journal of Industrial Medicine*, *50*(2), 150–153. https://doi.org/10.1002/ajim.20419

Centola, M., Abbruzzese, F., Scotti, C., Barbero, A., Vadalà, G., Denaro, V., … Marsano, A. (2013). Scaffold-based delivery of a clinically relevant anti-angiogenic drug promotes the formation of in vivo stable cartilage. *Tissue Engineering - Part A*, *19*(17–18), 1960–1971. https://doi.org/10.1089/ten.tea.2012.0455

Chang, D. K., Louis, M. R., Gimenez, A., & Reece, E. M. (2019). The Basics of Integra Dermal Regeneration Template and its Expanding Clinical Applications. *Seminars in Plastic Surgery*, *33*(3), 185–189. https://doi.org/10.1055/s-0039-1693401

Chang, D. T., Irace, A. L., Kawai, K., Rogers-vizena, C. R., Nuss, R., & Adil, E. A. (2017). International Journal of Pediatric Otorhinolaryngology Nasal septal perforation in children : Presentation , etiology , and management. *International Journal of Pediatric Otorhinolaryngology*, *92*, 176–180. https://doi.org/10.1016/j.ijporl.2016.12.003

Chen, L., Yan, D., Wu, N., Zhang, W., Yan, C., Yao, Q., … Fu, Y. (2020). 3D-Printed Poly-Caprolactone Scaffolds Modified With Biomimetic Extracellular Matrices for Tarsal Plate Tissue Engineering. *Frontiers in Bioengineering and Biotechnology*, *8*(March), 219. https://doi.org/10.3389/fbioe.2020.00219

Cheng, L. H., Wu, P. C., Shih, C. P., Wang, H. W., Chen, H. C., Lin, Y. Y., … Lee, J. C. (2019). Nasal septal abscess: a 10-year retrospective study. *European Archives of Oto-Rhino-Laryngology*, *276*(2), 417–420. https://doi.org/10.1007/s00405-018-5212-0

Cherubino, M., Valdatta, L., Balzaretti, R., Pellegatta, I., Rossi, F., Protasoni, M., … Gornati, R. (2016). Human adipose-derived stem cells promote vascularization of collagen-based scaffolds transplanted into nude mice. *Regenerative Medicine*, *11*(3), 261–271. https://doi.org/10.2217/rme-2015-0010

Chimene, D., Lennox, K. K., Kaunas, R. R., & Gaharwar, A. K. (2016). Advanced Bioinks for 3D Printing: A Materials Science Perspective. *Annals of Biomedical Engineering*, *44*(6), 2090–2102. https://doi.org/10.1007/s10439-016-1638-y

Chung, K., Wallace, J., Kim, S. Y., Kalyanasundaram, S., Andalman, A. S., Davidson, T. J., … Deisseroth, K. (2013). Structural and molecular interrogation of intact biological systems. *Nature*, *497*(7449), 332–337. https://doi.org/10.1038/nature12107

Clevers, H. (2016). Modeling Development and Disease with Organoids. *Cell*, *165*(7), 1586–1597. https://doi.org/10.1016/j.cell.2016.05.082

Cohen, B. P., Bernstein, J. L., Morrison, K. A., Spector, J. A., & Bonassar, L. J. (2018). Tissue engineering the human auricle by auricular chondrocyte-mesenchymal stem cell co-implantation. *PloS One*, *13*(10), e0202356. https://doi.org/10.1371/journal.pone.0202356

Costa, E. C., Silva, D. N., Moreira, A. F., & Correia, I. J. (2019). Optical clearing methods: An overview of the techniques used for the imaging of 3D spheroids. *Biotechnology and Bioengineering*, *116*(10), 2742–2763. https://doi.org/10.1002/bit.27105

Cunha, F. (1949). The Edwin Smith surgical papyrus. *American Journal of Surgery*, *77*(6), 793–795. https://doi.org/10.1016/0002-9610(49)90152-x

Dagalakis, N., Flink, J., Stasikelis, P., Burke, J. F., & Yannas, I. V. (1980). Design of an artificial skin. Part III. Control of pore structure. *Journal of Biomedical Materials Research*, *14*(4), 511–528. https://doi.org/10.1002/jbm.820140417

Daniel, R. K. (2009). Tip Refinement Grafts: The Designer Tip. *Aesthetic Surgery Journal*, *29*(6), 528–537. https://doi.org/10.1016/j.asj.2009.09.013

De la Puente, P., & Ludeña, D. (2014). Cell culture in autologous fibrin scaffolds for applications in tissue engineering. *Experimental Cell Research*. Elsevier. https://doi.org/10.1016/j.yexcr.2013.12.017

Dekkers, J. F., Alieva, M., Wellens, L. M., Ariese, H. C. R., Jamieson, P. R., Vonk, A. M., … Rios, A. C. (2019). High-resolution 3D imaging of fixed and cleared organoids. *Nature Protocols*, *14*(6), 1756–1771. https://doi.org/10.1038/s41596-019-0160-8

DeLise, A. M., Fischer, L., & Tuan, R. S. (2000). Cellular interactions and signaling in cartilage development. *Osteoarthritis and Cartilage*. https://doi.org/10.1053/joca.1999.0306

Denk, W., Strickler, J. H., & Webb, W. W. (1990). Two-photon laser scanning fluorescence microscopy. *Science*, *248*(4951), 73–76. https://doi.org/10.1126/science.2321027

Dodt, H. U., Leischner, U., Schierloh, A., Jährling, N., Mauch, C. P., Deininger, K., … Becker, K. (2007). Ultramicroscopy: Three-dimensional visualization of neuronal networks in the whole mouse brain. *Nature Methods*, *4*(4), 331–336. https://doi.org/10.1038/nmeth1036

Drost, J., & Clevers, H. (2017). Translational applications of adult stem cell-derived organoids. *Development (Cambridge)*, *144*(6), 968–975. https://doi.org/10.1242/dev.140566

Edmondson, R., Broglie, J. J., Adcock, A. F., & Yang, L. (2014). Three-dimensional cell culture systems and their applications in drug discovery and cell-based biosensors. *Assay and Drug Development Technologies*, *12*(4), 207–218. https://doi.org/10.1089/adt.2014.573

Eglen, R. M., & Reisine, T. (2019). Human iPS Cell-Derived Patient Tissues and 3D Cell Culture Part 2: Spheroids, Organoids, and Disease Modeling. *SLAS Technology*, *24*(1), 18–27. https://doi.org/10.1177/2472630318803275

Eisenberg, I. (1982). A history of rhinoplasty. *South African Medical Journal = Suid-Afrikaanse Tydskrif Vir Geneeskunde*, *62*(9), 286–292. https://doi.org/10.1136/bmj.315.7123.1718

Estes, B. T., Diekman, B. O., Gimble, J. M., & Guilak, F. (2010). Isolation of adipose-derived stem cells and their induction to a chondrogenic phenotype. *Nature Protocols*, *5*(7), 1294–1311. https://doi.org/10.1038/nprot.2010.81

Estes, B. T., & Guilak, F. (2011). Three-Dimensional Culture Systems to Induce Chondrogenesis of Adipose-Derived Stem Cells. In *Fish Passage Design for Road Crossings* (pp. 201–217). https://doi.org/10.1007/978-1-61737-960-4_15

Farah, S., Anderson, D. G., & Langer, R. (2016). Physical and mechanical properties of PLA, and their functions in widespread applications — A comprehensive review. *Advanced Drug Delivery Reviews*, *107*, 367–392. https://doi.org/10.1016/j.addr.2016.06.012

Fattah, A., Sebire, N. J., & Bulstrode, N. W. (2010). Donor site reconstitution for ear reconstruction. *Journal of Plastic, Reconstructive and Aesthetic Surgery*, *63*(9), 1459–1465. https://doi.org/10.1016/j.bjps.2009.07.036

Fedok, F. G., & Rihani, J. (2015). Essential Grafting in the Traumatized Nose. *Facial Plastic Surgery*, *31*(3), 238–251. https://doi.org/10.1055/s-0035-1555621

Fisher, J. N., Tessaro, I., Bertocco, T., Peretti, G. M., & Mangiavini, L. (2017). The Application of Stem Cells from Different Tissues to Cartilage Repair. *Stem Cells International*, *2017*, 2761678. https://doi.org/10.1155/2017/2761678

Formigli, L., Paternostro, F., Tani, A., Mirabella, C., Quattrini Li, A., Nosi, D., Zecchi-Orlandini, S. (2015). MSCs seeded on bioengineered scaffolds improve skin wound healing in rats. *Wound Repair and Regeneration*, *23*(1), 115–123. https://doi.org/10.1111/wrr.12251

Freeman, F. E., & Kelly, D. J. (2017). Tuning alginate bioink stiffness and composition for controlled growth factor delivery and to spatially direct MSC Fate within bioprinted tissues. *Scientific Reports*, *7*(1), 1–12. https://doi.org/10.1038/s41598-017-17286-1

Gasperini, L., Mano, J. F., & Reis, R. L. (2014). Natural polymers for the microencapsulation of cells. *Journal of the Royal Society Interface*, *11*(100). https://doi.org/10.1098/rsif.2014.0817

Genes, N. G., Rowley, J. A., Mooney, D. J., & Bonassar, L. J. (2004). Effect of substrate mechanics on chondrocyte adhesion to modified alginate surfaces. *Archives of Biochemistry and Biophysics*, *422*(2), 161–167. https://doi.org/10.1016/j.abb.2003.11.023

Gharravi, A. M. (2019). Shear bioreactors stimulating chondrocyte regeneration , a systematic review, *1*, 1–8.

Gillispie, G., Prim, P., Copus, J., Fisher, J., Mikos, A. G., Yoo, J. J., … Lee, S. J. (2020). Assessment methodologies for extrusion-based bioink printability. *Biofabrication*, *12*(2), 022003. https://doi.org/10.1088/1758-5090/ab6f0d

Ginsburg, Charles M.; Leach, J. L. (1995). INFECTED_NASAL_SEPTAL_HEMATOMA 1995 ginsburg.pdf. *The Pediatric Infectious Disease Journal*, *14*(11), 1012–1013.

Gogolewski, S., Jovanovic, M., Perren, S. M., Dillon, J. G., & Hughes, M. K. (1993). Tissue response and in vivo degradation of selected polyhydroxyacids: Polylactides (PLA), poly(3-hydroxybutyrate) (PHB), and poly(3-hydroxybutyrate-co-3-hydroxyvalerate) (PHB/VA). *Journal of Biomedical Materials Research*, *27*(9), 1135–1148. https://doi.org/10.1002/jbm.820270904

Gonzalez-Ulloa, M., CASTILLO, A., STEVENS, E., ALVAREZ FUERTES, G., LEONELLI, F., & UBALDO, F. (1954). Preliminary study of the total restoration of the facial skin. *Plastic and Reconstructive Surgery (1946)*, *13*(3), 151–161. https://doi.org/10.1097/00006534-195403000-00001

Grymer, L. F., Pallisgaard, C., & Melsen, B. (1991). The Nasal Septum in Relation to the Development of the Nasomaxillary Complex. *The Laryngoscope*, *101*(8), 863???868. https://doi.org/10.1288/00005537-199108000-00010

Guasti, L., Prasongchean, W., Kleftouris, G., Mukherjee, S., Thrasher, a. J., Bulstrode, N. W., & Ferretti, P. (2012). High Plasticity of Pediatric Adipose Tissue-Derived Stem Cells: Too Much for Selective Skeletogenic Differentiation? *Stem Cells Translational Medicine*, *1*(5), 384–395. https://doi.org/10.5966/sctm.2012-0009

Guasti, Leonardo, Prasongchean, W., Kleftouris, G., Mukherjee, S., Thrasher, A. J., Bulstrode, N. W., & Ferretti, P. (2012a). High Plasticity of Pediatric Adipose Tissue-Derived Stem Cells: Too Much for Selective Skeletogenic Differentiation? *STEM CELLS Translational Medicine*, *1*(5), 384–395. https://doi.org/10.5966/sctm.2012-0009

Guasti, Leonardo, Prasongchean, W., Kleftouris, G., Mukherjee, S., Thrasher, A. J., Bulstrode, N. W., & Ferretti, P. (2012b). High Plasticity of Pediatric Adipose Tissue-Derived Stem Cells: Too Much for Selective Skeletogenic Differentiation? *STEM CELLS Translational Medicine*. https://doi.org/10.5966/sctm.2012-0009

Guasti, Leonardo, Vagaska, B., Bulstrode, N. W., Seifalian, A. M., & Ferretti, P. (2014). Chondrogenic differentiation of adipose tissue-derived stem cells within nanocaged POSS-PCU scaffolds: A new tool for nanomedicine. *Nanomedicine: Nanotechnology, Biology, and Medicine*, *10*(2), 279–289. https://doi.org/10.1016/j.nano.2013.08.006

Gungor-Ozkerim, P. S., Inci, I., Zhang, Y. S., Khademhosseini, A., & Dokmeci, M. R. (2018). Bioinks for 3D bioprinting: An overview. *Biomaterials Science*, *6*(5), 915–946. https://doi.org/10.1039/c7bm00765e

Guntupalli, L., Patel, K., Faraji, F., & Brunworth, J. D. (2017). Autoimmune-Related Nasal Septum Perforation: A Case Report and Systematic Review. *Allergy & Rhinology*, *8*(1), ar.2017.8.0191. https://doi.org/10.2500/ar.2017.8.0191

Gupta, P., Geris, L., Luyten, F. P., & Papantoniou, I. (2018). An Integrated Bioprocess for the Expansion and Chondrogenic Priming of Human Periosteum-Derived Progenitor Cells in Suspension Bioreactors, *1700087*(2419), 1–12. https://doi.org/10.1002/biot.201700087

Hama, H., Kurokawa, H., Kawano, H., Ando, R., Shimogori, T., Noda, H., … Miyawaki, A. (2011). Scale: A chemical approach for fluorescence imaging and reconstruction of transparent mouse brain. *Nature Neuroscience*, *14*(11), 1481–1488. https://doi.org/10.1038/nn.2928

Hamilton, G. S. (2017). The External Nasal Valve. *Facial Plastic Surgery Clinics of North America*, *25*(2), 179–194. https://doi.org/10.1016/j.fsc.2016.12.010

Hartikainen-Sorri, A. L., Sorri, M., Vainio-Mattila, J., & Ojala, K. (1984). Aetiology and detection of congenital nasal deformities. *International Journal of Pediatric Otorhinolaryngology*. https://doi.org/10.1016/S0165-5876(83)80106-2

Hass, R., Kasper, C., Böhm, S., & Jacobs, R. (2011). Different populations and sources of human mesenchymal stem cells (MSC): A comparison of adult and neonatal tissue-derived MSC. *Cell Communication and Signaling*, *9*(1), 12. https://doi.org/10.1186/1478-811X-9-12

Hatano, A., Nagasao, T., Cho, Y., Shimizu, Y., Takano, N., Kaneko, T., & Kishi, K. (2014). Relationship between locations of rib defects and loss of respiratory function - a biomechanical study. *The Thoracic and Cardiovascular Surgeon*, *62*(4), 357–362. https://doi.org/10.1055/s-0033-1338107

Häuselmann, H. J., Aydelotte, M. B., Schumacher, B. L., Kuettner, K. E., Gitelis, S. H., & Thonar, E. J. M. A. (1992). Synthesis and Turnover of Proteoglycans by Human and Bovine Adult Articular Chondrocytes Cultured in Alginate Beads. *Matrix*, *12*(2), 116–129. https://doi.org/10.1016/S0934-8832(11)80053-3

Homicz, M. R., McGowan, K. B., Lottman, L. M., Beh, G., Sah, R. L., & Watson, D. (2003). A compositional analysis of human nasal septal cartilage. *Archives of Facial Plastic Surgery*, *5*(1), 53–58. https://doi.org/10.1001/archfaci.5.1.53

Hutmacher, D. W. (2000). Scaffolds in tissue engineering bone and cartilage. *The Biomaterials: Silver Jubilee Compendium*, *21*, 175–189. https://doi.org/10.1016/B978-008045154-1.50021-6

Hwang, K., Huan, F., & Kim, D. J. (2010). Mapping Thickness of Nasal Septal Cartilage. *Journal of Craniofacial Surgery*. https://doi.org/10.1097/SCS.0b013e3181c5a203

Irie, Y., Mizumoto, H., Fujino, S., & Kajiwara, T. (2008). Development of articular cartilage grafts using organoid formation techniques. *Transplantation Proceedings*, *40*(2), 631–633. https://doi.org/10.1016/j.transproceed.2008.01.024

Iyyanki, T., Hubenak, J., Liu, J., Chang, E. I., Beahm, E. K., & Zhang, Q. (2015). Harvesting technique affects adipose-derived stem cell yield. *Aesthetic Surgery Journal*, *35*(4), 467–476. https://doi.org/10.1093/asj/sju055

Joshi, K. N. (2004). Chrome induced nasal septal perforation - An occupational hazard. *Indian Journal of Otolaryngology and Head and Neck Surgery*, *56*(2), 166–167. https://doi.org/10.1007/BF02974332

Jurgens, W. J. F. M., Oedayrajsingh-Varma, M. J., Helder, M. N., ZandiehDoulabi, B., Schouten, T. E., Kuik, D. J., … Van Milligen, F. J. (2008). Effect of tissue-harvesting site on yield of stem cells derived from adipose tissue: Implications for cell-based therapies. *Cell and Tissue Research*, *332*(3), 415–426. https://doi.org/10.1007/s00441-007-0555-7

Kapur, S. K., & Katz, A. J. (2013). Review of the adipose derived stem cell secretome. *Biochimie*, *95*(12), 2222–2228. https://doi.org/10.1016/j.biochi.2013.06.001

Katira, K., & Guyuron, B. (2015). C o n t e m p o r a r y Tec h n i q u e s fo r Effect ive Nasal Lengthening. https://doi.org/10.1016/j.fsc.2014.09.006

Kim, B. S., Jang, J., Chae, S., Gao, G., Kong, J. S., Ahn, M., & Cho, D. W. (2016). Three-dimensional bioprinting of cell-laden constructs with polycaprolactone protective layers for using various thermoplastic polymers. *Biofabrication*, *8*(3). https://doi.org/10.1088/1758-5090/8/3/035013

Kim, J. H., Song, J. W., Park, S. W., Oh, W. S., & Lee, J. H. (2015). 10th Rib Cartilage: Another Option of the Costal Cartilage Graft for Rhinoplasty. *Archives of Aesthetic Plastic Surgery*, *21*(2), 47. https://doi.org/10.14730/aaps.2015.21.2.47

Kim, J. S., Kim, T. H., Kang, D. L., Baek, S. Y., Lee, Y., Koh, Y. G., & Kim, Y. Il. (2020). Chondrogenic differentiation of human ASCs by stiffness control in 3D fibrin hydrogel. *Biochemical and Biophysical Research Communications*, *522*(1), 213–219. https://doi.org/10.1016/j.bbrc.2019.11.049

Kim, Y. K., Shin, S., Kang, N. H., & Kim, J. H. (2017). Contracted Nose after Silicone Implantation: A New Classification System and Treatment Algorithm. *Archives of Plastic Surgery*, *44*(1), 59–64. https://doi.org/10.5999/aps.2017.44.1.59

Klymkowsky, M. W., & Hanken, J. (1991). Chapter 22 Whole-Mount Staining of Xenopus and Other Vertebrates. In *Methods in cell biology* (Vol. 36, pp. 419–441). https://doi.org/10.1016/S0091-679X(08)60290-3

Kobayashi, S., Takebe, T., Zheng, Y. W., Mizuno, M., Yabuki, Y., Maegawa, J., & Taniguchi, H. (2011). Presence of cartilage stem/progenitor cells in adult mice auricular perichondrium. *PLoS ONE*, *6*(10), 1–8. https://doi.org/10.1371/journal.pone.0026393

Kopacheva-Barsova, G., & Arsova, S. (2016). The impact of the nasal trauma in childhood on the development of the nose in future. *Macedonian Journal of Medical Sciences*, *4*(3), 413–419. https://doi.org/10.3889/oamjms.2016.081

Kundu, J., Shim, J.-H., Jang, J., Kim, S.-W., & Cho, D.-W. (2015). An additive manufacturing-based PCL-alginate-chondrocyte bioprinted scaffold for cartilage tissue engineering. *Journal of Tissue Engineering and Regenerative Medicine*, *9*(11), 1286–1297. https://doi.org/10.1002/term.1682

Kuwajima, T., Sitko, A. A., Bhansali, P., Jurgens, C., Guido, W., & Mason, C. (2013). ClearT: A detergent- and solvent-free clearing method for neuronal and non-neuronal tissue. *Development (Cambridge)*, *140*(6), 1364–1368. https://doi.org/10.1242/dev.091844

Lammi, M. J., Piltti, J., Prittinen, J., & Qu, C. (2018). Challenges in Fabrication of Tissue-Engineered Cartilage with Correct Cellular Colonization and Extracellular Matrix Assembly. *International Journal of Molecular Sciences*, *19*(9). https://doi.org/10.3390/ijms19092700

Laschke, M. W., & Menger, M. D. (2017). Life is 3D: Boosting Spheroid Function for Tissue Engineering. *Trends in Biotechnology*, *35*(2), 133–144. https://doi.org/10.1016/j.tibtech.2016.08.004

Lee, J. W., McHugh, J., Kim, J. C., Baker, S. R., & Moyer, J. S. (2013). Age-related histologic changes in human nasal cartilage. *JAMA Facial Plastic Surgery*, *15*(4), 256–262. https://doi.org/10.1001/jamafacial.2013.825

Lee, K. Y., & Mooney, D. J. (2012). Alginate: Properties and biomedical applications. *Progress in Polymer Science (Oxford)*, *37*(1), 106–126. https://doi.org/10.1016/j.progpolymsci.2011.06.003

Lee, S. M., Stewart, C. L., Miller, C. J., & Chu, E. Y. (2015). The histopathologic features of Integra® Dermal Regeneration Template. *Journal of Cutaneous Pathology*, *42*(5), 368–369. https://doi.org/10.1111/cup.12488

Lefebvre, V., & Dvir-Ginzberg, M. (2017). SOX9 and the many facets of its regulation in the chondrocyte lineage. *Connective Tissue Research*, *58*(1), 2–14. https://doi.org/10.1080/03008207.2016.1183667

Lehmann, M., Martin, F., Mannigel, K., Kaltschmidt, K., Sack, U., & Anderer, U. (2013). Three-dimensional scaffold-free fusion culture: The way to enhance chondrogenesis of in vitro propagated human articular chondrocytes. *European Journal of Histochemistry*, *57*(4), 206–216. https://doi.org/10.4081/ejh.2013.e31

Lewis, M. C., MacArthur, B. D., Tare, R. S., Oreffo, R. O. C., & Please, C. P. (2016). Extracellular matrix deposition in engineered micromass cartilage pellet cultures: Measurements and modelling. *PLoS ONE*, *11*(2), 1–12. https://doi.org/10.1371/journal.pone.0147302

Li, Y., Rodrigues, J., & Tomás, H. (2012). Injectable and biodegradable hydrogels: gelation, biodegradation and biomedical applications. *Chemical Society Reviews*, *41*(6), 2193–2221. https://doi.org/10.1039/c1cs15203c

Lin, H., Li, Q., & Lei, Y. (2017). Three-dimensional tissues using human pluripotent stem cell spheroids as biofabrication building blocks. *Biofabrication*, *9*(2), 025007. https://doi.org/10.1088/1758-5090/aa663b

Lin, S. -C, Tai, C. -C, Chan, C. -C, & Wang, J. -D. (1994). Nasal septum lesions caused by chromium exposure among chromium electroplating workers. *American Journal of Industrial Medicine*, *26*(2), 221–228. https://doi.org/10.1002/ajim.4700260207

Loosen, J. Van. (2000). Postnatal Development of the Human Nasal Septum and its Related Structures . *Thesis*.

Loosen, J. Van, Zanten, G. A. Van, Howard, C. V, Verwoerd-Verhoef, H. L., Velzen, D. Van, & Verwoerd, C. D. A. (1996). Growth characteristics of the human nasal septum *. *Rhinology*, *34*, 78–82.

Losee, J. E., Kirschner, R. E., Whitaker, L. A., & Bartlett, S. P. (2004). Congenital Nasal Anomalies: A Classification Scheme. *Plastic and Reconstructive Surgery*. https://doi.org/10.1097/01.PRS.0000101540.32533.EC

Luo, W., Yi, Y., Jing, D., Zhang, S., Men, Y., Ge, W. P., & Zhao, H. (2019). Investigation of Postnatal Craniofacial Bone Development with Tissue Clearing-Based Three-Dimensional Imaging. *Stem Cells and Development*, *28*(19), 1310–1321. https://doi.org/10.1089/scd.2019.0104

Magnoni, C., De Santis, G., Fraccalvieri, M., Bellini, P., Portincasa, A., Giacomelli, L., & Papa, G. (2019). Integra in Scalp Reconstruction After Tumor Excision: Recommendations From a Multidisciplinary Advisory Board. *The Journal of Craniofacial Surgery*, *30*(8), 2416–2420. https://doi.org/10.1097/SCS.0000000000005717

Mahmoudifar, N., & Doran, P. M. (2012). Chondrogenesis and cartilage tissue engineering: The longer road to technology development. *Trends in Biotechnology*, *30*(3), 166–176. https://doi.org/10.1016/j.tibtech.2011.09.002

Maliniak, J. (1924). Comparative study of ivory and organic transplants in rhinoplasty. Endo-Nasal operative technic of some nasal deformities with report of cases. *The Laryngoscope*, *34*(11), 882–900.

Marin, V. P., Landecker, A., & Gunter, J. P. (2008). Harvesting rib cartilage grafts for secondary rhinoplasty. *Plastic and Reconstructive Surgery*, *121*(4), 1442–1448. https://doi.org/10.1097/01.prs.0000302467.24489.42

Markstedt, K., Mantas, A., Tournier, I., Martínez Ávila, H., Hägg, D., & Gatenholm, P. (2015a). 3D bioprinting human chondrocytes with nanocellulose-alginate bioink for cartilage tissue engineering applications. *Biomacromolecules*, *16*(5), 1489–1496. https://doi.org/10.1021/acs.biomac.5b00188

Markstedt, K., Mantas, A., Tournier, I., Martínez Ávila, H., Hägg, D., & Gatenholm, P. (2015b). 3D bioprinting human chondrocytes with nanocellulose-alginate bioink for cartilage tissue engineering applications. *Biomacromolecules*, *16*(5), 1489–1496. https://doi.org/10.1021/acs.biomac.5b00188

Martínez Ávila, H., Schwarz, S., Feldmann, E. M., Mantas, A., Von Bomhard, A., Gatenholm, P., & Rotter, N. (2014). Biocompatibility evaluation of densified bacterial nanocellulose hydrogel as an implant material for auricular cartilage regeneration. *Applied Microbiology and Biotechnology*, *98*(17), 7423–7435. https://doi.org/10.1007/s00253-014-5819-z

Martínez Ávila, H., Schwarz, S., Rotter, N., & Gatenholm, P. (2016a). 3D bioprinting of human chondrocyte-laden nanocellulose hydrogels for patient-specific auricular cartilage regeneration. *Bioprinting*, *1–2*, 22–35. https://doi.org/10.1016/j.bprint.2016.08.003

Martínez Ávila, H., Schwarz, S., Rotter, N., & Gatenholm, P. (2016b). 3D bioprinting of human chondrocyte-laden nanocellulose hydrogels for patient-specific auricular cartilage regeneration. *Bioprinting*, *1–2*, 22–35. https://doi.org/10.1016/j.bprint.2016.08.003

Matta, C., & Mobasheri, A. (2014). Regulation of chondrogenesis by protein kinase C: Emerging new roles in calcium signalling. *Cellular Signalling*, *26*(5), 979–1000. https://doi.org/10.1016/j.cellsig.2014.01.011

Menger, D. J., Tabink, I. C., & Trenite, G. J. N. (2008). Nasal Septal Abscess in Children, *134*(8), 842–847.

Menick, F. J. (2010). Nasal reconstruction. *Plastic and Reconstructive Surgery*, *125*(4), 138–150. https://doi.org/10.1097/PRS.0b013e3181d0ae2b

Metzenbaum, M. (1928). Nasal reconstruction by means of auto and isografts. *The Laryngoscope*, *38*(3), 197–205. Retrieved from https://doi.org/10.1288/00005537-192803000-00007

Miles, B. A., Petrisor, D., Kao, H., Finn, R. A., & Throckmorton, G. S. (2007). Anatomical variation of the nasal septum: Analysis of 57 cadaver specimens. *Otolaryngology - Head and Neck Surgery*, *136*(3), 362–368. https://doi.org/10.1016/j.otohns.2006.11.047

Milstein, S. (1984). Motivation for reduction rhinoplasty and the practical significance of the operation in life. By Jacques Joseph. *Plastic and Reconstructive Surgery*, *73*(4), 692–693. https://doi.org/10.1097/00006534-198404000-00035

Miot, S., Woodfield, T., Daniels, A. U., Suetterlin, R., Peterschmitt, I., Heberer, M., … Martin, I. (2005). Effects of scaffold composition and architecture on human nasal chondrocyte redifferentiation and cartilaginous matrix deposition. *Biomaterials*, *26*(15), 2479–2489. https://doi.org/10.1016/j.biomaterials.2004.06.048

Moiemen, N. S., Staiano, J. J., Ojeh, N. O., Thway, Y., & Frame, J. D. (2001). Reconstructive surgery with a dermal regeneration template: Clinical and histologic study. *Plastic and Reconstructive Surgery*. https://doi.org/10.1097/00006534-200107000-00015

Moiemen, N., Yarrow, J., Hodgson, E., Constantinides, J., Chipp, E., Oakley, H., … Freeth, M. (2011). Long-term clinical and histological analysis of Integra dermal regeneration template. *Plastic and Reconstructive Surgery*, *127*(3), 1149–1154. https://doi.org/10.1097/PRS.0b013e31820436e3

Möller, T., Amoroso, M., Hägg, D., Brantsing, C., Rotter, N., Apelgren, P., … Gatenholm, P. (2017). In Vivo Chondrogenesis in 3D Bioprinted Human Cell-laden Hydrogel Constructs. *Plastic and Reconstructive Surgery - Global Open*, *5*(2), 1–7. https://doi.org/10.1097/GOX.0000000000001227

Moratin, K., Koch, P. S., Benecke, J., Orouji, A., Bauer, C., Faulhaber, J., … Felcht, M. (2019). Reconstruction of Nasal Defects With Dermal Skin Substitutes—A Retrospective Study of 36 Defects. *Journal of Cutaneous Medicine and Surgery*, *23*(4), 413–420. https://doi.org/10.1177/1203475419852060

Muir, H. (1995). The chondrocyte, architect of cartilage. Biomechanics, structure, function and molecular biology of cartilage matrix macromolecules. *BioEssays*, *17*(12), 1039–1048. https://doi.org/10.1002/bies.950171208

Müller, M., Öztürk, E., Arlov, Ø., Gatenholm, P., & Zenobi-Wong, M. (2017). Alginate Sulfate–Nanocellulose Bioinks for Cartilage Bioprinting Applications. *Annals of Biomedical Engineering*, *45*(1), 210–223. https://doi.org/10.1007/s10439-016-1704-5

Murphy, S. V., & Atala, A. (2014). 3D bioprinting of tissues and organs. *Nature Biotechnology*, *32*(8), 773–785. https://doi.org/10.1038/nbt.2958

Natvig, P., LA, S., Gingrass, R. P., & Gardner, W. (1971). Anatomical details of the osseous-cartilaginous framework of the nose. *Plastic and Reconstructive Surgery*, *48*(6), 528–532.

Neskey, D., Eloy, J. A., & Casiano, R. R. (2009, April). Nasal, Septal, and Turbinate Anatomy and Embryology. *Otolaryngologic Clinics of North America*. https://doi.org/10.1016/j.otc.2009.01.008

New, S. E. P., Ibrahim, A., Guasti, L., Zucchelli, E., Birchall, M., Bulstrode, N. W., … Ferretti, P. (2017). Towards reconstruction of epithelialized cartilages from autologous adipose tissue-derived stem cells. *Journal of Tissue Engineering and Regenerative Medicine*, *11*(11), 3078–3089. https://doi.org/10.1002/term.2211

Noori, A., Ashrafi, S. J., Vaez-Ghaemi, R., Hatamian-Zaremi, A., & Webster, T. J. (2017). A review of fibrin and fibrin composites for bone tissue engineering. *International Journal of Nanomedicine*, *12*, 4937–4961. https://doi.org/10.2147/IJN.S124671

Nürnberg, E., Vitacolonna, M., Klicks, J., von Molitor, E., Cesetti, T., Keller, F., … Rudolf, R. (2020). Routine Optical Clearing of 3D-Cell Cultures: Simplicity Forward. *Frontiers in Molecular Biosciences*, *7*(February), 1–19. https://doi.org/10.3389/fmolb.2020.00020

Ohara, K., Nakamura, K., & Ohta, E. (1997). Chest wall deformities and thoracic scoliosis after costal cartilage graft harvesting. *Plastic and Reconstructive Surgery*, *99*(4), 1030–1036. https://doi.org/10.1097/00006534-199704000-00017

Olsen, T. R. (2014). Bioprocessing of Tissues using Cellular Spheroids. *Journal of Bioprocessing & Biotechniques*, *04*(02), 2–5. https://doi.org/10.4172/2155-9821.1000e112

Olsen, T. R., Mattix, B., Casco, M., Herbst, A., Williams, C., Tarasidis, A., … Alexis, F. (2014). Processing cellular spheroids for histological examination. *Journal of Histotechnology*, *37*(4), 138–142. https://doi.org/10.1179/2046023614Y.0000000047

Ong, C. S., Yesantharao, P., Huang, C. Y., Mattson, G., Boktor, J., Fukunishi, T., … Hibino, N. (2018). 3D bioprinting using stem cells. *Pediatric Research*, *83*(1–2), 223–231. https://doi.org/10.1038/pr.2017.252

Ong, C. S., Zhou, X., Han, J., Huang, C. Y., Nashed, A., Khatri, S., … Hibino, N. (2018). In vivo therapeutic applications of cell spheroids. *Biotechnology Advances*, *36*(2), 494–505. https://doi.org/10.1016/j.biotechadv.2018.02.003

Ortega, E. S., Sanz-Garcia, A., Pernia-Espinoza, A., & Escobedo-Lucea, C. (2019). Efficient fabrication of polycaprolactone scaffolds for printing hybrid tissue-engineered constructs. *Materials*, *12*(4), 1–18. https://doi.org/10.3390/ma12040613

Ovsianikov, A., Khademhosseini, A., & Mironov, V. (2018). The Synergy of Scaffold-Based and Scaffold-Free Tissue Engineering Strategies. *Trends in Biotechnology*, *36*(4), 348–357. https://doi.org/10.1016/j.tibtech.2018.01.005

Özücer, B., Dinç, M. E., Paltura, C., Koçak, I., Dizdar, D., Çörtük, O., & Uysal, Ö. (2018). Association of Autologous Costal Cartilage Harvesting Technique With Donor-Site Pain in Patients Undergoing Rhinoplasty. *JAMA Facial Plastic Surgery*, *20*(2), 136–140. https://doi.org/10.1001/jamafacial.2017.1363

Palhazi, P., Daniel, R. K., & Kosins, A. M. (2015). The Osseocartilaginous Vault of the Nose : Anatomy and Surgical Observations. *Aesthetic Surgery Journal*, *35*(3), 242–251. https://doi.org/10.1093/asj/sju079

Panwar, A., & Tan, L. P. (2016). Current Status of Bioinks for Micro-Extrusion-Based 3D Bioprinting. *Molecules (Basel, Switzerland)*, *21*(6). https://doi.org/10.3390/molecules21060685

Parker Porter, J. (2000). Grafts in rhinoplasty: alloplastic vs. autogenous. *Archives of Otolaryngology--Head & Neck Surgery*, *126*(4), 558–561. https://doi.org/10.1001/archotol.126.4.558

Patel, R., & Orlandi, R. R. (2015). Fungal septal abscess complicating maxillary sinus fungus balls in an immunocompetent host. *Allergy & Rhinology*, *6*(3), 184–187. https://doi.org/10.2500/ar.2015.6.0139

Pensler, J. M. (2009). The Role of the Upper Lateral Cartilages in Aesthetic Rhinoplasty, *29*(4), 290–294. https://doi.org/10.1016/j.asj.2009.04.006
Pereira, C., Santamaría, A., Langdon, C., López-Chacón, M., Hernández-Rodríguez, J., & Alobid, I. (2018). Nasoseptal Perforation: from Etiology to Treatment. *Current Allergy and Asthma Reports*, *18*(1). https://doi.org/10.1007/s11882-018-0754-1
Permyakova, E. S., Kiryukhantsev-Korneev, P. V., Gudz, K. Y., Konopatsky, A. S., Polčak, J., Zhitnyak, I. Y., … Manakhov, A. M. (2019). Comparison of Different Approaches to Surface Functionalization of Biodegradable Polycaprolactone Scaffolds. *Nanomaterials (Basel, Switzerland)*, *9*(12). https://doi.org/10.3390/nano9121769
Pernia, N. E. R., Galvez, J. A. C., & Victoria, F. A. (2011). The Dimensions of the Nasal Septal Cartilage: A Preliminary Study in Adult Filipino Malay Cadavers. *Philippine Journal of Otolaryngology-Head and Neck Surgery*, *26*(2), 10–12. https://doi.org/10.32412/pjohns.v26i2.567
Pitanguy, I., Salgado, F., Radwanski, H. N., & Bushkin, S. C. (1995). The surgical importance of the dermocartilaginous ligament of the nose. *Plastic and Reconstructive Surgery*, *95*(5), 790–794. Retrieved from http://www.ncbi.nlm.nih.gov/pubmed/7708861
Plawecki, A., Bobian, M., Kandinov, A., Svider, P. F., Folbe, A. J., Eloy, J. A., & Carron, M. (2017). Recreational activity and facial trauma among older adults. *JAMA Facial Plastic Surgery*, *19*(6), 453–458. https://doi.org/10.1001/jamafacial.2017.0332
Regnault, P. (1980). Reconstructive rhinoplasty with nasal implants. *Aesthetic Plastic Surgery*, *4*(C), 79–86.
Ricard-Blum, S. (2011). The Collagen Family. *Cold Spring Harbor Perspectives in Biology*, *3*(1), 1–19. https://doi.org/10.1101/cshperspect.a004978
Richardson, D. S., & Lichtman, J. W. (2015). Clarifying Tissue Clearing. *Cell*, *162*(2), 246–257. https://doi.org/10.1016/j.cell.2015.06.067
Richmon, J.D., Sage, A., Wong, W. V., Chen, A. C., Sah, R. L., Watson, D., & Watston, D. (2006). Compressive biomechanical properties of human nasal septal cartilage. *American Journal of Rhinology*, *20*(5), 496–501. https://doi.org/10.2500/ajr.2006.20.2932
Richmon, Jeremy D, Sage, A., Wong, W. Van, Chen, A. C., Sah, R. L., Watson, D., & Watston, D. (2005). Tensile biomechanical properties of human nasal septal cartilage. *American Journal of Rhinology*, *19*(5), 617–622. Retrieved from http://www.ncbi.nlm.nih.gov/pubmed/17063745
Rippy, M. K., Baron, S., Rosenthal, M., & Senior, B. A. (2018). Evaluation of absorbable PLA nasal implants in an ovine model. *Laryngoscope Investigative Otolaryngology*, *3*(3), 156–161. https://doi.org/10.1002/lio2.166
Rodriguez, A., Cao, Y. L., Ibarra, C., Pap, S., Vacanti, M., Eavey, R. D., & Vacanti, C. A. (1999). Characteristics of cartilage engineered from human pediatric auricular cartilage. *Plastic and Reconstructive Surgery*. https://doi.org/10.1097/00006534-199904010-00001
Rogers, B. O. (1986). John Orlando Roe-Not Jacques Joseph-The father of Aesthetic Rhinoplasty. *Aesthetic Plastic Surgery*, *10*(1), 63–88. https://doi.org/10.1007/BF01575272
Rohrich, R. J., Pulikkottil, B. J., Stark, R. Y., Amirlak, B., & Pezeshik, R. (2016). The importance of the upper lateral cartilage in rhinoplasty. *Plastic and Reconstructive Surgery*, *137*(2), 476–483. https://doi.org/10.1097/01.prs.0000475771.91525.fd
Ronzière, M. C., Perrier, E., Mallein-Gerin, F., & Freyria, A. M. (2010). Chondrogenic potential of bone marrow- and adipose tissue-derived adult human mesenchymal stem cells. *Bio-Medical Materials and Engineering*, *20*(3–4), 145–158. https://doi.org/10.3233/BME-2010-0626

Rosenberger, E. S., & Toriumi, D. M. (2016). C o n t rov e r s i e s i n R e v i s i o n Rhinoplasty Revision rhinoplasty Nasal filler Cartilage grafting Dorsal augmentation. *Facial Plastic Surgery Clinics of NA*, *24*(3), 337–345. https://doi.org/10.1016/j.fsc.2016.03.010

Roy, R., Kohles, S. S., Zaporojan, V., Peretti, G. M., Randolph, M. A., Xu, J., & Bonassar, L. J. (2004a). Analysis of bending behavior of native and engineered auricular and costal cartilage. *Journal of Biomedical Materials Research - Part A*, *68*(4), 597–602. https://doi.org/10.1002/jbm.a.10068

Roy, R., Kohles, S. S., Zaporojan, V., Peretti, G. M., Randolph, M. A., Xu, J., & Bonassar, L. J. (2004b). *Analysis of bending behavior of native and engineered auricular and costal cartilage*. Retrieved from www.interscience.wiley.com.]

Rúa Gonzálvez, L., de Villalaín Álvarez, L., Novoa Gómez, A., de Vicente Rodríguez, J. C., & Peña González, I. (2018). Use of Integra in oral reconstruction: a case series. *Oral Surgery, Oral Medicine, Oral Pathology and Oral Radiology*, *125*(3), e72–e75. https://doi.org/10.1016/j.oooo.2017.11.003

Ruiz-Cantu, L., Gleadall, A., Faris, C., Segal, J., Shakesheff, K., & Yang, J. (2020). Multi-material 3D bioprinting of porous constructs for cartilage regeneration. *Materials Science and Engineering C*, *109*(December 2019). https://doi.org/10.1016/j.msec.2019.110578

Saban, Y., Amodeo, C. A., Hammou, J. C., & Polselli, R. (2008). An anatomical study of the nasal superficial musculoaponeurotic system surgical applications in rhinoplasty. *Archives of Facial Plastic Surgery*, *10*(2), 109–115. https://doi.org/10.1001/archfaci.10.2.109

Schuurman, W., Khristov, V., Pot, M. W., Van Weeren, P. R., Dhert, W. J. A., & Malda, J. (2011). Bioprinting of hybrid tissue constructs with tailorable mechanical properties. *Biofabrication*, *3*(2). https://doi.org/10.1088/1758-5082/3/2/021001

Seth, A. K., Ratanshi, I., Dayan, J. H., Disa, J. J., & Mehrara, B. J. (2019). Nasal Reconstruction Using the Integra Dermal Regeneration Template. *Plastic and Reconstructive Surgery*, *144*(4), 966–970. https://doi.org/10.1097/PRS.0000000000006072

Shafiee, Abbas, Kabiri, M., Ahmadbeigi, N., Yazdani, S. O., Mojtahed, M., Amanpour, S., & Soleimani, M. (2011). Nasal septum-derived multipotent progenitors: A potent source for stem cell-based regenerative medicine. *Stem Cells and Development*, *20*(12), 2077–2091. https://doi.org/10.1089/scd.2010.0420

Shafiee, Ashkan, & Atala, A. (2016). Printing Technologies for Medical Applications. *Trends in Molecular Medicine*, *22*(3), 254–265. https://doi.org/10.1016/j.molmed.2016.01.003

Sheen, J. H. (1998). The ideal dorsal graft: a continuing quest. *Plastic and Reconstructive Surgery*, *102*(7), 2490–2493. https://doi.org/10.1097/00006534-199812000-00036

Siddiqui, N., Asawa, S., Birru, B., Baadhe, R., & Rao, S. (2018). PCL-Based Composite Scaffold Matrices for Tissue Engineering Applications. *Molecular Biotechnology*, *60*(7), 506–532. https://doi.org/10.1007/s12033-018-0084-5

Sprunt, W. H. (1955). Imhotep. *The New England Journal of Medicine*, *253*(18), 778–780. https://doi.org/10.1056/NEJM195511032531808

Steding, G., & Jian, Y. (2010). The origin and early development of the nasal septum in human embryos. *Annals of Anatomy*, *192*(2), 82–85. https://doi.org/10.1016/j.aanat.2010.01.002

Stokes, D. G., Liu, G., Dharmavaram, R., Hawkins, D., Piera-Velazquez, S., & Jimenez, S. A. (2001). Regulation of type-II collagen gene expression during human chondrocyte de-differentiation and recovery of chondrocyte-specific phenotype in culture involves Sry-type high-mobility-group box (SOX) transcription factors. *Biochemical Journal*, *360*(2), 461–470. https://doi.org/10.1042/0264-6021:3600461

T.W.Sadler. (1995). *Langmans Medical Embryology Seventh Edition Williams & Wilkins*.

Tainaka, K., Kuno, A., Kubota, S. I., Murakami, T., & Ueda, H. R. (2016). *Chemical Principles in Tissue Clearing and Staining Protocols for Whole-Body Cell Profiling*. *Annual Review of Cell and Developmental Biology* (Vol. 32). https://doi.org/10.1146/annurev-cellbio-111315-125001

Tare, R. S., Howard, D., Pound, J. C., Roach, H. I., & Oreffo, R. O. C. (2005). Tissue engineering strategies for cartilage generation-Micromass and three dimensional cultures using human chondrocytes and a continuous cell line. *Biochemical and Biophysical Research Communications*, *333*(2), 609–621. https://doi.org/10.1016/j.bbrc.2005.05.117

Tasman, A. (2007). Rhinoplasty – indications and techniques. *Current Topics in Otorhinolaryngology Head and Neck Surgery*, *6*, 1–23.

Tay, A. G., Farhadi, J., Suetterlin, R., Pierer, G., Heberer, M., & Martin, I. (2004). Cell yield, proliferation, and postexpansion differentiation capacity of human ear, nasal, and rib chondrocytes. *Tissue Engineering*, *10*(5–6), 762–770. https://doi.org/10.1089/1076327041348572

Theer, P., & Denk, W. (2006). On the fundamental imaging-depth limit in two-photon microscopy. *Journal of the Optical Society of America A*, *23*(12), 3139. https://doi.org/10.1364/josaa.23.003139

Theer, P., Hasan, M. T., & Denk, W. (2003). Two-photon imaging to a depth of 1000 microm in living brains by use of a Ti:Al2O3 regenerative amplifier. *Optics Letters*, *28*(12), 1022–1024. https://doi.org/10.1364/ol.28.001022

Thomas, E. D. (1999). A history of haemopoietic cell transplantation. *British Journal of Haematology*, *105*(2), 330–339. https://doi.org/10.1111/j.1365-2141.1999.01337.x

Tiersch, T. R., & Monroe, W. T. (2016). Three-dimensional printing with polylactic acid (PLA) thermoplastic offers new opportunities for cryobiology. *Cryobiology*, *73*(3), 396–398. https://doi.org/10.1016/j.cryobiol.2016.10.005

Togo, T., Utani, A., Naitoh, M., Ohta, M., Tsuji, Y., Morikawa, N., … Suzuki, S. (2006). Identification of cartilage progenitor cells in the adult ear perichondrium: Utilization for cartilage reconstruction. *Laboratory Investigation*, *86*(5), 445–457. https://doi.org/10.1038/labinvest.3700409

Toriumi, D. M. (1995). Management of the middle nasal vault in rhinoplasty. *Operative Techniques in Plastic and Reconstructive Surgery*, *2*(1), 16–30. https://doi.org/10.1016/S1071-0949(05)80013-7

Toriumi, D. M. (2000). Autogenous grafts are worth the extra time. *Archives of Otolaryngology - Head and Neck Surgery*, *126*(4), 562–564. https://doi.org/10.1001/archotol.126.4.562

Toriumi, D. M. (2017). Dorsal Augmentation Using Autologous Costal Cartilage or Microfat-Infused Soft Tissue Augmentation, 162–178.

Toriumi, D. M., & Bared, A. (2012). Revision of the Surgically Overshortened Nose.

Ujam, A., Awad, Z., Wong, G., Tatla, T., & Farrell, R. (2012). Safety trial of Floseal®haemostatic agent in head and neck surgery. *Annals of the Royal College of Surgeons of England*, *94*(5). https://doi.org/10.1308/003588412X13171221590971

Ujam, A. B., & Bulstrode, N. W. (2019). International Journal of Pediatric Otorhinolaryngology Case Report A modified reconstructive technique for paediatric congenital alar rim deformity. *International Journal of Pediatric Otorhinolaryngology*, *118*(December 2018), 201–205. https://doi.org/10.1016/j.ijporl.2018.12.034

Ujam, A. B., Vig, N., & Nasser, N. (2019). Combined correction of the nasal tip and upper lip in bilateral cleft lip patients: A novel approach. *International Journal of Pediatric Otorhinolaryngology*, *126*(July), 109593. https://doi.org/10.1016/j.ijporl.2019.109593

Van Osch, G. J. V. M., Van der Veen, S. W., & Verwoerd-Verhoef, H. L. (2001). In vitro redifferentiation of culture-expanded rabbit and human auricular chondrocytes for cartilage reconstruction. *Plastic and Reconstructive Surgery*. https://doi.org/10.1097/00006534-200102000-00020

Verwoerd, C. D A, & Verwoerd-Verhoef, H. L. (2007). Rhinosurgery in children: Basic concepts. *Facial Plastic Surgery*. https://doi.org/10.1055/s-2007-995814

Verwoerd, Carel D A, & Verwoerd-Verhoef, H. L. (2010). Rhinosurgery in children: developmental and surgical aspects of the growing nose. *GMS Current Topics in Otorhinolaryngology, Head and Neck Surgery*, *9*(Figure 1), Doc05. https://doi.org/10.3205/cto000069

Vetter, U., Pirsig, W., & Heinze, E. (1983). Growth Activity in Human Septal Cartilage. *Plastic and Reconstructive Surgery*, *71*(2), 167–170. https://doi.org/10.1097/00006534-198302000-00001

Vetter, U., Pirsig, W., Helbing, G., Heit, W., & Heinze, E. (1984). Patterns of growth in human septal cartilage: a review of new approaches. *International Journal of Pediatric Otorhinolaryngology*, *7*(1), 63–74. https://doi.org/10.1016/S0165-5876(84)80054-3

Vilar-Sancho, B. (1987). An old story: an ivory nasal implant. *Aesthetic Plastic Surgery*, *11*(1), 157–161. https://doi.org/10.1007/bf01575503

Viswanathan, S., Shi, Y., Galipeau, J., Krampera, M., Leblanc, K., Martin, I., … Sensebe, L. (2019). Mesenchymal stem versus stromal cells: International Society for Cell & Gene Therapy (ISCT®) Mesenchymal Stromal Cell committee position statement on nomenclature. *Cytotherapy*, *21*(10), 1019–1024. https://doi.org/10.1016/j.jcyt.2019.08.002

von der Mark, K., & Conrad, G. (1979). Cartilage cell differentiation: review. *Clinical Orthopaedics and Related Research*, *No. 139*(139), 185–205. https://doi.org/10.1097/00003086-197903000-00033

Von Mangoldt, F. (1899). Von Mangoldt Reconstruction of saddlenose by artilage overlay.pdf. *Arch. f. Klin. Chir*, *39*, 926.

Wahl, E. A., Fierro, F. A., Peavy, T. R., Hopfner, U., Dye, J. F., Machens, H. G., … Schenck, T. L. (2015). In Vitro Evaluation of Scaffolds for the Delivery of Mesenchymal Stem Cells to Wounds. *BioMed Research International*, *2015*. https://doi.org/10.1155/2015/108571

Walter, C. (1988). The evolution of rhinoplasty. *The Journal of Laryngology & Otology*, *102*(November 1987), 1079–1085.

Weber, G. F., Bjerke, M. A., & DeSimone, D. W. (2011). Integrins and cadherins join forces to form adhesive networks. *Journal of Cell Science*, *124*(8), 1183–1193. https://doi.org/10.1242/jcs.064618

Wexler, D. B., & Davidson, T. M. (2004). *The Nasal Valve: A Review of the Anatomy, Imaging, and Physiology*. *American Journal of Rhinol-ogy* (Vol. 18).

Williams, N. (2000). What are the causes of a perforated nasal septum? *Occupational Medicine*, *50*(2), 135–136. https://doi.org/10.1093/occmed/50.2.135

Winkler, A. A., Soler, Z. M., Leong, P. L., Murphy, A., Wang, T. D., & Cook, T. A. (2012). Complications associated with alloplastic implants in rhinoplasty. *Archives of Facial Plastic Surgery*, *14*(6), 437–441. https://doi.org/10.1001/archfacial.2012.583

Xu, L., Matrova, E., & Dietz, N. E. (2016). Mycobacterium avium Infection of Nasal Septum in a Diabetic Adult: A Case Report. *Head and Neck Pathology*, *10*(4), 552–555. https://doi.org/10.1007/s12105-016-0738-1

Xu, T., Binder, K. W., Albanna, M. Z., Dice, D., Zhao, W., Yoo, J. J., & Atala, A. (2013). Hybrid printing of mechanically and biologically improved constructs for cartilage tissue engineering applications. *Biofabrication*, *5*(1). https://doi.org/10.1088/1758-5082/5/1/015001

Xue, K., Zhang, X., Qi, L., Zhou, J., & Liu, K. (2016). Isolation, identification, and comparison of cartilage stem progenitor/cells from auricular cartilage and perichondrium. *American Journal of Translational Research*, *8*(2), 732–741.

Yang, B., Treweek, J. B., Kulkarni, R. P., Deverman, B. E., Chen, C. K., Lubeck, E., … Gradinaru, V. (2014). Single-cell phenotyping within transparent intact tissue through whole-body clearing. *Cell*, *158*(4), 945–958. https://doi.org/10.1016/j.cell.2014.07.017

Yeatts, A. B., Choquette, D. T., & Fisher, J. P. (2013, February). Bioreactors to influence stem cell fate: Augmentation of mesenchymal stem cell signaling pathways via dynamic culture systems. *Biochimica et Biophysica Acta - General Subjects*. https://doi.org/10.1016/j.bbagen.2012.06.007

Yoon, H. H., Bhang, S. H., Shin, J. Y., Shin, J., & Kim, B. S. (2012). Enhanced cartilage formation via three-dimensional cell engineering of human adipose-derived stem cells. *Tissue Engineering - Part A*, *18*(19–20), 1949–1956. https://doi.org/10.1089/ten.tea.2011.0647.

Zankl, A., Eberle, L., Molinari, L., & Schinzel, A. (2002). Growth Charts for Nose Length , Nasal Protrusion , and Philtrum Length From Birth to 97 Years, *391*(September 2001), 388–391. https://doi.org/10.1002/ajmg.10472.

Zelnik, J., & Gingrass, R. P. (1979). Anatomy of the alar cartilage.pdf. *Plastic and Reconstructive Surgery*, *64*(5), 650–653.

Zhang, H., Zhou, L., & Zhang, W. (2014). Control of scaffold degradation in tissue engineering: a review. *Tissue Engineering. Part B, Reviews*, *20*(5), 492–502. https://doi.org/10.1089/ten.TEB.2013.0452.

Zhang, L., Su, P., Xu, C., Yang, J., Yu, W., & Huang, D. (2010). Chondrogenic differentiation of human mesenchymal stem cells: a comparison between micromass and pellet culture systems. *Biotechnology Letters*, *32*(9), 1339–1346. https://doi.org/10.1007/s10529-010-0293-x.

Zhang, X., Qi, L., Chen, Y., Xiong, Z., Li, J., Xu, P., … Liu, K. (2019). The in vivo chondrogenesis of cartilage stem/progenitor cells from auricular cartilage and the perichondrium. *American Journal of Translational Research*, *11*(5), 2855–2865.

Zhang, Y., Yang, F., Liu, K., Shen, H., Zhu, Y., Zhang, W., … Zhou, G. (2012). The impact of PLGA scaffold orientation on invitro cartilage regeneration. *Biomaterials*, *33*(10), 2926–2935. https://doi.org/10.1016/j.biomaterials.2012.01.006.

Zhou, G., Jiang, H., Yin, Z., Liu, Y., Zhang, Q., Zhang, C., … Cao, Y. (2018). In Vitro Regeneration of Patient-specific Ear-shaped Cartilage and Its First Clinical Application for Auricular Reconstruction. *EBioMedicine*, *28*, 287–302. https://doi.org/10.1016/j.ebiom.2018.01.011.

Zhu, Y., Liu, T., Song, K., Fan, X., Ma, X., & Cui, Z. (2008). Adipose-derived stem cell: a better stem cell than BMSC. *Cell Biochemistry and Function*, *26*(6), 664–675. https://doi.org/10.1002/cbf.1488.

Zucchelli, E. (2018). *In vivo and in vitro characterisation of microtic ear cartilage: Potential of patient -derived ear and fat stem cells for cartilage engineering* Univeristy College London.

Zuk, P. A., Zhu, M., Mizuno, H., Huang, J., Futrell, J. W., Katz, A. J., … Hedrick, M. H. (2001). Multilineage cells from human adipose tissue: Implications for cell-based therapies. *Tissue Engineering*, *7*(2), 211–228. https://doi.org/10.1089/107632701300062859.

Zuk, Patricia A., Zhu, M., Ashjian, P., De Ugarte, D. A., Huang, J. I., Mizuno, H., … Hedrick, M. H. (2002). Human Adipose Tissue Is a Source of Multipotent Stem Cells. *Molecular Biology of the Cell*, *13*(12), 4279–4295. https://doi.org/10.1091/mbc.e02-02-0105.

**